

UNIVERSITY OF CALIFORNIA SAN DIEGO

Problems on viscous dynamics of passive and active microfilaments

A dissertation submitted in partial satisfaction of the
requirements for the degree
Doctor of Philosophy

in

Engineering Sciences (Applied Mechanics)

by

Brato Chakrabarti

Committee in charge:

Professor David Saintillan, Chair
Professor Juan Lasheras
Professor Stefan G. Llewellyn Smith
Professor Padmini Rangamani
Professor William R. Young

2019

ProQuest Number: 27545737

All rights reserved

INFORMATION TO ALL USERS

The quality of this reproduction is dependent on the quality of the copy submitted.

In the unlikely event that the author did not send a complete manuscript and there are missing pages, these will be noted. Also, if material had to be removed, a note will indicate the deletion.



ProQuest 27545737

Published by ProQuest LLC (2020). Copyright of the Dissertation is held by the Author.

All Rights Reserved.

This work is protected against unauthorized copying under Title 17, United States Code
Microform Edition © ProQuest LLC.

ProQuest LLC
789 East Eisenhower Parkway
P.O. Box 1346
Ann Arbor, MI 48106 - 1346

Copyright
Brato Chakrabarti, 2019
All rights reserved.

The dissertation of Brato Chakrabarti is approved, and
it is acceptable in quality and form for publication on
microfilm and electronically:

Chair

University of California San Diego

2019

DEDICATION

In fond remembrance of

ছোটমামা, বড়মামা আৰ জেন্ট্ৰু

PIGRAPH

*Ajñāna-timirāndhasya, jñānāñjana-śalākayā;
caksur-unmīlitaṁ yena, tasmai śrī-gurave namah.*

I could not see my path in the deep darkness of my ignorance;

My Guru (Teacher) with his knowledge opened my eyes.

I revere him.

—Dedicated to all my Gurus.

TABLE OF CONTENTS

Signature Page	iii
Dedication	iv
Epigraph	v
Table of Contents	vi
List of Figures	xii
List of Tables	xviii
Acknowledgements	xix
Vita	xxiv
Abstract of the Dissertation	xxv
Chapter 1 Introduction	1
1.1 Life at low Reynolds number	4
1.1.1 Stokes equation	5
1.1.2 Resistance and mobility	6
1.1.3 The representation theorem	8
1.2 Primer on selected topics	9
1.2.1 Brownian motion	9
1.2.2 Semiflexible polymers	11
1.3 Overview of present work	14
Chapter 2 Elasticity, hydrodynamics and fluctuations of slender structures . . .	16
2.1 Introduction	16
2.2 Elasticity of slender structures	17
2.2.1 Preliminary continuum mechanics	17

2.2.2	Hookean elasticity and geometric nonlinearities	21
2.2.3	Euler elastica	22
2.2.4	Aspects of buckling instabilities	27
2.3	Hydrodynamics of slender structures	29
2.3.1	Non-local slender body theory	30
2.3.2	Special case: local SBT	33
2.3.3	Brownian filaments	33
2.3.4	Nondimensionalization and boundary conditions	34
2.4	Computational methods	37
2.4.1	Discretization and tension	37
2.4.2	Time marching	39
2.4.3	Treatment of Brownian forces	39
2.4.4	Interactions and recent developments	41
2.5	Brownian motion in slender structures	42
2.5.1	Dynamics of Brownian rods	42
2.5.2	Scaling laws for semi-flexible filaments	46
2.6	Suppression of fluctuations	50
2.6.1	Actin in extensional flow	51
2.6.2	Pulling from the ends	53
2.7	Conclusions	55
 Chapter 3	Morphological transitions and rheology of actin in shear flow	56
3.1	Introduction	56
3.2	Polymer dynamics and conformations	58
3.2.1	Governing parameters and key features	58
3.2.2	Characterization of temporal dynamics	60
3.2.3	Order parameters	62
3.2.4	Buckling alters tumbling frequency	65
3.3	Morphological transitions: mechanisms	66
3.3.1	Origin of snaking motion: <i>J</i> shape	68
3.3.2	Dynamics of the <i>J</i> -shaped configuration	70

3.3.3	Dynamics of <i>U</i> -turns	75
3.4	Rheology of dilute suspension	78
3.4.1	Rheology of rigid rod suspension	79
3.4.2	Summary of asymptotic results	81
3.4.3	Computing stress for Brownian suspensions	82
3.4.4	2D non-Brownian simulations	84
3.4.5	A fictitious stress: role of fluctuations	85
3.4.6	Rheology of weakly deformable Brownian filaments	87
3.5	Conclusion	92
 Chapter 4	 Helical buckling of filaments in compressional flow	94
4.1	Introduction	94
4.2	Problem setup	95
4.3	Helical buckling: morphologies	97
4.3.1	Evolution of conformations	97
4.3.2	Quantitative characterization	100
4.3.3	Coiling radius and scaling laws	102
4.4	Origin of coiling: mode interaction	105
4.4.1	Linear stability analysis	106
4.4.2	Amplitude equations: weakly nonlinear theory	109
4.4.3	Spontaneous symmetry breaking	112
4.5	Conclusion and outlook	114
 Chapter 5	 Spontaneous oscillations of active microfilaments	117
5.1	Introduction to active filaments	117
5.2	Dynamics of cilia and flagella: overview	118
5.3	Model for axonemal beating	123
5.3.1	Viscous dynamics of an elastic filament	123
5.3.2	Forces, moment densities and motor kinetics	126
5.3.3	Non-dimensionalization	130
5.3.4	Numerical methods and parameter selection	132

5.4	Spontaneous filament oscillations	134
5.4.1	Linear stability and geometrically linear regime	134
5.4.2	Large deformations in the nonlinear regime	136
5.4.3	Asymmetric beating patterns	139
5.5	Waveform analysis	143
5.5.1	Tangent angle dynamics and motor populations	143
5.5.2	Reduced-order dynamics and limit cycles	145
5.6	Flow fields and fundamental singularities	149
5.6.1	Instantaneous and time-averaged flow fields	149
5.6.2	Singularity representation	153
5.7	Conclusion	156
Chapter 6	Elastohydrodynamic synchronization in pair filaments	157
6.1	Fundamentals of sync	157
6.2	Synchronization in cilia and flagella	158
6.3	Comments on waveforms	160
6.3.1	Symmetric sperm like beating	160
6.3.2	Waveforms of <i>Chlamydomonas</i>	161
6.3.3	Ciliary beating patterns	164
6.4	Review of the governing equations	165
6.5	Synchronization in sperm waveforms	165
6.6	Synchronization in ciliary beating	167
6.7	Adler equation and minimal models	168
6.8	Biochemical noise: phase slips	173
6.9	Conclusions	176
Chapter 7	Transport of semiflexible filaments in porous media	177
7.1	Introduction	177
7.2	Problem setup and methods	180
7.3	Results and discussion	182
7.3.1	Modes of transport	182

7.3.2	Probability distributions and filament trajectories	184
7.3.3	Asymptotic transport and hydrodynamic dispersion	188
7.4	Chromatographic separation	192
7.5	Concluding remarks	194
 Chapter 8		
	Shear dispersion in peristaltic pumping	196
8.1	Introduction	196
8.2	Problem definition	199
8.2.1	Review of peristaltic flow	199
8.2.2	Brief review of Brenner's theory	201
8.3	Hydrodynamics: long wavelength approximation	207
8.4	Dispersion in the long wavelength approximation	211
8.4.1	Fokker-Planck in the translating frame	211
8.4.2	Asymptotic moments and mean velocity of transport . .	212
8.4.3	Dimensionless B -field equation and boundary conditions	213
8.4.4	Asymptotics for large and small Péclet	217
8.4.5	Brownian simulations	219
8.4.6	Results	221
8.5	Beyond small aspect ratio	224
8.5.1	Boundary integral for hydrodynamics	224
8.5.2	Finite volume method for dispersivity	226
8.5.3	Numerical method and validation	228
8.6	Results and Discussion	231
8.6.1	Pure diffusion	231
8.6.2	Effect of re-circulation	233
8.7	Concluding remarks	236
 Chapter 9	Concluding remarks and future direction	238
9.1	Conclusion	238
9.2	Ongoing work and future directions	240
 Appendix A	Measurement of bend radius	243

Appendix B	Diatom chains and regularized Stokeslets	245
B.1	Fiber model as a network of springs	245
B.2	Method of regularized Stokeslets	246
B.3	Simulation parameters and computed values	249
Appendix C	Adjoint operator of the linearized SBT	251
Appendix D	Algorithm for filament contact	253
Bibliography	255

LIST OF FIGURES

Figure 1.1: Schematic of geometry considered for the representation theorem.	8
Figure 1.2: Conformation of a semiflexible polymer at different length scales. Image borrowed from [1].	12
Figure 2.1: Schematic of a solid object deforming from its reference condition $\Omega(0)$ to its current configuration $\Omega(t)$	18
Figure 2.2: Schematic of a space curve embedded in \mathbb{E}^3 and parameterized by arc length s . The Frenet-Serret triad is shown on the curve.	20
Figure 2.3: Examples of geometric nonlinearities in nature.	22
Figure 2.4: Schematic showing stretching and bending of a slender elastic rod. . . .	24
Figure 2.5: Schematic showing force and moment balance for an inextensible, un-shearable, planar elastic rod.	25
Figure 2.6: Examples of buckling instabilities in nature.	28
Figure 2.7: Schematic of a cylindrical slender object with diameter a and length L . .	30
Figure 2.8: Boundary conditions for a Brownian filament in viscous flow.	37
Figure 2.9: Typical orbits of prolate spheroids in simple shear flow for different orbit constants.	44
Figure 2.10: Diffusion and advection dominated regimes of a rigid rod tumbling in 2D shear flow.	46
Figure 2.11: Monge representation of a fluctuating filament.	48
Figure 2.12: End-to-end fluctuations of actin filaments in extensional flow. Simulations are compared against experimental results of [2] and from [3]. . . .	51
Figure 2.13: Schematic of a polymer getting pulled from two ends.	53
Figure 2.14: Force extension curve for an actin filament with $\ell_p/L = 1.8$	54
Figure 3.1: Morphologies of actin filaments in shear flow.	59
Figure 3.2: Time evolution of geometric and dynamic order parameters for filaments in shear flow.	61
Figure 3.3: Evolution of order parameters as a function of the elastoviscous number. .	63

Figure 3.4: Scaling of tumbling frequency as a function of dimensionless flow strength.	65
Figure 3.5: Phase chart showing relevant regimes of morphological transitions of actin filaments.	66
Figure 3.6: Statistics of number of <i>C</i> shaped buckling as a function of the elastoviscous number.	68
Figure 3.7: Initiation of the <i>J</i> shape.	69
Figure 3.8: Schematic of the theoretical model for the <i>J</i> shape.	70
Figure 3.9: Comparison of geometric parameters predicted from theory against experimental and numerical results.	76
Figure 3.10: Signature of buckling in shear stress and the normal stress difference. We observe shear-thinning and positive normal stress. Parameter values: $\bar{\mu}/c = 1 \times 10^4$	84
Figure 3.11: A fictitious measure of extra stress illustrating the role of buckling instabilities and fluctuations.	86
Figure 3.12: Shear viscosity of a filament with $\ell_p/L = 1000$ as a function of the elastoviscous number.	88
Figure 3.13: Coefficient of normal stress and the first normal stress difference as a function of the elastoviscous number.	89
Figure 3.14: Various components of the stress tensor as a function of the elastoviscous number from 2D simulations.	90
Figure 3.15: η and Ψ_1 as a function of $\bar{\mu}/c$. Pre-buckling we have, $\eta \sim \bar{\mu}^{-1/3}$ and $\Psi_1 \sim \bar{\mu}^{-4/3}$. Post-buckling we have $\eta \sim \bar{\mu}^{-1/2}$ and $\Psi_1 \sim \bar{\mu}^{-1}$	91
Figure 4.1: Geometry of the microfluidic setup and the essential features of the velocity field.	96
Figure 4.2: Time evolution of filament morphologies reveal emergence of helical conformations in strong flows.	98
Figure 4.3: Projection of filament cross-section for the cases presented in Figure 4.2.	99
Figure 4.4: Filament conformations from non-Brownian simulations with finitely extendible filaments.	99
Figure 4.5: Schematics illustrating methods to characterize filament conformations.	100

Figure 4.6:	Post buckling evolution of the end-to-end distance and coil radius of the filaments.	101
Figure 4.7:	Measurement of radius from experiments and two different simulations confirm the proposed scaling law.	103
Figure 4.8:	Schematic illustrating the compression of an inextensible ideal helix of radius R and pitch p as used for scaling arguments.	104
Figure 4.9:	Eigenspectra for the linear stability problem and associated unstable mode shapes.	108
Figure 4.10:	Time evolution of the amplitudes of modes for $\bar{\mu} = 1.8 \times 10^4$.	112
Figure 4.11:	Shape evolution from weakly non-linear theory compared against non-Brownian simulations.	113
Figure 4.12:	Three-dimensional buckling of a very long actin filament placed in a linear shear flow.	115
Figure 4.13:	Evolution of the bending energy showing a favorable energy landscape after helical buckling.	116
Figure 5.1:	Electron micrograph image of the cross section of <i>Chlamydomonas</i> axoneme and a simple schematic.	119
Figure 5.2:	Schematic of a clamped elastic rod that serves as a model of cilia.	123
Figure 5.3:	Schematic of the 2D model of axoneme with molecular motors and protein linkers.	128
Figure 5.4:	Phase chart highlighting different modes of possible oscillations.	137
Figure 5.5:	Dependence of amplitude, wavelength and frequency with activity of molecular motors.	138
Figure 5.6:	Three distinctive waveforms obtained from the present model.	141
Figure 5.7:	Power spectral density of the averaged tangent angle for sperm and <i>Chlamydomonas</i> like beating patterns.	143
Figure 5.8:	Oscillations in the population of molecular motors for different waveforms.	144
Figure 5.9:	Kymographs, covariance matrix and PCA modes for sperm and ciliary beating patterns.	146

Figure 5.10: Limit cycle representation of sperm-like and ciliary beating patterns. . .	148
Figure 5.11: Instantaneous velocity fields for different waveforms in free-space and against a no-slip wall.	150
Figure 5.12: Time-averaged velocity fields and their far-field decay.	152
Figure 5.13: PCA modes for sperm-like beating.	153
Figure 5.14: Instantaneous velocity fields reconstructed with distribution of regularized Stokeslets.	155
Figure 6.1: Several sperm-like waveforms in mediums with varying viscosity.	161
Figure 6.2: Modal analysis of Chlamydomonas waveform.	163
Figure 6.3: Possible ciliary beating patterns under pure sliding (left) and a combination of sliding and curvature (right) control.	164
Figure 6.4: In-phase synchronization of anterograde sperm waveforms.	166
Figure 6.5: Evolution of motor populations during the process of synchrony and a cartoon illustrating the feedback mechanism.	167
Figure 6.6: In-phase and anti-phase synchronization in ciliary beating patterns. . .	168
Figure 6.7: Phase evolution in the process of synchronization and variation of coupling constant with distance.	169
Figure 6.8: Schematic of coarse-grained minimal model where the beating filaments are represented as rotors on circular orbits [4].	170
Figure 6.9: Phase dependent force profile used to drive the micro-spheres.	171
Figure 6.10: Fluctuations in the synchronized state due to biochemical noise and effective interaction potentials.	174
Figure 6.11: Comparison of the measured frequency of phase slips G in s^{-1} to the analytical prediction.	175
Figure 7.1: Streamlines inside an unit cell for two different lattice porosity and incidence angle of the flow.	181
Figure 7.2: Schematic of the 2D lattice and a representative unit cell.	182
Figure 7.3: Fundamental modes of polymer transport in porous media.	183

Figure 7.4: Polymer conformation and the center-of-mass distribution over an unit cell.	185
Figure 7.5: Probability distribution of polymer center-of-mass for different flow strengths. Parameter values identical to that in Figure 7.4 with $\Theta = \pi/6$	186
Figure 7.6: Overlayed polymer conformations reveal periodic, quasi-periodic and chaotic trajectories.	187
Figure 7.7: Power spectral density of the mean orientation angle ϕ of the filament with the flow as a function of dimensionless frequency.	188
Figure 7.8: Components of the mean squared displacement as a function of time for two different incidence angles of the streaming flow.	190
Figure 7.9: Variation of dispersivity as a function of flow strength and incident flow angle.	191
Figure 7.10: Chromaotographic sorting of polymers in porous media.	193
Figure 8.1: Cartoon of the periodic geometry and unit cell.	202
Figure 8.2: Snapshot of Brownian simulations for $\epsilon = 0.05$, $\gamma = 0.3$ and $Pe = 50$. . .	221
Figure 8.3: Mean squared displacement, $\sigma^2(t)$ as function of time and the linear fit from which dispersivity. The parameters are identical to that of figure 8.2.	221
Figure 8.4: Variation of effective dispersivity with Pe calculated quadratures and its comparisons with Brownian simulations and large Pe asymptotics. . .	223
Figure 8.5: Collocation points for approximating the boundary.	225
Figure 8.6: Mapping between physical and computational domain.	227
Figure 8.7: Representative contour plot of b^* field for $\epsilon = 0.7$ and $\gamma = 0.4$ in the diffusive limit. Only upper half of the channel is shown.	232
Figure 8.8: Streamlines (on left) and contour lines of b^* field for $Pe = 20$. The aspect ratio of the channel, $\epsilon = 0.7$ and width modulation parameter, $\gamma = 0.4$	233
Figure 8.9: Same conditions as in figure 8.8 except now the width modulation parameter, $\gamma = 0.6$. This leads to recirculation bubbles in the flow.	234

Figure 8.10: Variation of the effective dispersivity, d^* with Pe number for $\epsilon = 0.7$ with different pore openings. Recirculation bubbles exist only for $\gamma = 0.6$.	234
Figure 8.11: Appearance of re-circulation bubbles for different aspect ratio at a fixed pore opening of, $\gamma = 0.5$.	235
Figure 8.12: Variation of the effective dispersivity, d^* with Pe number for $\gamma = 0.5$ with different aspect ratios. Streamlines for each of the cases are shown in figure 8.11.	236
Figure A.1: Variation of curvature κ along the filament centerline for a typical J shape chosen from a simulation. The length marked as δ_s provides an estimate for the arclength of the bent portion.	244
Figure B.1: Schematic of a non-Brownian filament comprised of network of Hookean springs as viewed from the side (a) and from the end (b).	246
Figure B.2: Schematic of channel from non-Brownian simulations.	249
Figure D.1: Schematic of a polymer close to contact with a pillar and the relevant quantities.	254

LIST OF TABLES

Table 3.1: Asymptotic forms of relevant rheological measures [5, 6].	82
Table 5.1: Table listing the numerical values of the dimensional parameters as reported in various experiments.	133
Table 5.2: Range of the dimensionless groups of the problem estimated using the parameter values of Table 5.1	134
Table 8.1: Comparison between effective diffusivity between FVM and asymptotics in absence of flow ($\text{Pe} = 0$). The aspect ratio for the FVM simulation was chosen to be, $\epsilon = 0.05$	230
Table 8.2: Comparison of effective dispersivity, d^* , between Brenner's theory and Brownian dynamics for a channel with $\epsilon = 0.7$ and $\gamma = 0.2$	231
Table 8.3: Effect of varying geometric parameters in the pure diffusive limit.	232
Table B.1: Simulation parameters and computed values from non-Brownian simulations.	250

ACKNOWLEDGEMENTS

This is the most read section of a thesis and probably the only one that is entirely due to me. Please bear with me if this is long.

SME 344C, La Jolla

Not out of convention but simply due to sheer importance I would like to thank my advisor David Saintillan for his patience, guidance, and support that made this thesis possible. David has provided me the independence and presented the resources to pursue virtually anything and everything that I wished for during my Ph.D. and has always encouraged me to take up fundamental problems. Whenever I got lost in details of a problem, David made sure that I did not lose the sight of the bigger picture. Besides being a wonderful mentor with the eyes to identify important problems, David has been an inspiration as a teacher and I owe all my knowledge of viscous flow to him. Thank you for everything!

I would also like to thank my committee members: Juan Lasheras for always being there for help and suggestions, Stefan Llewellyn Smith for his comments on my work and proof-reading every line of this thesis, Padmini Rangamani for suggestions on how to improve my presentation and career advice and William Young for wonderful lectures on asymptotics and for pointing me to subtle issues related to kinetic theory and Brownian motion. I am also thankful to Mike Shelley at the Courant Institute for several comments and discussion on the work, Lisa Fauci at Tulane University and Cristina Marchetti at UC Santa Barbara for fruitful discussions.

Streets of Paris

I have been extremely fortunate that I had an opportunity to be a part of a collaboration with Anke Lindner and Olivia du Roure at ESPCI, France. Besides the wonderful

papers from the collaboration they have been very kind and warm in inviting me to visit Paris several times to work on exciting problems that have led to an exchange of various interesting ideas and I have been able to appreciate the importance of experiments. I am especially thankful to Anke for all the carrier advice, unconditional support, and help. I hope that this is just the start of our collaboration.

I want to thank Yanan Liu who did the heavy lifting in Paris, doing all the difficult experiments with actin filaments. Yanan's infectious enthusiasm and critical questions coupled with envious Matlab skills made us a great team.

Polar vortex in Virginia

Before my westward journey in search of better weather, I stayed in Virginia for two years doing mechanics. My story is incomplete without my friends and family there. James Hanna, my advisor had the most profound impact on me in terms of scientific philosophy. I am grateful to him for his frequent emails, support, life advice. I am glad that I knew you!

Saikat Da and Hossain Da have been like my elder brothers who have loved me unconditionally. I have learnt a lot about life and academia from both of them. They have put a lot of faith in me and I could always rely on them whenever I felt lost. I cannot thank you two enough.

Saurabh knows how important he has been in my life. He can fit in any section of this acknowledgment since our interactions have spanned a decade over continents. Paris would have been half as good without his craziness, Blacksburg much colder and fluid dynamics would not have been fun without you!

Back to the sunny shores: 9226 A

My happy memories of Ph.D. are largely due to the wonderful people around me in San Diego. To begin with I would like to thank all the group members. In particular

Hari for being the go-to person, Roberto for uncountable trips to Indian restaurants and for a great collaboration, and finally Achal for being the soundboard for all the academic problems of my life. I would also like to thank Deba, Barath, Max, Danny, Piyush, Yixuan, Hossein, Albert and Charles for all the fun memories. I have learnt a lot about science from you people. It was great to share the corridor and space with people who bright up the usual days: Asish, Ernesto, Gopesh, Jenny and Lucas. This goes out to you. And finally thanks to the administrative staff at the MAE department and especially to Lusia who ensured things are always running smooth.

San Diego would not have been sunny without our routine Friday night parties with a crazy group of friends at 9226A Regents Road. In particular, I will always cherish my endless conversations, road-trips and gastronomical adventures with Ahanjit, Shouvik and Sridip. Apart from being my lifeline in San Diego, you guys have taught me puzzles, maths, history, language, and have always amazed me with your wit and smartness. The love and passion of you folks to do science have also been a great inspiration for me. I am thankful to you guys for always sticking with me. I also cherished my friendship with Bodhi and Sumit, and all the fun memories that we had during our road-trip. Finally, I would like to thank Anindita Mami and Netai Mama for their love, affection, parties and constant support. I was quite blessed to have you guys as my home away from India.

The heroes

Perhaps a bit unconventional but this goes out to all the great minds and people out there who made a difference in my life but whom I never met. A big shout out to folks who take time to answer and solve problems on Stack Exchange. Because of you, people like me can be lousy and afford to forget resolutions to compiling errors over and over again. My life would have been frustrating without your help. I want to thank Professor V. Balakrishnan for his incredible set of lectures on Classical Mechanics, Nonlinear Dynamics

and Statistical Mechanics that motivated me to pursue research along similar lines. I am grateful to the great *Sarod* and *Sitar* maestros for their divine music that never failed to wash away my worries after a struggling day.

We, the people

Finally, this is to all my beloved ones from home. The best time of my life was spent at Jadavpur University during my undergrad where I made a lot of great friends. Pratyaya and Saurav have been my friends to discuss and Sumit to debate football. Discussions with Spandan covered life, politics and beyond. I cannot thank him enough for his love and support over the years. And finally, Subhra has been my go-to person for all the little problems in life: from relationship to academia. I could share all my insecurities with him for I knew that he will understand. You guys made me believe! I would like to thank my teachers at Jadavpur University particularly Debabrata Nag, Himadri Chattopadhyay and Sumanta Neogi for all the encouragement, love and teachings.

Words can't explain what my parents meant to me during this journey. I could have never done this without the love and support from you guys and kaka. Not to mention all the sacrifices you made for me. I am forever indebted to Ma for invoking the love for *Hindustani* classical music that has been my source of inspiration and to Baba for teaching me the joy of science. Everything here is because of you people. I hope this thesis puts up a smile on your face! Finally thank you Shreya for all the love over the last decade, for putting up with the not-so-good me, for never losing faith and for always staying strong by my side.

My life, my ideas and my values that have guided me all these years were shaped by the people I grew up with. I am grateful to all of them. I hope and I hope that this thesis is a step towards coming back home. *We, the people...*

Chapter 3 is primarily based on the material that has appeared in *Proceedings of the National Academy of Sciences* (2018), authored by Yanan Liu, Brato Chakrabarti, David Saintillan, Anke Lindner and Olivia du Roure [7]. The dissertation author performed numerical simulations and worked on theoretical modeling for this paper.

Chapter 4 is primarily based on the material that is presently under review and is authored by Brato Chakrabarti, Yanan Liu, John LaGrone, Ricardo Cortez, Lisa Fauci, Olivia du Roure, David Saintillan and Anke Lindner [8]. The dissertation author performed numerical simulations and worked on theoretical modeling for this paper.

Chapter 5 is primarily based on the material published in *Physical Review Fluids* (2019) authored by Brato Chakrabarti and David Saintillan [9]. The dissertation author was the primary researcher and author of this paper.

Chapter 6 is primarily based on the material published in *Physical Review Letters* (2019) authored by Brato Chakrabarti and David Saintillan [10]. The dissertation author was the primary researcher and author of this paper.

Chapter 7 in part is a manuscript in preparation authored by Brato Chakrabarti, Charles Gaillard and David Saintillan. The dissertation author was the primary researcher of this work.

Chapter 8 in part is a manuscript in preparation authored by Brato Chakrabarti and David Saintillan. The dissertation author was the primary researcher of this work.

VITA

- 2013 B.E in Mechanical Engineering
 Jadavpur University, Kolkata (India)
- 2015 M.S in Engineering Sciences and Mechanics
 Virginia Polytechnic Institute and State University
- 2019 PhD in Engineering Sciences (Applied Mechanics)
 University of California, San Diego

ABSTRACT OF THE DISSERTATION

Problems on viscous dynamics of passive and active microfilaments

by

Brato Chakrabarti

Doctor of Philosophy in Engineering Sciences (Applied Mechanics)

University of California San Diego, 2019

Professor David Saintillan, Chair

The dynamics and morphological transitions of elastic filaments and semiflexible polymers in viscous fluids underlie the complex non-Newtonian behavior of their suspensions and also play a role in many small-scale biophysical processes from ciliary and flagellar propulsion to intracellular streaming. Elucidating the physics behind the dynamic microstructural instabilities and transitions of such elastic filaments is key to unraveling the mechanisms underlying their complex rheological behaviors, from shear thinning and normal stress differences to viscoelastic instabilities. In this work, we use slender-body-theory from low Reynolds number hydrodynamics along with tools from nonlinear stability theory and scaling analyses to understand various problems relevant to suspension dynamics and biophysics. After discussing numerical experiments that probe fluctuations in semiflexible

polymers we proceed to explain morphological instabilities of passive actin filaments in simple shear flow and their role in the rheology of dilute suspensions. We then analyze a spontaneous symmetry-breaking instability of lone actin filaments in compressional flow that gives rise to chiral structures and draw similarities with classical helical buckling of elastic rods. Both of these studies are complemented by microfluidic experiments performed by collaborators as well as analytical solutions to simplified dynamical systems. We then turn to the dynamics of active filaments that are driven by molecular motors. Far from equilibrium, these filaments undergo a Hopf bifurcation leading to spontaneous oscillations that mimic the beating patterns of eukaryotic cilia and flagella. We elucidate the crucial roles of hydrodynamics and biochemical noise in their collective behavior and highlight the relevance of our model in the context of biological experiments. Finally, we study the asymptotic transport properties of Brownian filaments in 2D porous media and of passive tracers in 1D lattices. Our computations identify various modes of filament transport that involve trapping, gliding and vaulting past obstacles, and suggest a design for a chromatographic device. Studies with passive Brownian tracers in peristaltic pumping explain how dispersion is altered due to shear and the presence of entropic traps and barriers.

Chapter 1

Introduction

This thesis is a collection of problems that can be considered as an excursion to the interface of soft-matter, biological physics and fluid-structure interaction with one dimensional elastic continua in highly viscous flows. Soft matter or soft condensed matter is an outgrowth of condensed matter physics that comprises a variety of physical systems that can be structurally manipulated by thermal or mechanical stress of the magnitude of thermal fluctuations. Pierre-Gilles de Gennes, often called as the ‘founding father of soft matter’ physics, provided a number of illustrative examples and utilities of soft materials in his 1991 Nobel prize lecture, when the field was emerging [11]. He pointed out that in the spirit of Americans calling soft-matter as ‘complex-fluids’, two major characteristics of the subject are its apparent *complexity* and *flexibility* that are evident in numerous examples of dynamics of polymers, surfactants, colloids, foams, gels and liquid crystals. It is beyond the scope of this thesis to discuss all such examples, and the interested reader is pointed to available standard texts [12–14]. Here we discuss one fascinating example concerning polymer dynamics that is borrowed straight from de Gennes’ lecture [11] and serves as a good motivation for the central theme of the present work.

Andrew Keller and his co-workers presented a beautiful experiment where a dilute

solution of flexible polymers (or coils) was subjected to a purely longitudinal shear achieved by a four-roller setup [15]. It was found that beyond a critical shear rate $\dot{\gamma}_c$ the medium became birefringent and this was termed the ‘coil-stretch transition’ by de Gennes [16]. This phase-transition can be attributed entirely to hydrodynamics, and has to do with the flexible chain offering more ‘grip’ to the flow as it opens up due to shear. The example emphasizes a key aspect of soft-matter physics and also highlights the backbone of this thesis: *the coupling between mechanics and conformations*. This central idea is explored in all the problems presented here in the spirit of fluid-structure interaction problems in viscous flow. We will focus on how competition between hydrodynamic and elastic forces of polymers shape the emerging conformations that in turn dictate macroscopic properties.

Typical examples where polymer conformations and their dynamical behaviors in viscous flow result in emergent behavior arise in the field of *biophysics* and *rheology*. Inside all cells including bacteria and archea is a complex dynamic network of interlinked protein filaments known as the *cytoskeleton* that forms the backbone of the cytoplasm [17]. The cytoskeleton involves stiff biological polymers like actin, microtubules and certain intermediate filaments [17]. Actin filaments have the ability to resist tension and compression, allowing them to provide structural integrity to the cell membrane. They also participate in important sub-cellular processes involving cell-signaling, muscle contraction and cytoplasmic streaming [18,19]. Microtubules are another biopolymer made of tubulin that are typically stiffer compared to actin and participate in intra-cellular transport, cell-division and gene regulations. Microtubules are also central to the internal structure of thin hair-like cellular appendages called ‘cilia’ and ‘flagella’ that help eucaryotic cells like sperm, *Chlamydomonas* and *Paramecium* to swim in viscous environment. Collective beating of cilia results in metachronal waves that are responsible for large-scale fluid flows which help in mucus transport and play a crucial role in developmental biology [20,21]. Finally one of

the most important and well-studied biological macromolecules is Deoxyribonucleic acid (DNA). This molecule is composed of two chains that coil around each other to form a double helix carrying genetic instructions for the development, functioning, growth and reproduction of all known organisms and many viruses.

DNA has been pretty much the model polymer used to study and understand dynamics of flexible chains in flows. Indeed, almost 30 years after de Gennes's theoretical prediction of a hysteresis loop in polymer solutions in extensional flow, Schroeder *et al.* [22] were the first to observe this experimentally with λ -DNA. The case of such long-chain polymers [23], for which the persistence length ℓ_p is much smaller than the contour length L , has been characterized extensively in experiments [22, 24] as well as in numerical simulations [25] and mean-field models [26]. The dynamics in this case is governed by the competition between thermal entropic forces favoring coiled configurations and viscous stresses that tend to stretch the polymer in strain-dominated flows. The interplay between these two effects is responsible for the coil-stretch transition in elongational flows and tumbling and stretching motions in shear flows, both of which are well captured by classic entropic models [27–29] that approximate the flexible polymer chain as monomers (beads) connected to each other by springs. On the contrary, the dynamics of shorter polymers such as actin filaments [30], for which $L \sim \ell_p$, has been much less investigated and is still not fully understood. Here, it is the subtle interplay of bending forces, thermal fluctuations and internal tension under viscous loading that instead dictates the dynamics. This distinguishes these filaments from long entropy-dominated polymers such as DNA in which chain bending plays little role. The dynamics and conformational transitions of these polymers and elastic filaments in viscous fluids also underlie the complex non-Newtonian behavior of their suspensions [31]. The striking rheological properties of polymer solutions hinge on the microscopic dynamics of individual polymers, and partic-

ularly on their rotation, stretching and deformation under flow in the presence of thermal fluctuations. Elucidating the physics behind these microstructural instabilities and transitions is key to unraveling the mechanisms for their complex rheological behaviors [32], from shear thinning and normal stress differences [33] to viscoelastic instabilities [34] and turbulence [35].

As highlighted throughout the above discussion, the dynamics of elastic filaments and polymers requires modeling of their deformation, hydrodynamics in the low Reynolds number regime and the thermal fluctuations. In the next chapter we delve into the detailed hydrodynamic framework known as the ‘slender body theory’ particularly suitable for modeling slender filaments and discuss associated geometrically nonlinear elasticity theories. The rest of this chapter is devoted to outline the foundational principles that come up in the following chapters. After discussing general properties of Stokes flow in the next section we will briefly review Brownian motion and basic models for semiflexible polymers.

1.1 Life at low Reynolds number

As discussed previously we are interested in studying dynamics of solid or deformable particles in viscous flow. The governing equations of motion are the classical Newton’s laws for the particles and the Navier-Stokes equation for the suspending fluid which is the continuum version of Newton’s second law applied to material points in the fluid. We are interested in the limit of creeping flows where both the fluid and particle inertia are negligible compared to the viscous forces. This can be translated in terms of the Reynolds and Stokes number as:

$$Re = \frac{\rho UL}{\mu} \rightarrow 0, \quad St = \frac{mU}{6\pi\mu L^2} \rightarrow 0, \quad (1.1)$$

where ρ and μ are the density and viscosity of the suspending fluid, L and m are the particle size and mass respectively, and U is a characteristic velocity scale of the particle with respect to the fluid. It is instructive to note that for biopolymers the typical length and velocity scales are $L \sim \mathcal{O}(\mu\text{m})$ and $U \sim \mathcal{O}(\mu\text{m/s})$. If we take water as the suspending medium then the Reynolds number turns out to be $\mathcal{O}(10^{-5} - 10^{-4})$. Similar scaling arguments are true for swimming microorganisms [36] and various microfluidic applications [37] where both the length and velocity scales involved are small. But this need not be the case for the low Reynolds number approximation to hold true. For example, flows in glaciers involve large length scales, but their velocity scales are extremely small, $\sim \mathcal{O}(\text{m}/\text{years})$ and the flows typically have much higher viscosity, rendering the approximation of creeping flow valid.

1.1.1 Stokes equation

In the limit of $Re \rightarrow 0$ the Navier-Stokes equation simplify considerably and the fluid motion is described by the following linear Stokes equation:

$$-\mu\nabla^2\mathbf{u} + \nabla p = \mathbf{0}, \quad \nabla \cdot \mathbf{u} = 0, \quad (1.2)$$

where $\mathbf{u}(\mathbf{x})$ is the velocity field and $p(\mathbf{x})$ is the pressure field that acts as a Lagrange multiplier in enforcing incompressibility. We notice that the governing equations do not involve time. This suggests that unsteadiness in flow can only be a result of time-dependent forcing or boundary conditions. Since the governing equations are linear the velocity field is always proportional to the driving force, which makes the steady Stokes equation time reversible. In other words a reversal in the direction of forcing reverses velocity field at all the points instantaneously. This is wonderfully demonstrated in a classic experiment designed by G.I. Taylor [38] and has profound consequences for the swimming of micro-organisms [36]. A number of physical problems can be understood based on these principles, and for an

extensive discussion the interested reader is pointed to [39].

1.1.2 Resistance and mobility

A fundamental problem of interest in Stokes flow is obtaining the dynamics of a single or collection of particles in a flow-field. This requires solving the Stokes equation (1.2) subjected to the no-slip boundary condition:

$$\mathbf{u}(\mathbf{x}) = \mathbf{U}_\alpha + \boldsymbol{\Omega}_\alpha \times \mathbf{x}, \quad \text{for } \mathbf{x} \in S_\alpha, \quad (1.3)$$

where \mathbf{U}_α and $\boldsymbol{\Omega}_\alpha$ is the rigid-body translational and rotational velocity and S_α is the surface of a given solid particle α . For the moment we restrict ourselves to dynamics of rigid particles and avoid discussions of complex boundary conditions on deformable surfaces like drops or bubbles [40]. Far away from the particles or walls the fluid velocity must decay to the external flow field that is assumed to be known:

$$\mathbf{u}(\mathbf{x}) \rightarrow \mathbf{u}^\infty(\mathbf{x}) \quad \text{as } |\mathbf{x}| \rightarrow \infty. \quad (1.4)$$

If the particle motion is known, then we can solve (1.2) subject to the appropriate boundary conditions. However in most cases the particle motions are unknown and it need to be determined as part of the problem. For this we use Newton's laws of motion for the particles in the limit of zero Stokes number, which yields:

$$\mathbf{F}_\alpha^H + \mathbf{F}_\alpha^E = \mathbf{0}, \quad \mathbf{T}_\alpha^H + \mathbf{T}_\alpha^E = \mathbf{0}, \quad (1.5)$$

where $\mathbf{F}_\alpha^{H,E}$ and $\mathbf{T}_\alpha^{H,E}$ denote the hydrodynamic and externally imposed forces and torques on the particles. The hydrodynamic forces and torques can be computed from the traction as follows:

$$\mathbf{F}_\alpha^H = \int_{S_\alpha} \sigma(\mathbf{x}_\alpha) \cdot \mathbf{n}^\alpha dS_\alpha, \quad \mathbf{T}_\alpha^H = \int_{S_\alpha} \mathbf{x}^\alpha \times [\sigma(\mathbf{x}_\alpha) \cdot \mathbf{n}^\alpha] dS_\alpha, \quad (1.6)$$

where $\boldsymbol{\sigma} = -p\mathbf{I} + \mu [\nabla \mathbf{u} + \nabla \mathbf{u}^T]$ is the Newtonian stress tensor in the fluid. We now notice that since the Stokes equations are linear, the velocity field \mathbf{u} will be linear in the forcing \mathbf{U}_α . Since the stress-tensor is linear in the velocity field the hydrodynamic force \mathbf{F}_α^H will also be linear in the forcing \mathbf{U}_α . One can argue along similar lines to establish a linear relationship between the hydrodynamic torque \mathbf{T}_α^H and the angular velocity Ω_α . We exploit this to write the most-general relationship between the forces (or torques) and velocity (or angular velocity) as:

$$\mathbf{F}_\alpha^H = -\mathcal{R} \cdot \mathbf{V}_\alpha, \quad (1.7)$$

where $\mathbf{F}^H = [\mathbf{F}^H; \mathbf{T}^H]$ and $\mathbf{V} = [\mathbf{U}; \boldsymbol{\Omega}]$ are six-dimensional vectors containing forces and velocities. \mathcal{R} is a 6×6 matrix termed the resistance tensor. For an isolated axisymmetric and isotropic particle the resistance matrix is diagonal which suggests that there is no coupling between rotation and translation [39]. However for chiral objects this is often not the case and the matrix is typically dense with off-diagonal terms that couple rotational and translational motion. This coupling allows micro-organisms like *E. Coli* to translate by rotating a helical flagella [36]. One can re-arrange Equation (1.7) to obtain:

$$\mathbf{V}_\alpha = \mathcal{M} \cdot \mathbf{F}_\alpha^E, \quad (1.8)$$

where $\mathcal{M} = \mathcal{R}^{-1}$ is the mobility matrix. As an illustrative example we note that a spherical particle of radius a translating with a velocity \mathbf{U} experiences Stokes drag given by: $\mathbf{F}^H = -6\pi\mu a \mathbf{U}$. The resistance matrix in this example is simply given by $\mathcal{R} = 6\pi\mu a \mathbf{I}$. In many problems related to flows of particulate matter in Stokes flow it becomes pivotal to compute the resistance or mobility tensors. In Chapter 2 we will compute the mobility matrix for a deforming elastic filament and see how knowing these tensors allows one to understand Brownian fluctuations.

1.1.3 The representation theorem

We now focus on an integral representation of the solutions to the Stokes equations. This is obtained from the representation theorem that states: the velocity field at any point inside a fluid domain can be represented in terms of the traction fields on the boundaries of the domain. The theorem is a consequence of the linearity of the Stokes equation and the derivation relies on generalized reciprocal theorem and fundamental solutions of the Stokes equations [41, 42]. We avoid the details of the derivation and present the main result here.

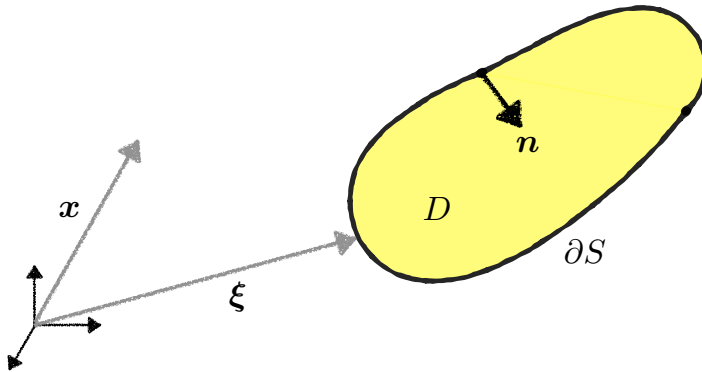


Figure 1.1: Schematic of geometry considered for the representation theorem.

Consider a particle shown in Figure 1.1 with a surface ∂S that separates a finite domain D from the space and \mathbf{n} is the inward unit normal on ∂S . The representation theorem allows us to express the velocity at any point in the domain in terms of two convolution integrals on the surface ∂S . In index notation this is given by:

$$u_i(\mathbf{x}) = u_i^\infty(\mathbf{x}) - \frac{1}{8\pi\mu} \int_{\partial S} G_{ij}(\mathbf{x} - \boldsymbol{\xi}) f_j(\boldsymbol{\xi}) dS - \frac{1}{4\pi} \int_{\partial S} T_{ijk}(\mathbf{x} - \boldsymbol{\xi}) u_j(\boldsymbol{\xi}) n_k(\boldsymbol{\xi}) dS, \quad (1.9)$$

where $\mathbf{f}(\boldsymbol{\xi}) = \mathbf{n} \cdot \boldsymbol{\sigma}(\boldsymbol{\xi})$ is the traction on ∂S , \mathbf{G} is the Green's function for the velocity field (also known as the Oseen-tensor) and \mathbf{T} is the associated stress tensor:

$$G_{ij}(\mathbf{x}) = \frac{\delta_{ij}}{x} + \frac{x_i x_j}{x^3}, \quad T_{ijk}(\mathbf{x}) = \frac{1}{2} [G_{ij,k}(\mathbf{x}) + G_{ik,j}(\mathbf{x})] = -3 \frac{x_i x_j x_k}{x^5}. \quad (1.10)$$

A couple of comments are in order. The integral representation in Equation (1.9), sometimes known as the boundary integral equation, allows one to compute the velocity field at any point in the domain with the knowledge of the traction and velocity on the surface ∂S . The integral equation representation is extremely useful since it reduces the dimensionality of the problem by one. We can now compute three-dimensional field variables by solving problems on two dimensional surfaces. This gives rise to a set of numerical techniques known as the boundary element method [40]. In Chapter 2 we will see that how for slender objects like elastic filaments or polymers the boundary integral equations can be asymptotically reduced on a curve giving rise to the *slender body theory*.

Before closing our discussion on Stokes flow it is important to point out that the Green's function G_{ij} provided in Equation (1.10) is valid for free space in three dimensions. The associated velocity field known as the Stokeslet decays as $\sim 1/r$. The derivatives of this fundamental solution also satisfies the Stokes equation and can be combined together to satisfy relevant boundary conditions. This gives rise to the so called *singularity solution* method of Stokes flow [39].

1.2 Primer on selected topics

1.2.1 Brownian motion

Brownian motion or *pedesis* (meaning ‘leaping’) can be define as the random motion of particles suspended in a fluid resulting from their collision with the fast-moving molecules in the fluid [43]. In the spirit of the botanist Robert Brown if one studies Brownian trajectories of particles then these trajectories may appear random, uncorrelated and with no mean transport. In soft-matter physics, as we will see in the thesis, Brownian motion of fluid molecules is sufficient to perturb and cause deformation to *soft* materials.

We reserve our discussion on Brownian polymers for the next section and instead highlight here how to model thermal fluctuation or Brownian forces mathematically.

Consider a spherical particle of mass m and radius a immersed in a Newtonian fluid bath. Its characteristic size a is very large compared to the size of the fluid molecules, but is sufficiently small such that it is susceptible to Brownian motion. In order to study its dynamics, one can follow an individual fluid parcels in a Lagrangian sense that are bombarding the particle using Newton's laws of motion. This is the fundamental basis of molecular dynamics simulation and can often be intractable due to computational expenses. An alternative is to appreciate the scale separation between the size of the particle and fluid molecules, and represent the effect of collisions of molecules in a continuum framework by an effective Brownian force [44]. This idea is made concrete by the fluctuation-dissipation theorem of Statistical Mechanics that applies to system obeying the principle of detailed balance. The theorem states that whenever there is a process that dissipates energy, turning it into heat, there is a reverse process related to thermal fluctuations. In the example at hand the random force that results in the erratic motion of the particle in the fluid would also cause drag if the particle was pulled through the fluid. In other words, the fluctuation of the particle at rest has the same origin as the dissipative frictional force one must do work against, if one tries to perturb the system in a particular direction.

The above idea is best captured through the Stokes-Einstein-Sutherland relation that relates the diffusivity \mathbf{D} of the immersed particle to its mobility \mathcal{M} as:

$$\mathbf{D} = k_B T \mathcal{M}, \quad (1.11)$$

where k_B is the Boltzmann constant and T is the absolute temperature of the suspending fluid bath. For a spherical particle this simply translates to:

$$\mathbf{D} = \frac{k_B T}{6\pi\mu a} \mathbf{I}. \quad (1.12)$$

The diffusion tensor is isotropic for a spherical particle, but the above relation is general and can be applied to anisotropic shapes, it also holds true for rotational diffusion. We now expect that the Brownian force \mathbf{f}^{Br} that mimics the effect of jiggling thermal motion of the fluid parcels on the particle to have a zero mean as it stems from random collision processes. The force is specified by its second moment that follows from the fluctuation-dissipation theorem, and can be shown to obey:

$$\langle \mathbf{f}^{\text{Br}}(t) \rangle = \mathbf{0}, \quad (1.13)$$

$$\langle \mathbf{f}^{\text{Br}}(t) \mathbf{f}^{\text{Br}}(t') \rangle = 2k_B T \mathcal{M}^{-1} \delta(t - t'), \quad (1.14)$$

where $\langle \cdot \rangle$ denotes ensemble average [44]. In Chapter 2 we will see that how the above relation can be adapted to specific models of semiflexible polymers like actin to describe their shape fluctuations.

1.2.2 Semiflexible polymers

Polymers are macromolecules. A lot of detailed theories have been devoted to developing models of polymers that are perfectly flexible or completely rigid. String like floppy polymers are sensitive to Brownian fluctuations and can be modeled as freely-jointed chains that approximate the polymer as a random walk. On the other end of this spectrum are rigid rod-like molecules that only have orientational diffusion without any shape fluctuations [14]. However a large number of biopolymers in the cell cytoskeleton are somewhere in between these two limits, and this is the main focus of this thesis.

For these biological polymers elasticity play a crucial role. Typically the energy associated with deformation of these polymers is comparable to the thermal energy. As a result the Brownian fluctuations act to deform the backbone of these soft objects. There is an energy penalty associated with bending these elastic filaments [45]. The energetic cost is larger for shorter or stiffer bends compared to longer sweeping deformations. As a

result, fluctuation-induced deformations are most evident at larger length scales than at smaller scales. This is illustrated in Figure 1.2 that shows a schematic of conformation of an elastic thread. We observe that due to bending energy at the molecular scale the polymer behaves like a rigid rod, but when we zoom out the chain appears flexible. This behavior is termed as *semiflexibility* and these polymers are known as *semiflexible polymers*.

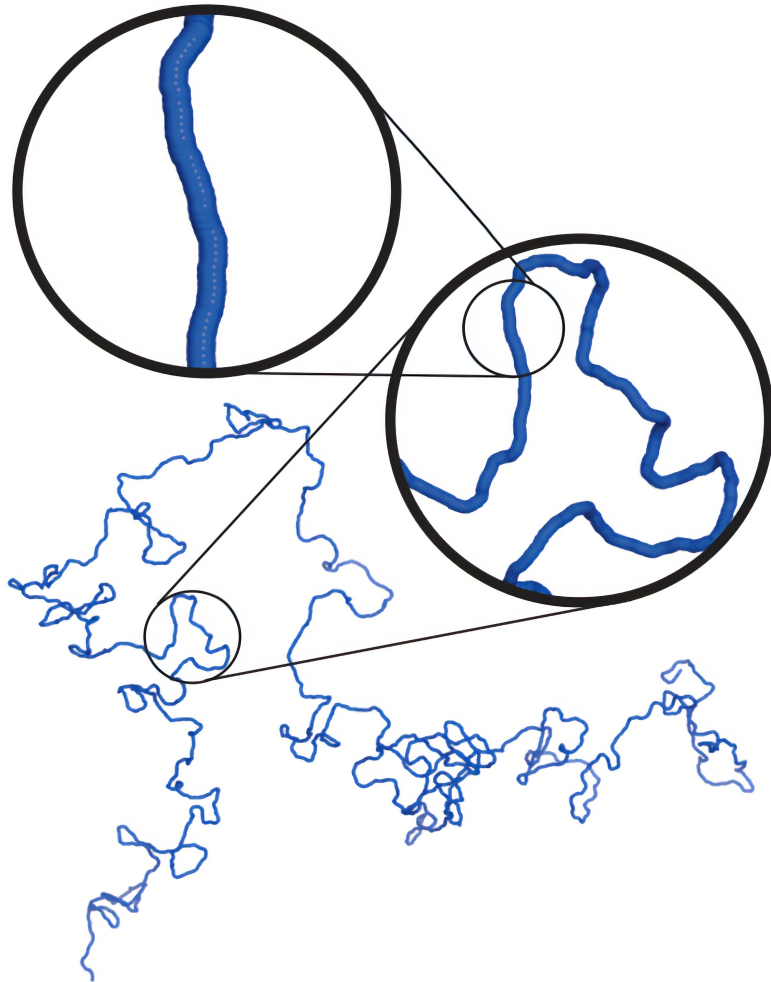


Figure 1.2: Conformation of a semiflexible polymer at different length scales. Image borrowed from [1].

Theoretical modeling of a single semiflexible polymer remained a non-trivial sta-

tistical mechanics problem and was first answered by Kratky and Prod in 1949 [46] for a discrete setup. The continuous version of the Kratky-Porod model is known as the worm-like-chain (WLC). In this model the polymer is parametrized as a space curve $\mathbf{x}(s)$ in terms of the arc-length s . Associated with this is a energy penalty in bending or Hamiltonian, given as:

$$E_B = \frac{B}{2} \int_0^L |\mathbf{x}_{ss}|^2 ds, \quad (1.15)$$

where B is the bending rigidity, L is the length of the polymer and the functional is quadratic in local curvature. The tangent-tangent correlation function for this model can be computed analytically, yielding:

$$\langle \mathbf{x}_s(s) \cdot \mathbf{x}(s') \rangle = \exp \left[-\frac{(s - s')}{\ell_p} \right], \quad (1.16)$$

where $\ell_p = B/k_B T$ is called the persistence length of the polymer. In other words the persistence length is a length scale over which the polymer loses memory of its tangent correlation. Alternatively for a chain of length $L = \ell_p$ the characteristic bending energy B/ℓ_p is comparable to thermal fluctuations $k_B T$ [47]. The limit $\ell_p/L \gg 1$ corresponds to rigid rods, as deformations are highly correlated, and the limit $\ell_p/L \ll 1$ mimics flexible chains. Another useful property that can be analytically computed for WLC is the mean-square end-to-end distance:

$$\langle R^2 \rangle = 2\ell_p^2 (e^{-L/\ell_p} - 1 + L/\ell_p). \quad (1.17)$$

From the above relation it is evident that for $\ell_p/L \rightarrow \infty$ we have $\langle R^2 \rangle \rightarrow L^2$ as expected for a rigid rod. On the other hand for $\ell_p/L \rightarrow 0$ we have $\langle R^2 \rangle \rightarrow 2\ell_p L$. This is the limit of a flexible polymer, and the expression for mean-squared end-to-end distance is identical to that of a freely-jointed chain performing a random walk.

It is to be noted that for DNA molecules the contour length $L \sim \mathcal{O}(\mu\text{m} - \text{mm})$ while the persistence length is $\ell_p \sim 50 \text{ nm}$. As a result these chains are predominantly

entropic, preferring coiled conformations, and bead-spring models are well suited when one is interested in length scales larger than the persistence length. On the other hand for microtubules and actin filaments with $B \sim \mathcal{O}(10^{-26} \text{ Nm}^2)$ we have $L \sim \ell_p$ [48]. As a result we need to account for both elasticity and thermal fluctuations. We will explore in the subsequent chapters how the interplay between classical elastic instabilities and Brownian shape fluctuations lead to non-trivial filament dynamics.

1.3 Overview of present work

This work tries to broadly address two set of problems involving dynamics of elastic filaments. One set of problems involves understanding the behavior of *passive* filaments that are transported, rotated and deformed by a competition of three forces: viscous, elastic and thermal. We try to develop theoretical models to understand their morphologies and long-time transport properties that are crucial for suspensions and design of chromatographic devices. The second set of problems involves the study of *active* micro-filaments. These elastic fibers are non-Brownian but their dynamics is dictated by stochastic active molecular processes that drive them out of equilibrium. Understanding active polymer dynamics is a fundamental challenge in biophysics, and our study particularly sheds light on the hydrodynamics of cilia and flagella.

Chapter 2 develops much of the theoretical and computational framework used in this thesis in a pedagogical manner. Based on our qualitative discussion of Brownian fluctuations and polymers in this chapter we try to understand simple scaling laws of Brownian rods in shear flows and polymers in equilibrium. We also perform two numerical stretching experiments of semiflexible polymers that highlight some key mechanical properties of these Brownian filaments.

Chapter 3 and 4 are centered on understanding morphologies of actin filaments in

two canonical flows: shear and compression. In particular we develop dynamical models and nonlinear elastic theories that explain for the first time several morphological transitions associated with buckling instabilities of semiflexible polymers. These two chapters incorporate the central idea of how conformations and mechanics of soft materials are interlinked, and highlights the subtle role of viscous loading competing with thermal and elastic forces.

Having studied passive filaments we move on to model active polymers in Chapter 5 and 6. For the first time, we propose a microscopic bottom-up model of the axoneme, the internal structure of cilia and flagella. We show that due to the action of molecular motors there can be dynamic bifurcations leading to spontaneous oscillations in elastic filaments that mimic the beating patterns of various ciliated micro-organisms, and elucidate the role of hydrodynamics in their collective behavior.

Chapter 7 and 8 are focused on transport of polymers and passive Brownian tracers in structured lattices that serve as idealization of porous media. DNA gel electrophoresis is a classical method to sort DNA strands according to their length from a mixture. Chapter 7 extends this idea to semiflexible polymers where we explore transport properties of these filaments in a 2D porous media and finally highlight a possible design of chromatographic device. Chapter 8 is in some sense a digression since it focuses on transport of Brownian tracers in 1D lattice. However it embodies the idea of understanding asymptotic transport properties in viscous flow and highlight the role of peristalsis in the context of classical Taylor dispersion.

We finish with concluding remarks and possible future direction in Chapter 9.

Chapter 2

Elasticity, hydrodynamics and fluctuations of slender structures

2.1 Introduction

As discussed in Chapter 1 the dynamics of flexible filaments or more generally slender structures in viscous flow are quite ubiquitous with applications in rheology and biophysics. This chapter primarily discusses various aspects of theoretical mechanics and Brownian motion relevant for the thesis in a pedagogical manner. The discussion covers three main aspects. First, we will focus on elasticity of beams and rods that can be used to model dynamics of deformable filaments with a primer on the elementary differential geometry of curves. Then we will move on to discuss hydrodynamics of slender structures in viscous flow where we will outline the main results of the ‘slender-body-theory’ and discuss associated numerical methods. Finally we will talk about a set of problems related to understanding thermal fluctuations of Brownian filaments and associated scaling theories. This part is in the spirit of works on scaling theories of polymer by de Gennes [49], but will primarily focus on semi-flexible filaments. Discussions from this chapter will help us

to develop physical intuitions of several phenomena which will facilitate discussions in the upcoming chapters.

2.2 Elasticity of slender structures

A slender structure is a quasi-one-dimensional elastic body whose extent in one direction is much larger than in the two perpendicular (cross-sectional) directions. There is a rich history of literature in elasticity that deals with dynamics of such one-dimensional continua. However there are a very few pedagogical notes or books that develop the theory of mechanics of slender structures and their interesting behaviors in a self-contained way. Derivations are often lengthy, cumbersome and complicated. This section attempts to discuss the bare minimum of elasticity keeping things self-contained and clearing various terminologies. Much of the following discussion is borrowed and inspired from the book of Audoly and Pomeau [50], the chapter by Audoly in [49] and finally from a recent paper [51]. We start with a brief review of kinematics of deformation and geometry of curves. Then we discuss the fundamental difference between materials with nonlinear constitutive laws and geometric nonlinearities. We then derive the governing equation of a particular one-dimensional model of elastic curves, namely the Euler *elastica*, from variational principles and discuss its static and dynamics. Finally we conclude with a brief discussion on the statics and dynamics of Euler buckling and morphologies of elastic filaments.

2.2.1 Preliminary continuum mechanics

Consider a solid object with a regular rectangular grid drawn on it at time $t = 0$ which we term as its ‘reference condition’. With respect to some global co-ordinate system we identify any material point on this reference configuration by a Lagrangian marker \mathbf{X} . Now after a period of deformation this regular rectangular grid has transformed. In

this ‘current configuration’ the material point previously identified as \mathbf{X} is now given by $\mathbf{x}(\mathbf{X}, t)$ as shown in Figure 2.1. We can associate a displacement field or map with this material description that is given by $\mathbf{u}(\mathbf{X}, t) = \mathbf{x}(\mathbf{X}, t) - \mathbf{X}$. Associated with the map that takes the object from the ‘reference configuration’, $\Omega(0)$ to its ‘current configuration’, $\Omega(t)$, one can define a deformation gradient tensor as follows:

$$F_{ij}(\mathbf{X}, t) = \frac{\partial x_i(\mathbf{X}, t)}{\partial X_j}. \quad (2.1)$$

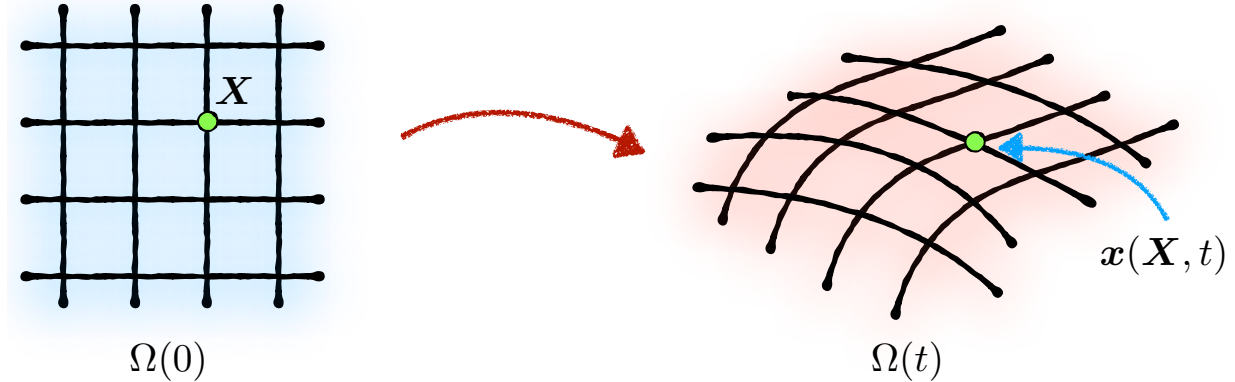


Figure 2.1: Schematic of a solid object deforming from its reference condition $\Omega(0)$ to its current configuration $\Omega(t)$.

It is straight-forward to see that line elements in $\Omega(t)$ are related to that in $\Omega(0)$ by

$$dx_i = F_{ij}dX_j. \quad (2.2)$$

Usually when we think of strain we are interested in the magnitude of the deformation of elemental lengths. For a step towards that let us first evaluate the magnitude of elemental lengths in $\Omega(t)$. We have:

$$|d\mathbf{x}| = \sqrt{\delta_{ij}dx_i dx_j} = \sqrt{\delta_{ij}F_{im}dX_m F_{jl}dX_l} = \sqrt{dX_m F_{im} F_{il} dX_l}. \quad (2.3)$$

In the final expression shown above the following tensor appears $C_{ml} = F_{im}F_{il}$. In Gibbs notation this is written as $\mathbf{C}(\mathbf{X}, t) = \mathbf{F}^T \cdot \mathbf{F}$ and we term this tensor as the right Cauchy-

Green deformation tensor. It is now straight forward to see that the difference in elemental lengths between the two configurations are related by

$$d\mathbf{x}^2 - d\mathbf{X}^2 = (C_{ij} - \delta_{ij}) dX_i dX_j. \quad (2.4)$$

We define the Green-Lagrange strain tensor, simply referred to as strain tensor hereafter as $\epsilon_{ij} = \frac{1}{2}(C_{ij} - \delta_{ij})$. It is often convenient to think and derive expressions in terms of the displacement field $\mathbf{u}(\mathbf{X}, t)$ instead of the deformation gradient tensor [52]. They are related to each other by the following relation:

$$\frac{\partial u_i}{\partial X_j} = F_{ij} - \delta_{ij}. \quad (2.5)$$

Using the above result in the expression for the strain tensor we find:

$$\epsilon_{ij} = \frac{1}{2} \left(\frac{\partial u_i}{\partial X_j} + \frac{\partial u_j}{\partial X_i} + \frac{\partial u_k}{\partial X_i} \frac{\partial u_k}{\partial X_j} \right). \quad (2.6)$$

It is also evident from the above expression that the strain tensor is symmetric. Physically the strain-tensor characterizes local deformations near a point \mathbf{X} in the solid through a displacement field $\mathbf{u}(\mathbf{X}, t)$ and by construction it vanishes for rigid-body rotations and translations. It is also important to appreciate that the strain tensor in terms of displacement is *nonlinear* due to the presence of quadratic terms. Since the components of the strain-tensor are dimensionless, their magnitude has an absolute meaning. In particular we would say that the strain is small if $|\epsilon_{ij}| \ll 1$. We will see in subsequent discussions that how ‘small strain’ has ramifications in the elastic response of a material. However for now we conclude our discussion on kinematics.

Before moving on to discussions on material response and nonlinearities we briefly review geometry and kinematics of space curves that provide a convenient mathematical framework to describe quasi one-dimensional elastic objects. In this thesis we will represent the centerline of elastic filaments as one-dimensional space curves embedded in Euclidean

space \mathbb{E}^3 as shown in Figure 2.2. Why we chose to do so is discussed later and for the moment we simply focus on the geometry.

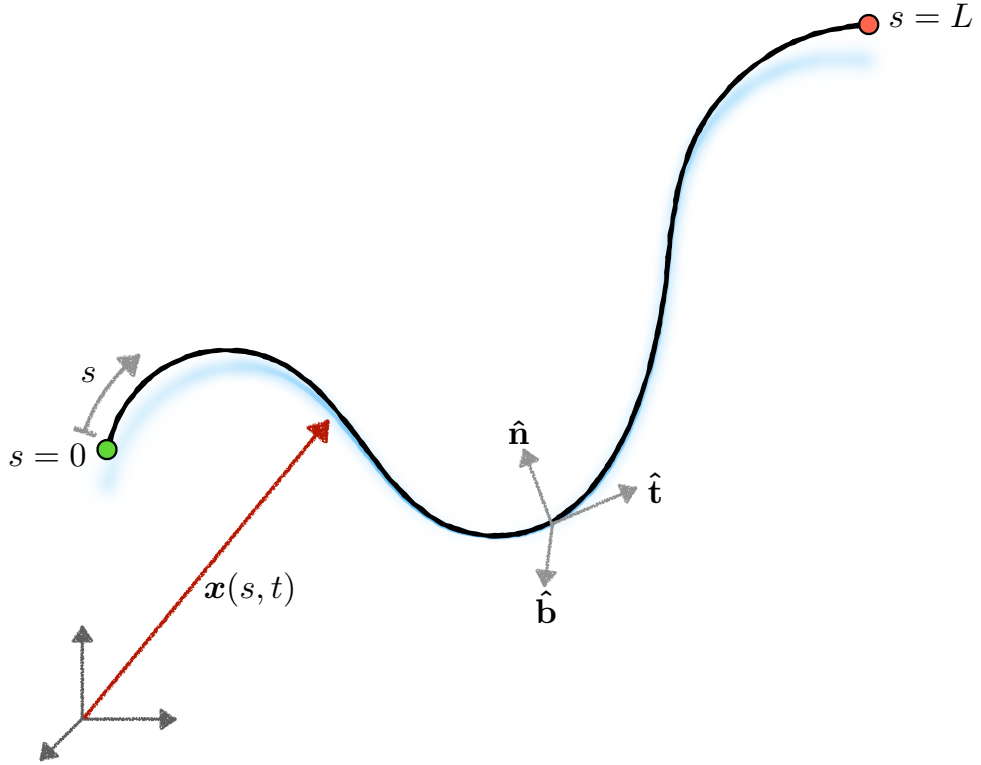


Figure 2.2: Schematic of a space curve embedded in \mathbb{E}^3 and parameterized by arc length s . The Frenet-Serret triad is shown on the curve.

This curve has a length L and is parameterized by the arc-length $s \in [0, L]$. At any instant of time, position along the curve is identified by a Lagrangian marker $\mathbf{x}(s, t)$. The unit tangent vector to the curve at any point is simply defined by $\partial_s \mathbf{x} \equiv \hat{\mathbf{t}}$ and it follows that $\partial_s \mathbf{x} \cdot \partial_s \mathbf{x} = 1$. Differentiating the last relation we find $\partial_{ss} \mathbf{x} \cdot \partial_s \mathbf{x} = 0$. This points to the fact that the vector $\partial_{ss} \mathbf{x}$ is perpendicular to the tangent vector and we define $\partial_{ss} \mathbf{x} = \kappa(s) \hat{\mathbf{n}}$ where $\kappa(s)$ is the curvature and $\hat{\mathbf{n}}$ is called the unit normal vector. As the name suggests $\kappa(s)$ measures the local tendency of a space curve to form bends (or curvatures) and is zero for a straight line. The unit tangent and the unit normal vector

together defines what is known as the osculating plane of the curve. In order to form a triad of vectors at any point along the curve that can span \mathbb{E}^3 we define $\hat{\mathbf{b}} \equiv \hat{\mathbf{t}} \times \hat{\mathbf{n}}$, as the binormal vector that points perpendicular to the osculating plane. The orthonormal basis vectors $\{\hat{\mathbf{t}}, \hat{\mathbf{n}}, \hat{\mathbf{b}}\}$ are related to each other by the Frenet-Serret formulas

$$\frac{\partial}{\partial s} \begin{bmatrix} \hat{\mathbf{t}} \\ \hat{\mathbf{n}} \\ \hat{\mathbf{b}} \end{bmatrix} = \begin{bmatrix} 0 & \kappa & 0 \\ -\kappa & 0 & \tau \\ 0 & -\kappa & 0 \end{bmatrix} \begin{bmatrix} \hat{\mathbf{t}} \\ \hat{\mathbf{n}} \\ \hat{\mathbf{b}} \end{bmatrix}, \quad (2.7)$$

where $\tau(s)$ is the torsion of the curve that serves as a measure of deviation of the curve from the local osculating plane. For an entirely planar curve $\tau(s)$ is identically zero. The Frenet-Serret frame has several subtle issues associated with non-uniqueness of the triad when $\kappa = 0$, but we won't delve into that and will point the interested reader to a detailed discussion to [53].

2.2.2 Hookean elasticity and geometric nonlinearities

When considering equilibria or dynamics of elastic objects, we need to think of stress. For a deforming object in equilibrium the sum of external forces is zero. The balance of internal stress then leads to Cauchy's equation:

$$\frac{\partial \sigma_{ij}}{\partial x_j} + \rho g_i = 0, \quad (2.8)$$

where σ_{ij} is the stress tensor and g_i is a body force per unit volume. The dynamic description is completed or closed by prescribing a relationship between the stress and the displacement field or strain which is known as the *constitutive* law of the material. For isotropic material undergoing small strain, the stress is proportional to the strain which forms the basis of *Hookean* or linear elasticity. Throughout this thesis we will restrict ourselves to the case of Hookean or linear elasticity. However the aim of this discussion

is to stress and highlight the distinction between small strain and small displacement. It is evident that if the displacement field $\mathbf{u}(\mathbf{X}, t)$ defined in previous section is small then $\mathbf{x} \approx \mathbf{X}$ and the strain $|\epsilon_{ij}| \ll 1$. However the converse is not true as the strain depends only on the gradient of the displacement field and not on its absolute value. As a result one can have finite and large displacements or rotations that are perfectly compatible with small strains [54]. This introduces what is known as *geometric nonlinearities* and is at the heart of the theories described in this thesis. Figure 2.3 provides a few examples where geometric nonlinearities with large deformations lead to a number of interesting observations. We will cover one such geometrically nonlinear 1D continuum model known as the Euler elastica in great detail.

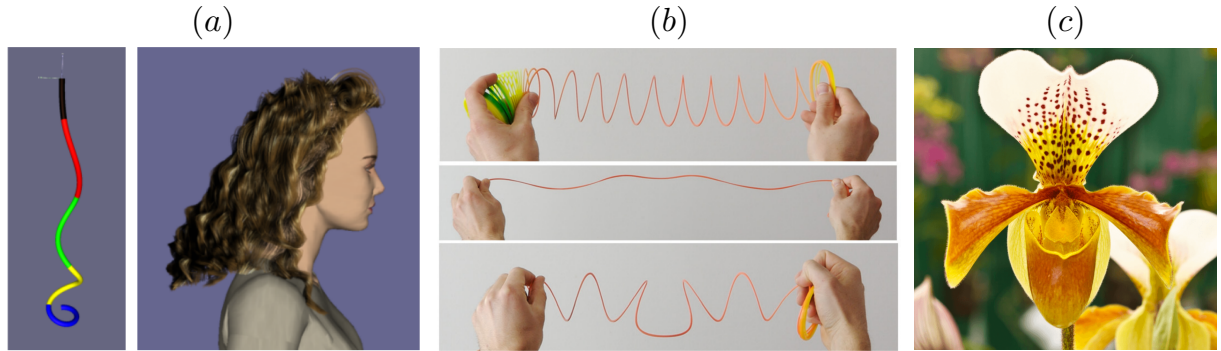


Figure 2.3: Examples of geometric nonlinearities in nature: (a) Simulations with discrete Kirchoff rods are used to model curly human hairs in computer graphics [55]. (b) Formation of persistent perversions in slinky [56]. (c) The leaves of Paphiopedilum orchid exhibits Godet patterns and ripples. Image from [57].

2.2.3 Euler elastica

Elastica is the Latin for a thin strip of elastic material [58]. The planar Euler elastica has a simple curvature dependent bending energy that makes it appealing as a model of a one-dimensional continuum. It has been used to model a variety of physical systems such as from thin beams, structural cables, polymers and biological macromolecules [59], and

will be the fundamental model for various fluid-structure interaction problems explored in this thesis. We will look at two complementary approaches to derive governing equations for the elastica. The first one is in the spirit of Cosserat rod theories of classical continuum mechanics [60] and will be restricted to the planar case [54]. In the second approach we will look into a variational treatment of the problem and discuss related boundary conditions for a three dimensional elastic curve [51].

Geometry and constraints: Before getting into the dynamics it is convenient to discuss some preliminary geometry. For an undeformed elastica with its centerline parameterized as a space curve the tangent vector has unit magnitude with $|\mathbf{x}_s| = 1$. A convenient measure of stretching of the filament (or strain) can be to see the departure of this magnitude from unity, and can be defined as [54]:

$$\epsilon = \frac{1}{2}(\mathbf{x}_s \cdot \mathbf{x}_s - 1). \quad (2.9)$$

We also define a measure of shear as:

$$\gamma = \mathbf{x}_{ss} \cdot \mathbf{x}_s. \quad (2.10)$$

The shear γ vanishes when the transverse material vector remains perpendicular to the tangent at the centerline. As discussed in previous sections, we are interested in small strain theories that are limited to $|\epsilon| \ll 1$ and $|\gamma| \ll 1$. We will go one step ahead in the following discussion and limit ourselves to un-shearable and inextensible elastic rods with $\gamma = 0$ and $\epsilon = 0$. We justify the inextensibility condition in the next paragraph. If the filament remains inextensible the arc-length serves as a material description of the curve or elastic rod, which is why it is convenient to parametrize relevant quantities in terms of s . It is worth pointing out that we are in the special limit of zero strain and all the constitutive relations remain linear.

Stretching vs bending: Consider a slender rod of diameter a and length L .

Suppose we apply some force to stretch the filament in the x direction with typical displacement in the order of u . In the sense of scaling the strain is then given as $\epsilon \sim \partial_x u$. The associated axial stress scales as $\sigma_S \sim Y \partial_x u$ where Y is the Young's modulus and the subscript S is for stretching. We can then estimate the typical energy required per unit length to stretch the rod as $E_S \sim a^2 \sigma_S \partial_x u \sim Y a^2 u^2 / L^2$.

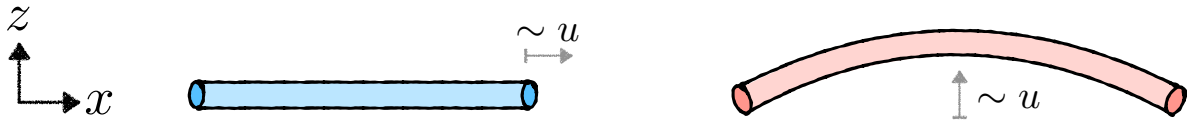


Figure 2.4: Schematic showing stretching and bending of a slender elastic rod.

We can carry out the same calculation to estimate the typical bending energies if we want to create a transverse displacement of the same order. The typical curvature induced by these displacements are $\kappa \sim \partial_x^2 u$. Noting that the bending rigidity of a rod $B \sim Y a^4$ the bending energy per unit length scales as $E_B \sim B \kappa^2 \sim Y a^4 u^2 / L^4$. We can now compare the ratio of bending and stretching energies and we find:

$$\frac{E_S}{E_B} \sim \left(\frac{L}{a} \right)^2 \gg 1. \quad (2.11)$$

Since $a/L \ll 1$ for a slender elastic rod the energy required to stretch a rod is much larger compared to the energy required to bend it. This is easily appreciated if we try to stretch one of our strands of hair while it is very easy to bend it. For filaments in this thesis $a/L \sim 10^{-2} - 10^{-3}$ and thus it is very reasonable to assume that the the filaments are inextensible. In viscous flow one can show that the time-scale of relaxation of stretching modes is much faster than that of the bending modes, and thus in a dynamic situation it is the bending modes that govern the emergent behaviors [58].

Derivation à la Cosserat rods: Here we present a simplified derivation of the

governing equation of inextensible, unshearable planar elastic rods [61]. The rod is in the $x - y$ plane and is in equilibrium when acted on by external forces and moments with force density $\mathbf{f}(s)$ and moment density $\mathbf{n}(s)$. We now balance forces and moments along the centerline of the filament over an arbitrary segment $s \in [s_1, s_2]$. The ‘contact’ forces and moments of the rod is denoted by $\mathbf{F}(s)$ and $\mathbf{M}(s)$ respectively. The internal bending moment $\mathbf{M}(s)$ is in the out of plane direction and can be written as $\mathbf{M}(s) = M(s)\hat{\mathbf{z}}$.

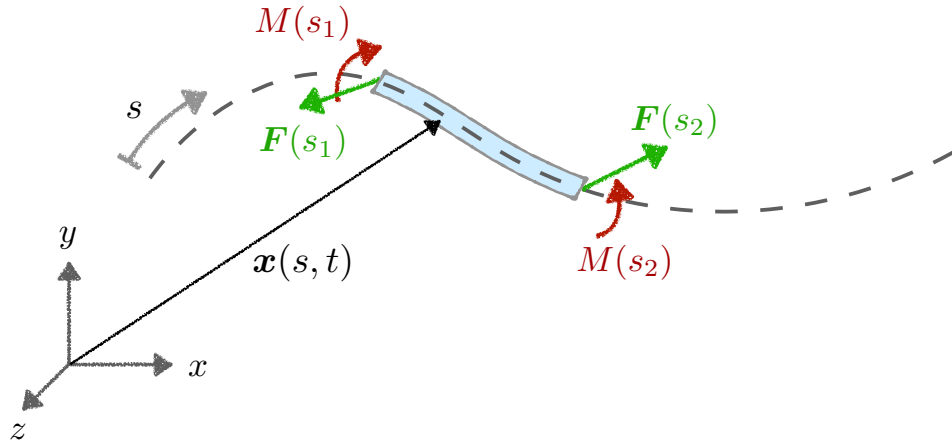


Figure 2.5: Schematic showing force and moment balance for an inextensible, unshearable, planar elastic rod.

Force and moment balance in the elemental area demands:

$$\mathbf{0} = \int_{s_1}^{s_2} \mathbf{f}(s) ds + \mathbf{F}(s) \Big|_{s_1}^{s_2}, \quad (2.12)$$

$$\mathbf{0} = \int_{s_1}^{s_2} [\mathbf{x}(s, t) \times \mathbf{f}(s) + \mathbf{n}(s)] ds + [\mathbf{x}(s, t) \times \mathbf{F}(s) + \mathbf{M}(s)] \Big|_{s_1}^{s_2}. \quad (2.13)$$

Under Leibniz rule and noting the fact that bending moments act in the z direction only we can simply the balance laws to:

$$\mathbf{0} = \mathbf{f} + \frac{\partial \mathbf{F}}{\partial s}, \quad (2.14)$$

$$0 = (\mathbf{n} + \mathbf{x}_s \times \mathbf{F}) \cdot \hat{\mathbf{z}} + \frac{\partial M}{\partial s}. \quad (2.15)$$

The above equations govern the dynamics of the rod in equilibrium. In order to close the system of governing equations we need a constitutive law. For an Euler elastica the bending energy $E_B \sim \kappa^2$ where κ is the curvature. This leads to the linear constitutive law that $M = B\kappa$ where B is the bending rigidity. Typically the force densities that act on the filament can be due to viscous stresses or gravitational forces or electrostatic forces due to charge distributions. In this thesis we are interested in viscous stresses and will revisit this formulation later on while discussing hydrodynamics.

Variational treatment: We start by noting that the bending energy of a filament is given by:

$$E_B = \frac{B}{2} \int_0^L |\mathbf{x}_{ss}|^2 ds. \quad (2.16)$$

We can incorporate the constraint of inextensibility through a Lagrange multiplier $\sigma(s)$ and define an Energy functional given by:

$$\mathcal{E} = \frac{1}{2} \int_0^L [B|\mathbf{x}_{ss}|^2 + \sigma(s)(\mathbf{x}_s \cdot \mathbf{x}_s - 1)] ds. \quad (2.17)$$

We can now perform variation of the above functional under a small shift of position $\mathbf{x} \rightarrow \mathbf{x} + \delta\mathbf{x}$. Upon successive integration by parts the first order variation yields:

$$\delta\mathcal{E} = \int_0^L \delta\mathbf{x} \cdot [B\partial_s^4\mathbf{x} - \partial_s(\sigma\partial_s\mathbf{x})] ds + [B\partial_s^2\mathbf{x} \cdot \partial_s\delta\mathbf{x} + (\sigma\partial_s\mathbf{x} - B\partial_s^3\mathbf{x}) \cdot \delta\mathbf{x}] \Big|_0^L. \quad (2.18)$$

Setting this variation to zero for arbitrary $\delta\mathbf{x}$ gives us the bulk field equation:

$$B\partial_s^4\mathbf{x} - \partial_s(\sigma\partial_s\mathbf{x}) = \mathbf{0}. \quad (2.19)$$

If we had a force per unit length acting on the filament as before then that would have balanced this bulk stress. This will be the case for dynamics of these filaments in a viscous fluid. The boundary terms from the variation provides the boundary condition of the

problem. For a filament that is free at both ends we have:

$$\sigma \partial_s \mathbf{x} - B \partial_s^3 \mathbf{x} = \mathbf{0}, \quad \text{at } s = 0, L \quad (2.20)$$

$$B \partial_s^2 \mathbf{x} = \mathbf{0}, \quad \text{at } s = 0, L. \quad (2.21)$$

For a detailed discussion on various boundary conditions the interested reader is pointed to [51, 54]. We will list the relevant boundary conditions considered in this thesis later on while discussing the viscous dynamics of the slender structures.

Comment on 3D elastica: The models of biopolymers presented in this thesis center around the elastica both in two and three dimensions. Besides having curvatures in three dimension, a filament can have torsion as discussed previously. Typically one would account for penalties in energy due to both torsion and curvature. Kirchoff rods [50, 60] for energetic contributions of different modes like twisting and bending of an elastic rod and is probably more appropriate for three dimensional problems. However we do not include these in our formulations and restrict ourselves to the simpler energetic form.

2.2.4 Aspects of buckling instabilities

Chapter 3 and 4 of this thesis are centered around buckling of biopolymers in two canonical flow setups. Here we briefly discuss the main features of the classical Euler buckling instability and helical buckling of twisted elastic rods that become relevant in the subsequent chapters. Euler buckling is concerned with the simplest example of elastic instability of a rod subjected to longitudinal compressing forces. In the absence of transverse bending forces the equilibrium equations have the solution of $\mathbf{x}(s) = s\hat{\mathbf{y}}$. This gives rise to a stable equilibrium of a rod remaining straight with an internal tension $\sigma(s) = |P|$, where $P < 0$ is the compressing force. However this solution becomes unstable beyond a critical value of P_{cr} and any infinitesimal small perturbation leads to a large bending (or deformation) of the rod to a buckled state via a supercritical pitchfork bifurcation. The

resulting shape resembles the letter *C*. A schematic along with the bifurcation diagram is shown in Figure 2.6(a). As the longitudinal force increases, one excites higher-order buckling modes with more wave-numbers. The critical force at the onset is given by

$$P_{cr} = \alpha \frac{\pi^2 B}{L^2}, \quad (2.22)$$

where α is a numerical prefactor whose value depends on the specific choice of boundary condition.

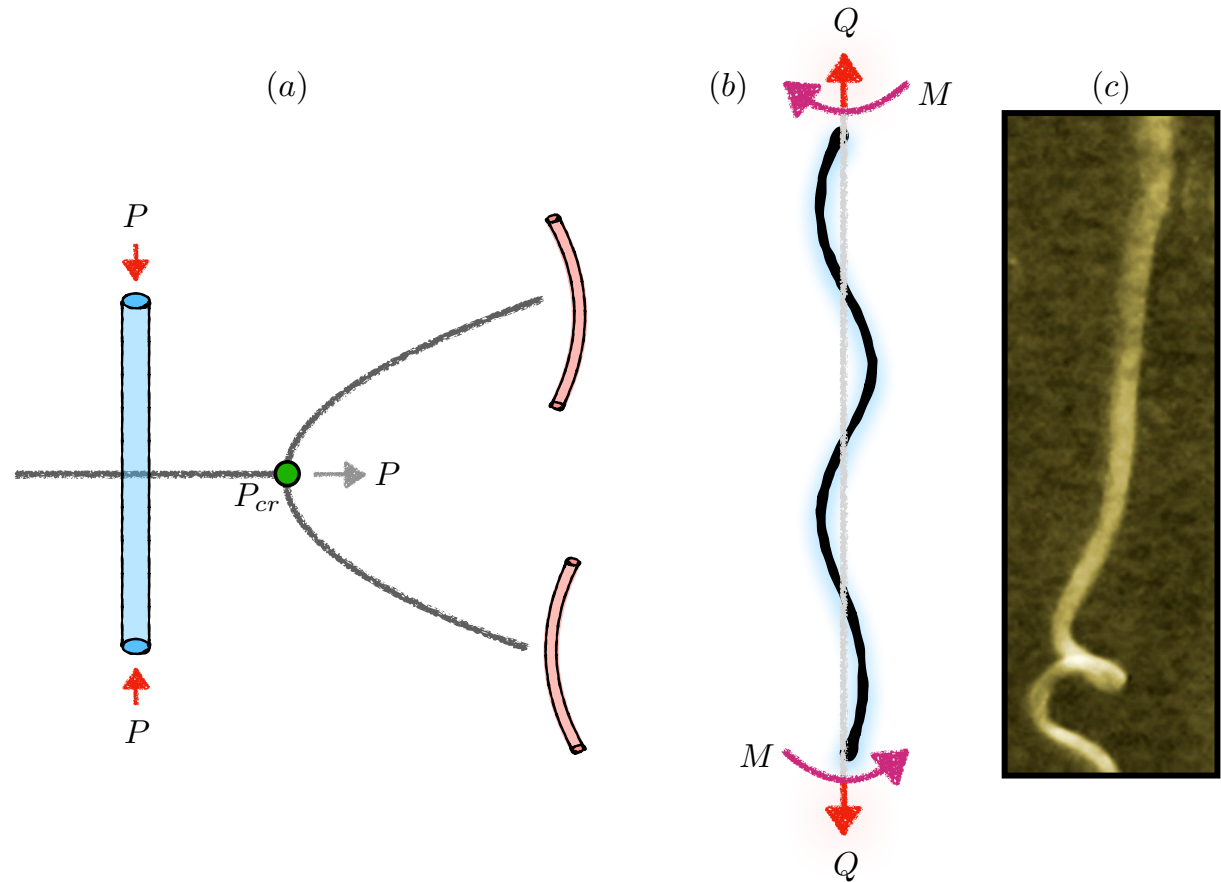


Figure 2.6: (a) Supercritical pitchfork bifurcation giving way to buckled configurations. (b) Schematic of a typical helical buckling setup with tensile forces and end moment. (c) Plant root undergoing helical buckling [62].

Helical buckling of elastic rods is another classical instability that has been studied

in the context of loop formation in twisted cables [63, 64], buckling of oil-drills [65, 66] and is relevant for problems related to growth driven morphologies of plant roots [62]. In these set of problems a rod is acted by a tensile (or compressional) axial force Q and is also subjected to twist or end moments M as illustrated in Figure 2.6(*b*). Beyond a critical value of the twisting moment the straight twisted configuration of the filament becomes unstable and the rod subsequently attains a helical shape. The bifurcation can be subcritical as well as supercritical depending on specific boundary conditions. This is an illustration of coupling of bending and twisting modes in three dimension and is a result of the fact that helical configurations provide favorable energy landscapes. We refrain from the mathematical treatment of such instabilities and the interested reader is pointed to [50, 67]. We will re-visit this problem in an hydrodynamic setup where we will illustrate that how helical conformations can emerge without twisting moments.

2.3 Hydrodynamics of slender structures

The dynamics of elastic filaments and rods in a Stokesian fluid has a special structure for which a number of mathematical and computational tools have been developed. Examples of such methods include the classical immersed-boundary-method (IBM) [61,68], bead-rod and bead-spring models [69, 70], regularized Stokeslet formulation [71–73] and mesoscale methods such as dissipative particle dynamics or multi-particle collision dynamics [74]. A discussion and review of all such methods and formulation is beyond the scope of this thesis. Here we discuss the hydrodynamics described by slender-body-theory which is an asymptotic reduction of the boundary integral equations described in the previous chapter for a slender object.

2.3.1 Non-local slender body theory

Consider a cylindrical filament of length L as shown in Figure 2.7 with a cross-sectional diameter a such that $\epsilon = a/L \ll 1$. Like before the centerline of this filament is parametrized by arc length s . This slender structure is placed in an unbounded Stokesian fluid with a background velocity $\mathbf{u}_\infty(\mathbf{x})$. We are interested in computing the velocity field of the fluid $\mathbf{u}(\mathbf{x})$ that satisfies the Stokes equation subjected to the boundary condition:

$$\mathbf{u}(\mathbf{x}) = \begin{cases} \mathbf{U}_S, & \text{for } \mathbf{x} \in \Omega_S \\ \mathbf{u}_\infty(\mathbf{x}), & \text{for } |\mathbf{x}| \rightarrow \infty \end{cases} \quad (2.23)$$

In the above equation Ω_S is the surface of the filament. Formally if we know the surface traction for the filament then it is possible to evaluate the velocity field at any point using the boundary integral formulation.

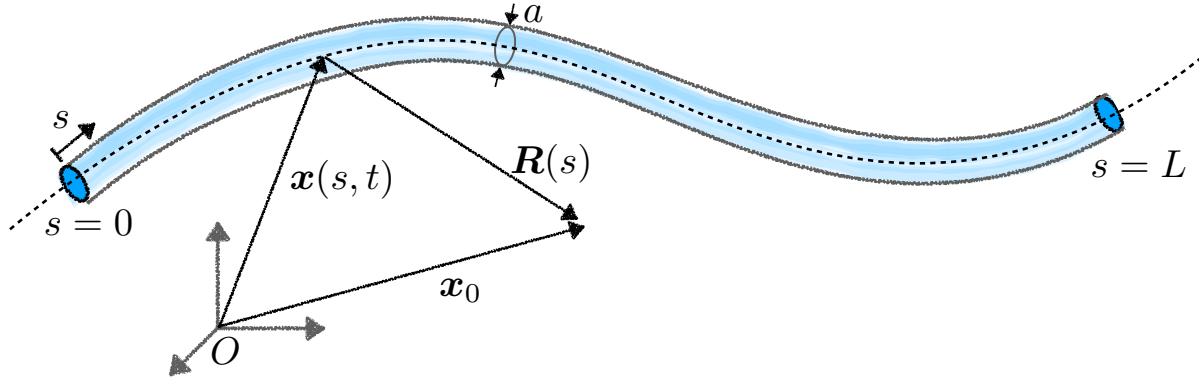


Figure 2.7: Schematic of a cylindrical slender object with diameter a and length L .

However one can go one step further exploiting the slenderness of the particle. The fundamental idea in slender-body-theory (SBT hereafter) for Stokes flow is that the disturbance (motion) due to the presence of the body is approximately the same as that due to a suitably chosen distribution of Stokeslets distributed along the centerline of the

filament. Batchelor [75] derived the approximate form of the strength of the Stokeslet distribution that will satisfy the boundary conditions for rigid body motions. However, when we permit the filament to have arbitrary deformation and velocities, additional care needs to be taken. In particular, close to the filament the flow is similar to that past a cylinder and constitutes what is known as an ‘inner solution’. This inner flow is matched asymptotically to the ‘outer solution’ of far field $\mathbf{u}_\infty(\mathbf{x})$. This form of the SBT is inherently non-local and is due to Keller and Rubinow [76]. Johnson [77] improved the accuracy by carefully accounting for the ends, and Götz [78] established a connection of non-local operators to Legendre polynomials. An alternative approach to derive the SBT equations relies on reductions of the full boundary integral equation to the centerline of the filament with ϵ being the small parameter [79].

As discussed in previous sections often one knows the force-density exerted by a flexible filament on the fluid from its elasticity. This force per unit length $\mathbf{f}(\mathbf{x}(s), t)$ that is exerted by the filament on the fluid can be interpreted as the azimuthally-averaged surface traction that depends on its instantaneous configuration. Far from the filament at some point \mathbf{x}_0 , the leading order velocity field is given by:

$$\mathbf{u}(\mathbf{x}_0) = \mathbf{u}_\infty(\mathbf{x}_0) - \int_0^L \mathbf{G}[\mathbf{x}_0 - \mathbf{x}(s')] \cdot \mathbf{f}(\mathbf{x}(s')) ds', \quad (2.24)$$

where $\mathbf{G}[\mathbf{x}_0 - \mathbf{x}(s')]$ is the appropriate Greens function and is simply the Stokeslet in free-space. It is appealing to evaluate the self-induced velocity of the filament centerline \mathbf{x}_t from the above integral taking $\mathbf{x}_0 \rightarrow \mathbf{x}(s, t)$. However this naive evaluation gives rise to logarithmically divergent integrals as there remains a singular piece over which the 1D approximation breaks down. Using careful matched asymptotic expansions as suggested previously [76–78] one finds the following form of the centerline velocity:

$$8\pi\mu(\mathbf{x}_t(s, t) - \mathbf{u}^\infty) = -\mathbf{\Lambda}[\mathbf{f}(\mathbf{x}(s, t))] - \mathbf{\mathbf{K}}[\mathbf{f}(\mathbf{x}(s, t))], \quad (2.25)$$

where Λ and \mathbf{K} are called the local and non-local operator that we define below and μ is the viscosity of the fluid. The above version of the SBT is accurate up to $(\epsilon^2 \ln \epsilon)$ provided certain conditions on the variation of transverse radius a along the arc-length is satisfied [77]. For a circular filament the accuracy is smaller but we avoid such technical subtleties. The local operator is given by:

$$\Lambda[\mathbf{f}(s)] = [(2 - c)\mathbf{I} - (c + 2)\mathbf{x}_s \mathbf{x}_s] \cdot \mathbf{f}(s), \quad (2.26)$$

where $c = -\ln(\epsilon^2 e) < 0$ is an asymptotic parameter that depends on the aspect ration of the filament. This local operator accounts for the drag anisotropy of slender objects in Stokes flow that we discuss later on. The non-local operator is given by:

$$\mathbf{K}[\mathbf{f}(s)] = \int_0^L \left[\frac{\mathbf{I} + \hat{\mathbf{R}}(s, s') \hat{\mathbf{R}}(s, s')}{|\mathbf{R}(s, s')|} \cdot \mathbf{f}(s') - \frac{\mathbf{I} + \mathbf{x}_s(s) \mathbf{x}_s(s)}{|s - s'|} \cdot \mathbf{f}(s) \right] ds', \quad (2.27)$$

where $\mathbf{R}(s, s') = \mathbf{x}(s) - \mathbf{x}(s')$ and $\hat{\mathbf{R}} = \mathbf{R}/|\mathbf{R}|$. This integral is often called a finite part-integral and is singular at $s = s'$. This accounts for the self-induced velocity of the filament or hydrodynamic interactions between different parts. We will discuss later on how to solve the integro-differential equation numerically treating the singular integrals appropriately. While eqn (2.24) provides the far-field approximation of the induced velocity field, a more accurate representation is given by

$$\mathbf{u}(\mathbf{x}_0) = \mathbf{u}_\infty(\mathbf{x}_0) - \frac{1}{8\pi\mu} \int_0^L \left[\frac{\mathbf{I} + \mathbf{R}(s') \mathbf{R}(s')}{|\mathbf{R}(s')|} + \frac{\epsilon^2}{2} \frac{I - 3\mathbf{R}(s') \mathbf{R}(s')}{|\mathbf{R}(s')|^3} \right] \cdot \mathbf{f}(s') ds', \quad (2.28)$$

where $\mathbf{R}(s') = \mathbf{x}_0 - \mathbf{x}(s')$. In the above integral the first term is a contribution from the Stokeslet and the second term is due to a distribution of source doublets. The contribution from the doublets become only important at length scales of $\mathcal{O}(\epsilon)$. Unless specified we will restrict ourselves to the simpler far-field representation of the velocity field as given in (2.24). We close the discussion by pointing out that the SBT can be interpreted as a force-mobility relationship. In particular we can represent eqn (2.25) as $\mathbf{x}_t(s) = \mathbf{u}_\infty(s) + \mathcal{M} \cdot \mathbf{f}(s)$

where $\mathcal{M} = -\boldsymbol{\Lambda} - \mathbf{K}$ is the mobility matrix. This interpretation becomes useful in the later sections when discussing thermal fluctuations.

2.3.2 Special case: local SBT

Here we consider the special case of the SBT where we neglect the non-local terms associated with long-range hydrodynamic interactions. This leads to the leading order local anisotropic drag model. The local terms of the SBT operators are $\mathcal{O}(\ln \epsilon)$ and the non-local terms are of $\mathcal{O}(1)$. While the approximation remains crude the local SBT and its variants have been widely used for theoretical analysis of dynamics of flexible fibers. We can re-write the local operator in the following manner:

$$\boldsymbol{\Lambda}[\mathbf{f}(s)] = [(2 - c)(\mathbf{I} - \mathbf{x}_s \mathbf{x}_s) - 2c \mathbf{x}_s \mathbf{x}_s] \cdot \mathbf{f}(s). \quad (2.29)$$

From the above expression one can define local anisotropic friction coefficients as

$$\zeta_{\parallel} = -\frac{1}{2c} \quad \text{and} \quad \zeta_{\perp} = \frac{1}{2 - c}. \quad (2.30)$$

In the limit of infinitely slender rods one recovers what is popularly known as resistive force theory with $\zeta_{\perp}/\zeta_{\parallel} \rightarrow 2$. In this limit the governing equations are further simplified to:

$$\mathbf{x}_t(s) = \mathbf{u}_{\infty}(\mathbf{x}(s)) + \frac{1}{8\pi\mu} (\mathbf{I} + \mathbf{x}_s \mathbf{x}_s) \cdot \mathbf{f}(s). \quad (2.31)$$

While the above expression is accurate to $\mathcal{O}(1)$, one can make a lot of analytical progress because of its simple form. We will revisit this formulation for the linear stability of elastic rods in compressional flows.

2.3.3 Brownian filaments

In order to proceed with the dynamics of filaments, we need to prescribe the force density $\mathbf{f}(s)$ appearing in the equations of SBT. As discussed previously, here we will use

the model of an Euler elastica or Euler-Bernoulli beam [80, 81] for the elasticity. A number of problems presented in this thesis involve semi-flexible polymers that are subjected to Brownian fluctuations. As a result along with the typical elastic forces we will have contributions from stochastic Brownian forces as well. The general form of the force density for an inextensible semi-flexible polymer is given by:

$$\mathbf{f}(s, t) = B\mathbf{x}_{ssss} - (\sigma\mathbf{x}_s)_s + \mathbf{f}^{\text{Br}}. \quad (2.32)$$

In the above expression \mathbf{f}^{Br} is a stochastic Brownian force that obeys the fluctuation dissipation theorem:

$$\langle \mathbf{f}^{\text{Br}}(s, t) \rangle = \mathbf{0}, \quad (2.33)$$

$$\langle \mathbf{f}^{\text{Br}}(s, t) \mathbf{f}^{\text{Br}}(s', t') \rangle = 2k_B T \mathcal{M}^{-1} \delta(s - s') \delta(t - t'), \quad (2.34)$$

where $\delta(x)$ is the Dirac's delta function and \mathcal{M} is the mobility operator defined previously.

2.3.4 Nondimensionalization and boundary conditions

The length scale of the problem scales with the filament length L . The flow time scale is given as $\mathbf{u}_\infty(\mathbf{x}) \sim \dot{\gamma}L$ where $\dot{\gamma}$ is a shear rate. For non-Brownian filaments it is convenient to use $\dot{\gamma}^{-1}$ as the time scale of the problem. However for Brownian filaments it is appropriate to introduce the relaxation time scale $\tau \sim 8\pi\mu L^4/B$. This is a characteristic timescale over which bending modes of a filament relax [82]. We notice that the elastic force scale per unit length is set by bending and scales as B/L^3 . We will see later on that typical length scales of transverse fluctuations of a Brownian filament is $r_\perp \sim L\sqrt{L/\ell_p}$. Considering this, the Brownian forces per unit length is scaled as $\mathbf{f}^{\text{Br}} \sim \sqrt{L/\ell_p}B/L^3$ [83].

Upon invoking the following scalings the dimensionless governing equation becomes:

$$\boldsymbol{x}_t(s) = \bar{\mu} \boldsymbol{u}_\infty(\boldsymbol{x}(s)) + \mathcal{M} \cdot \boldsymbol{f}(\boldsymbol{x}(s)), \quad (2.35)$$

$$\boldsymbol{f}(\boldsymbol{x}(s)) = \boldsymbol{x}_{ssss} - (\sigma \boldsymbol{x}_s)_s + \sqrt{\frac{L}{\ell_p}} \boldsymbol{\eta}. \quad (2.36)$$

In the above expression \mathcal{M} is the mobility matrix defined by slender-body-theory and $\boldsymbol{\eta}$ is the dimensionless thermal fluctuation satisfying:

$$\langle \boldsymbol{\eta}(s, t) \boldsymbol{\eta}(s', t') \rangle = 2\mathcal{M}^{-1} \delta(s - s') \delta(t - t'). \quad (2.37)$$

The nondimensionalization results in two dimensionless number. The first one is called the elasto-viscous number and is defined as:

$$\bar{\mu} = \frac{8\pi\mu\dot{\gamma}L^4}{B}. \quad (2.38)$$

This can be interpreted as the hydrodynamic forcing of the problem and shows a strong dependence on the length of the polymer. We can also interpret it as a competition between the time scale of bending relaxation to that imposed by the background flow. The other dimensionless number is ℓ_p/L that characterizes the strength of thermal fluctuations in the problem with the limit $\ell_p/L \gg 1$ corresponding to that of Brownian rods. If the hydrodynamics is given by the local SBT then it is appropriate to define the elasto-viscous number as: $\bar{\mu} = 8\pi\mu\dot{\gamma}L^4/(Bc)$ where $c = -\ln(\epsilon^2 e)$ is the geometric factor that dictates the local friction coefficient of filament.

We reserve our discussion on computational methods to solve the evolution equations for the next section and conclude the present section by a discussion on appropriate boundary conditions for the problem in different setups. For a filament that is free at both ends the boundary terms of the variation of energy functional in eqn (2.18) requires:

$$\sigma(s=0) = \sigma(s=1) = 0, \quad (2.39)$$

$$\boldsymbol{x}_{ss} = \boldsymbol{x}_{sss} \Big|_{s=0,1} = \mathbf{0}. \quad (2.40)$$

These boundary conditions simply mean that the filament is force and moment free. We now consider two additional cases of filaments that are clamped or hinged at one end. Without any loss of generality we assume the end $s = 1$ to be free where we have $\sigma = 0$ and $\mathbf{x}_{ss} = \mathbf{x}_{sss} = \mathbf{0}$. In the fixed end of the filament we have by construction $\mathbf{x}(s = 0) = \mathbf{0}$. Here we have conveniently placed the origin at $s = 0$. (i) A hinged filament is free to rotate and is moment free so additionally we have $\mathbf{x}_{ss}(s = 0) = \mathbf{0}$. (ii) A clamped filament however cannot rotate and is thus not moment free. Typically the tangent vector at the clamping point remains fixed in a particular direction. Thus the boundary condition translates to $\mathbf{x}_s(s = 0) = \hat{\mathbf{e}}$, where $\hat{\mathbf{e}}$ is the unit vector along which the tangent points. However the boundary condition for the tension σ at the fixed end is non-trivial and has been calculated incorrectly in a number of problems in the literature [84]. The condition can be obtained by realizing that the velocity of the filament at the fixed end is identically zero. In the context of local SBT demanding $\mathbf{x}_t(s = 0)$ translates to

$$\begin{aligned} 2c\sigma_s \mathbf{x}_s + (c - 2)\sigma \mathbf{x}_{ss} - (c - 2)\mathbf{x}_s^{(4)} - (c + 2)(\mathbf{x}_s \cdot \mathbf{x}_s^{(4)})\mathbf{x}_s \\ + \sqrt{\frac{L}{\ell_p}} [(2 - c)\boldsymbol{\eta} - (c + 2)\mathbf{x}_s(\mathbf{x}_s \cdot \boldsymbol{\eta})] = \mathbf{0} \quad \text{at } s = 0. \end{aligned} \quad (2.41)$$

We can project the above equation on to the tangential direction $\mathbf{x}_s(s = 0)$ to obtain the appropriate boundary condition for tension. Noting the identity that $\mathbf{x}_s \cdot \mathbf{x}_s^{(4)} = -3\mathbf{x}_{ss} \cdot \mathbf{x}_{sss}$ and recalling that for a hinged filament $\mathbf{x}_{ss}(s = 0) = \mathbf{0}$ we obtain:

$$\sigma_s(s = 0) = \sqrt{\frac{L}{\ell_p}} (\boldsymbol{\eta} \cdot \mathbf{x}_s) \Big|_{s=0}, \quad (\text{hinged filament}) \quad (2.42)$$

$$\sigma_s(s = 0) = \left[\sqrt{\frac{L}{\ell_p}} (\boldsymbol{\eta} \cdot \mathbf{x}_s) + \mathbf{x}_s \cdot \mathbf{x}_s^{(4)} \right] \Big|_{s=0}. \quad (\text{clamped filament}) \quad (2.43)$$

Note that for a non-Brownian filament $\boldsymbol{\eta} = \mathbf{0}$ and the expressions simplify considerably. The relevant boundary conditions are illustrated pictorially for this case in Figure 2.8.

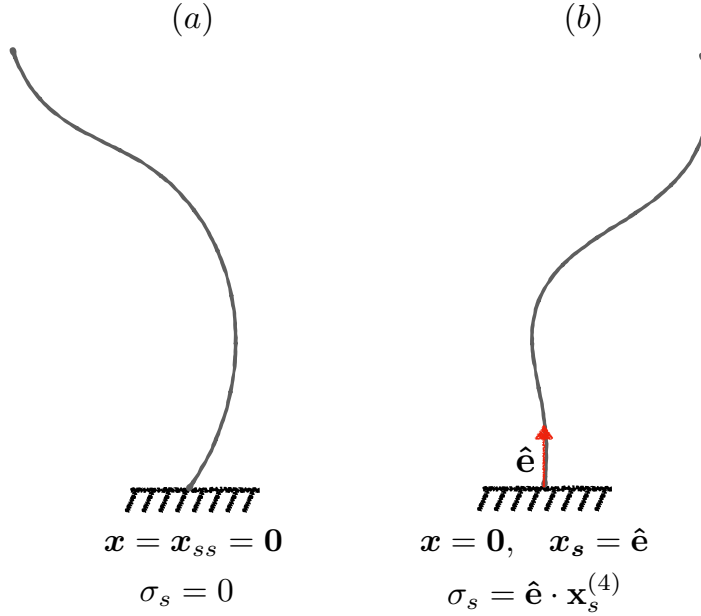


Figure 2.8: Schematic of boundary conditions at the fixed end of a non-Brownian filament with (a) hinged and (b) clamped conditions. At the free end we always have $\mathbf{x}_{ss} = \mathbf{x}_{sss} = \mathbf{0}$ and $\sigma = 0$.

2.4 Computational methods

In the previous section we have outlined the foundations of SBT and discussed appropriate boundary conditions for relevant problems. The computational method to solve the evolution equation for the centerline motion follows closely previous formulations [81, 85]. Here we briefly outline the primary aspects and point the interested reader to previous references for further details.

2.4.1 Discretization and tension

Since the filament is inextensible the arc-length is a material description and we discretize it uniformly. For simulations presented here we typically use $N = 128$ points with

the spacing between points being $\Delta s = 1/(N - 1)$. The linear operators are represented using second order accurate finite difference approximations [81].

In order to proceed with the time evolution of the filament conformation we first need to determine the unknown tensions $\sigma(s)$ that acts as a Lagrange multiplier imposing inextensibility. Given any conformation of the filament, this unknown tension can be solved for by deriving an auxiliary equation from the constraint of inextensibility. From inextensibility we have: $\mathbf{x}_s \cdot \mathbf{x}_s = 1$. Differentiating this with respect to time we obtain:

$$\partial_t \mathbf{x}_s \cdot \mathbf{x}_s = 0 \implies \mathbf{x}_s \cdot \frac{\partial}{\partial s} [\bar{\mu} \mathbf{u}_\infty(s) - \mathcal{M} \cdot \mathbf{f}(s)] = 0. \quad (2.44)$$

Upon invoking a series of identities from differential geometry of curves and expanding the mobility operator we arrive at the following second order linear differential equation for the tension:

$$\begin{aligned} 2c\sigma_{ss} + (2 - c)\sigma|\mathbf{x}_{ss}|^2 - \mathbf{x}_s \cdot \frac{\partial}{\partial s} \mathbf{K}[(\sigma \mathbf{x}_s)_s] &= \bar{\mu} \mathbf{x}_s \cdot \mathbf{u}_\infty + (2 - 7c)(\mathbf{x}_{ss} \cdot \mathbf{x}_s^{(4)}) \\ &\quad - 6c|\mathbf{x}_{sss}|^2 - \mathbf{x}_s \cdot \frac{\partial}{\partial s} \mathbf{K}[\mathbf{x}_s^{(4)} - \sqrt{L/\ell_p} \boldsymbol{\eta}] + \\ &\quad 2c\sqrt{\frac{L}{\ell_p}}(\mathbf{x}_s \cdot \boldsymbol{\eta}_s) + (2 + c)\sqrt{\frac{L}{\ell_p}}(\mathbf{x}_{ss} \cdot \boldsymbol{\eta}). \end{aligned} \quad (2.45)$$

The above equation is solved with the appropriate boundary condition as discussed in previous section. For the non-local SBT the linear system for the unknown tension resulting upon discretization is dense. Solution with a direct solver requires $\mathcal{O}(N^3)$ operations. On the other hand, for a local SBT the linear system is tridiagonal and one can employ fast solvers to solve in $\mathcal{O}(N)$ complexity. During computations it is common to encounter round-off errors and the inextensibility is not exactly satisfied by the computed tension. To overcome this problem one can add a heuristic term $-\beta(1 - \mathbf{x}_s \cdot \mathbf{x}_s)$ on the right hand side of the tension equation [81]. This term is identically zero if inextensibility is exactly

satisfied. Otherwise this term acts like a spring that penalizes for extensibility and thus the parameter β is called the penalty parameter [68, 81].

2.4.2 Time marching

The fourth order derivative of the Lagrangian marker \mathbf{x} with respect to s stemming from bending forces make the equations of motions extremely stiff. In order to overcome severe time-step restrictions we use a second order accurate time scheme that treats the linear stiff terms implicitly and the non-linear terms explicitly. Schematically one can write the evolution equation as:

$$\mathbf{x}_t = \mathbf{F}(\mathbf{x}, \mathbf{x}_{ssss}) + \mathbf{G}(\mathbf{x}). \quad (2.46)$$

The terms in \mathbf{F} involve expressions with \mathbf{x}_{ssss} and will be treated implicitly. Suppose Δt is the time step and $t^n = n\Delta t$. Then the above decomposition is used to give

$$\frac{1}{2\Delta t} (3\mathbf{x}^{n+1} - 4\mathbf{x}^n + \mathbf{x}^{n-1}) = \mathbf{F}(2\mathbf{x}^n - \mathbf{x}^{n-1}, \mathbf{x}_{ssss}^{n+1}) + 2\mathbf{G}(\mathbf{x}^n) - \mathbf{G}(\mathbf{x}^{n-1}). \quad (2.47)$$

This system is accompanied by appropriate boundary conditions which for free filaments translate to $\mathbf{x}_{ss} = \mathbf{x}_{sss} = \mathbf{0}$ at $s = 0, L$. The above discretization yields a band-diagonal matrix for the unknown \mathbf{x}^{n+1} that can be inverted efficiently at the cost $\mathcal{O}(N)$. It is interesting to note that in absence of the non-local interactions the solution to the problem can be done in $\mathcal{O}(N)$ operations as the equation for tension is tridiagonal. However in presence of hydrodynamic interactions the computational cost increases to $\mathcal{O}(N^3)$ details of which can be found in [81, 85].

2.4.3 Treatment of Brownian forces

We know that the Brownian fluctuations have zero mean and a variance that is prescribed by the fluctuation dissipation theorem by eqn. (2.37). Numerically this can be

approximated as follows:

$$\boldsymbol{\eta} = \sqrt{\frac{2}{\Delta s \Delta t}} \mathbf{B} \cdot \mathbf{w}, \quad (2.48)$$

where $\mathbf{B} = \sqrt{\mathcal{M}^{-1}}$ and \mathbf{w} is a Gaussian random vector with zero mean and unit variance. Δs and Δt are the resolution of the spatial and temporal discretization respectively. In the presence of hydrodynamic interactions \mathcal{M} is a dense matrix and computing the square root is an $\mathcal{O}(N^3)$ operation that requires approximations using Cholesky decomposition [86]. Recently there has been significant developments in evaluating this using efficient iterative solvers such as the Lanczos algorithm [87]. However one does not gain significantly unless the system size is sufficiently large. The problems presented in this thesis are restricted to smaller size of $N = 64\text{--}256$ and for fast solution we introduce an approximation. We approximate the square root as follows:

$$\mathbf{B} = \sqrt{(\boldsymbol{\Lambda} + \mathbf{K})^{-1}} \approx \sqrt{\boldsymbol{\Lambda}^{-1}}. \quad (2.49)$$

This approximation is not entirely correct as we retain the non-local operator in our formulation but do not include it in the evaluation of Brownian fluctuations. However this approximation allows us analytically compute the square root of the local resistance matrix which yields:

$$\mathbf{B} = \sqrt{\boldsymbol{\Lambda}^{-1}} = \frac{1}{\sqrt{2-c}} \left[\mathbf{I} + \left(\sqrt{\frac{c-2}{2c}} - 1 \right) \mathbf{x}_s \mathbf{x}_s \right]. \quad (2.50)$$

There are a couple of other subtle aspects associated with Brownian polymers. The solution to the unknown line tension involves taking spatial derivatives of the Brownian noise. However $\boldsymbol{\eta}$ is uncorrelated in space and time and is not differentiable. In order to obtain numerically stable solution we follow [85] and remove the large wave-numbers of the noise by designing a ‘low-pass-filter’ that allows us to obtain numerical derivatives. However unlike [85] we do not rescale the filtered noise to preserve variance as this leads to introducing back the energy of the removed modes.

Inclusion of thermal fluctuations also severely restricts the allowable time-steps in the problem. Since the Brownian fluctuations are inversely proportional to the square root of the time step, the accuracy of the solution is reduced to first order in time. In this case, one can indeed choose to use an EulerMaruyama time stepping method instead of the second order accurate backward difference method discussed in the previous section.

2.4.4 Interactions and recent developments

Previously we have discussed about tools and methods for single filament dynamics. We close our discussion with some remarks on modeling and simulation of multiple filaments that interact with each-other hydrodynamically. Consider M fibers indexed by $\alpha = 1, 2, \dots, M$. For any filament α , the equation of motion to the leading order takes the following form:

$$8\pi\mu [\partial_t \mathbf{x}^\alpha - \mathbf{u}_\infty(\mathbf{x}^\alpha(s, t))] = -\boldsymbol{\Lambda}[\mathbf{f}^\alpha](s) - \boldsymbol{\mathcal{K}}[\mathbf{f}^\alpha](s) - \sum_{\beta=1, \beta \neq \alpha}^M \mathbf{G}_\beta[\mathbf{x}^\alpha], \quad (2.51)$$

where the contribution of the other filaments at a point $\bar{\mathbf{x}} = \mathbf{x}^\alpha(s, t)$ is accounted as:

$$\mathbf{G}_\beta[\bar{\mathbf{x}}] = \int_{\Gamma_\beta} \left[\frac{\mathbf{I} + \hat{\mathbf{R}}(s') \hat{\mathbf{R}}(s')}{|\mathbf{R}(s')|} \right] \cdot \mathbf{f}^\beta(s') ds'. \quad (2.52)$$

In the above expression $\mathbf{R}(s) = \bar{\mathbf{x}} - \mathbf{x}^\beta(s)$ and $\hat{\mathbf{R}}$ is the associated unit vector. This simply states that to the leading order interactions in free-space are accounted by Stokeslets. One would choose the appropriate Greens function depending on specific cases. Typically due to the finite size of the slender object, there are also contributions from a distribution of source doublets that scales as ϵ^2/r^3 and is neglected in the above expression [81]. One may be tempted to think that to leading order the interactions decay as $1/r$ due to the nature of Stokeslet interactions which is indeed the case in problems involving sedimentations where long range hydrodynamic interactions lead to various instabilities [88, 89]. However

for force-free filaments the interactions decay as $1/r^2$ and are dominated by doublet contributions. This can be appreciated from an integration by parts of the interactions and by noticing that the force density $\mathbf{f}(s)$ is a total derivative of the arc-length [81].

Simulations with multiple filaments are computationally expensive. For M fibers with N discretization points, evaluation of hydrodynamic interaction mounts to a matrix vector multiplication that costs $\mathcal{O}(M^2N^2)$. This quadratic dependence becomes the main bottleneck in evaluating direct sums for large system size. Apart from classical Stokesian dynamics [90], SPME techniques in periodic domain [91], there have been significant recent developments that extend ideas of Fast Multipole Method (FMM) [92] for Stokes kernels [93] and the evaluations can be done in $\mathcal{O}(MN)$ operations. As a part of ongoing work we will discuss later how some of these ideas can be incorporated to study problems involving long-range interactions in a bed of flexible filaments.

2.5 Brownian motion in slender structures

The previous discussions have outlined key aspects of elasticity and hydrodynamics of slender objects. We have also discussed how Brownian fluctuations can be incorporated in the model and dealt with numerically. In this section we focus on various physical phenomenon and simple scaling arguments that illustrate how Brownian motion can introduce rich physics into various problems ranging from the dynamics of rigid rods to semi-flexible polymers.

2.5.1 Dynamics of Brownian rods

The simplest possible example of a slender structure is a rigid rod that serves as a model of an object whose persistence length ℓ_p is much larger than its contour length L . While a rigid rod is a theoretical idealization, its orientational dynamics in the presence of

flow does provide practical means to understand microstructure and rheology of structures fluids [14,94–96]. We reserve discussions on rheology for the next chapter and instead focus here on some results based on scaling arguments that describe the orientation dynamics of a rod in a simple shear flow. We will see in subsequent chapters that this study serves as a benchmark for understanding how hydrodynamics, shape-fluctuations and elastic-instabilities modify dynamics of semi-flexible polymers.

We focus on the case of a fore-aft symmetric and axisymmetric rod, in which case the translational and rotational degrees of freedom are decoupled from one another. We can then describe the rod by the position of its center of mass and an orientation vector \mathbf{p} that lives on the unit sphere. The slowest relaxation process in a dilute suspension of rods is rotational diffusion. The rotational diffusivity can be defined as the inverse of a time scale over which a rigid rod forgets about its orientation due to Brownian fluctuations. From typical friction coefficients of rods in viscous flow, one can employ Stokes-Einstein relation to obtain the rotary diffusivity which is given by

$$d_r = \frac{3k_B T \ln(2/\epsilon)}{\pi \mu L^3}, \quad (2.53)$$

where $\epsilon = a/L$ is the aspect ratio of the rod. In absence of any external flow the rod samples all possible configuration on the unit-sphere and the equilibrium distribution is isotropic.

Let us now consider the other limit of a non-Brownian rod in a simple shear flow. In this case the rods exhibit periodic tumbling behavior similar to Jeffery orbits for an ellipsoidal particle [97].

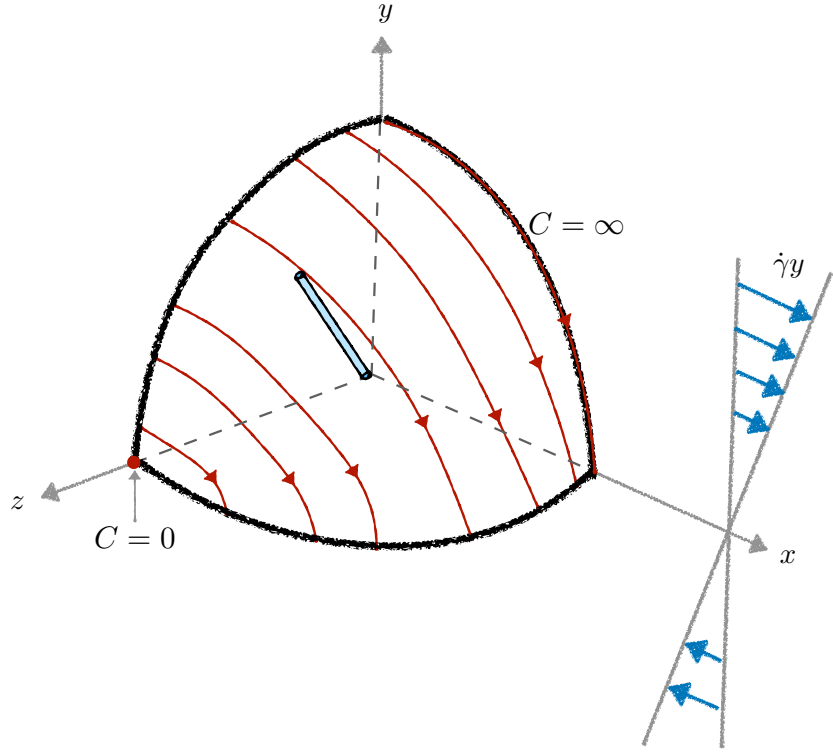


Figure 2.9: Typical orbits of prolate spheroids in simple shear flow for different orbit constants.

Periodic orbits in three dimension are characterized by an orbit constant C and the time period of such periodic orbits is given by:

$$T = \frac{2\pi}{\dot{\gamma}} \left(\epsilon + \frac{1}{\epsilon} \right). \quad (2.54)$$

As illustrated in Figure 2.9, the limit of $C \rightarrow \infty$ corresponds to tumbling confined in the plane of shear while the limit $C \rightarrow 0$ corresponds to rolling motion on a plane perpendicular to the shear plane. In 2D the orientation of the rod is characterized by the angle θ with the horizontal plane whose evolution is given by:

$$\theta_t = -\dot{\gamma} \sin^2 \theta + \mathcal{O}(\epsilon^2). \quad (2.55)$$

This simple equation helps us to appreciate a few scaling laws that we discuss below. When both Brownian motion and flow are present there is a competition between the time

scale set by the external flow that tries to align the filament with the time scale set by rotational diffusion. The dynamics in this case is characterized by a single dimensionless number called the rotary Péclet that compares shear to diffusion, defined as:

$$\text{Pe}_r = \dot{\gamma}/d_r. \quad (2.56)$$

For a shear flow in the $x - y$ plane the orientational dynamics of the rigid rod is described by a Langevin equation that results from the balance of Brownian and hydrodynamic torques. It is given by

$$\dot{\mathbf{p}} = p_y (\hat{\mathbf{e}}_x - p_x \mathbf{p}) + \sqrt{\frac{2}{\text{Pe}_r \Delta t}} (\mathbf{I} - \mathbf{p}\mathbf{p}) \cdot \mathbf{w}, \quad (2.57)$$

where \mathbf{w} is a Gaussian random vector with zero mean and unit variance. In 2D the leading order Langevin equation takes a simple form:

$$\theta_t = -\dot{\gamma} \sin^2 \theta + \xi(t), \quad (2.58)$$

where $\langle \xi(t)\xi(t') \rangle = 4d_r \delta(t-t')$. If $\xi = 0$ the system has a fixed point at $\theta = 0$ which means that the rod simply tumbles and aligns with the zero shear plane and remains there. However a nonzero ξ corresponds to a bifurcation where the filament gets stochastically kicked out of the zero-shear plane that forces it to perform tumbling. A natural question that comes up is how does the frequency of such tumbling scales with the flow strength?

It turns out that when the rod is aligned with the zero-shear plane its dynamics is dominated by Brownian fluctuations. In 2D it is possible to show that at an angle $\theta = \theta_0 \sim (d_r/\dot{\gamma})^{1/3}$ there is a balance of advective fluxes from rotation due to flow and Brownian diffusion [30]. As illustrated in Figure 2.10 the regime $\theta < \theta_p$ is dominated by diffusion. The typical time spent by the rod in this regime is given by:

$$\tau_{\text{diff}} \sim \theta_p^2/d_r \sim d_r^{-1/3} \dot{\gamma}^{-2/3}. \quad (2.59)$$

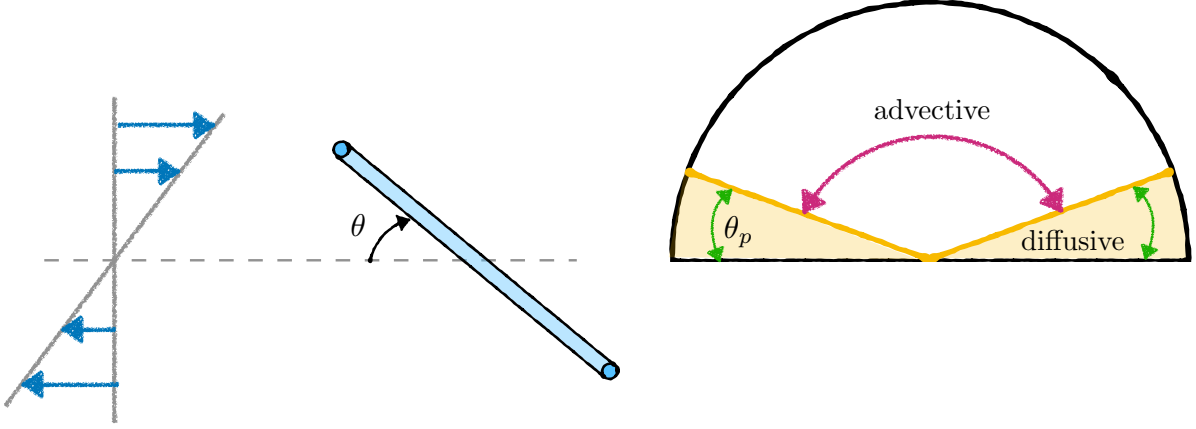


Figure 2.10: Diffusion and advection dominated regimes of a rigid rod tumbling in 2D shear flow.

The regime $\theta > \theta_p$ is dominated by advection and we can get an estimate of the time spent in this regime by simply integrating the equations of motion in absence of Brownian fluctuations. On doing so we obtain:

$$\tau_{\text{adv}} \sim \int_{\theta_p}^{\pi - \theta_p} \frac{d\theta}{\dot{\gamma} \sin^2 \theta} = \frac{2}{\dot{\gamma} \tan \theta_p} \sim d_r^{-1/3} \dot{\gamma}^{-2/3}, \quad (2.60)$$

where we have used the approximation $\tan \theta_p \sim \theta_p$. Now it is straightforward to compute the frequency of tumbling. It is given as

$$\nu = \frac{1}{\tau_{\text{adv}} + \tau_{\text{diff}}} \sim \dot{\gamma}^{2/3}. \quad (2.61)$$

This is a classic result and in dimensionless form simply states $\nu \sim \text{Pe}_r^{2/3}$ [98]. We will revisit this result in next chapter and discuss how buckling instabilities of flexible polymers modify this scaling.

2.5.2 Scaling laws for semi-flexible filaments

We know from our discussions in Chapter 1 that long-chain polymer molecules like DNA are typically entropic with $\ell_p \ll L$. For semi-flexible polymers like actin, $L \sim \ell_p$ and

we have a interplay between elasticity and Brownian fluctuation. Following our discussion on rigid rods here we outline some key features in terms of scaling of a fluctuating semi-flexible polymer in a Newtonian solvent.

Static properties: For a filament with length $L \lesssim \ell_p$ the filament remains nearly straight with small transverse fluctuations. We let the x axis define the average orientation of the filament and use a single transverse co-ordinate $u(x, t)$ for simplicity as illustrated in Figure 2.11. For small transverse fluctuations the bending energy can be represented as:

$$E_B = \frac{B}{2} \int_0^L \left(\frac{\partial^2 u}{\partial x^2} \right)^2 dx. \quad (2.62)$$

We now represent the transverse fluctuations in terms of a Fourier decomposition:

$$u(x, t) = \sum_q u_q(t) \sin(qx), \quad (2.63)$$

where q is simply the wavenumber [99]. The above Fourier representation is valid for a filament with fixed ends having $u = 0$ at $x = 0, L$ with $q = n\pi/L$, where $n = 1, 2, 3 \dots$. On invoking orthogonality of the Fourier modes the bending energy can be represented as sums of the Fourier modes as:

$$E_B = \frac{BL}{4} \sum_q q^4 u_q^2. \quad (2.64)$$

We now notice that there is a quadratic dependence of the energy on u_q^2 and one can invoke the principle of equipartition of energy. On doing so, we obtain:

$$\langle u_q^2 \rangle = \frac{2k_B T}{BL} \frac{1}{q^4} \equiv \frac{2}{L\ell_p} \frac{1}{q^4}. \quad (2.65)$$

Thus the expected value of the ensemble averaged transverse mode fluctuation is obtained by performing a sum over all wave-numbers and in scaling terms is given as:

$$\langle u^2 \rangle \sim \frac{L^3}{\ell_p}. \quad (2.66)$$

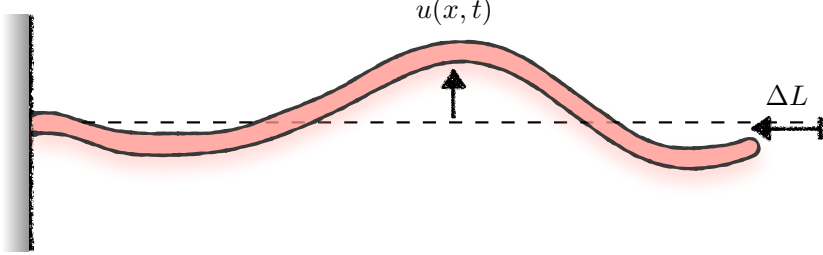


Figure 2.11: Schematic of a fluctuating filament. The figure shows the transverse coordinate and the longitudinal compression due to Brownian fluctuations.

Recall that while discussing non-dimensionalizing the SBT, we used the same scaling as above for Brownian forces without explaining its origin. For an inextensible chain the end-to-end contraction of the chain due to presence of transverse fluctuations is given by:

$$\Delta L = \int_0^L \left(\sqrt{1 + \left| \frac{\partial u}{\partial x} \right|^2} - 1 \right) dx \approx \frac{1}{2} \int_0^L \left| \frac{\partial u}{\partial x} \right|^2 dx = \frac{L}{4} \sum_q q^2 u_q^2. \quad (2.67)$$

Invoking the previous result on transverse fluctuations we find,

$$\langle \Delta L \rangle \sim \frac{L^2}{\ell_p}. \quad (2.68)$$

Dynamic properties: In the above we have considered static properties of individual polymer chains. The dynamics of semiflexible filaments help us appreciate various results on relaxation times and evolution of end-to-end distance. As before, considering small transverse fluctuations. The equation of motion for $u(x, t)$ in the over-damped limit is given by:

$$\xi_{\perp} \frac{\partial u}{\partial t} = -B \frac{\partial^4 u}{\partial x^4} + \eta_{\perp}, \quad (2.69)$$

where $\xi_{\perp} \approx 4\pi\mu/\ln(2/\epsilon)$ is the friction coefficient in the transverse direction and η_{\perp} is the Brownian noise projected onto $u(x, t)$. Representing $u(x, t)$ in terms of its Fourier series and performing an ensemble average we obtain

$$\xi_{\perp} \left\langle \frac{du_q}{dt} \right\rangle = -Bq^4 \langle u_q \rangle, \quad (2.70)$$

where the noise drops out due to averaging. The above expression hints to us that the characteristic relaxation time of a bending mode is:

$$\omega(q) \sim \frac{\mu}{Bq^4}. \quad (2.71)$$

The quartic dependence on the wavenumber stands out in the above expression for relaxation time. This means that if a mode of wavelength $1\mu m$ takes 10^{-3} s to relax then a mode of wavelength $10\mu m$ will take 100 s. This results in a large time scale separation on the problem which makes it difficult for any numerical method to capture all the time scales of the problem. In any problem, typically the longest wave-lengths have the largest amplitude and the typical conformations of the filament is dominated by them. This explains why we chose the longest relaxation time τ to non-dimensionalize the governing equation of the SBT.

With this simple scaling arguments we can predict a few more interesting results.

After time t the dominant mode relaxes over a distance [100, 101]:

$$\ell_{\perp}(t) \sim \left(\frac{Bt}{\mu} \right)^{1/4}. \quad (2.72)$$

As seen before the magnitude of transverse fluctuations increases with length. Thus at any time t , the expected mean-squared transverse motion is given by,

$$\langle u(t)^2 \rangle \sim \frac{\ell_{\perp}(t)^3}{\ell_p} \sim t^{3/4} \quad (2.73)$$

The dynamics of longitudinal motion can be computed similarly. Here, however, we must account for the fact that the mean-square longitudinal fluctuations $\langle \delta\ell(t)^2 \rangle$ of a long filament involve the sum (in quadrature) of independently fluctuating segments along a full filament of length L . The typical size of such independently fluctuating segments at time t is $\ell_{\perp}(t)$, of which there are $L/\ell_{\perp}(t)$. We have previously computed the average extension in (2.68). Using that result we find,

$$\langle \delta\ell(t)^2 \rangle \sim \frac{L}{\ell_{\perp}(t)} \frac{\ell_{\perp}(t)^4}{\ell_p^2} \sim t^{3/4}. \quad (2.74)$$

This result tells us about the scaling of the mean-squared-displacement of the end-to-end distance of a polymer before it saturates [83, 102]. We have reproduced such dynamic scaling laws for validation of our numerical method [85].

2.6 Suppression of fluctuations

In the previous section we have outlined various static and dynamic scaling laws for semi-flexible polymers. We end this chapter by discussing the most elementary problem in polymer physics: stretching a fluctuating filament by applying force. The 1970s and 1980s saw the advent of various advanced biochemical methods for manipulating single molecules optical tweezers [103] and atomic-force microscopy [104] that provided tools to investigate the mechanical behavior of flexible polymers. Historically most of the initial studies focused on long chain polymer molecules like DNA where work done by external forces went in reducing the conformational entropies of the chain. DNA chains were either pulled by magnetic beads from one end by holding the other end fixed [105] or an anchored filament was stretched out by electric field or external flow [106, 107] from which it was possible to obtain force-extension relations. For small forces these polymers behaved like a linear spring that can be reconciled with the entropic nature and a freely jointed chain model [95]. However for strong forces one needs to account for the bending stiffness as in a worm like chain (WLC) model presented in the previous section to obtain the correct force-extension behavior [108, 109].

On the other hand stiff biopolymers like actin have not received much attention and there are few systematic studies on how hydrodynamic or external forces iron out fluctuations. In the following discussion we present two canonical problems that highlight the process of suppression of fluctuation and briefly mention a few questions that are yet to be resolved.

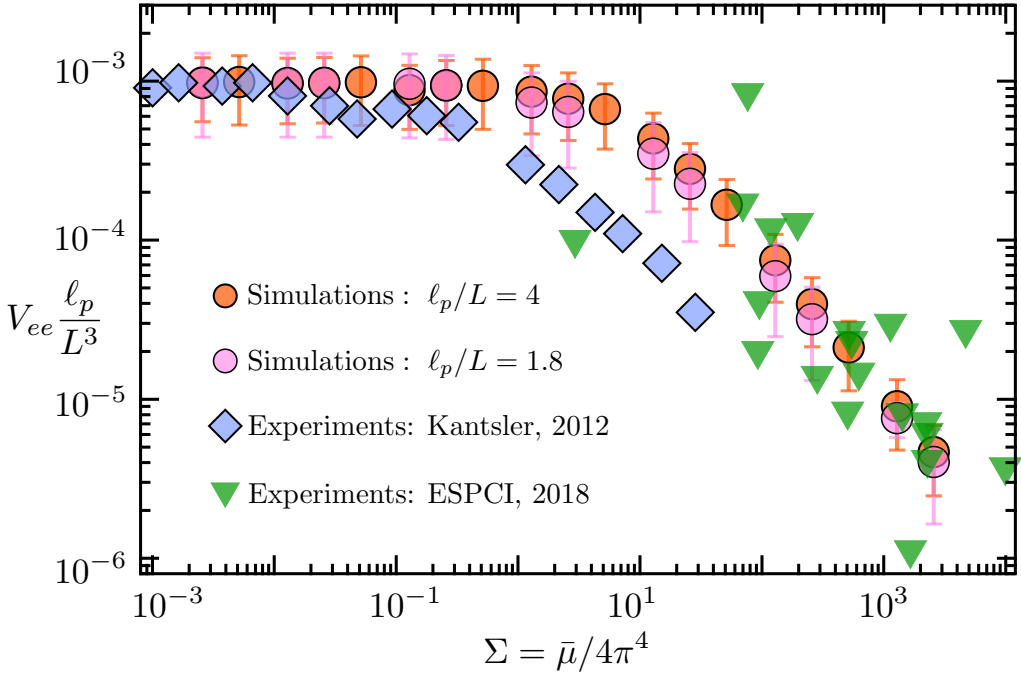


Figure 2.12: End-to-end fluctuations of actin filaments in extensional flow. Simulations are compared against experimental results of [2] and from [3].

2.6.1 Actin in extensional flow

We will consider a semiflexible filament placed in a 2D stagnation point flow with its center at the stagnation point. This can be realized in a cross-slot microchannel as studied in [2] with the external flow being given by $\mathbf{u}^\infty = \dot{\epsilon} (x, -y, 0)$, where $\dot{\epsilon}$ is the extension rate. More recently helical buckling of actin filaments was studied in a hyperbolic channel [8]. While this is the focus of Chapter 4, it is important to highlight that in the convergent part of an hyperbolic channel the flow is also well described by the 2D stagnation point flow approximations. In such a setup the flow tries to stretch the filament along its axis. For sufficiently strong flow or equivalently large $\bar{\mu}$ the fluctuations are suppressed. To

quantify this we introduce the variance of the fluctuations defined as:

$$V(x) = \langle [h(x) - \bar{h}(x)]^2 \rangle, \quad (2.75)$$

where $h(x)$ is the transverse co-ordinated of the filament and $\bar{h}(x)$ is the mean-shape. We have used x as the parameterizing co-ordinate which is accurate in the limit of strong flow and weak fluctuations. The Figure 2.12 shows the re-scaled variance of the end points from our simulations and two different experiments with $V_{ee} = [V(0) + V(L)]/2$. From our discussion on scaling argument for transverse fluctuation we know that a rescaling by ℓ_p/L^3 will collapse all the data as done in Figure 2.12.

In weak flow the filament does not feel hydrodynamic forces and it's end-to-end fluctuation remains fairly constant and close to what one expect in absence of flow. However as the hydrodynamic drag increases we observe that fluctuations are strongly suppressed and decrease monotonically with $\bar{\mu}$. Our simulation results are in partial agreement with [2] in weak flow. Due to long filaments used in [3] the $\bar{\mu}$ is much larger and covers a regime unexplored in [2]. Our simulations compare very well with the experiments in strong flows as seen in Figure 2.12. A simple theory to predict the end-to-end fluctuation was proposed in [2] based on the Monge representation of the filament. While the theory that relies on an eigenfunction expansion of the fluctuations on an appropriate basis [85] predicts the right trend in the behavior it does not agree quantitatively with simulations and experiments. Finally it is instructive to estimate in scaling sense the drag force experienced by the filament when there is complete suppression of fluctuation at large $\bar{\mu}$. For a filament that is almost straight the viscous force is given by $F_v \sim \bar{\mu}B/16L^2 \sim 0.8 - 1.8\text{pN}$. In other words one needs to apply a distributed force of this magnitude in order to straighten the fluctuating filament.

2.6.2 Pulling from the ends

We now consider another canonical problem in which we pull the filament from two ends by applying a force. There are various versions and flavors of this experiment. Examples include holding one end of the filament fixed and pulling the free end by magnetic forces, or pulling both ends of the filament by optical tweezers in harmonic traps. We consider the case when an external force $\mathbf{F} = F\hat{\mathbf{e}}_x$ is applied along the x axis of the filament at the two end points. A schematic of this numerical experiment is shown in Figure 2.13. For our 3D simulations this translate to the following boundary conditions:

$$\mathbf{x}_{ss} = \mathbf{0}, \quad s = 0, L \quad (2.76)$$

$$-(B\mathbf{x}_{sss} - \sigma\mathbf{x}_s) = -F\hat{\mathbf{e}}_x, \quad s = 0 \quad (2.77)$$

$$B\mathbf{x}_{sss} - \sigma\mathbf{x}_s = F\hat{\mathbf{e}}_x, \quad s = L \quad (2.78)$$

where the first equation prescribes the moment-free condition and the last two states the balance of forces. On exploiting the first boundary condition it is possible to obtain the boundary condition for tension as: $\sigma(0, L) = -F\hat{\mathbf{e}}_x \cdot \mathbf{x}_s(0, L)$.

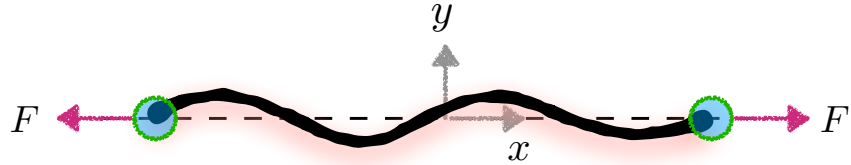


Figure 2.13: Schematic of a polymer getting pulled from two ends.

While stretching the filament the force does work on the system. We can write an effective Hamiltonian for the problem that combines the bending energy and this work. It is given by:

$$\mathcal{H} = \frac{B}{2} \int_0^L |\mathbf{x}_{ss}|^2 ds - \mathbf{F} \cdot [\mathbf{x}(L) - \mathbf{x}(0)] \equiv \int_0^L \left[\frac{B}{2} |\mathbf{x}_{ss}|^2 - F\hat{\mathbf{e}}_x \cdot \partial_s \mathbf{x} \right] ds. \quad (2.79)$$

In the limit of strong-force $F \gg B/\ell_p^2$ the filament is almost straight. In this limit it is possible to simplify the work done by the force considerably. For the planar problem the calculation is outlined in a pedagogical manner in [110]. Using the equipartition theorem or calculations based on path integrals, it is possible to obtain the expression for mean axial extension in 2D. For large forces this is given as [110]:

$$\langle x(L) - x(0) \rangle \equiv \langle \Delta x \rangle \approx L \left[1 - \frac{1}{4\sqrt{f\ell_p}} \coth \left(\frac{L}{\ell_p} \sqrt{f\ell_p} \right) + \frac{1}{4f\ell_p} \frac{\ell_p}{L} \right], \quad (2.80)$$

where $f = F/k_B T$. We can compute the extension from 3D Brownian simulations as well. The comparison between the 2D theory given by eqn (2.80) and the 3D simulations are shown in Figure 2.14. We find an excellent comparison between the theory and the simulations in the strong force limit when the fluctuations are mostly suppressed. The typical magnitude of force required for suppressing fluctuations was found to be $\mathcal{O}(0.5 - 1)$ pN.

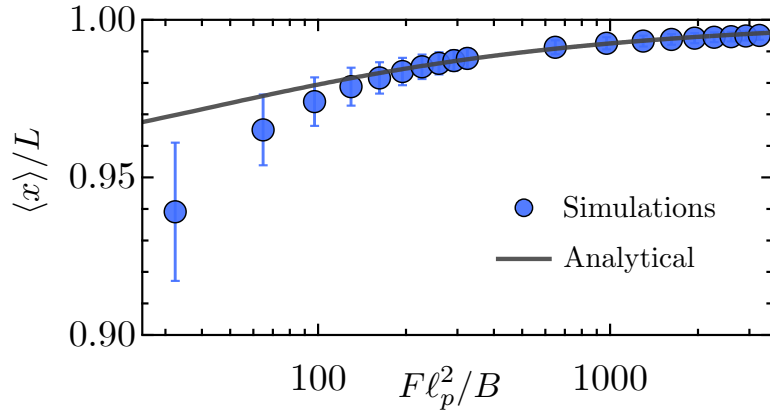


Figure 2.14: Force extension curve for an actin filament with $\ell_p/L = 1.8$.

2.7 Conclusions

In this chapter we have outlined the fundamentals of elasticity and hydrodynamics of slender flexible filaments. The tools developed in this chapter form the backbone of the upcoming discussions on various specific problems related to filaments in flows. We have also outlined the role of Brownian forces in introducing shape fluctuations and various analytical results related to stretching and pulling a filament by forces or flows. These theoretical and numerical experiments allow us to probe and understand mechanical properties polymers, and will help us to develop simple models in the upcoming chapters.

Chapter 3

Morphological transitions and rheology of actin in shear flow

3.1 Introduction

In the previous chapter we laid the foundations for the theoretical and computational tools to study the dynamics of semi-flexible filaments in flows. Our discussions on elasticity of slender structures suggested that inextensible elastic beams can buckle in the presence of compressive viscous forces leading to formation of strongly deformed structures. These deformations change various scaling laws for tumbling of rigid rods in simple shear and have the potential to fundamentally alter rheological properties of suspensions. In this chapter we combine microfluidic experiments with theoretical and numerical modeling to study morphologies of actin filaments in simple shear and reveal their role in emerging rheology.

The case of long-chain polymers such as DNA [23], for which the persistence length ℓ_p is much smaller than the contour length L , has been characterized extensively in experiments [22, 24] as well as numerical simulations [25] and mean-field models [26]. The

dynamics in this case is governed by the competition between thermal entropic forces favoring coiled configurations and viscous stresses that tend to stretch the polymer in strain-dominated flows. The interplay between these two effects is responsible for the coil-stretch transition in elongational flows and tumbling and stretching motions in shear flows, both of which are well captured by classic entropic bead-spring models [27–29].

On the contrary, the dynamics of shorter polymers such as actin filaments [30], for which $L \sim \ell_p$, has been much less investigated and is still not fully understood. Here, it is the subtle interplay of bending forces, thermal fluctuations and internal tension under viscous loading that instead dictates the dynamics. Indeed, bending energy and thermal fluctuations are now of comparable magnitudes, while the energy associated with stretching is typically much larger due to the small diameter of the molecular filaments [31] as discussed in the previous chapter. This distinguishes these filaments from long entropy-dominated polymers such as DNA in which chain bending plays little role.

In the previous chapter we have discussed the classical case of a rigid rod tumbling periodically in shear flow [97], now known as Jeffery orbits. When flexibility becomes significant, viscous stresses applied on the filament can overcome bending resistance and lead to structural instabilities reminiscent of Euler buckling of elastic beams [2, 81, 111–115]. On the other hand, Brownian orientational diffusion has been shown to control the characteristic period of tumbling [30, 116]. In shear flow, the combination of rotation and deformation leads to particularly rich dynamics [30, 83, 117–121], which have yet to be fully characterized and understood. Here we elucidate these dynamics in a simple shear flow [7]. The filaments we consider here have a contour length L in the range of $4 - 40\,\mu\text{m}$ and a diameter $a \sim 8\,\text{nm}$. By analyzing the fluctuating shapes of the filaments, we measured the persistence length, as shown in [48], to be $\ell_p = 17 \pm 1\,\mu\text{m}$ independent of the solvent viscosity. We combine fluorescent labeling techniques, microfluidic flow devices and

an automated-stage microscopy apparatus to systematically identify deformation modes and conformational transitions. Our experimental results are confronted against Brownian dynamics simulations and theoretical models that describe actin filaments as thermal inextensible Euler-Bernoulli beams whose hydrodynamics follows nonlocal slender-body theory [81]. The experiments had access to planar conformations of the filament that are in the focal plane of the microscope. To this end, we restrict the simulations also to be planar, which results in better quantitative agreement. By varying the contour length as well as applied shear rates in the range of $\dot{\gamma} \sim 0.5\text{--}10 \text{ s}^{-1}$, we identify and characterize transitions from Jeffery-like tumbling dynamics of stiff filaments to buckled and finally strongly bent configurations for longer filaments.

3.2 Polymer dynamics and conformations

3.2.1 Governing parameters and key features

In 2.3.4 we outlined the control parameters of a semi-flexible filament in flow. Here we briefly review the dimensionless numbers for consistency. The filament dynamics results from the interplay of three physical effects – elastic bending forces, thermal fluctuations and viscous stresses, and is governed by three independent dimensionless groups. First, the ratio of the filament persistence length ℓ_p to the contour length L characterizes the amplitude of transverse fluctuations due to thermal motion, with the limit of $\ell_p/L \rightarrow \infty$ describing rigid Brownian fibers. Second, the elasto-viscous number $\bar{\mu}$ compares the characteristic time scale for elastic relaxation of a bending mode to the time scale of the imposed flow, and is defined in terms of the solvent viscosity μ , applied shear rate $\dot{\gamma}$, filament length L and bending rigidity B as $\bar{\mu} = 8\pi\mu\dot{\gamma}L^4/B$. Third, the anisotropic drag coefficients along the filament involve a geometric parameter $c = -\ln(\epsilon^2e)$ capturing the

effect of slenderness, where $\epsilon = a/L$.

The elasto-viscous number is the main control parameter of the problem and can be interpreted as the dimensionless measure of the flow strength. By varying L and $\dot{\gamma}$, we have systematically explored filament dynamics over several decades of $\bar{\mu}$ and observed a variety of filament configurations, the most frequent of which we illustrate in Figure 3.1.

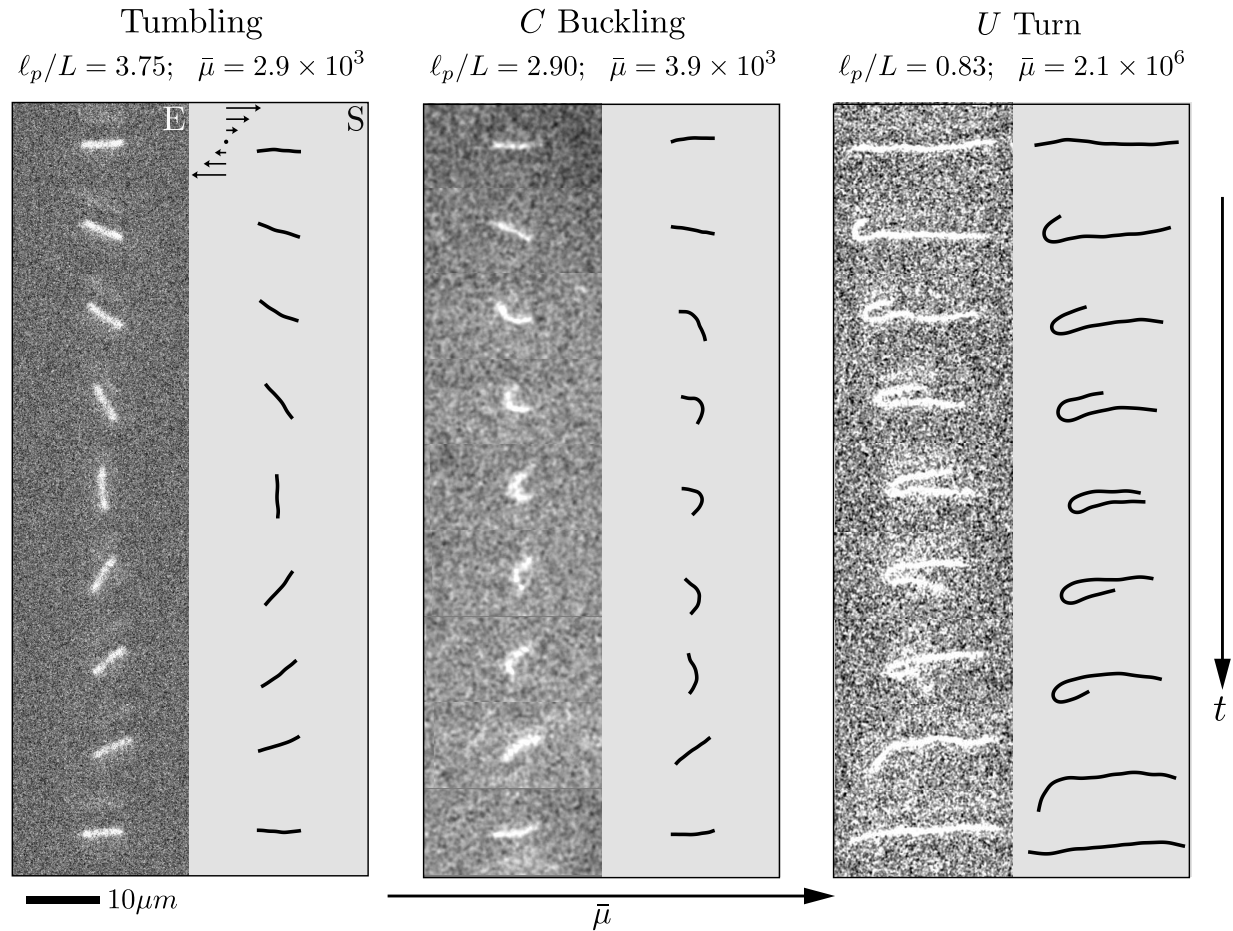


Figure 3.1: Temporal evolution of filament shape in planar shear over one period of motion, showing three representative cases corresponding to increasing elasto-viscous number. In each case, we compare fluorescence images from experiments (E) to Brownian dynamics simulations (S).

In relatively weak flows, the filaments are found to tumble without any significant deformation in a manner similar to rigid Brownian rods, is to the description in 2.5.1.

On increasing the elasto-viscous number, a first transition is observed whereby compressive viscous forces overcome bending rigidity and drive a structural instability towards a characteristic *C* shaped configuration during the tumbling motion. By analogy with Euler beams, we term this deformation mode ‘global buckling’ as it occurs over the full length of the filament. In stronger flows, this instability gives way to highly bent configurations, which we call *U* turns, that are akin to the snaking motions previously observed with flexible fibers [30, 118]. During those turns, the filament remains roughly aligned with the flow direction while a curvature wave initiates at one end and propagates towards the other end. At yet higher values of $\bar{\mu}$, more complex shapes can also emerge, including an *S* turn which is similar to the *U* turn but involves two opposing curvature waves emanating simultaneously from both ends. In all cases, excellent agreement is observed between experimental measurements and Brownian dynamics simulations. Our focus here is in describing and explaining the first three deformation modes and corresponding transitions.

3.2.2 Characterization of temporal dynamics

We characterize the temporal shape evolution more quantitatively for each case in Figure 3.2. In order to describe the overall shape and orientation of the filament, we introduce the gyration tensor, or the second mass moment, as

$$G_{ij}(t) = \frac{1}{L} \int_0^L [\mathbf{r}_i(s, t) - \bar{\mathbf{r}}(t)][\mathbf{r}_j(s, t) - \bar{\mathbf{r}}(t)] ds, \quad (3.1)$$

where $\mathbf{r}(s, t)$ is a two-dimensional parametric representation of the filament centerline with arclength $s \in [0, L]$ in the flow-gradient plane, and $\bar{\mathbf{r}}(t)$ is the instantaneous center-of-mass position. The angle χ between the mean filament orientation and the flow direction is provided by the eigenvectors of G_{ij} , while its eigenvalues (λ_1, λ_2) can be combined to define a sphericity parameter $\omega = 1 - 4\lambda_1\lambda_2/(\lambda_1 + \lambda_2)^2$.

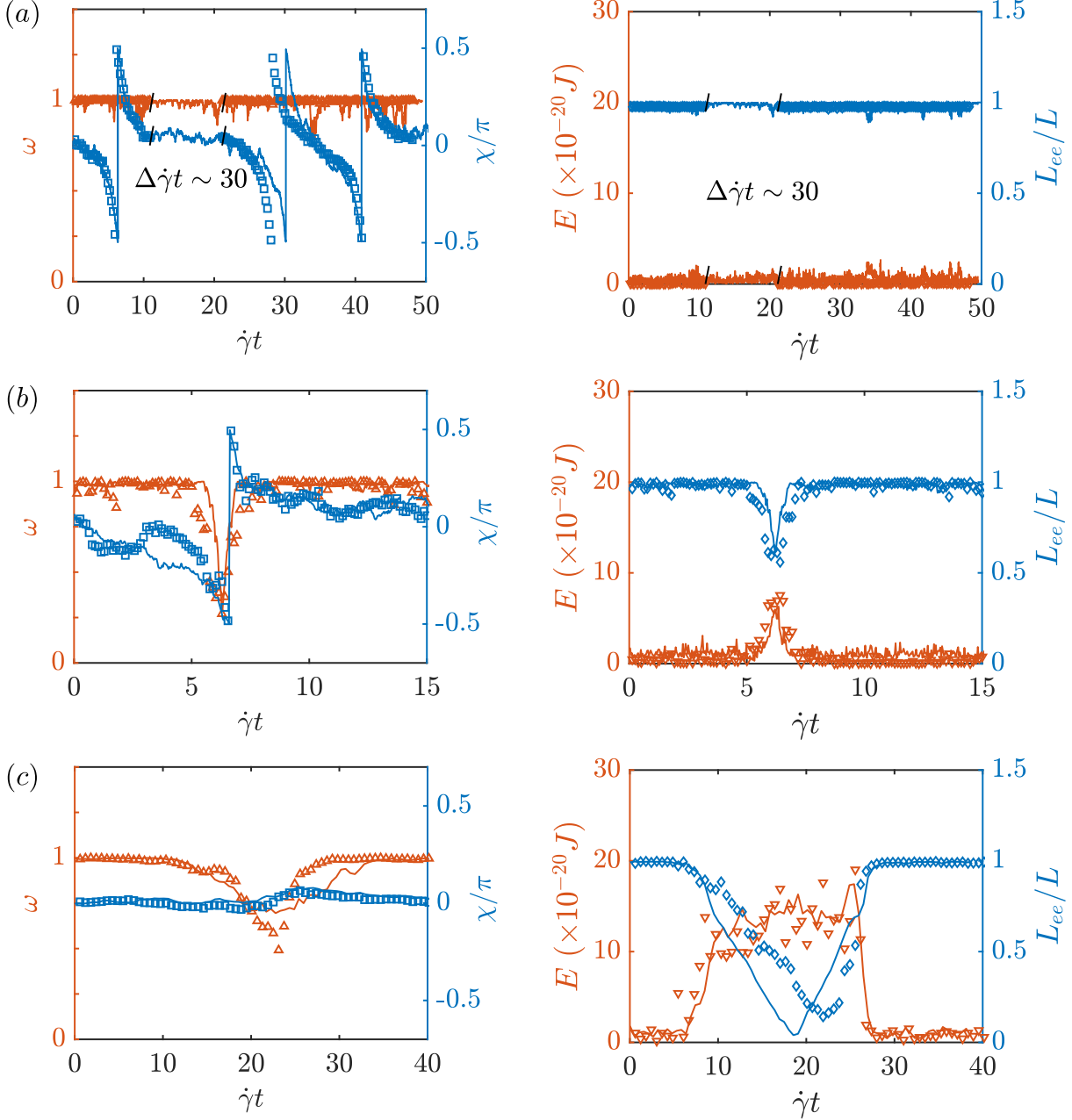


Figure 3.2: Evolution of the sphericity parameter ω , mean angle χ with respect to the flow direction, bending energy E and scaled end-to-end distance L_{ee}/L over one period of motion for (a) Jeffery-like tumbling, (b) C buckling, and (c) U turn. Symbols: experiments. Solid lines: simulations. Parameter values are the same as in Figure 3.1. The lack of experimental data during the interval $\Delta\dot{\gamma}t \sim 30$ in (a) is due to a temporary loss of focus caused by tumbling of the filament out of the flow-gradient plane.

The sphericity parameters quantifies the filament anisotropy: $\omega \approx 0$ for nearly

isotropic configurations ($\lambda_1 \approx \lambda_2$), and $\omega \approx 1$ for nearly straight shapes ($\lambda_1 \gg \lambda_2 \approx 0$)/ Other relevant measures of filament conformation are the scaled end-to-end distance $L_{ee}(t)/L = |\mathbf{r}(L, t) - \mathbf{r}(0, t)|/L$, whose departures from its maximum value of 1 are indicative of bent or folded shapes, and the total bending energy $E(t) = B/2 \int_0^L \kappa^2(s, t) ds$, which is an integrated measure of the filament curvature $\kappa(s, t)$. As is evident in Figure 3.2, these different variables exhibit distinctive signatures in each of the three regimes and can be used to differentiate between configurations systematically. During Jeffery-like tumbling, filaments remain nearly straight with $\omega \approx 1$, $L_{ee} \approx L$ and $E \approx 0$ while the angle χ quasi-periodically varies from $-\pi/2$ to $\pi/2$ over the course of each tumble. During a *C* buckling event, the angle χ still reaches $\pi/2$, but the other quantities now deviate from their baseline as the filament bends and straightens again. This provides a quantitative measure for distinguishing tumbling motion and *C* buckling. During a *U* turn, however, deformations are also significant, but χ deviates only weakly from 0 as the filament remains roughly aligned with the flow direction and executes a tank-treading motion rather than an actual tumble. This feature provides a simple test for distinguishing *C* and *U* turns in both experiments and simulations. Other hallmarks of *U* turns are the increased bending energy during the turn, which exhibits a nearly constant plateau while the localized bend in the filament shape travels from one end to the other, and a strong minimum in the end-to-end distance $L_{ee}(t)$, which reaches nearly zero halfway through the turn when the filament is symmetrically folded.

3.2.3 Order parameters

This descriptive understanding of the dynamics allows us to investigate transitions between deformation regimes as the elasto-viscous number increases. The dependence on $\bar{\mu}$ of the maximum bending energy E , minimum value of the sphericity parameter ω , and

range $\Delta\chi$ of the mean angle over one or several periods of motion is shown in Figure 3.3. In the case of U turns, the maximum bending energy is calculated as an average over the plateau seen in Figure 3.2(c). In the tumbling regime, deformations are negligible beyond those induced by thermal fluctuations, as evidenced by the nearly constant values of $\max(E) \approx 0$ and $\min(\omega) \approx 1$.

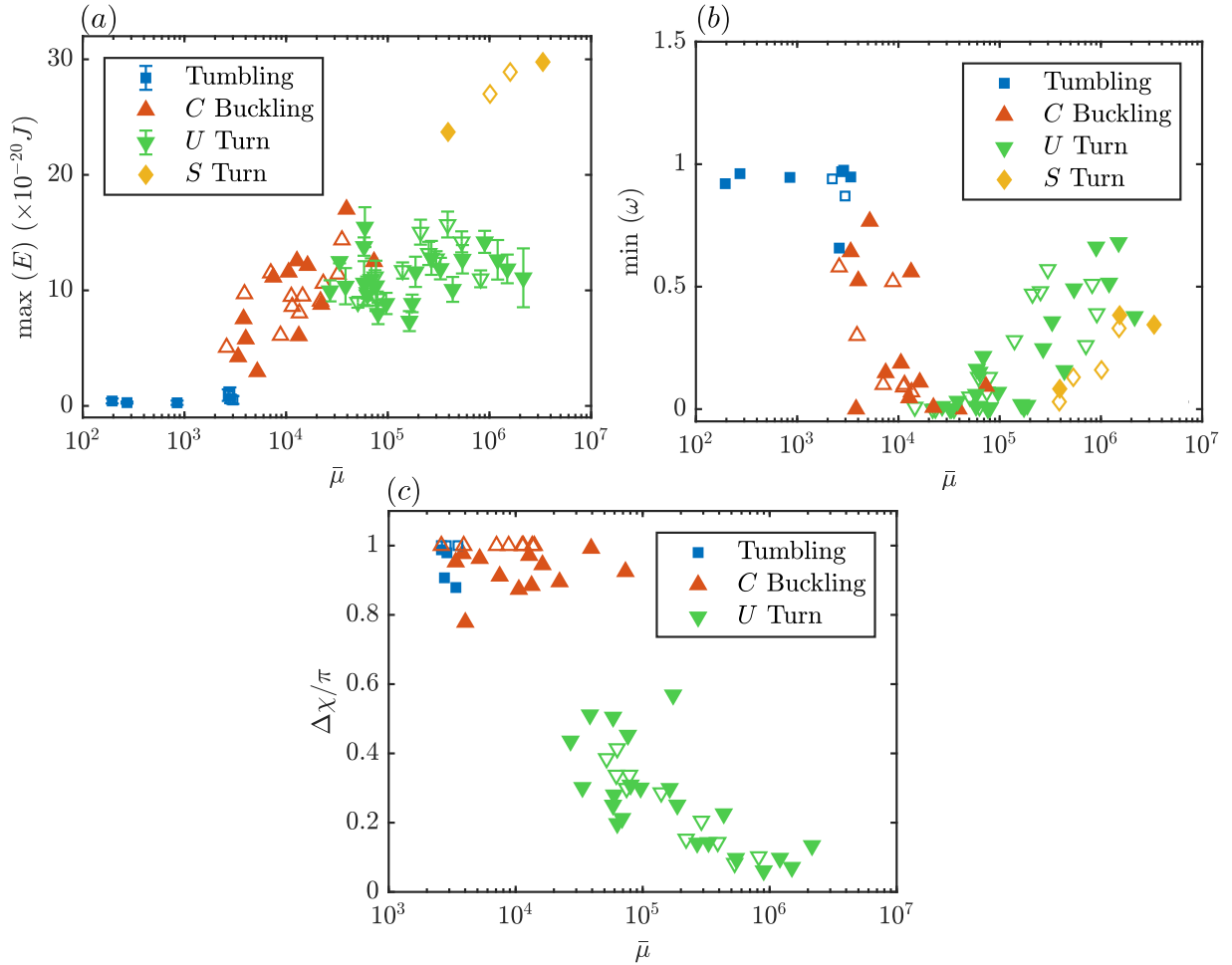


Figure 3.3: Dependence on elasto-viscous number $\bar{\mu}$ of: (a) the maximum value of the bending energy E , (b) the minimum value of the sphericity parameter ω , and (c) the range $\Delta\chi$ of the mean angle in the various tumbling and deformation regimes. Full symbols: experiments; open symbols: simulations. For experimental data, the measurement error in $\bar{\mu}$ (due to errors in contour length ($\pm 0.5 \mu\text{m}$) and in local shear rate ($\pm 0.1 \text{s}^{-1}$)) is comparable to the marker size.

After the onset of buckling, however, the maximum bending energy starts increasing monotonically with $\bar{\mu}$ as viscous stresses cause increasingly stronger bending of the filament. This increased bending is accompanied by a decrease in ω as bending renders shapes increasingly isotropic, finally reaching $\min(\omega) \approx 0$. Interestingly, the transition to U turns is marked by a plateau of the bending energy, which subsequently only very weakly increases with $\bar{\mu}$. This plateau is indicative of the emergence of strongly bent configurations where the elastic energy becomes localized in one sharp fold, and suggests that the curvature of the folds during U turns depends only weakly on flow strength. The parameter ω also starts increasing again after the onset of U turns, as the filaments adopt hairpin shapes that become increasingly anisotropic. Figure 3.3(*a,b*) also shows a few data points for S turns at high values of $\bar{\mu}$: in this regime, the maximum bending energy is approximately twice that of U turns, as bending deformations now become localized in two sharp folds instead of one. S shapes are, however, more compact than U shapes and thus show lower values of ω . Orientational dynamics are summarized in Figure 3.3(*c*), showing the range $\Delta\chi = \chi_{\max} - \chi_{\min}$ of the mean angle χ over one period of motion. During a typical Jeffery-like tumbling or C buckling event, the main filament orientation rotates continuously and as a result $\Delta\chi = \pi$. The scatter in the experimental data is the result of the finite sampling rate during imaging. During U turns, the filament no longer performs tumbles but instead remains globally aligned with the flow direction as it undergoes its snaking motion, resulting in $\Delta\chi < \pi$. This explains the discontinuity in the data of Figure 3.3(*c*), where C and U turns stand apart. As $\bar{\mu}$ increases beyond the transition, we find that $\Delta\chi \rightarrow 0$ suggesting a nearly constant mean orientation for the folded shapes characteristic of U turns.

3.2.4 Buckling alters tumbling frequency

During our discussion of Brownian rigid rods in the previous chapters we identified two distinct regimes of tumbling: one which is dominated by rotational diffusion and the other that is dictated by advection. We can employ simple calculations to obtain a scaling relation that suggests that the tumbling frequency $\nu \sim \dot{\gamma}^{2/3} \sim \bar{\mu}^{2/3}$. Interestingly as shown in Figure 3.4, this scaling relation holds true even when the filament buckles into C shapes. However one starts to see a deviation as strongly deformed hairpin shapes emerge that are typical of U turns. In this regime the exponent tends towards $3/4$ and is also confirmed from the limited amount of simulations.

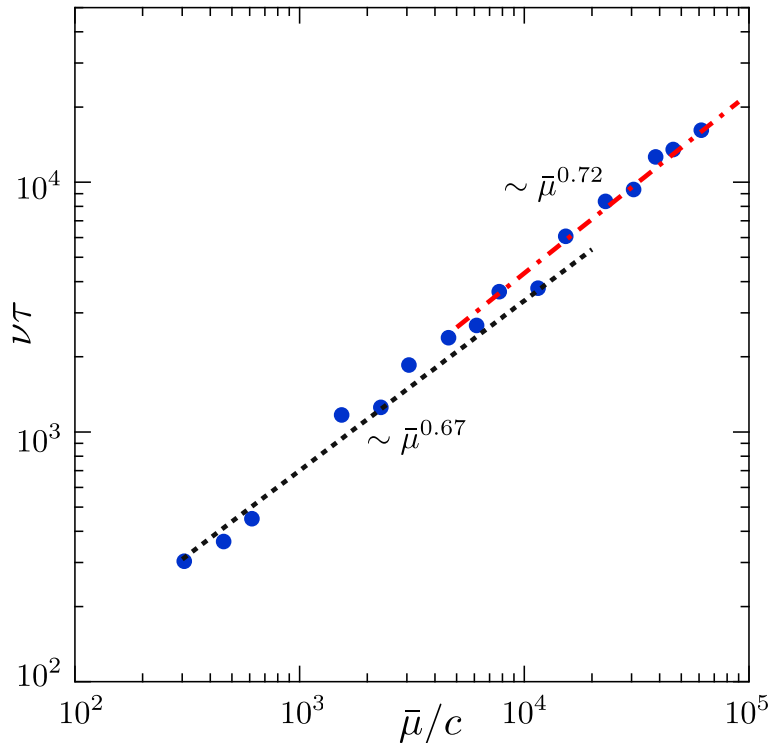


Figure 3.4: Scaling of tumbling frequency ν non-dimensionalized by the longest relaxation time τ as a function of the elasto-viscous number. In strong flows the scaling exponent tends towards $3/4$.

This systematic deviation towards $3/4$ in strong flows is in agreement with results

from Lang et al. [116]. This deviation was rationalized in [116] by an argument of ‘local buckling’ at the length scales of the typical transverse fluctuations $r_\perp \sim L\sqrt{L/\ell_p}$ in strong flows which we discuss in the subsequent sections.

3.3 Morphological transitions: mechanisms

Our experiments and simulations have uncovered three dynamical regimes with increasing values of $\bar{\mu}$, the transitions between which we now proceed to explain. A summary of our results is provided in Figure 3.5 as a phase diagram in the $(\bar{\mu}/c, \ell_p/L)$ parameter space, where the transitions are found to occur at fixed values of $\bar{\mu}/c$ independent of ℓ_p/L .

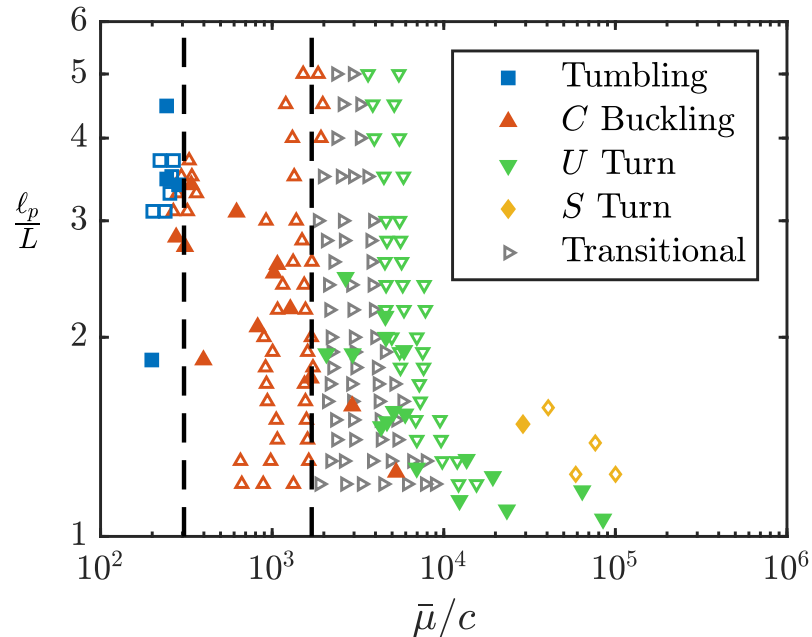


Figure 3.5: Phase chart indicating the different dynamical regimes in the $(\bar{\mu}/c, \ell_p/L)$ parameter space. The dashed black lines show the theoretical transitions from tumbling motion to C buckling ($\bar{\mu}_c^{(1)}/c \approx 306.4$), and from C buckling to U turns ($\bar{\mu}_c^{(2)}/c \approx 1700$). Full symbols: experiments; open symbols: simulations.

The first transition from tumbling motion to C buckling has received much attention in the past, primarily in the case of non-Brownian filaments [33, 81, 117]. This limit

is amenable to a linear stability analysis [33], which predicts a supercritical pitchfork bifurcation whereby compressive viscous stresses exerted along the filament as it rotates into the compressional quadrant of the flow are sufficiently strong to induce buckling. The stability analysis is based on local slender-body theory, where the natural control parameter arises as $\bar{\mu}/c$, and predicts buckling above a critical value of $\bar{\mu}_c^{(1)}/c \approx 306.4$ [33], in reasonable agreement with our measurements (Figure 3.5). Thermal fluctuations do not significantly alter this threshold, but instead result in a blurred transition [2, 112, 122] with an increasingly broad transitional regime where both tumbling and C buckling can be observed for a given value of $\bar{\mu}$. When Brownian fluctuations are strong, i.e., for low values of ℓ_p/L , it becomes challenging to differentiate deformations caused by viscous buckling vs fluctuations, and thus the distinction between the two regimes becomes irrelevant.

Upon increasing $\bar{\mu}/c$, the second conformational transition from C shaped filaments to elongated hairpin-like U turns undergoing snaking motions occurs. The appearance of U turns (shown in green in Figure 3.5) occurs above a critical value $\bar{\mu}_c^{(2)}/c$ that is again largely independent of ℓ_p/L . However, the transition is not sharp, and near the critical value both shapes can be observed simultaneously (as indicated by gray points). In fact, a single filament in the transitional regime will typically execute both types of turns, switching stochastically between them. This stochastic transitional regime can be characterized more precisely by the probability of observing either shape, which we can estimate in simulations and is shown in Figure 3.6 as a function of $\bar{\mu}$ for a fixed value of $\ell_p/L = 1.2$. Consistent with the phase chart in Figure 3.5 we find that the probability of U turns continuously increases from 0 to 1 as $\bar{\mu}$ is varied across the transition. Similar stochastic transitions have been reported for the onset of buckling in compressional flows [2, 112].

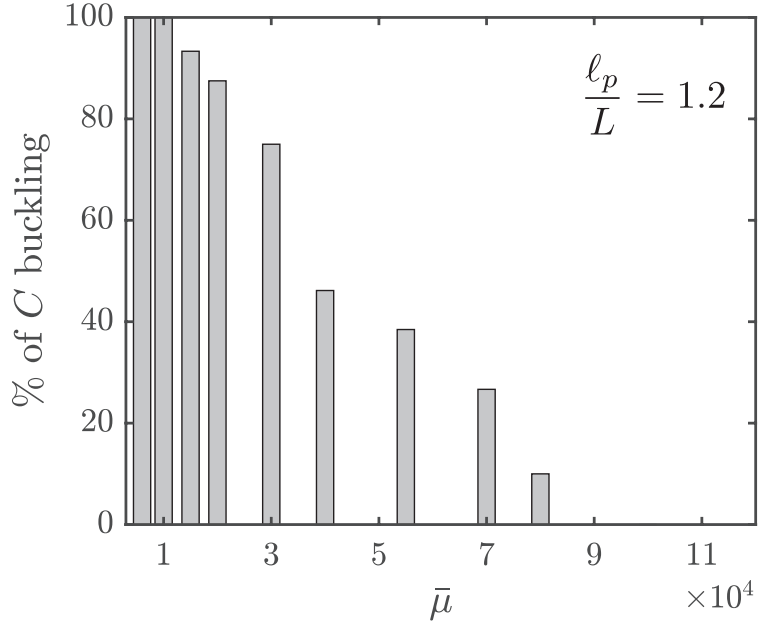


Figure 3.6: Percentage of C buckling events as a function of $\bar{\mu}$ near the transition from C buckling to U turns in numerical simulations. The probability was estimated over a minimum of 10 distinct turns. The results shown are for $\ell_p/L = 1.2$.

3.3.1 Origin of snaking motion: J shape

The transition towards snaking dynamics has not been characterized previously. Our attempt at understanding its mechanism focuses on the onset of a U turn, which always involves the formation of a J shaped configuration as visible in Figure 3.1 and also illustrated in Figure 3.7. To elucidate the transition mechanism, we develop a theoretical model for a J configuration, which can be viewed as a precursor to the U turn. We discuss this model in great detail in the following section. Here we focus on the possible mechanisms that may lead to a formation of a J shape.

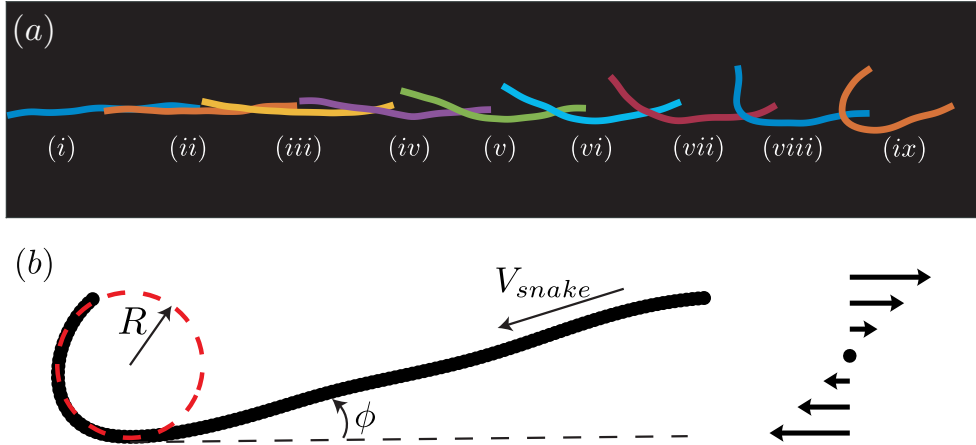


Figure 3.7: (a) Numerical snapshots of filament shapes during the formation of a *J* shape before the initiation of a *U* turn. (b) Typical geometric features of the *J* shape. During snaking, the filament translates tangentially with an axial velocity V_{snake} .

In the process of initiation two possible mechanisms may be at play. On the one hand, it may be caused by the global buckling of the filament in the presence of highly compressive viscous forces, in a manner consistent with the sequence of shapes of Figure 3.7(a). Under sufficiently strong shear, compressive forces can induce a buckling instability on a filament that has not yet aligned with the compressional axis and forms only a small angle with the flow direction. Alignment of the deformed filament with the flow then results in differential tension (compression vs tension) near its two ends, thus allowing one end to bend while the other remains straight. A second potential mechanism proposed in [116] is of a local buckling occurring on the typical length scale of transverse thermal fluctuations. The scaling for Euler buckling force at the length of transverse fluctuations is given by $f_B \sim B/r_\perp^2 \sim B\ell_p/L^3$. We can obtain the characteristic viscous forces at this scale as $f_v \sim \mu\dot{\gamma}r_\perp^2 \sim \mu L^3\dot{\gamma}/\ell_p$. Seeking a balance between these we obtain:

$$f_B \sim f_v \implies \bar{\mu} \sim \left(\frac{\ell_p}{L}\right)^2. \quad (3.2)$$

This scaling for transition towards *U* turns suffices to explain the behavior of tumbling frequency described previously. However our data, as shown in Figure 3.5 clearly indicates

that the transition to U turns is independent of thermal fluctuations, allowing us to discard this hypothesis. Brownian motion are nonetheless responsible for the existence of the transitional regime above $\bar{\mu}_c^{(2)}/c$, where they can destabilize J shapes towards C shapes and thus prevent the occurrence of U turns. This interpretation is consistent with the increasing extent of the transitional regime with decreasing ℓ_p/L that was further discussed in Figure 3.6.

3.3.2 Dynamics of the J -shaped configuration

To understand the transition to U turns, we seek a simplified, non-Brownian model of the tilted J shaped configuration as illustrated in Figure 3.7. We idealize the conformation using the geometry shown in Figure 3.8.

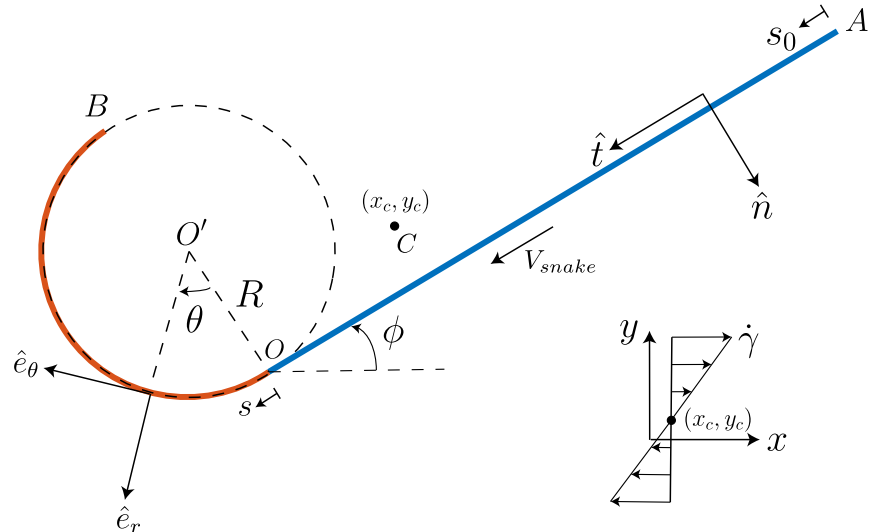


Figure 3.8: Theoretical model of the J configuration. The bent part is approximated by a semi-circle of radius R . There is a snaking velocity V_{snake} along the contour of the shape. The straight part of the configuration makes a tilt angle of ϕ with the direction of the flow.

We approximate the bent portion of the filament by a semi-circle of yet unknown radius R and assume that the rest of the filament is straight and has a tilt angle ϕ with

respect to the flow direction. We also introduce the following notations:

- $T^{(1)} \equiv$ velocity of the straight arm in the tangential direction $\hat{\mathbf{t}}$.
- $v_{\perp}^{AO} \equiv$ velocity of the straight arm in the normal direction $\hat{\mathbf{n}}$.
- $T(\theta) \equiv$ velocity of the semi-circle along $\hat{\mathbf{e}}_\theta$.
- $v_{\perp}^{OB}(\theta) \equiv$ Velocity of the semi-circle in the $\hat{\mathbf{e}}_r$ direction.
- $C(x_c, y_c) \equiv$ filament center of mass.
- $(x, y) \equiv$ global coordinate axes centered at O .
- $l \equiv$ length of the straight arm, also given by: $l = L - \pi R$ where L is the filament contour length.

Note that the assumption of a semi-circular shape for the bend leads to some inconsistencies. In particular, it is not possible to satisfy the force- and moment-free boundary conditions at point B . Adding a second straight arm emanating from B would allow this issue to be circumvented, and the model we present here is justified in the limit of the length of that second arm becoming zero. Additional inconsistencies also arise at point O , where not all derivatives of the filament shape are continuous. These assumptions are necessary to make analytical progress, and we will see *a posteriori* that the model produces results that are in good agreement with experimental and simulation data. As we discuss later, the model does also satisfy a global energy balance that serves to make the assumptions rigorous while neglecting the boundary layers that may arise at geometric discontinuities.

With the definitions above, the relative velocity between the fluid and the straight

arm in the tangential and normal directions can be expressed as:

$$v_{\parallel}^{rel} = T^{(1)} + \dot{\gamma} [(l - s_0) \sin \phi - y_c] \cos \phi, \quad (3.3)$$

$$v_{\perp}^{rel} = v_{\perp}^{AO}(s_0) - \dot{\gamma} [(l - s_0) \sin \phi - y_c] \sin \phi. \quad (3.4)$$

As there are no forces acting in the normal direction inside the straight arm, we set $v_{\perp}^{rel} = 0$ which yields

$$v_{\perp}^{AO}(s_0) = \dot{\gamma} [(l - s_0) \sin \phi - y_c] \sin \phi. \quad (3.5)$$

In the tangential direction, the internal tension $\sigma(s)$ induces an elastic force density $\mathbf{f}(s) = \sigma_s \hat{\mathbf{t}}$. This force density is balanced by viscous stresses using resistive force theory as $-\sigma_s = c_{\parallel} v_{\parallel}^{rel}$, which can be integrated using the force-free boundary condition at point A to yield

$$\sigma(s_0) = -c_{\parallel} T^{(1)} s_0 + c_{\parallel} \dot{\gamma} [(ls_0 - \frac{1}{2}s_0^2) \sin \phi - y_c s_0] \cos \phi. \quad (3.6)$$

We have introduced the coefficient of resistance per unit length in the tangential direction, which is expressed as

$$c_{\parallel} \approx \frac{2\pi\mu}{\log(2L/a)}, \quad (3.7)$$

and we similarly define $c_{\perp} \approx 2c_{\parallel}$ as the resistance coefficient for transverse motion.

We analyze the kinematics and force balance on the semi-circular arc in a similar fashion, and first express the relative velocities along the arc as

$$v_{\parallel}^{rel} = T + \underbrace{v_f \cos(\theta - \phi)}_{v_{\parallel}^f}, \quad (3.8)$$

$$v_{\perp}^{rel} = v_{\perp}^{OB} + \underbrace{v_f \sin(\theta - \phi)}_{v_{\perp}^f}, \quad (3.9)$$

where $v_f = \dot{\gamma}R[\cos \phi - \cos(\theta - \phi)] - \dot{\gamma}y_c$. Seeking a balance between elastic and viscous

forces in the tangential and normal directions, we obtain:

$$-\frac{1}{R} \frac{d\sigma}{d\theta} = c_{\parallel} v_{\parallel}^{rel}, \quad (3.10)$$

$$\frac{\sigma}{R} + \frac{B}{R^3} = c_{\perp} v_{\perp}^{rel}. \quad (3.11)$$

The constraint of inextensibility introduces a kinematic relation between the Lagrangian velocities in the tangential and perpendicular directions everywhere along OB , and provides the condition:

$$\frac{dT}{d\theta} + v_{\perp}^{OB} = 0. \quad (3.12)$$

Eqs. (3.8)–(3.12) can be combined to yield a second-order inhomogeneous ODE for $v_{\perp}^{OB}(\theta)$:

$$2 \frac{d^2 v_{\perp}^{OB}}{d\theta^2} - v_{\perp}^{OB} = 2 \frac{d^2 v_{\perp}^f}{d\theta^2} + \frac{d^2 v_{\parallel}^f}{d\theta^2}. \quad (3.13)$$

This ODE can be solved analytically subject to continuity of the velocity at point O and to the tension-free boundary condition at point B :

$$v_{\perp}^{OB}(\theta) = C_1 \cosh(\lambda\theta) + C_2 \sinh(\lambda\theta) + \sum_{n=1,2} [\alpha_n \cos(n\theta) + \beta_n \sin(n\theta)], \quad (3.14)$$

where $\lambda = 1/\sqrt{2}$ and

$$C_1 = \frac{\dot{\gamma} R \sin 2\phi}{18}, \quad (3.15)$$

$$C_2 = \frac{B}{c_{\perp} R^3 \sinh(\pi\lambda)} - \frac{\dot{\gamma} R}{18} \sin 2\phi \tanh\left(\frac{\pi\lambda}{2}\right), \quad (3.16)$$

$$\alpha_1 = \dot{\gamma}(y_c - R \cos \phi) \sin \phi, \quad \alpha_2 = -\frac{5}{9} \dot{\gamma} R \sin 2\phi, \quad (3.17)$$

$$\beta_1 = -\dot{\gamma}(y_c - R \cos \phi) \cos \phi, \quad \beta_2 = \frac{5}{9} \dot{\gamma} R \cos 2\phi. \quad (3.18)$$

From v_{\perp}^{OB} , the tangential velocity along the bend is easily obtained as

$$T = v_{\parallel}^f - 2 \left(\frac{dv_{\perp}^{OB}}{d\theta} - \frac{dv_{\perp}^f}{d\theta} \right). \quad (3.19)$$

Seeking continuity of tangential velocity and internal tension at point O , we obtain two distinct expressions for the tangential velocity $T^{(1)}$ of the straight arm:

$$T^{(1)} = -\frac{2B\lambda}{c_{\perp}R^3 \sinh(\pi\lambda)} + \dot{\gamma}y_c \cos \phi - \frac{2}{9}\dot{\gamma}R \cos 2\phi + \frac{\dot{\gamma}R\lambda}{9} \sin 2\phi \tanh\left(\frac{\pi\lambda}{2}\right), \quad (3.20)$$

$$T^{(1)} = \frac{B}{c_{\parallel}R^2 l} - \frac{\dot{\gamma}l}{4} \sin 2\phi + \dot{\gamma}y_c \cos \phi. \quad (3.21)$$

Interestingly, (3.21) can be shown to also satisfy the torque balance on the filament.

For consistency, we require that Eqs. (3.20)–(3.21) be equal. Note, however, that both R and ϕ remain unknown at this point. We therefore seek a third condition based on dissipation arguments similar to those used to explain the tank-treading motion of vesicles [123]. Over the course of an infinitesimal time interval δt during a U turn, a length of $\delta L \equiv V_{\text{snake}}\delta t$ that was initially straight becomes bent into the semi-circular curve of radius R , where V_{snake} is the snaking velocity. During that same time, the same small amount of length becomes straight on the other side of the bend. The amount of work required to bend the straight part can be estimated as the change in its elastic energy:

$$\delta E = \frac{B}{2} \frac{V_{\text{snake}}\delta t}{R^2}. \quad (3.22)$$

This expression provides an estimate for the rate of change $\dot{E} = \delta E/\delta t$ of bending energy due to the deformation of the filament as it undergoes snaking. An alternative expression can be obtained from first principles by differentiating the bending energy as:

$$\dot{E} = B \int_0^L \mathbf{r}_{ss} \cdot \mathbf{r}_{tss} ds. \quad (3.23)$$

Applying two integrations by parts and using the fact that tension forces do not perform any work leads to:

$$\dot{E} = B \int_0^L \mathbf{r}_t \cdot \mathbf{r}_{ssss} ds = \int_0^L \mathbf{r}_t \cdot \mathbf{f}^e ds \equiv - \int_0^L \mathbf{r}_t \cdot \mathbf{f}^h ds. \quad (3.24)$$

where \mathbf{r}_t is the velocity of a material point along the filament, and $\mathbf{f}^e = B\mathbf{r}_{ssss}$ is the local elastic force density whose work balances that of the hydrodynamic force density $\mathbf{f}^h = -[c_{\parallel}\hat{\mathbf{t}}\hat{\mathbf{t}} + c_{\perp}(\mathbf{I} - \hat{\mathbf{t}}\hat{\mathbf{t}})] \cdot \mathbf{v}^{rel}$. The detailed expression for the integral in Eq. (3.24) is cumbersome and therefore omitted here. The above derivation involves integration by parts and assumes continuity of derivatives. Equating (3.24) with $\delta E/\delta t$ from Eq. (3.22), and identifying the snaking velocity with the tangential velocity $T^{(1)}$ of the straight arm in the *J* shape, we obtain the additional condition

$$\frac{BT^{(1)}}{2R^2} = - \int_0^L \mathbf{r}_t \cdot \mathbf{f}^h ds. \quad (3.25)$$

The above relation is essentially an integral energy balance in the system where we have included the dominant terms that come from the approximated *J* shape. In principle, there may be other terms arising from boundary layers near the junctions of approximate straight and semi-circular arcs which are ignored here in an asymptotic sense to facilitate analytical progress.

It is possible to combine (3.20), (3.21) and (3.25) to form two equations for the unknowns R and ϕ . These two equations are then solved numerically using a Newton-search algorithm. The equations essentially specify two curves in the $\phi - R$ plane, and a solution only exists when the curves intersect. For a given aspect ratio of the filament, we find that there exists a critical value of $\bar{\mu}$ below which the curves do not intersect. This suggests that below this value *J*-shapes can no longer form and therefore *U* turns cannot occur. The theoretically calculated value of $\bar{\mu}_c^{(2)}/c \approx 1700$ is plotted as a dashed line on Figure 3.5 and indeed provides a very good estimate for the onset of *U* turns.

3.3.3 Dynamics of *U*-turns

We further characterize the dynamics during *U* turns, for which our theoretical model also provides predictions. The filament orientation at the onset of a turn is plotted

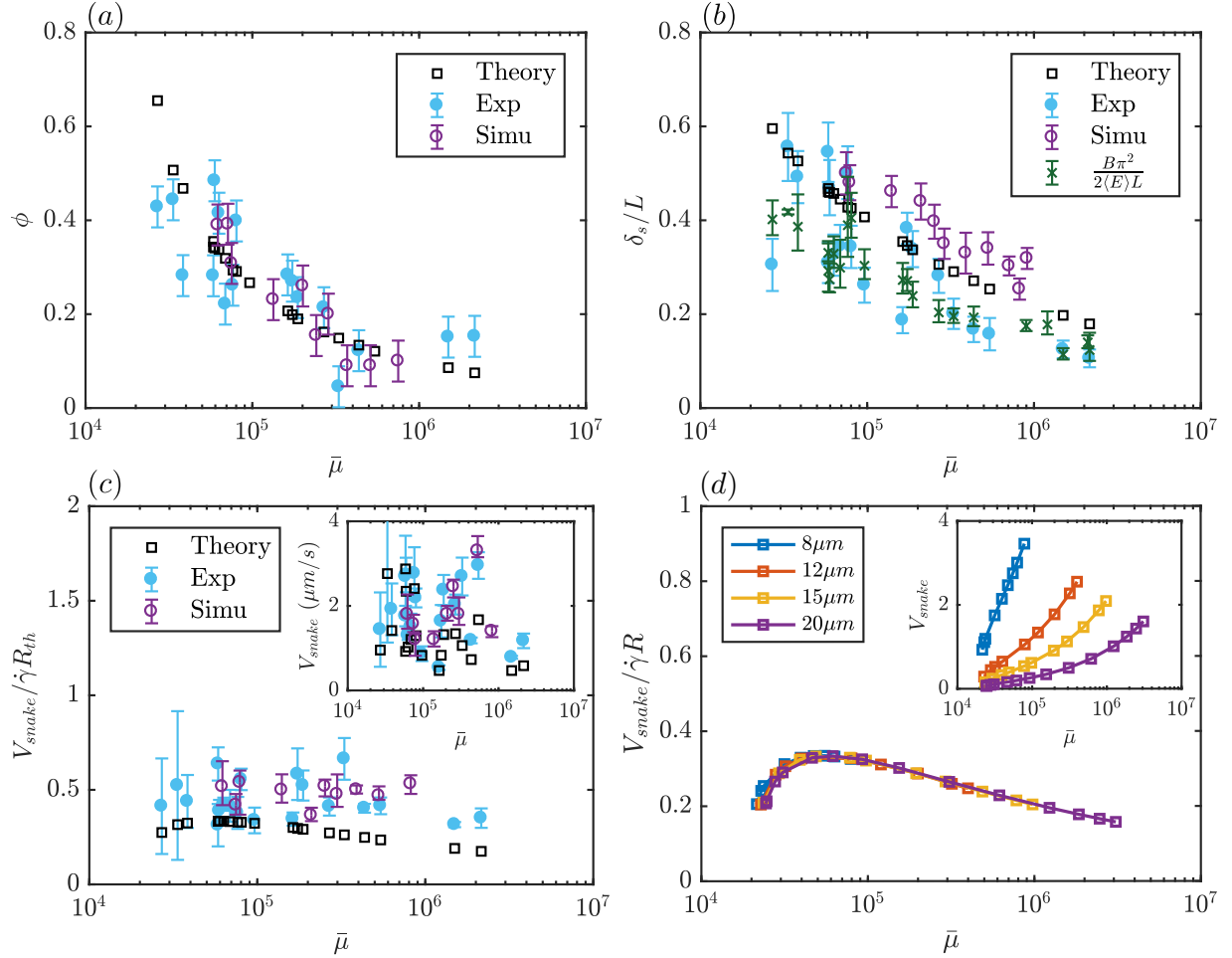


Figure 3.9: (a) Dependence on $\bar{\mu}$ of the tilt angle ϕ formed by J shapes with respect to the flow direction in experiments, simulations and in our theoretical model. (b) Fraction δ_s/L of the filament length that is bent during a U turn (see Appendix A for detailed definition of δ_s). (c) Snaking velocity V_{snake} rescaled with $\dot{\gamma}R_{\text{th}}$ and plotted against $\bar{\mu}$ from experiments, simulations and theory; here, R_{th} is the theoretically predicted fold radius. (d) A perfect collapse of snaking velocity from the theoretical model.

in Figure 3.9(a), showing the tilt angle ϕ formed by the straight arm of the J shape with respect to the flow direction as a function of $\bar{\mu}$. Our theoretical model for dynamics of the J shape also provides the value of ϕ , in excellent agreement with experiments. In both cases, the tilt angle decreases with increasing flow strength due to increased alignment by the flow. For very long filaments (limit of large $\bar{\mu}$), accurate measurements of the tilt angle

become challenging due to shape fluctuations, hence the increased scatter in the data. After a J shape is initiated, the curvature of the folded region remains nearly constant in time as suggested by the plateau in the bending energy (Figure 3.3(*c*)). This provides a strong basis for approximating the bent part of the filament as a semi-circle of radius R in our model. The theoretical prediction R_{th} and measurements of the radius on J shapes from experiments and simulations agree quite well in Figure 3.9(*b*) (see Appendix A for details). The radius of the bend is seen to decrease with $\bar{\mu}$, as compressive viscous stresses in strong flows allow increasingly tighter folding of the filament.

The rotation of the end-to-end vector during the U turn results primarily from tank-treading of the filament along its arclength, unlike the global rotation that dominates the tumbling and C buckling regimes. While the snaking velocity is not constant during a turn, its average value can be quantitatively measured through the time derivative of the end-to-end distance, yielding the approximation $V_{\text{snake}} \approx \dot{L}_{ee}/2$. The relevant dynamic length and time scales during this snaking motion are the radius of curvature R of the bent segment and shear rate $\dot{\gamma}$. This is supported by our theory, where rescaling V_{snake} by $\dot{\gamma}R_{th}$ collapses the predicted velocities over a range of filament lengths as shown in Figure 3.9(*d*). The same rescaling applied to the experimental and numerical data and using the theoretical radius R_{th} also provides a good collapse in Figure 3.9(*c*).

Harasim *et al.* [30] previously proposed a simplified theory of the U turn, which shares similarities with ours but assumes that the filament is aligned with the flow direction and neglects elastic stresses inside the fold. Their predictions are in partial agreement with our results in the limit of very long filaments and strong shear. However their theory is unable to predict and explain the transition from buckling to U turns.

3.4 Rheology of dilute suspension

So far our discussions of filament morphology has outlined how competition between elastic and viscous forces can lead to Euler-buckling instabilities that make way to deformed filament configurations. While the transitions were found to be fairly independent of the Brownian motion of the filaments, fluctuations however introduce shape perturbations and can smooth out sharp bifurcations [112]. The natural question that follows from studies on morphologies is that does microscopic dynamics alter macroscopic properties of such suspensions? We know from our introductory discussion on rheology that it is indeed the deformation, rotation and dissipation induced by the micro-structure of a suspension that leads to bulk rheological properties. The majority of previous research has focused on fully flexible polymers, which are characterized, both in solution and in the melt, by a self-similar fractal structure from the scale of a monomer up to the coil size [95]. This peculiar property allows for the development of elegant and simple scaling arguments for the dynamic properties of polymer solutions. Another limit that has received significant attention is the rheological properties of bead-rod chains that model inextensible but flexible polymers [124–126]. In the past decades, several studies have focused on the conformational and rheological properties of single semiflexible polymers under flow using theory [127], simulations [25] and experiments [26, 107]. However λ -DNA which has been the model polymer for most of these studies have $L \gg \ell_p$ and its dynamics is distinctly different from actin filaments that are of interest in the present study. Only recently there have been experiments [128] and mesoscopic simulations [129] of semi-dilute polymer suspensions with $L \sim \ell_p$ that exhibit shear thinning and positive normal stress difference.

On the other hand there has also been a few studies on the rheological properties of semi-dilute non-Brownian suspensions [130, 131] that are important for various industrial processes [118]. Becker and Shelley [33] first mapped these macroscopic behaviors to buck-

ling instabilities of non-Brownian filaments that were further explored through detailed nonlinear simulations [81]. A natural extension of the present study is to understand the role of thermal fluctuations and buckling in dilute suspension of actin filaments. This is distinctly different from studies in semi-dilute suspension since we can relate each component of microscopic deformations to macroscopic stress and single out the role of elasticity and shape fluctuations. In an attempt to understand the role of flow induced deformations we start by a brief review of classical rheology of rigid rods [5, 6, 132] that serves as the reference for our problem. We then discuss methods of computing ensemble averaged stress, a few open questions related to non-Brownian fibers, and finally discuss new results of rheology for dilute suspensions.

3.4.1 Rheology of rigid rod suspension

This problem has received a considerable amount of interest starting from the pioneering work by Leal and Hinch [5, 132], Stewart and Sorensen [133] and Brenner [6] who investigated the role of Brownian fluctuations in orientational distribution of rigid rods in shear flow and the subsequent effect in rheology. Our aim is to summarize the key results and outline the methodology for some of the calculations without going into much of the technical details.

We consider a Brownian rigid rod with aspect ratio $\epsilon = a/L \ll 1$ where a is the characteristic diameter and L is the length of the object placed in a simple shear flow with $\mathbf{u}_\infty = (\dot{\gamma}y, 0, 0)$. We also define $r = 1/\epsilon$ the inverse of the aspect ratio for the sake of notational convenience. We restrict ourselves to the dilute regime with $nL^3 \ll 1$ where n is the mean particle density in the suspension, and thus neglect inter-particle hydrodynamic interactions. As discussed in Chapter 2 the rods are characterized by an orientation vector \mathbf{p} that rotates in presence of an externally imposed shear flow and is acted on by Brownian

torques that causes it to diffuse. The dimensionless number that governs the dynamics of these rods is the rotary Péclet number $\text{Pe}_r = \dot{\gamma}/d_r$ number where d_r is the rotational diffusivity of the rod. The Péclet number and the elasto-viscous number employed in our simulations of semi-flexible polymers are related as follows:

$$\text{Pe}_r = \frac{\bar{\mu}}{24 \ln(2r)} \frac{\ell_p}{L}. \quad (3.26)$$

In the limit of $\ell_p/L \rightarrow \infty$ the flexible polymers behave like Brownian rigid rods. The orientational dynamics of the Brownian rod is governed by (2.57). We can find the Fokker-Planck description for the probability distribution of orientation $\psi(\mathbf{p}, t)$ associated with the Langevin dynamics. It is given by:

$$\frac{\partial \psi}{\partial t} + \nabla_{\mathbf{p}} \cdot (\dot{\mathbf{p}}\psi) = d_r \nabla_{\mathbf{p}}^2 \psi, \quad (3.27)$$

where $\nabla_{\mathbf{p}}$ is the gradient operator on the unit sphere of orientations and is defined as:

$$\nabla_{\mathbf{p}} = (\delta_{ij} - p_i p_j) \partial / \partial p_j.$$

The extra stress due to the slender particles can be obtained by computing the stresslet or the moment of force exerted by the particles on the fluid as outlined in [134, 135]. The net extra-stress that we denote by Σ will have two contributions: one from orientational dynamics of the particles in presence of flow and one from the Brownian stress. They are given by [136–139]:

$$\Sigma_{ij}^f = \frac{\pi \mu n L^3}{6 \ln(2r)} \left[\langle p_i p_j p_k p_l \rangle - \frac{1}{3} \delta_{ij} \langle p_k p_l \rangle \right] E_{kl}^{\infty}, \quad (3.28)$$

$$\Sigma_{ij}^B = 3nkT \left[\langle p_i p_j \rangle - \frac{1}{3} \delta_{ij} \right]. \quad (3.29)$$

The superscript f and B denote contributions from flow and Brownian fluctuations. \mathbf{E}^{∞} denotes the rate of strain tensor of the problem and $\langle \cdot \rangle$ denotes orientational average and is defined as:

$$\langle \cdot \rangle = \int_{\Omega_p} \cdot \psi^{\infty}(\mathbf{p}) \, d\mathbf{p}, \quad (3.30)$$

where $\psi^\infty(\mathbf{p})$ is the steady state orientational distribution obtained by a balance of advective and diffusive flux in (3.27). This reduces the problem of rheology to simply finding orientational moments of the unit vector \mathbf{p} . We can now define the shear-viscosity and normal stress coefficients in terms of the orientational moments for a simple shear flow.

We have

$$\eta = \frac{\Sigma_{xy}}{\mu\dot{\gamma}L^3} \implies \ln(2r)\eta = \pi \left[\frac{1}{6}\langle p_x^2 p_y^2 \rangle + \frac{1}{\text{Pe}_r} \langle p_x p_y \rangle \right], \quad (3.31)$$

$$\Psi_1 = \frac{N_1 \equiv \Sigma_{xx} - \Sigma_{yy}}{\mu\dot{\gamma}^2 L^3} \implies \ln(2r)d_r\Psi_1 = \frac{\pi}{\text{Pe}_r} \left[\langle p_x^3 p_y \rangle - \langle p_x p_y p_z^2 \rangle + \frac{1}{\text{Pe}_r} (\langle p_x^2 \rangle - \langle p_y^2 \rangle) \right], \quad (3.32)$$

$$\Psi_2 = \frac{N_2 \equiv \Sigma_{yy} - \Sigma_{zz}}{\mu\dot{\gamma}^2 L^3} \implies \ln(2r)d_r\Psi_2 = \frac{\pi}{\text{Pe}_r} \left[\langle p_x p_y^3 \rangle - \langle p_x p_y p_z^2 \rangle + \frac{1}{\text{Pe}_r} (\langle p_y^2 \rangle - \langle p_z^2 \rangle) \right]. \quad (3.33)$$

In most of the cases one need to compute $\psi^\infty(\mathbf{p})$ numerically to obtain the orientational moments. However for certain regimes it is possible to compute the asymptotic form of the probability distribution function that allows us to understand the rheology. We discuss the main asymptotic results in the next section.

3.4.2 Summary of asymptotic results

In absence of flow the distribution of particles are isotropic due to Brownian motion. In very weak flow, $\text{Pe}_r \ll 1$ it is possible to use a regular perturbation expansion of the distribution function in Pe_r to obtain its asymptotic form. In three dimensions this asymptotic expansion takes the following form:

$$\psi(\mathbf{p}) = \frac{1}{4\pi} + \frac{\text{Pe}_r}{8\pi} [p_x p_y] + \frac{\text{Pe}_r^2}{96\pi} [p_x^2 + 3p_x^2 p_y^2 - p_y^2]. \quad (3.34)$$

In the limit of strong flows characterized by $\text{Pe}_r \gg r^3 + r^{-3}$ the probability distribution function is peaked at the zero-shear plane as the rods spend most of their time remaining

aligned with the flow. Using boundary layer analysis, it is possible to determine the asymptotic form of the distribution function that allows us to compute the rheological properties [132]. Finally there emerges an intermediate asymptotic regime with $r^3 + r^{-3} \gg \text{Pe}_r \gg 1$, where it is possible to obtain the scaling for shear viscosity and normal stress coefficients [5]. We summarize these results in the table below

Table 3.1: Asymptotic forms of relevant rheological measures [5, 6].

Regimes	Scalings
$\text{Pe}_r \ll 1$	$\eta_p, d_r \Psi_1, d_r \Psi_2 \sim \text{constant}$
$r^3 + r^{-3} \gg \text{Pe}_r \gg 1$	$\eta_p \sim \text{Pe}_r^{-1/3}, d_r \Psi_1, d_r \psi_2 \sim \text{Pe}_r^{-4/3}$
$\text{Pe}_r \gg r^3 + r^{-3}$	$\eta_p, d_r \Psi_1, d_r \Psi_2 \sim \text{constant}$

3.4.3 Computing stress for Brownian suspensions

Stresslet: Kramers-Kirkwood expression

The simplest way to compute the stress in a suspension is to use the expression of a stresslet that generalizes the Kirkwood formula [140] commonly used for molecular systems. We start by recalling the force balance for individual filaments. We have:

$$\mathbf{f}^v + \mathbf{f}^e + \mathbf{f}^{\text{Br}} = \mathbf{0}, \quad (3.35)$$

where \mathbf{f}^v is the viscous force, \mathbf{f}^e is the elastic force and \mathbf{f}^{Br} are the Brownian force. The stresslet or the Kramer-Kirkwood expression for particle stress is defined as

$$\boldsymbol{\Sigma} = \left\langle \int_0^L (\mathbf{x} - \mathbf{x}_c) \mathbf{f}^v ds \right\rangle = - \left\langle \int_0^L (\mathbf{x} - \mathbf{x}_c) (\mathbf{f}^e + \mathbf{f}^{\text{Br}}) ds \right\rangle, \quad (3.36)$$

where the center of mass \mathbf{x}_c has been subtracted from the position. Now note that the Brownian fluctuations have contributions of order $(\Delta t)^{-1/2}$ in the above expression. This results in poor convergence of the stress if the above expression is used. One way to avoid this is to use noise filtering that filters out these correlations [126].

Giesekus stress in steady flow

Starting from the definition of the stresslet it is possible to derive an alternative form of the stress tensor that depends only on the conformation of the polymer. Simply re-arranging the expression of stresslet we find

$$\boldsymbol{\Sigma} = \left\langle \int_0^L (\mathbf{x} - \mathbf{x}_c) \mathbf{f}^v \, ds \right\rangle = \left\langle \int_0^L (\mathbf{x} - \mathbf{x}_c) (\mathcal{R} \cdot (\dot{\mathbf{x}} - \mathbf{u}^\infty)) \, ds \right\rangle. \quad (3.37)$$

In the above expression $\mathcal{R} \equiv \mathcal{M}^{-1}$ is the resistance tensor and \mathbf{u}^∞ is the background velocity field. At steady state, the ensemble-averaged correlation between \mathbf{x} and $\dot{\mathbf{x}}$ is identically zero [126, 141] and we are left with:

$$\boldsymbol{\Sigma} = - \left\langle \int_0^L (\mathbf{x} - \mathbf{x}_c) (\mathcal{R} \cdot \mathbf{u}^\infty) \, ds \right\rangle. \quad (3.38)$$

The above expression known as the Giesekus stress is strictly valid in the steady state and cannot be applied for unsteady flows [126]. However in the steady state the Giesekus expression is identical to the Kramer-Kirkwood stress. The advantage of using this expression is that one do not need to worry about $\mathcal{O}(\Delta t^{-1/2})$ correlations of Brownian fluctuations and the convergence is much faster [69]. The Giesekus expression also directly relates the macroscopic stress to the conformation of the micro-structure. In order to see this, consider a case where the background velocity field is linear and we have $\mathbf{u}^\infty = \boldsymbol{\kappa} \cdot \mathbf{x}$, where $\boldsymbol{\kappa}$ is the velocity gradient tensor. For further simplification if we assume a constant friction coefficient ζ then we have:

$$\boldsymbol{\Sigma} = -\boldsymbol{\kappa}\zeta \cdot \left\langle \int_0^L (\mathbf{x} - \mathbf{x}_c) \mathbf{x} \, ds \right\rangle. \quad (3.39)$$

The above expression contains the ensemble average of the gyration tensor and thus depends purely on the conformation of the filament.

3.4.4 2D non-Brownian simulations

We first consider the case of planar non-Brownian filaments that has previously been well studied [33,81]. The non-Brownian simulations help us appreciate how buckling instabilities have the potential to alter rheology of suspensions. In order to highlight the role of deformation we performed two sets of simulations. The first one involves studying the dynamics of a rigid rod that simply rotates and aligns itself with the zero-shear plane. The second one is with a flexible fiber for which we introduce small numerical perturbations in the initial confirmations to observe buckling. This results in *S* shaped buckling for the results reported here.

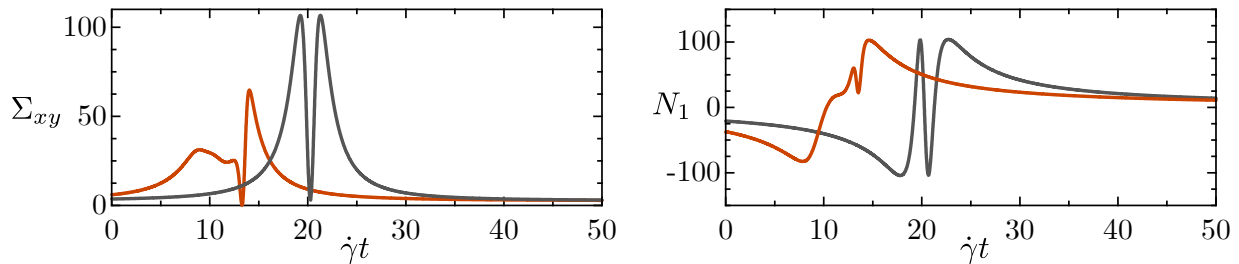


Figure 3.10: Signature of buckling in shear stress and the normal stress difference. We observe shear-thinning and positive normal stress. Parameter values: $\bar{\mu}/c = 1 \times 10^4$.

The above figure shows the shear stress and the first normal-stress difference for rigid rod in gray. We notice that the period-averaged shear stress is positive, but the first normal stress vanishes due to symmetry. In color we show the same when the filament buckles. While the exact nature of the evolution of stress depends on the initial perturbation and the geometry of buckling, we clearly see the symmetry in normal stress is broken. It is also evident that the integrated shear stress will be smaller compared to the rigid rod

which points to shear thinning. Interestingly due to the asymmetry of N_1 the integrated normal stress is positive.

3.4.5 A fictitious stress: role of fluctuations

Our non-Brownian simulations suggest that buckling leads to shear thinning and positive normal stress differences. These observations are in agreement with previous theoretical results [33, 81]. However in [33] it was suggested that beyond a critical $\bar{\mu}$ the normal stress difference becomes negative. This is in disagreement with experiments with flexible fibers where the normal stress typically grows linearly with the shear rate. This discrepancy was attributed to long-range hydrodynamic interactions present in experiments with semi-dilute suspensions.

In the reported regime of negative normal stress the filaments typically exhibit snaking motions or *S* shaped buckling. We believe that one possible source of error in [33] can be the method of introducing numerical perturbations that are required to initiate buckling in non-Brownian filaments. The aim of this section is to probe into this effect and investigate normal stress-differences for hairpin shaped conformations due to deformations. To this end we compute a fictitious stress from a numerical thought experiment. The steps of the numerical experiment are as follows:

- Start a Brownian simulation with the filament aligned with the zero shear flow plane.
- Whenever the filament starts deforming switch off Brownian fluctuations artificially and allow the filament to deform purely in presence of flow. The criterion to determine onset of deformation was set to: $L_{ee} \leq 0.98L$, where L_{ee} is the end-to-end distance.
- Compute the stresslet during the period of deformation.

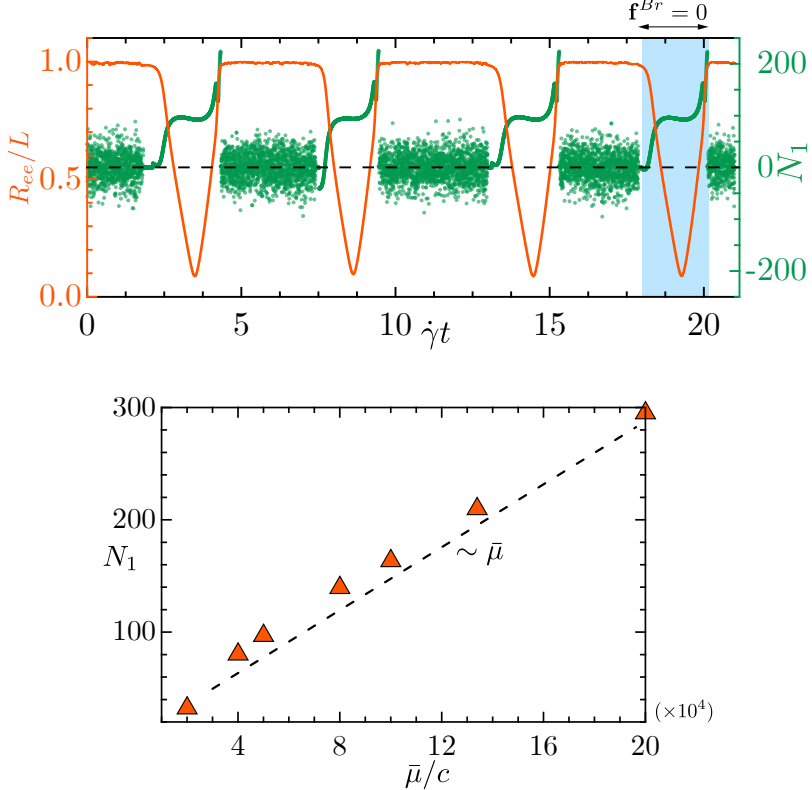


Figure 3.11: Positive normal stress difference that scales linearly with flow-strength. On top we show how the fictitious stress is computed and the time evolution of both the end-to-end distance and N_1 . Below we show the period averaged normal stress difference that increases linearly with shear rate. Parameter: $\bar{\mu}/c = 4 \times 10^4$ and $\ell_p/L = 5$.

This method of computing a fictitious stress has certain advantages. First, it decouples the Brownian stress present even when the filament is aligned and the stress due to purely elastic instabilities. The second advantage is that instead of artificial numerical perturbations, the typical transverse fluctuations r_\perp that induces buckling come from physical Brownian motion with $r_\perp \sim \sqrt{L^3/\ell_p}$. This is a reliable way to observe changes in normal stress difference or the shear stress due to buckling. In order to facilitate comparison with [33] we performed the simulations in 2D. Figure 3.11 illustrates the key features of the method of calculating this artificial stress. When the filament is aligned with the flow, Brownian fluctuations are present. The stresslet then results in a noisy signal as observed

above. On the other hand, for a non-Brownian filament a perfect alignment will lead to zero N_1 . As the filament starts deforming, the fluctuations are switched off and we observe a smooth signal as expected that has striking similarities with the signatures in 2D for non-Brownian filaments as shown in Figure 3.10. We notice that while $N_1(t)$ can be negative, the time-averaged stress over one period of deformation is always positive. This averaged stress over a period of tumbling is plotted at the bottom of Figure 3.11 and is seen to increases monotonically with shear rate.

This now highlights the key difference from the simulations in [33]. The normal stress remains positive in strong flows, even in the absence of long range hydrodynamic interactions.

3.4.6 Rheology of weakly deformable Brownian filaments

Three-dimensional rheology

We now move on to discuss rheology of dilute suspension of Brownian filaments. We are particularly interested in the weakly deformable limit where $\ell_p/L \gg 1$. This limit allows us to map our results to rigid rod rheology in weak flow and appreciate the differences once we enter the buckling regime. Before discussing rheology let us recall that the onset of Euler-buckling instability is $\bar{\mu}^{(1)}/c \sim 300$ and the onset of snaking motion is around $\bar{\mu}^{(2)}/c \sim 2 \times 10^3$. It is important to highlight that these results were obtained in 2D simulations and was confirmed by planar linear stability analysis [33].

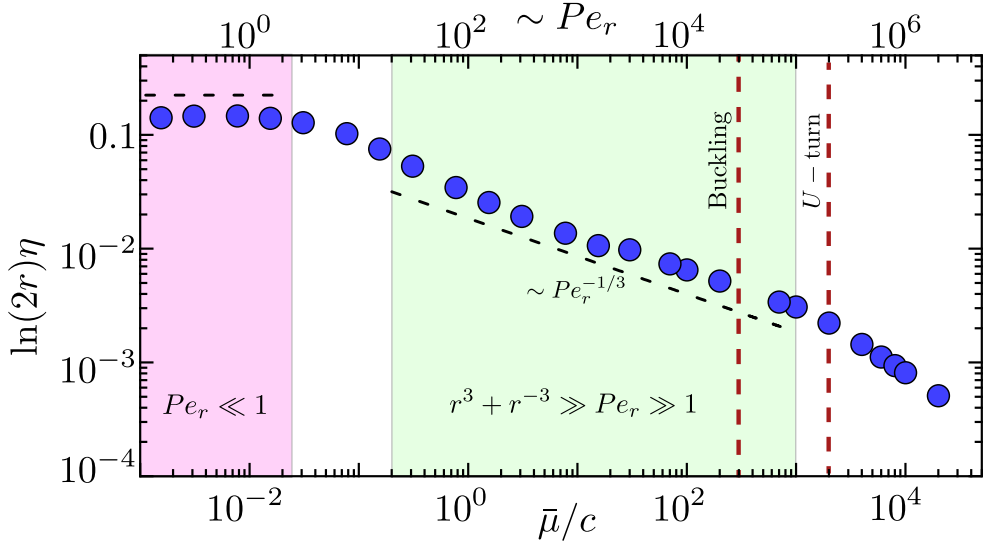


Figure 3.12: Shear thinning of a weakly deformable polymer in three dimensions with $\ell_p/L = 1000$. The limits of rigid rods and asymptotics are highlighted along with the onset of buckling instabilities.

We discuss the rheology of filaments with $\ell_p/L = 1000$. In this almost rigid limit we first recover the asymptotic results in weak flow that are dominated by Brownian motion [5, 139]. Both the shear viscosity and the first normal stress coefficient remain constant as seen in Figure 3.12 and 3.13. As the strength of the flow increases we start observing shear thinning along with monotonic increase of the first normal stress N_1 . In the intermediate asymptotic regime defined by $r^3 + r^{-3} \gg Pe_r \gg 1$, we indeed recover the scaling law as suggested in [5]. Quite surprisingly, what stands out is that this scaling law holds true even after initiation of buckling instability as seen in Figure 3.12. This is in sharp contrast with the 2D non-Brownian results that suggest rheology is significantly altered due to buckling. This apparently puzzling result can be understood from the fact that a C shaped buckling as observed at the onset requires rotation of the fiber in the plane of shear which subsequently leads to strong compressive forces and eventually buckling. In 3D, the filament has the freedom to rotate out of the plane. As a result the effective

$\bar{\mu}$ responsible for inducing buckling is much smaller compared to the actual flow strength. This delays the onset of buckling and removes its signature from the stress by averaging.

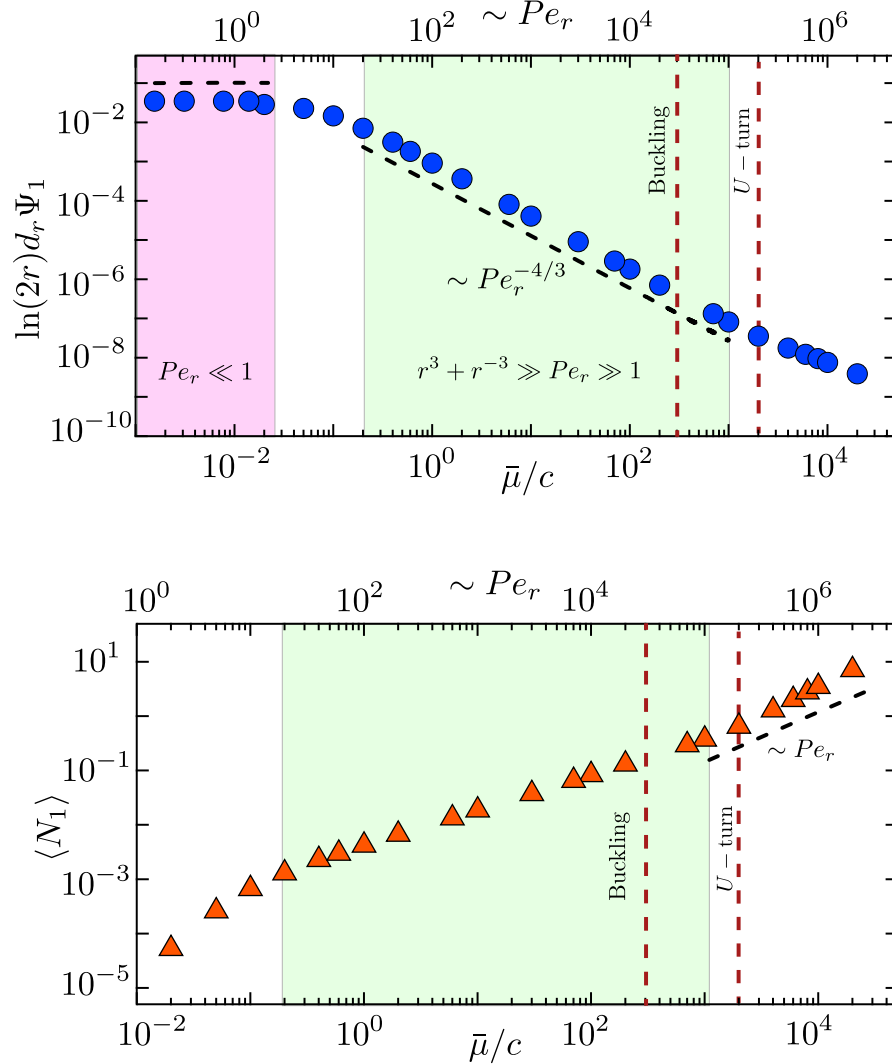


Figure 3.13: Positive normal stress difference and viscosity coefficient in three dimension with $\ell_p/L = 1000$. The limits of rigid rods and asymptotics are highlighted along with the onset of buckling instabilities. When the flow is sufficiently strong we find $\langle N_1 \rangle \sim \dot{\gamma}$.

On the other hand, if the filament was more flexible with $\ell_p/L \sim \mathcal{O}(10)$, the signature would have been smeared out by strong fluctuations along with the effects of non-planarity. However one finds a signature of buckling in both shear viscosity and normal

stress once the filament transitions to snaking motion or *U* turns. For the initiation of a hairpin shape the filament buckles remaining almost aligned with the plane of shear. This can happen in strong flows whenever the filament is aligned in the zero-shear plane.

It is interesting to note that the normal stress difference N_1 is proportional to the shear rate in the strongly deformed regime of snaking motions, in agreement with experiments [130, 131].

Two dimensional rheology

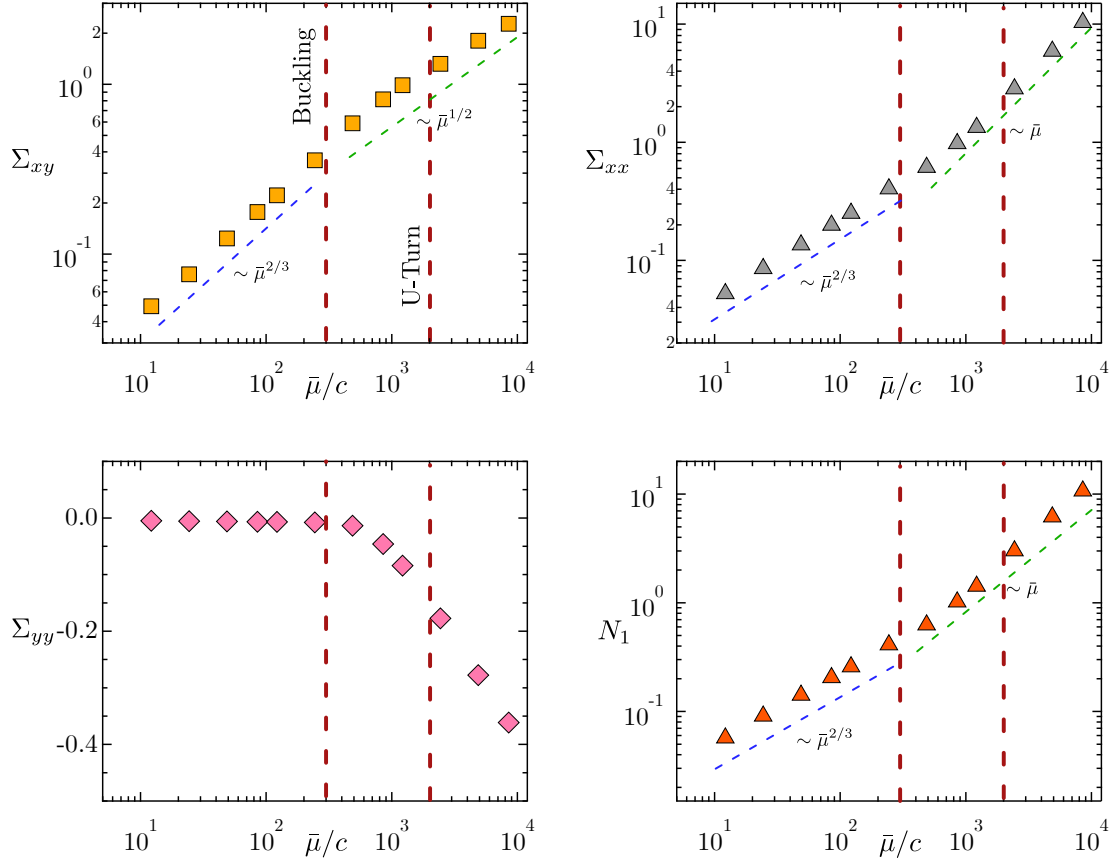


Figure 3.14: Components of stress tensor and the normal stress difference as a function of the elasto-viscous number. The data shows change of scaling law at the onset of buckling.

Our previous discussions on rheology in three dimensions have highlighted why it is difficult to observe signatures at the onset of buckling in 3D. Thus it is interesting to probe the problem in 2D. Here we perform simulations with $\ell_p/L = 50$ and look for signatures of buckling in the stress.

In the above figure we have illustrated the scaling law for the components of the stress tensor as a function of $\bar{\mu}/c$. Unlike the case for 3D we observe that the stress shows different scaling laws once we transition from tumbling to buckling regime. This behavior is in contrast to 3D where changes in scaling law were only observed post initiation of snaking. As expected the signatures in stress is reflected in shear viscosity and normal stress coefficients shown in Figure 3.15.

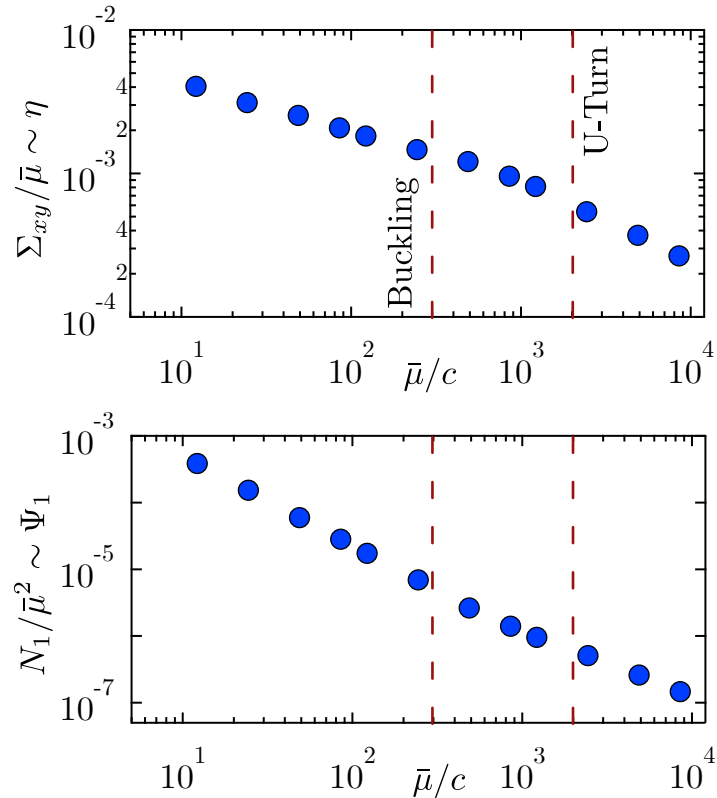


Figure 3.15: η and Ψ_1 as a function of $\bar{\mu}/c$. Pre-buckling we have, $\eta \sim \bar{\mu}^{-1/3}$ and $\Psi_1 \sim \bar{\mu}^{-4/3}$. Post-buckling we have $\eta \sim \bar{\mu}^{-1/2}$ and $\Psi_1 \sim \bar{\mu}^{-1}$.

3.5 Conclusion

In this chapter, using stabilized actin filaments as a model polymer, we have systematically studied and analyzed the conformational transitions of elastic Brownian filaments in simple shear flow as the elasto-viscous number is increased. Our experimental measurements were shown to be in excellent agreement with a computational model describing the filaments as fluctuating elastic rods with slender-body hydrodynamics. By varying filament contour length and applied shear rate, we performed a broad exploration of the parameter space and confirmed the existence of a sequence of transitions, from rod-like tumbling to elastic buckling to snaking motions. While snaking motions had been previously observed in a number of experimental configurations, the existence of a *C* buckling regime had not been confirmed clearly. This is due to the fact that *C* buckling is only visible over a limited range of elasto-viscous numbers and occurs only in simple shear flow, challenging to realize experimentally. We showed that both transitions are primarily governed by $\bar{\mu}/c$. Brownian fluctuations do not modify the thresholds but tend to blur the transitions by allowing distinct dynamics to coexist over certain ranges of $\bar{\mu}$.

While the first transition from tumbling to buckling had been previously described as a supercritical linear buckling instability [33], the transition from buckling to snaking was heretofore unexplained. Using a simple analytical model for the dynamics of the *J* shape that is the precursor to snaking turns, we were able to obtain a theoretical prediction for the threshold elasto-viscous number above which snake turns become possible. The model did not take thermal noise into account, but highlighted the subtle role played by tension and compression during the onset of the turn.

Our analysis lays the foundations to study rheology of dilute suspensions. Initial results on non-Brownian filaments suggest that buckling instability results in shear thinning, consistent with previous observations [33,81]. However as opposed to [33] the normal

stress remained positive and increased monotonically with shear rate. Preliminary studies for Brownian filaments point to subtle differences in 3D and 2D rheological behaviors. We find that unlike non-Brownian filaments the signature of buckling on stress is weak. In 3D the effect is smeared out due to out-of-plane rotation of the filament and the behavior is prominent only after emergence of hairpin conformations.

Part of this Chapter was published in *Proceedings of the National Academy of Sciences* (2018), authored by Yanan Liu, Brato Chakrabarti, David Saintillan, Anke Lindner and Olivia du Roure [7]. The dissertation author performed numerical simulations and worked on theoretical modeling for this paper.

Chapter 4

Helical buckling of filaments in compressional flow

4.1 Introduction

In the previous chapter we have discussed morphologies of actin filaments in simple shear. We have outlined how competition between viscous loading and elasticity can lead to the formation of buckled conformation and how such instabilities have the potential to alter rheological properties of suspensions. Such buckling instabilities have also been predicted in stagnation point flows [2, 111, 112, 142–144] and result in characteristic two-dimensional buckling modes. Flexible filaments can also be compressed into more compact, three-dimensional conformations under stronger forcing, which is going to be the main focus of this chapter. Here we will discuss a rather surprising finding that a freely suspended straight flexible filament can buckle into a helical shape in a purely compressional flow. The first such instance can perhaps be traced back to hand-drawn sketches of the coiling of elastic wood pulp fibers in strong shear flow [118], which was later also observed with actin filaments [30] and in simulations of diatom chains [117, 145]. Helically

coiled structures have also been observed during the manufacturing of synthetic wet-spun fibers for cosmetics, where long fibers undergo buckling in a compressional flow [146]. In biology, the sessile protozoan *Vorticella* is known to propel itself by exploiting the sudden calcium-powered contraction of its slender stalk, which has been shown to form coiled structures [147]. Helical shapes of elastic fibers transported in turbulent flows have also recently been reported [148]. For specific initial conditions one can also observe formation of knots [149].

These helicoidal structures are reminiscent of the classical ‘helical buckling’ problem of solid mechanics that has received wide attention [64, 150, 151] and was discussed briefly in Chapter 2. In the classical version of the problem, a straight elastic rod subjected to tension and end moments buckles into helical shapes that are relevant in a variety of situations such as the morphology of plant roots [62], the jamming of nanorods [152], the packing of DNA inside viral capsids [153], and oil-drilling processes [66]. The phenomenon discussed here thus stands out from classical helical buckling in that the filament spontaneously adopts a chiral helicoidal morphology in the absence of any intrinsic twist or external moments.

4.2 Problem setup

We elucidate this generic morphological transition through a combination of experiments, simulations and theoretical modeling. For the experiments performed at ESPCI France, we used our model semiflexible actin filaments with $\ell_p = 17 \pm 1 \mu\text{m}$. To induce and visualize buckling, we flowed fluorescently labeled filaments through a convergent-divergent hyperbolic microfluidic channel (shown in Figure 4.1(a)) specially designed and optimized to provide uniform extension and compression rates over large distances while ensuring a long residence time for the filaments [154, 155]. These experiments are complemented by

two sets of very different simulations. The first model closely mimics the experimental conditions where we have performed Langevin simulations of inextensible Euler elastica with the local slender body theory as outlined in previous chapters. In the second model, we simulated non-Brownian elastic fibers composed of surface nodes connected by a network of springs providing structural rigidity and bending resistance [117, 156] in an axisymmetric channel [145] with the method of regularized Stokeslets. These filaments are finitely extensible and point to the robustness of the observed phenomenon. We provide the details of this simulation in Appendix B.

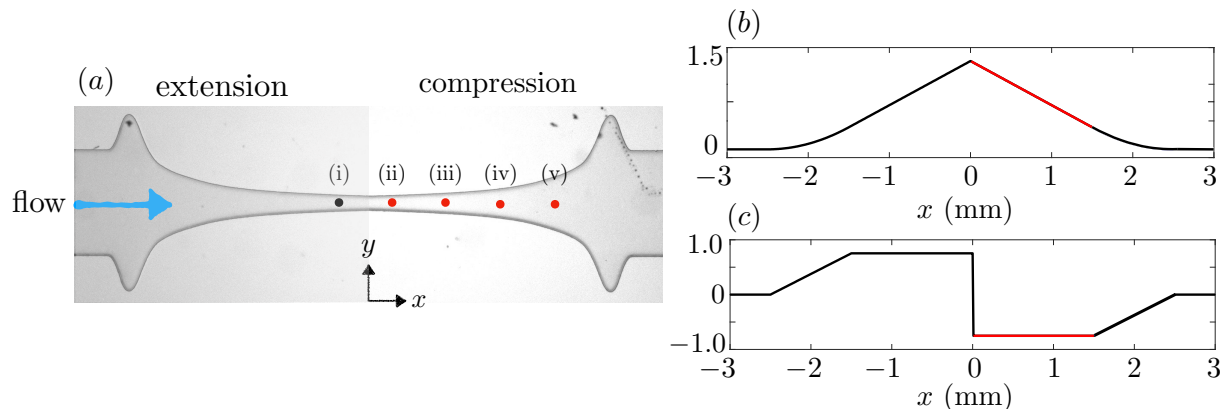


Figure 4.1: (a) Geometry of the optimized hyperbolic microfluidic channel used in experiments, with markers indicating the positions where snapshots of filament conformation will be taken. (b)-(c) Axial velocity u and strain rate $\dot{\epsilon}$ as functions of streamwise position x along the channel centerline where filaments are transported. A constant strain rate $\dot{\epsilon}$ occurs over a given distance, and measurements are made in the compressional region highlighted in red.

As discussed in the following section, both types of simulations, as well as seminal simulations by Chelakkot et al. [157], recapitulate the helix formation seen in experiments, pointing to a very generic transition that only requires a strong compressional flow as we rationalize below using a nonlinear stability analysis. Our findings highlight a new mechanism by which a one-dimensional object can buckle into a chiral helicoidal shape under viscous loading. This mechanism remained undiscovered until now as typical experimental

setups in stagnation point flows do not allow for sufficiently strong compression rates or long residence times, and as past theoretical analyses have been limited to two dimensions. Our results also underscore the robustness of this phenomenon, which occurs independent of the presence of thermal fluctuations and across very different flow environments.

4.3 Helical buckling: morphologies

4.3.1 Evolution of conformations

Typical buckling events in experiments and Brownian simulations are shown in Figure 4.2 for increasing values of the elastoviscous number $\bar{\mu}$ [144], a dimensionless measure of compression rate which serves as the primary control parameter of the problem. We focus here on the dynamics in the divergent part of a microfluidic hyperbolic channel (see Figure 4.1(a-c)) where compression at constant strain rate $\dot{\epsilon}$ occurs, with the convergent part mainly serving to align and pre-stretch the filaments before measurements begin. As the filaments enter the compressional region (column (i)), they are indeed mostly straight since thermal shape fluctuations have been largely suppressed as discussed in Chapter 2.6 and in [2]. Snapshots at increasing values of the dimensionless time $\dot{\epsilon}t$ in panels (ii) to (v) show the growth of deformations with distinct emergent morphologies for increasing elastoviscous numbers (top to bottom). In relatively weak flows (first row), deformations are mostly planar and resemble those seen in past studies in stagnation point flows [2, 112, 113]. As $\bar{\mu}$ is increased in subsequent rows, more complex shapes emerge that are fully three-dimensional, as evidenced by the blurriness of some parts of the filaments in the experimental images due to deformations out of the focal plane. Another indicator of three-dimensionality is the presence of apparent kinks (orange arrows) in the 2D images, which must result from the projection of 3D shapes. In some cases, actual loops (purple

arrows) can be observed and strongly hint at helicoidal shapes.

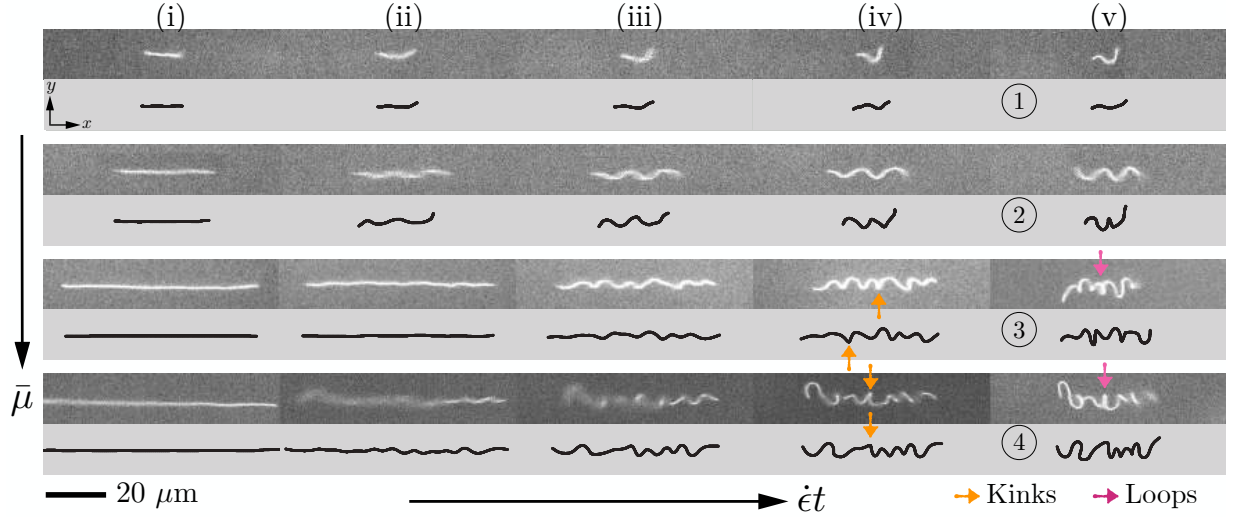


Figure 4.2: Snapshots of evolving filament morphologies from experiments and Brownian simulations compared at the same dimensionless time $\dot{\epsilon}t$, measured from the instant the filament enters the compressional region. Vertical panels correspond to increasing values of the elastoviscous number in the range $\bar{\mu} \sim 2 \times 10^3 - 10^6$. For sufficiently large $\bar{\mu}$, 3D shapes emerge, as evidenced by kinks (orange arrows) and loops (purple arrows) in the 2D projections

The three dimensionality of the conformations is further confirmed in Figure 4.3(a), showing simulated Brownian filament projections in the cross-sectional plane corresponding to panel (v) of Figure 4.2, where these loops are now clearly visible. A few conformations re-oriented due to fluctuations in the focal plane of the experiment making it possible to image the projections. This is shown in Figure 4.3(b) and further reveals the helical structure. The number of loops along the filament increases with $\bar{\mu}$ as higher unstable buckling modes become excited. The emerging coiled structures have no preferred chirality as expected from symmetry, and in some cases reversals in the handedness occur at topological perversions along the contour length. As the filament is transported downstream, the helix is further compressed by the flow until it exits the compressional region and is finally allowed to relax.

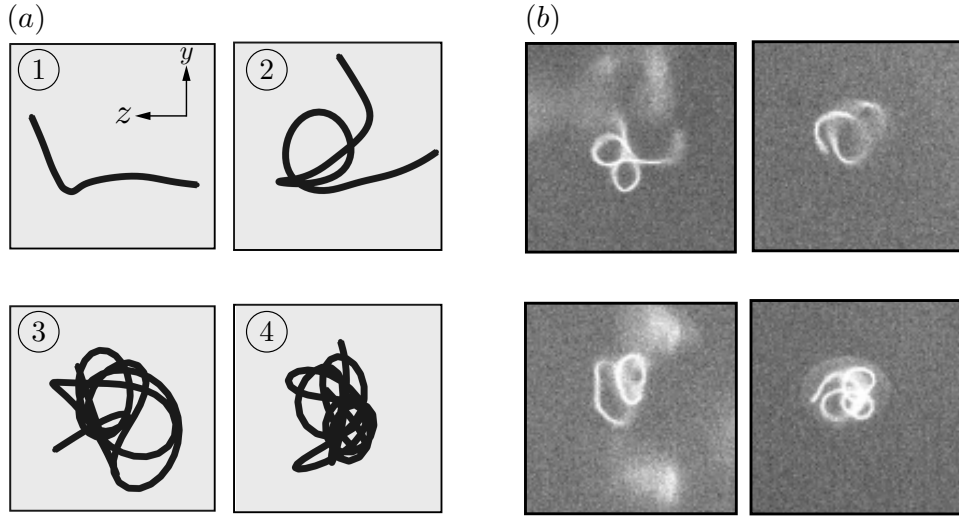


Figure 4.3: (a) Projections of simulated filament conformations corresponding to (v) in the cross-sectional plane of the channel, highlighting the 3D helicoidal nature of the morphologies at large $\bar{\mu}$. (b) Projections of some conformations from experiments that randomly rotate in the focal plane.

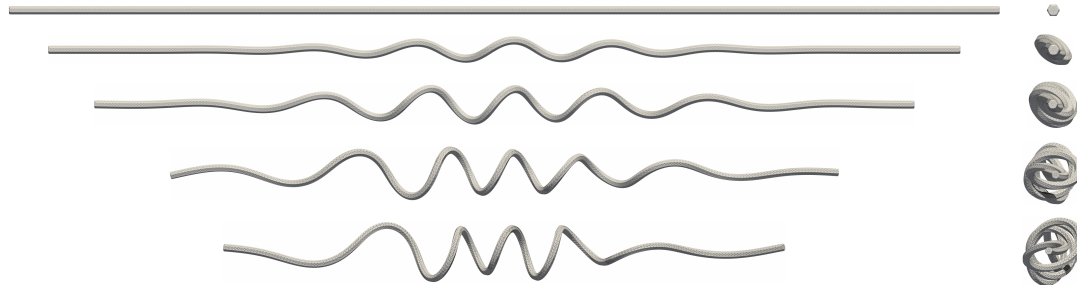


Figure 4.4: Typical buckling sequence in a simulation of a non-Brownian filament with $\bar{\mu} = 6.5 \times 10^4$. In the simulation shown, deformations first occur in a 2D plane before the 3D helical shape develops. Deformations also tend to be largest near the center of the filament.

Simulations of a non-Brownian fiber in Figure 4.4 are consistent with these observations and provide a cleaner picture of the buckling process. In absence of thermal fluctuations, deformations are typically concentrated near the center of the filament, with the filament ends remaining mostly straight and aligned with the flow axis. In simulations at moderate flow strengths, we find that deformations first occur in a two-dimensional

plane before three-dimensional effects kick in and lead to helix formation. This curious sequence of events, which we elucidate below, disappears in very strong flows where three-dimensional shapes emerge almost instantly. As in the Brownian case, shape perversions occasionally arise along the filament and cause handedness reversals [150, 158].

4.3.2 Quantitative characterization

The evolution of the shape during a buckling event is quantified in Figure 4.6(*a-b*), where we plot the helix length and radius as functions of time from experiments and Brownian simulations. The length is simply estimated by the end-to-end-distance $L_{ee}(t) = \|\mathbf{x}(L, t) - \mathbf{x}(0, t)\|$ in the plane of motion, where $\mathbf{x}(s, t)$ is a Lagrangian parameterization of the filament centerline with arc-length $s \in [0, L]$.

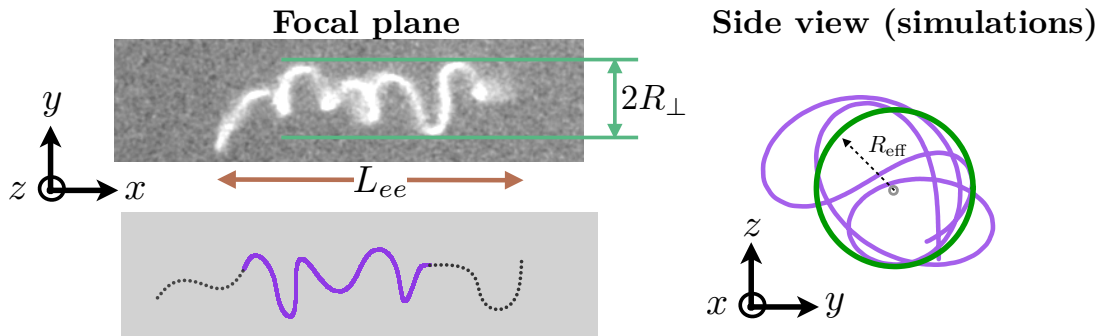


Figure 4.5: A representative helical coiled conformation of the filament from experiments and simulations illustrating the end-to-end distance and two complementary ways of estimating coiling radius. In experiments: $R_\perp(t) = (y_{\max}(t) - y_{\min}(t)) / 2$; in simulations: $R_{\text{eff}}^2(t) = \langle y(s, t)^2 + z(s, t)^2 \rangle_s$. Only the central part of the filament (in purple) is considered when estimating R .

Estimating the coil radius is more challenging and is done using two complementary approaches illustrated in Fig. 4.5. As experiments only provide shape projections in the (x, y) plane, we estimate the radius in terms of the lateral extent of the filament as $R_\perp(t) = (y_{\max}(t) - y_{\min}(t)) / 2$. In simulations, the full filament shape is available and we define an

effective radius by fitting the cross-sectional projection in the (y, z) plane with a circle: $R_{\text{eff}}^2(t) = \langle y(s, t)^2 + z(s, t)^2 \rangle_s$. In both cases, we only consider the central part of the filament where the conformation is mostly helical and omit filament ends.

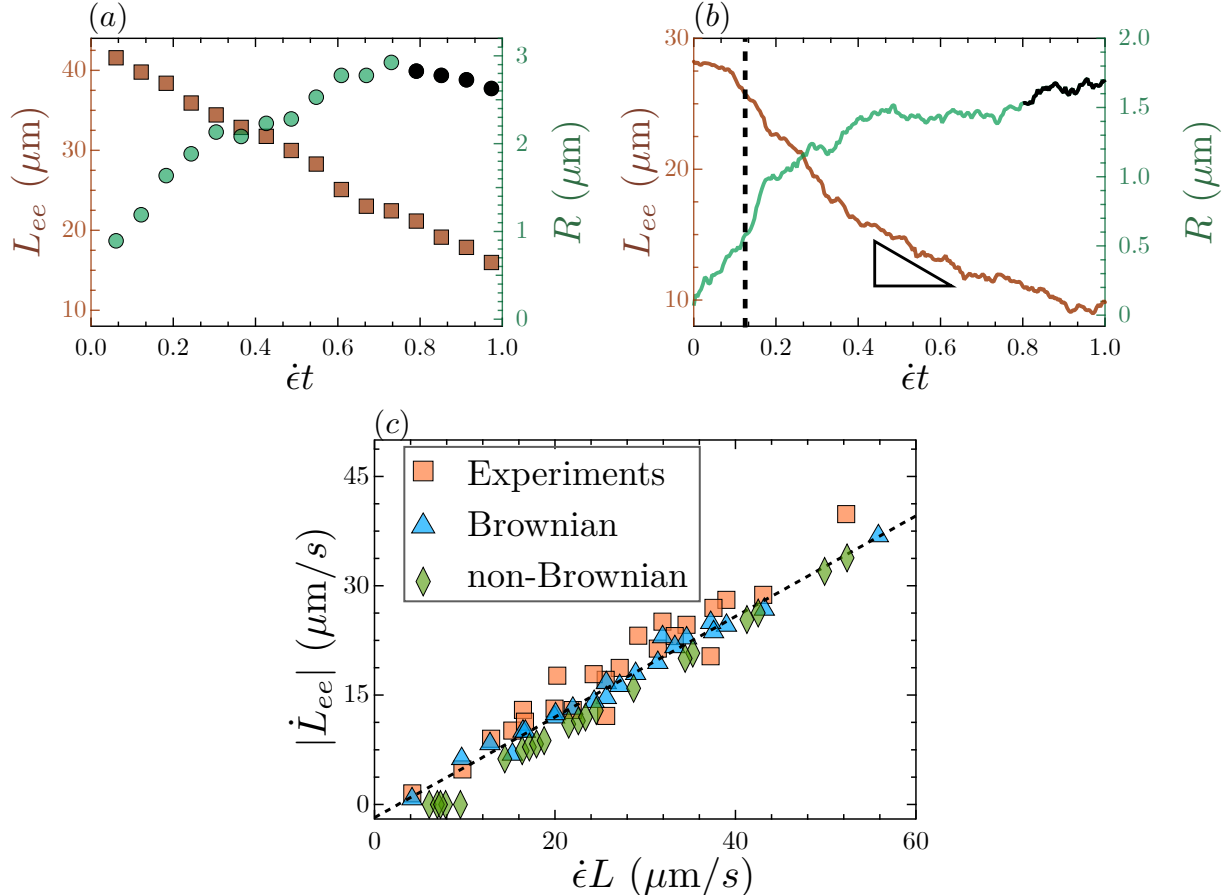


Figure 4.6: (a-b) Evolution of the end-to-end distance L_{ee} and the coiling radius R as functions of Hencky strain $\dot{\epsilon}t$ in experiments (a) and Brownian (b) simulations. The range used to estimate the final coil radius in each case is shown in black. In (b) the vertical dashed line shows the onset of buckling. (c) The compression speed of the helix, estimated as the rate of change of the end-to-end distance, depends linearly on $\dot{\epsilon}L$ with a slope of ~ 0.7 .

The time evolution of the length and radius is similar in experiments and both types of simulations: in all cases, L_{ee} decreases and R increases while the helix forms and gets compressed by the flow. The decrease in L_{ee} is found to be nearly linear with time.

This allows us to extract a characteristic speed $|\dot{L}_{ee}|$ for compression of the helix, which we plot as a function $\dot{\epsilon}L$ in Figure 4.6(c). A linear relationship $|\dot{L}_{ee}| \sim 0.7\dot{\epsilon}L$ is found in both experiments and simulations, with a slope of less than unity that we attribute to the finite elastic resistance of the buckled helical shapes.

4.3.3 Coiling radius and scaling laws

In the final stage of compression, the growth of the helix radius slows down as seen in Figure. 4.6(a-b), and a nearly steady shape is reached with a roughly constant radius. In experiments and Brownian simulations, this occurs near a Hencky strain of unity, and we estimate the final radius by averaging either $R_{\perp}(t)$ or $R_{\text{eff}}(t)$ over $\dot{\epsilon}t \sim 0.8 - 1$. In non-Brownian simulations, filaments typically experience larger Hencky strains, though the key features of the dynamics remain unaltered; in this case, we estimate the final radius by performing the average over $\dot{\epsilon}t \sim 1.6 - 2$. By this procedure, we measured the final coiling radius of the filaments over three decades of the elastoviscous number $\bar{\mu}$, where $\bar{\mu}$ was varied by changing the contour length L . The results, displayed in Figure. 4.7(a), are quite stunning and show a nearly constant dimensional radius over a large range of $\bar{\mu}$, indicating that the final helix radius is largely independent of contour length. The agreement between experiments and simulations is again very good, with a weak systematic deviation attributed to the different ways of estimating R and to the weak extensibility of the filaments in the non-Brownian model. We rationalize this peculiar result by developing a scaling theory for the radius of an inextensible helix undergoing compression in flow.

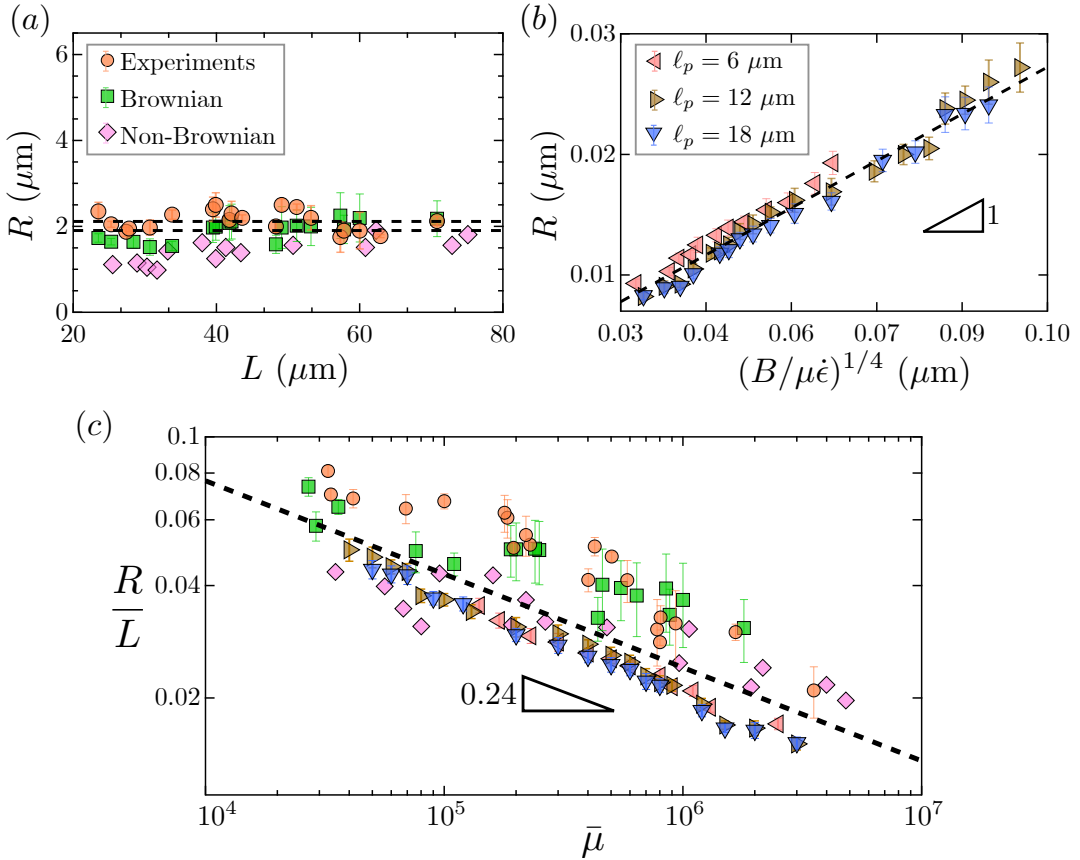


Figure 4.7: (a) Final dimensional radius as a function of contour length in experiments and both types of simulations, for strain rates in the range $\dot{\epsilon} \sim 0.3-0.61 \text{ s}^{-1}$. The two dashed lines show the mean radius for experiments (top) and Brownian simulations (bottom), which differ slightly due to the two different methods for estimating R . (b) Final dimensional radius R as a function of elastoviscous length $(B/\mu\dot{\epsilon})^{1/4}$ in Brownian simulations for varying persistence lengths ℓ_p , showing a linear dependence in agreement with Eq. (4.4). In these simulations, $L = 0.6 \mu\text{m}$, and $\dot{\epsilon} \sim 10^5-10^7 \text{ s}^{-1}$. (c) Collapse of all the data from experiments, Brownian and non-Brownian simulations when plotted in dimensionless variables, showing a power-law scaling of the form $R/L \sim \bar{\mu}^{-0.24}$.

For simplicity, we idealize a post-buckling coiled conformation as a perfect helix parameterized by $\theta \in [0, 2m\pi]$, where m is the total number of loops. The position of a Lagrangian marker along the curve is then given by $\boldsymbol{x} = (R \cos \theta, R \sin \theta, \lambda \theta)$, where R is the radius and λ is related to the pitch $p = 2\pi\lambda$. As the helix is compressed by the flow, its pitch decreases while its radius increases as depicted in Fig. 4.8. This is a consequence

of inextensibility, which dictates that

$$R\dot{R} + \lambda\dot{\lambda} = 0. \quad (4.1)$$

During compression, viscous stresses due to the flow balance elastic forces inside the filament. In both experiments and simulations, we observe that $\lambda < R$, which allows us to approximate the dominant viscous force experienced by the helix as $F_v \sim \xi_{\perp}\dot{p}L$, where ξ_{\perp} is the coefficient of viscous resistance by unit length in the normal direction. The associated viscous dissipation can then be estimated as

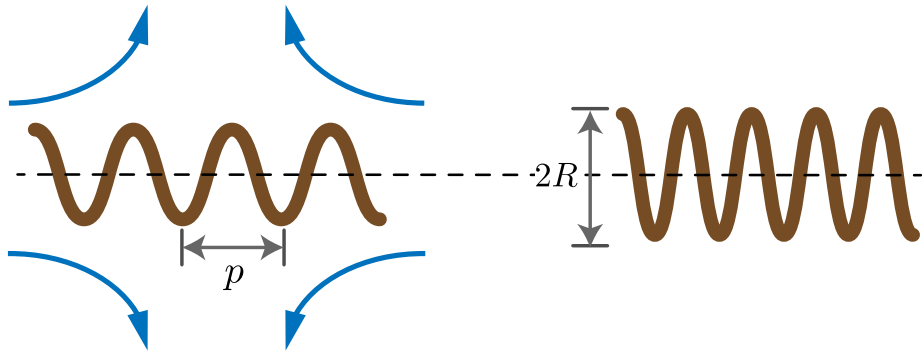


Figure 4.8: Schematic illustrating the compression of an inextensible ideal helix of radius R and pitch p as used for scaling arguments.

$$\Phi_v \sim \xi_{\perp}\dot{p}^2L \sim \xi_{\perp}\dot{\lambda}^2L, \quad (4.2)$$

and must balance the rate of change of elastic bending energy due to compression. For a helical conformation, the bending energy is given by $E_B = BLR^2/2(R^2 + \lambda^2)^2$. Using the kinematic relation (4.1) and the fact that $\lambda < R$, we find its rate of change as

$$\dot{E}_B \sim BL\frac{\lambda\dot{\lambda}}{R^4}. \quad (4.3)$$

In absence of inertia, we seek a balance between Φ_v and \dot{E}_B [7]. Recalling that $\dot{\lambda} \sim \dot{\epsilon}L$ as found in Figure. 4.6(c), we arrive at

$$R \sim \left(\frac{B}{\xi_{\perp} \dot{\epsilon}} \right)^{1/4} \quad \text{i.e.,} \quad \frac{R}{L} \sim \bar{\mu}^{-1/4}. \quad (4.4)$$

This scaling law suggests that the helix radius is independent of contour length L and has only a weak dependence on compression rate $\dot{\epsilon}$. Experiments typically have access to a limited range of strain rates, and as a result the sampling of the three decades of $\bar{\mu}$ in Fig. 4.7(a) was primarily due to variations in filament length while keeping $\dot{\epsilon}$ in the range $\sim 0.4 - 0.6 \text{ s}^{-1}$. This explains why no dependence on $\bar{\mu}$ was found. To further test the scaling law and probe the dependence on flow strength, we performed additional Brownian simulations in which the strain rate was varied while keeping L constant. The measured radius for three different values of ℓ_p/L is displayed in Fig. 4.7(b) and shows a clear collapse of the data with an exponent close to $-1/4$ when plotted in dimensionless form. This corroborates the scaling prediction and further confirms that thermal fluctuations play a secondary role. Finally, we display all the data from experiments and both types of simulations in dimensionless form in Figure 4.7(c). A similar collapse is found, with some scatter arising mainly from fluctuation-induced defects and from the two distinct methods for estimating R . A numerical fit provides an exponent of -0.24 , in excellent agreement with the proposed scaling law.

4.4 Origin of coiling: mode interaction

So far we have discussed the key features of the filament morphologies and have quantified the emerging coiled conformations through various order parameters. Now we proceed to explain the emergence of helical morphologies using a 3D weakly nonlinear stability analysis.

4.4.1 Linear stability analysis

Previous 2D linear analyses in planar flows have been very successful at predicting the onset of buckling and subsequent mode shapes [33, 111, 112, 143]. We will attempt to show how the interaction of pairs of planar eigenmodes growing in different planes is responsible for the observed 3D helices. In past studies of viscous buckling, the role of thermal fluctuations was shown to be limited to triggering the instability while smoothing the buckling transition [2, 7, 112]. We neglect fluctuations in our theory and start by performing a three dimensional linear stability analysis in the spirit of [111].

In the reference frame of the translating filament, the local flow field is well approximated by a planar compressional flow in experiments and Brownian simulations, and by a uniaxial compressional flow in non-Brownian simulations; we focus here on the former case and thus take the dimensionless flow field to be $\mathbf{u}_\infty = (-x, y, 0)$. In the base state, the filament is straight with its center at the stagnation point and its axis aligned with the direction of compression: $\mathbf{x}_0(s) = s\hat{\mathbf{x}}$ with $s \in [-0.5, 0.5]$. Its motion is described using local slender-body theory for low-Reynolds-number hydrodynamics [159],

$$\bar{\mu}(\dot{\mathbf{x}} - \mathbf{u}_\infty) = (\mathbf{I} + \mathbf{x}_s \mathbf{x}_s) \cdot [(T \mathbf{x}_s)_s - \mathbf{x}_{ssss}], \quad (4.5)$$

where the elastoviscous number $\bar{\mu}$ appears as the sole control parameter. Indices in Eq. (4.5) denote differentiation with respect to arclength, with \mathbf{x}_s describing the local tangent vector. The scalar $T(s)$ is the internal tension that enforces filament inextensibility. Eq. (4.5) is accompanied by force- and moment-free boundary conditions: $\mathbf{x}_{sss} = \mathbf{x}_{ss} = T = 0$ at $s = \pm 1/2$. In the base state, the compressional flow induces a parabolic tension profile $T_0(s) = \frac{1}{4}\bar{\mu}(s^2 - \frac{1}{4})$ typical of undeformed filaments in linear flows [33, 111].

The straight configuration is perturbed as $\mathbf{x}(s, t) = (s, h_y, h_z)$, where $h_y(s, t)$ and $h_z(s, t)$ are in-plane (x, y) and out-of-plane (x, z) shape perturbations, respectively, and are assumed to be small $\mathcal{O}(\varepsilon)$ quantities. We first perform a linear analysis and simplify

Eq. (4.5) to

$$\bar{\mu}(\dot{\mathbf{x}} - \mathbf{u}_\infty) = T_0 \mathbf{x}_{ss} + 2T_{0,s} \mathbf{x}_s - \mathbf{x}_{ssss} + \mathcal{O}(\varepsilon^2), \quad (4.6)$$

where the velocity field experienced by the filament is $\mathbf{u}_\infty = (-s, h_y, 0)$. We seek normal-mode perturbations of the form $\{h_y, h_z\} = \{\Phi_y(s), \Phi_z(s)\} \exp(\sigma t)$, where Φ_y and Φ_z are in-plane and out-of-plane mode shapes and σ is the complex growth rate. Inserting this ansatz into Eq. (4.6) yields two eigenvalue problems in the y and z directions:

$$\bar{\mu}(\sigma - 1)\Phi_y = \mathcal{L}[\Phi_y], \quad (4.7)$$

$$\bar{\mu}\sigma\Phi_z = \mathcal{L}[\Phi_z], \quad (4.8)$$

where \mathcal{L} is the differential operator $\mathcal{L}[\Phi] = T_0(s)\Phi_{ss} + T_{0,s}(s)\Phi_s - \Phi_{ssss}$. Inspection of Eqs. (4.7)–(4.8) shows that the eigenvalue problems in the two orthogonal planes are uncoupled and thus have their own growth rates (σ_y, σ_z) . Incidentally, the two eigenvalue problems are found to be identical under the transformation $\sigma_z = \sigma_y - 1$. This points to a key aspect of the eigenspectrum: for a given value of $\bar{\mu}$, in-plane and out-of-plane mode shapes are identical but have offset growth rates. Out-of-plane deformations grow slightly more slowly as a consequence of the 2D nature of the flow; both growth rates would be identical in uniaxial flow.

The eigenvalue problem of Eq. (4.7) was solved numerically using a Chebyshev spectral collocation method with boundary conditions $\Phi_{yss} = \Phi_{ysss} = 0$ at $s = \pm 1/2$, and results are summarized in Figure 4.9. The growth rates $\text{Re}[\sigma_y]$ of unstable modes are plotted versus $\bar{\mu}$ in Fig. 4.9(a). In very weak flows, all modes are stable with negative growth rates. As the elastoviscous number is increased, a supercritical pitchfork bifurcation occurs giving rise to the first onset of buckling. In agreement with past planar analyses [111–113], the first buckling threshold is found to be $\bar{\mu}_c \approx 153.2$ with an even mode shape ($\Phi(-s) = \Phi(s)$) resembling the canonical C shape typical of Euler buckling. At yet larger values of $\bar{\mu}$, higher-order buckling modes with larger wavenumbers are excited and can

become unstable, leading to the complex eigenspectrum of Fig. 4.9(a). Three essential features stand out: (i) at large elastoviscous numbers, the first two eigenvalues $\{\sigma_y^{(1)}, \sigma_y^{(2)}\}$ dominate the spectrum and the corresponding eigenmodes are expected to dictate the emergent morphologies; (ii) these two dominant eigenmodes always come in an odd–even pair, i.e., if $\Phi^{(1)}$ is odd then $\Phi^{(2)}$ is even and vice-versa; (iii) the difference in growth rate between these two dominant modes becomes negligible in strong flows. This last point is made clear in the inset of Fig. 4.9(a), where the difference $\Delta\sigma$ between the two growth rates is seen to decay rapidly with $\bar{\mu}$.

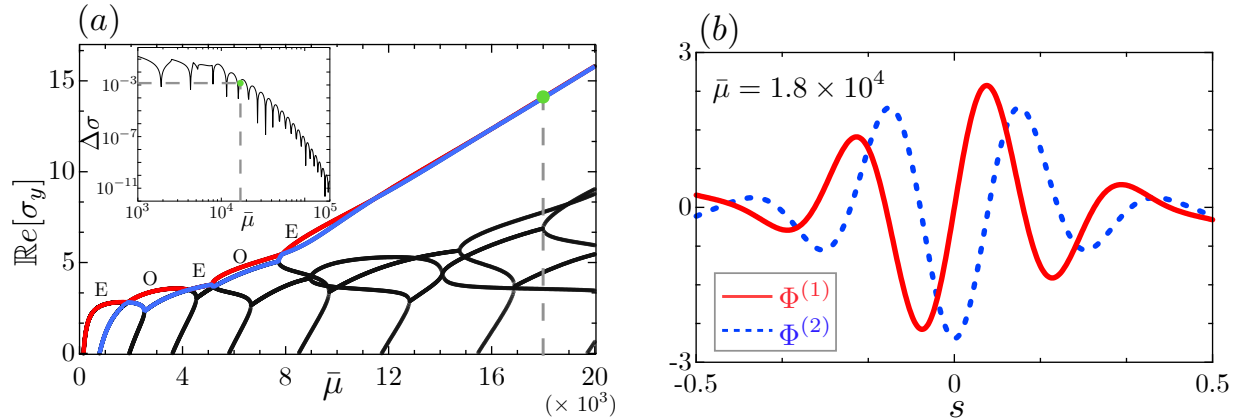


Figure 4.9: (a) Growth rates of unstable planar eigenmodes plotted vs. elastoviscous number. As $\bar{\mu}$ increases, additional modes become unstable. The two dominant eigenvalues are colored in red and blue and labeled as either even (E) or odd (O) functions of s . Inset: difference $\Delta\sigma$ between the two most unstable eigenvalues as a function of $\bar{\mu}$, showing convergence in strong flows. (b) Eigenmodes associated with the two largest eigenvalues for a value of $\bar{\mu} = 1.8 \times 10^4$ corresponding to the green dot in (a). The dominant mode $\Phi^{(1)}$ is odd, whereas $\Phi^{(2)}$ is even.

We are now in a position to explain the emergence of helicoidal shapes. In a strong flow, unstable eigenmodes are planar but can develop and grow in any plane containing the flow axis. In addition, dominant modes always come in odd–even pairs with nearly identical growth rates. When a straight filament is perturbed, there is thus a strong likelihood for both modes to grow simultaneously. The superposition of two adjacent odd–even planar

modes such as those shown in Fig. 4.9(b) and growing in different planes produces a coiled three-dimensional conformation that resembles a helix and continues to grow as such, with the two modes interacting as a consequence of geometric nonlinearities. A similar mechanism was previously proposed to explain the buckling of elastic rods in soft elastomer matrices [160], though the governing equations and forces at play are very different in that problem.

4.4.2 Amplitude equations: weakly nonlinear theory

This modal interaction process can be formalized by deriving a nonlinear amplitude equation of the Ginzburg-Landau form [142, 161]. At the onset of buckling we make the assumption that the tension profile inside the filament can still be approximated by the parabolic tension in the undeformed base state. We start by expanding the governing equation Eq. (4.5) with this tension much in the spirit of Monge representation but retaining the nonlinear terms. Thus we have:

$$\bar{\mu} \dot{\mathbf{x}} = \bar{\mu} \mathbf{u} + T_0 \mathbf{x}_{ss} + 2T_{0,s} \mathbf{x}_s - \mathbf{x}_{ssss} - \mathbf{x}_s (\mathbf{x}_s \cdot \mathbf{x}_{ssss}). \quad (4.9)$$

Recognizing the linear operator from the stability analysis the above equation can be written as:

$$\bar{\mu} \dot{\mathbf{x}} = \bar{\mu} \mathbf{u} + \mathcal{L}[\mathbf{x}] - \mathbf{x}_s (\mathbf{x}_s \cdot \mathbf{x}_{ssss}), \quad (4.10)$$

We now expand the transverse deformations on the basis of the first two linear eigenmodes as they dominate the unstable spectrum: $h_{y,z}(s, t) = A_1^{y,z}(t)\Phi_1(s) + A_2^{y,z}(t)\Phi_2(s)$. Our aim is to derive ordinary differential equations for the amplitudes of the perturbations that illustrate coupling between unstable modes. To this end, we first explicitly derive the functional form of the nonlinear terms, which we denote by $\mathcal{N}(s, t) = \mathbf{x}_s (\mathbf{x}_s \cdot \mathbf{x}_{ssss})$. We

first calculate:

$$\beta \equiv \mathbf{x}_s \cdot \mathbf{x}_{ssss} = (1, h_s^y, h_s^z) \cdot (0, h_{ssss}^y, h_{ssss}^z) = h_s^y h_{ssss}^y + h_s^z h_{ssss}^z. \quad (4.11)$$

Using the chosen form of expansion of the perturbations on the basis of eigenfunctions the above expression can be written as:

$$\beta = \left(A_1^y \Phi_s^{(1)} + A_2^y \Phi_s^{(2)} \right) \left(A_1^y \Phi_{ssss}^{(1)} + A_2^y \Phi_{ssss}^{(2)} \right) + \left(A_1^z \Phi_s^{(1)} + A_2^z \Phi_s^{(2)} \right) \left(A_1^z \Phi_{ssss}^{(1)} + A_2^z \Phi_{ssss}^{(2)} \right). \quad (4.12)$$

The above expression can be further simplified to:

$$\beta = [(A_1^y)^2 + (A_1^z)^2] \gamma_1(s) + [A_1^y A_2^y + A_1^z A_2^z] \gamma_2(s) + [(A_2^y)^2 + (A_2^z)^2] \gamma_3(s). \quad (4.13)$$

In the above expression, the functions $\{\gamma_1, \gamma_2, \gamma_3\}$ are given by:

$$\gamma_1 = \Phi_s^{(1)} \Phi_{ssss}^{(2)}, \quad (4.14)$$

$$\gamma_2 = \Phi_s^{(1)} \Phi_{ssss}^{(2)} + \Phi_s^{(2)} \Phi_{ssss}^{(1)}, \quad (4.15)$$

$$\gamma_3 = \Phi_s^{(2)} \Phi_{ssss}^{(2)}. \quad (4.16)$$

The transverse components of the nonlinear term $\mathcal{N}(s, t)$ are then obtained as $\mathcal{N}_y = h_s^y \beta$ and $\mathcal{N}_z = h_s^z \beta$, and we emphasize that these nonlinear terms couple in-plane and out-of-plane modes.

We now proceed to derive amplitude equations of the Ginzburg-Landau form, first starting with the y component of the slender-body equation. Inserting the expansion for $h_y(s, t)$ into Eq. (4.10) yields

$$\bar{\mu} \Phi^{(1)} \frac{dA_1^y}{dt} + \bar{\mu} \Phi^{(2)} \frac{dA_2^y}{dt} = \bar{\mu} \left(A_1^y \Phi^{(1)} + A_2^y \Phi^{(2)} \right) + A_1^y \mathcal{L}[\Phi^{(1)}] + A_2^y \mathcal{L}[\Phi^{(2)}] - \mathcal{N}_y. \quad (4.17)$$

Recalling that the eigenfunctions satisfy Eq. (4.7), this simplifies to

$$\bar{\mu} \Phi^{(1)} \frac{dA_1^y}{dt} + \bar{\mu} \Phi^{(2)} \frac{dA_2^y}{dt} = \bar{\mu} A_1^y \sigma_1 \Phi^{(1)} + \bar{\mu} A_2^y \sigma_2 \Phi^{(2)} - \mathcal{N}_y. \quad (4.18)$$

In order to derive the amplitude equation for each mode it is tempting to use the orthogonality of eigenfunctions. However we are plagued with a subtle issue. The linear operator \mathcal{L} appearing in the linearized stability problem is not self-adjoint. As a result, the computed eigenfunctions are not orthonormal to each other. In order to proceed with the non-linear theory, we need to find the adjoint L^\dagger of the linear operator (as derived in Appendix C) and associated adjoint eigenfunctions, which we denote by ϕ^\dagger . This subtlety was previously identified by Guglielmini et al. [142] in their weakly nonlinear theory for clamped filaments in 2D stagnation point flows. Using the orthogonality of adjoint eigenfunction we obtain the amplitude equations as:

$$\frac{dA_1^y}{dt} = \sigma_1 A_1^y - \frac{1}{\bar{\mu}} \frac{\langle \mathcal{N}_y, \phi^{\dagger(1)} \rangle}{\langle \phi^{\dagger(1)}, \Phi^{(1)} \rangle}, \quad (4.19)$$

$$\frac{dA_2^y}{dt} = \sigma_2 A_2^y - \frac{1}{\bar{\mu}} \frac{\langle \mathcal{N}_y, \phi^{\dagger(2)} \rangle}{\langle \phi^{\dagger(2)}, \Phi^{(2)} \rangle}, \quad (4.20)$$

where:

$$\langle a(s), b(s) \rangle = \int_{-1/2}^{1/2} a(s)b(s) ds, \quad (4.21)$$

is the inner-product definition. If we neglect the nonlinear terms in the above amplitude equations, we will recover the prediction of the linear stability problem, where unstable modes grow exponentially with respective growth rates given by the eigenvalues. Nonlinear terms not only introduce additional complexity but also couple the various modes. We can similarly obtain amplitude equations for the out-of plane problem:

$$\frac{dA_1^z}{dt} = (\sigma_1 - 1) A_1^z - \frac{1}{\bar{\mu}} \frac{\langle \mathcal{N}_z, \phi^{\dagger(1)} \rangle}{\langle \phi^{\dagger(1)}, \Phi^{(1)} \rangle}, \quad (4.22)$$

$$\frac{dA_2^z}{dt} = (\sigma_2 - 1) A_2^z - \frac{1}{\bar{\mu}} \frac{\langle \mathcal{N}_z, \phi^{\dagger(2)} \rangle}{\langle \phi^{\dagger(2)}, \Phi^{(2)} \rangle}. \quad (4.23)$$

The fact that the growth rates of the out-of-plane modes are smaller compared to in-plane modes is evident from the the linear terms. All four amplitude equations (4.19)–(4.23) are coupled to each other through the nonlinear terms and thus need to be integrated numerically.

4.4.3 Spontaneous symmetry breaking

We can now integrate the system of amplitude equations to study the evolution of the filament morphology as predicted from the nonlinear theory. We start with an entirely planar initial condition that has contributions from only the dominant mode. We can write this as:

$$\mathbf{A}(0) = \begin{bmatrix} A_1^y(0) \\ A_2^y(0) \\ A_1^z(0) \\ A_2^z(0) \end{bmatrix} = \epsilon \begin{bmatrix} 1 \\ 0 \\ 1 \\ 0 \end{bmatrix}, \quad (4.24)$$

where $\epsilon \approx 10^{-4}$ is a small parameter typical of the amplitude at the initiation of the buckling. In Figure 4.10 we show the time evolution of the amplitudes for $\bar{\mu} = 1.8 \times 10^4$ with dominant eigenmodes as shown in Fig 4.9.

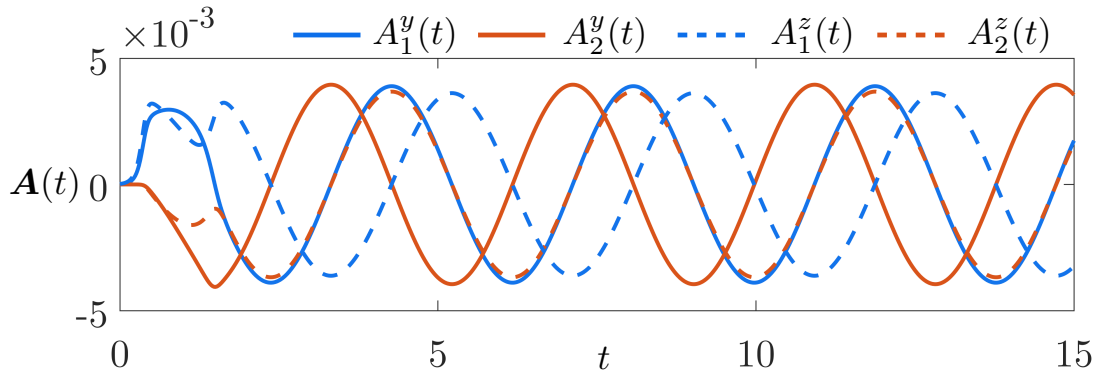


Figure 4.10: Time evolution of the amplitudes of modes for $\bar{\mu} = 1.8 \times 10^4$.

A number of interesting features stand out from the solution of this ODE system. First we notice that the nonlinearities are sufficient for amplitude saturation. Second, the nonlinear coupling sets a non-zero amplitude for the mode $\Phi^{(2)}(s)$. This solidifies our idea of mode-interaction and indeed now a linear superposition of the even and odd modes lead to a coiled conformation for the filament. The evolution of the filament morphology as

given by $\mathbf{x} = [s, h^y(t), h^z(t)]$ is shown in Figure 4.11.

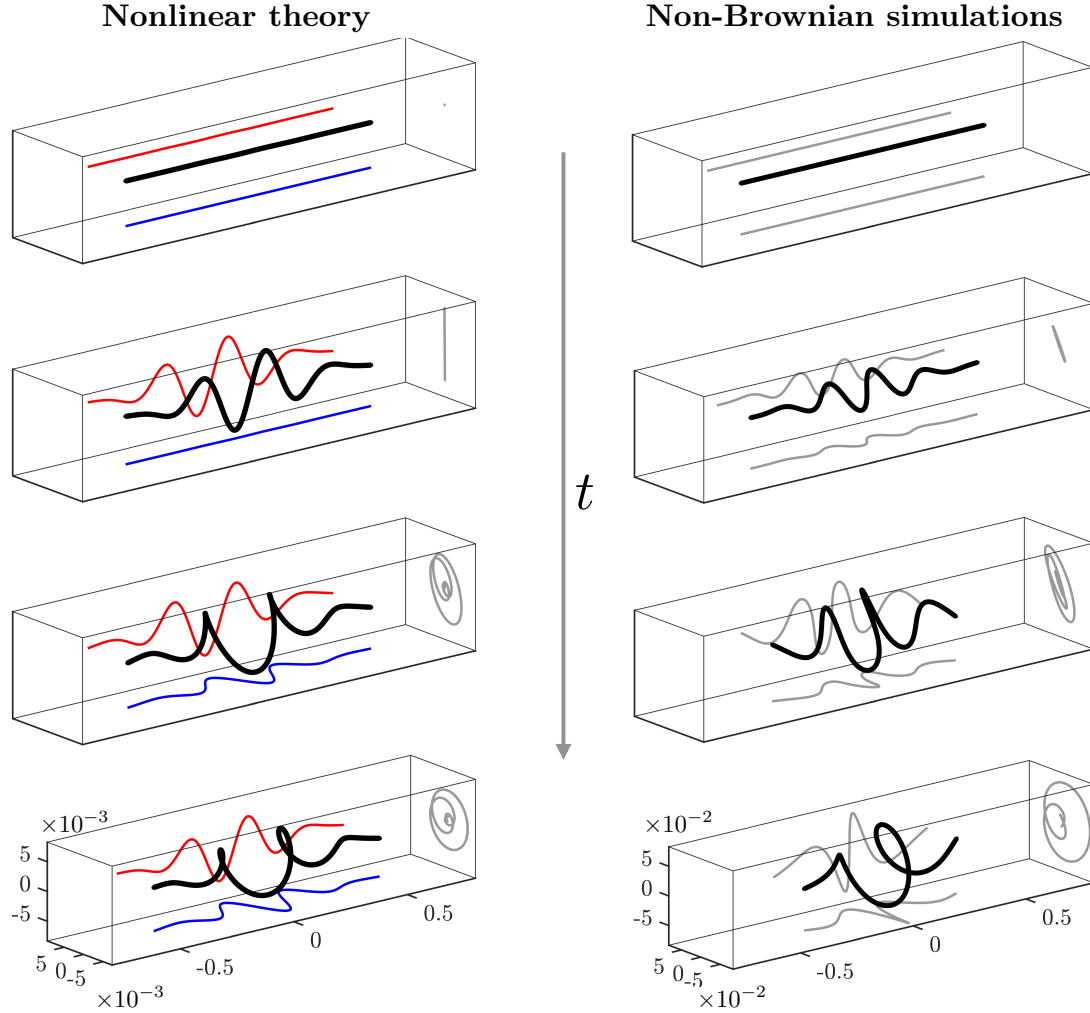


Figure 4.11: Shape evolution of a filament from nonlinear theory (left) and non-Brownian simulations (right) for $\bar{\mu} = 1.8 \times 10^4$. On the two orthogonal planes on the left we show the projections of the conformations that are identical to the dominant even and odd modes of the linear stability analysis shown in Figure 4.9.

Comparison of the theoretical prediction against full nonlinear simulations from non-Brownian filaments show remarkable agreement. In both the cases we find that at the onset of buckling the filament remains planar: consistent with the result of linear stability analysis. However the unstable modes interact soon in the presence of geometric nonlin-

earities that lead to a spontaneous symmetry breaking giving way to helical structures. Oscillations in amplitudes as seen in Figure 4.10 lead to rotation of the chiral structure in the space of shapes. Interestingly in weak flows (for $\bar{\mu} < 8 \times 10^4$), when the eigenvalues are well separated we do not observe growth of adjacent modes from the nonlinear theory. This suggests that the nonlinearities are not sufficient to excite growth of the secondary mode and as a result the filament conformation remains planar.

4.5 Conclusion and outlook

We have elucidated the coiled morphologies of actin filaments in compressional flow through a combination of experiments, simulations, scaling analysis and weakly nonlinear stability theory. The two distinct approaches used in numerical simulations highlight the robustness of this phenomenon, in which neither Brownian fluctuations nor a three-dimensional flow field are necessary conditions for helical buckling. The stability theory also supports this idea and explained the origin of these structures in a simple two-dimensional stagnation point flow. As uncovered in our analysis, the key to helical coiling is the nature of the eigenspectrum associated with the linearized buckling problem, in which dominant eigenmodes come in odd–even pairs with nearly identical growth rates and interact nonlinearly to form helicoidal shapes. Our analysis is an addition to the study of post-buckling mode interactions that are often responsible for non-planar structures [162]. Remarkably, this distribution of eigenvalues is quite generic, and helical buckling has also recently been observed for very flexible filaments in shear flow as illustrated in Figure 4.12, where the dynamics is more subtle due to the non-stationary base state of a tumbling straight filament.

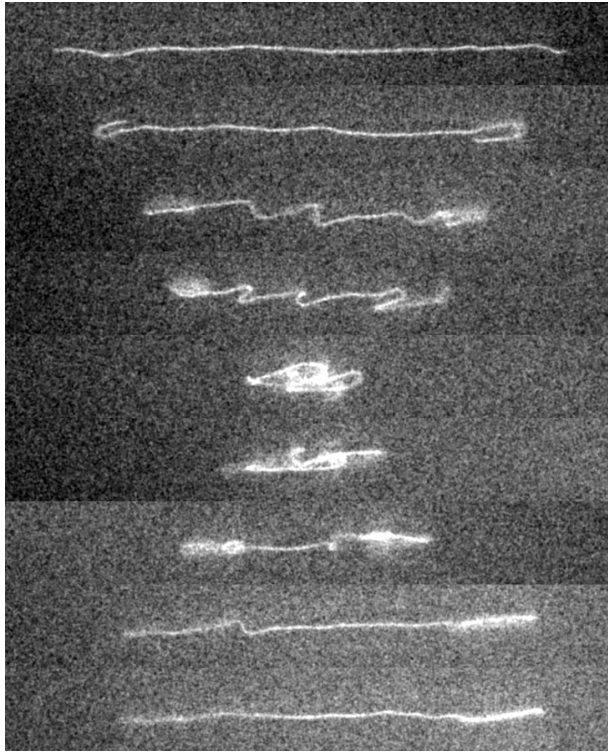


Figure 4.12: Three-dimensional buckling of a very long actin filament placed in a linear shear flow.

The helicoidal shapes in this case are not as regular as in purely compressional flow, and are also unsteady as the filaments undergo tumbling by a tank-treading motion. We have also not discussed the energetic aspect of helical buckling as probed in [157]. Helix formation is essentially supported by a favorable energetic landscape as shown in Figure 4.13. A filament that is forcefully restricted to buckle and compress in two dimensions indeed shows a monotonic growth of its bending energy that is avoided by the provision of coil.

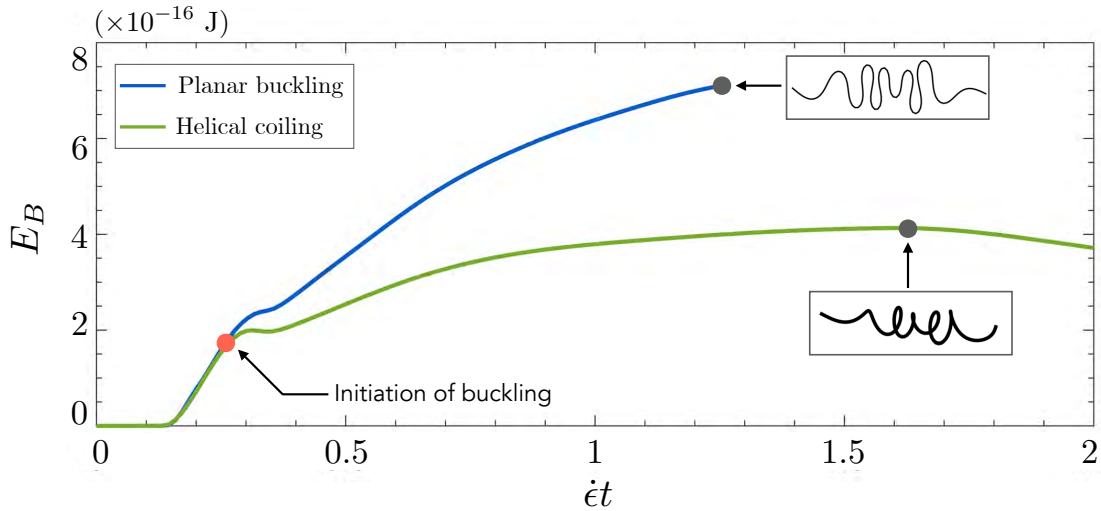


Figure 4.13: Evolution of the total bending energy in planar and fully three-dimensional Brownian simulations. The planar simulations were stopped when parts of the filament come in contact. Parameters: $\ell_p/L = 200$ and $\bar{\mu} = 5 \times 10^5$.

The fundamental mechanism highlighted by our analysis should advance our understanding of these various phenomena and may also be exploited for the controlled microfabrication of chiral objects from one-dimensional elastic filaments.

This chapter is primarily based on the material that is presently under review and was authored by Brato Chakrabarti, Yanan Liu, John LaGrone, Ricardo Cortez, Lisa Fauci, Olivia du Roure, David Saintillan and Anke Lindner [8]. The dissertation author performed numerical simulations and worked on theoretical modeling for this paper.

Chapter 5

Spontaneous oscillations of active microfilaments

5.1 Introduction to active filaments

In the previous chapters we have discussed dynamics and morphologies of actin filaments in two canonical flows. We term the studied actin polymers as ‘passive’ filaments that are simply deformed by the hydrodynamic forces and respond to thermal fluctuations that obey the fluctuation-dissipation theorem. In this chapter we will focus on the dynamics of ‘active’ polymers or filaments. Typical of active matter problems, the dynamics of these filaments is driven by non-equilibrium processes where some agent converts internal chemical energy to directed motion [163]. Canonical example of well studied active polymer system include motility assays. Here biopolymers like actin and microtubule are propelled on carpets of motor proteins anchored on a substrate, which results in directed motion [164–167]. Mixtures of active and passive components are a characteristics of eukaryotic cells with the active cytoskeleton on the one hand and an embedded large variety of passive colloidal and polymeric objects on the other hand. Here, an enhanced random

motion of tracer particles has been observed [168]. An extensive review of the intriguing dynamics of active polymers is beyond the scope of this thesis and the interested reader is pointed to [169]. This chapter focuses on one canonical case of active filaments related to cilia and flagella that can oscillate spontaneously due to the action of molecular motors.

5.2 Dynamics of cilia and flagella: overview

Cilia and flagella are thin hair-like cellular projections that play a variety of crucial roles where motion at the cellular level is required. Flagella, found on sperm cells and in a number of protozoa, enable swimming in viscous media by propagating bending waves along their axis [17]. Cilia are typically shorter than flagella and beat in an asymmetric whipping pattern. The coordinated beating in carpets of cilia gives rise to ‘metachronal waves’ that allow organisms such as *Paramecium* to swim efficiently. Motile cilia also play a crucial role in ovum transport and in transport of mucus across the respiratory track, known as mucociliary clearance [170]. The movement of the cilium is produced by the bending of its core known as the axoneme. The axoneme architecture, which is illustrated in Figure 5.1, has been remarkably conserved across evolution [171]. It involves nine peripheral microtubule doublets known as the ‘A–B’ microtubules [17], which are arranged in regular intervals and centered around a pair of singlet microtubules. The outer doublets are linked to a sheath around the central pair by radial spokes and are connected among themselves through protein linkers known as nexin links. The network of links along with the radial spokes provide constraints that help to maintain the structural integrity of the axoneme. This characteristic arrangement of microtubules that extends for the entire length of the axoneme (10–200 μm) is found in most eucaryotic flagella and cilia and is known as the ‘9+2’ structure [17].

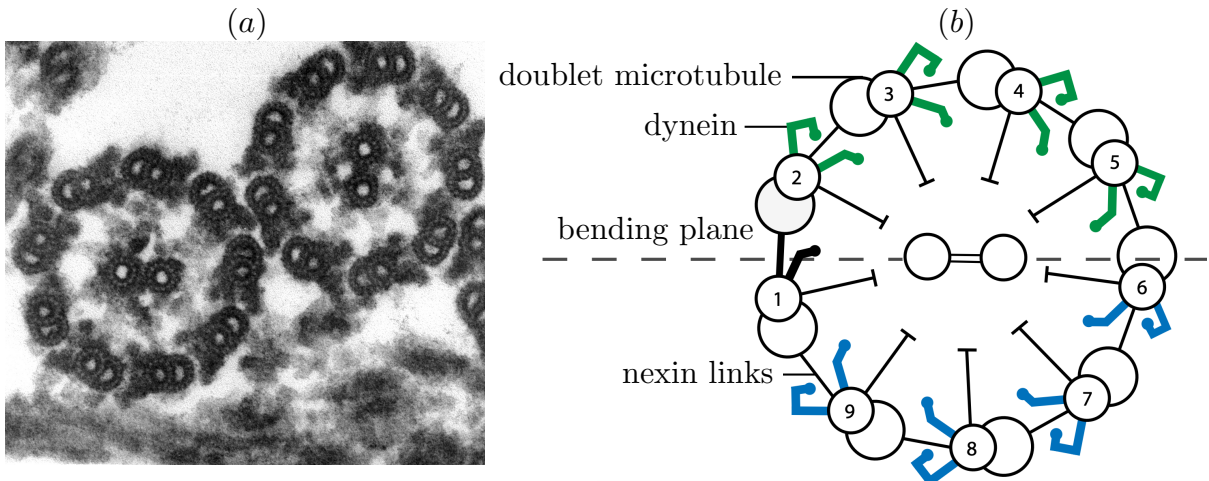


Figure 5.1: (a) Thin section electron micrograph of axonemes of the green algae *Chlamydomonas reinhardtii*. Reproduced from Smith and Lefebvre [172]. (b) A simplified schematic of the cross-section of an axoneme showing the ‘9+2’ structure from [173].

Thousands of dynein molecular motors are distributed along the A-tubule in groups that are responsible for force generation. The heads of these motors extend to the B-tubule of the adjacent doublet [174, 175]. In the presence of adenosine triphosphate (ATP), the motor proteins undergo cycles of attachment and detachment generating forces that cause sliding between the doublets. It has been shown that in demembranated flagellar axonemes this sliding can actually cause microtubules to slide apart [176]. However, inside cilia and flagella the protein linkers (nexin links) as well as the basal structure prevent free sliding, leading instead to bending deformations [17]. In swimming spermatozoa, these deformations take the form of bending waves that propagate along the flagellum from head to tip [175]. These highly coordinated motions suggest a complex regulation mechanism for the action of molecular motors along the length of the axoneme. While the structure of the axoneme and the mechanism for internal shear generation by dynein motors is understood [177], it still remains unknown how spontaneous oscillations can emerge from the coordinated action of thousands of molecular motors.

A number of approaches have been proposed to explain the spontaneous generation of oscillations in actuated elastic filaments. Several such models coarse-grain the role of molecular motors and the internal mechanics of the axoneme and focus instead on qualitative beating patterns that resemble those of cilia or flagella. One such recent approach [178–180] models the spontaneous oscillations observed in flagella as a buckling instability reminiscent of the classical flutter problem [181] in the presence of a follower-force. In a similar spirit, it was previously shown [182] that self-propelled Brownian particles connected as a chain can display periodic deformations that mimic ciliary beating patterns. In another model, Goldstein *et al.* [183] prescribed a suitable form of the internal shear force density to induce spontaneous oscillations resembling the bending waves seen in sperm.

On the other hand, there have also been considerable efforts over the last few decades in the development of theoretical models that capture some aspects of the geometric details of the axoneme and motor activity in an attempt to explain experimentally observed beating patterns. The bulk of these models rely on some form of geometric feedback from the axoneme on the activity of the molecular motors. The three geometric features that may be involved in this feedback are: (a) curvature, (b) inter-doublet distance and (c) sliding displacement. In the curvature-controlled models, the dynein activity is regulated by the instantaneous curvature or by a delayed curvature of the axoneme [184–186]. Once the curvature exceeds a predefined threshold the dyneins are de-activated. This feedback mechanism was able to produce propagating wave patterns as observed in flagella [185,186] as well as ciliary beating patterns [184]. Recently it has been proposed [187] that the breaststroke-like beating patterns of *Chlamydomonas* are best explained through curvature-controlled feedback. However, these models coarse-grain the detailed kinetics of dynein activity. The geometric-clutch model [188] instead argues

that dynein activity is regulated by inter-doublet separation. This separation is governed by the transverse force generated from stretched nexin links in a bent configuration that further dictates the probability of formation of dynein bridges. The attachment and detachment of dynein is determined dynamically from the instantaneous transverse force. This model has been able to reproduce both flagellar and ciliary waveforms. While the initial discrete model [188] had a poor model of hydrodynamics, a recent continuum extension [189] includes a more detailed hydrodynamic model. It was shown by [189] that the excitable dynein model can be mapped back to the Fisher-Kolmogorov equation, which admits traveling wave solutions. However, as pointed out in [174], their model [190] does not lead to self-regulated saturation of the unstable modes of oscillation and instead relies on the addition of stiff non-linear springs. Finally, the sliding control model assumes a linear relationship between the internal shear force and sliding displacements. Other studies [191–193] have prescribed the internal shear force to have a form of traveling wave that results in sperm-like beating patterns. However, this approach not only sets the intrinsic beating frequency but also coarse-grains the dynamics of the molecular motors. Sliding control models can also be equipped with a two-state model for molecular motors that depends on both the sliding displacement and the rate of sliding [175, 194]. Beyond a critical activity of the motors, a Hopf bifurcation takes place leading to spontaneous oscillations of the filament. Numerical simulations [174, 175, 195] involving two-state models have been performed only close to the bifurcation threshold and in the small curvature limit. These simulations suggest that for a clamped filament bundle, bending waves propagate from the tip to the base (retrograde) as opposed to the base-to-tip (anterograde) propagation observed in swimming sperm. A change of boundary conditions [193] or including basal compliance [175] can affect the direction of bend propagation. Nevertheless, results from weakly nonlinear theories, while valid close to the bifurcation, may not provide an accurate

picture of the far-from-equilibrium, geometrically nonlinear cases of beating.

Oriola *et al.* [174] recently proposed a detailed microscopic description of dynein kinetics coupled to flagellar shape in the framework of sliding controlled beating. Their model led to the saturation of unstable modes from nonlinear interactions without any additional need for nonlinear springs [189,190]. However, their analysis [174] was limited to the geometrically linear small-curvature limit close to the bifurcation. While the observed waves resembled flagellar waveforms, their direction was retrograde. In the present paper, we use the microscopic kinetic model of Oriola *et al.* [174] to derive a more complete set of nonlinear governing equations that include hydrodynamic interactions and can be solved numerically. We discover that, when all the nonlinearities are retained, anterograde bend propagation can occur away from the bifurcation and results purely from nonlinear interactions of the dynein activity with axoneme geometry and hydrodynamics.

The chapter is organized as follows. First, we present in Sec. 5.3 the geometrically nonlinear model for a microtubule bundle and dynein activity that follows Oriola *et al.* [174]. We then discuss in Sec. 5.4 the various beating patterns away from equilibrium, transitions in the direction of wave propagation, and the dependence of the amplitude and frequency of the bending waves on the level of activity of molecular motors. The model is also modified to allow for the possibility of asymmetric beats, and we show that an appropriate choice of parameters can induce ciliary beating patterns. Following past studies [174,196], we analyze the beating patterns using principal component analysis in Sec. 5.5.2. Finally, the disturbance velocity fields and their minimal representations in terms of fundamental singularities of Stokes flow both in free space and next to a no-slip wall are discussed in Sec. 5.6. These representations could provide a basis for studying hydrodynamic interactions between spontaneously beating filaments and potential mechanisms for synchronization.

5.3 Model for axonemal beating

5.3.1 Viscous dynamics of an elastic filament

Geometry and force balance: We idealize a beating flagellum or cilium as an inextensible unshearable planar elastic rod submerged in a fluid with viscosity ν . Its motion is described by a set of geometrically nonlinear equations following Euler's elastica theory [197], with viscous stresses captured by non-local slender-body hydrodynamics. We have discussed various aspects of the elasticity and hydrodynamics in great detail previously (see Chapter 2). Here we focus on deriving a set of simplified governing equation for the planar case of the general elastica. As shown in Figure 5.2, we consider a filament with length L and diameter a such that $\epsilon = a/L \ll 1$, where ϵ is the slenderness ratio. We impose that one end of the filament is fixed, as in the case of a cilium attached to a wall or a flagellum affixed to a sperm head, and we assume clamped boundary conditions at that end.

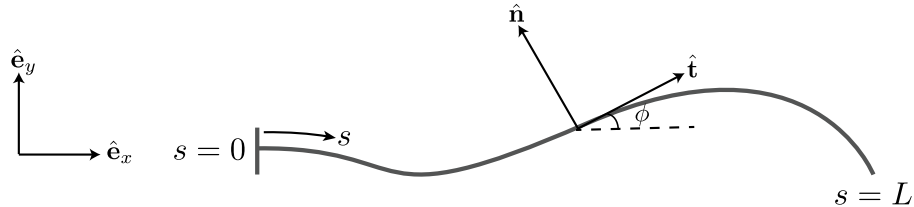


Figure 5.2: Schematic of an elastic rod of length L and arclength s that is clamped at $s = 0$. The rod is represented as a space curve in the (x, y) plane, which we parametrize by the tangent angle $\phi(s, t)$.

We parametrize the filament centerline with arc-length $s \in [0, L]$, and in the case of planar deformations, conformations are fully described by the tangent angle $\phi(s, t)$.

Expressions for the tangent and normal vectors to the curve follow as

$$\hat{\mathbf{t}} = \cos \phi \hat{\mathbf{e}}_x + \sin \phi \hat{\mathbf{e}}_y, \quad (5.1)$$

$$\hat{\mathbf{n}} = -\sin \phi \hat{\mathbf{e}}_x + \cos \phi \hat{\mathbf{e}}_y. \quad (5.2)$$

The Lagrangian marker $\mathbf{x}(s, t)$ describing points along the centerline can alternatively expressed as:

$$\mathbf{x}(s, t) = \mathbf{x}(0, t) + \int_0^s \hat{\mathbf{t}}(s', t) ds'. \quad (5.3)$$

The velocity at any point on the filament can be projected onto the tangent and normal, yielding $\mathbf{v} = v_t \hat{\mathbf{t}} + v_n \hat{\mathbf{n}} \equiv \partial_t \mathbf{x}$. It can be shown after manipulations that the velocity components are related as

$$\partial_s v_t = \partial_s \phi v_n, \quad (5.4)$$

$$\partial_s v_n = \partial_t \phi - \partial_s \phi v_t. \quad (5.5)$$

The elastica is subjected to general contact forces $\mathbf{F}(s, t) = \sigma \hat{\mathbf{t}} + N \hat{\mathbf{n}}$ as well as out of plane contact moments $\mathbf{M}(s, t) = M \hat{\mathbf{k}}$. These have both passive and active contributions resulting from elasticity and from molecular motor forces, which we discuss in Sec. 5.3.2. Previously in 2.2.3 we dervied force and torque balance inside an elastic rod in absence of inertia. Using that result we find:

$$\mathbf{f}_{vis} + \partial_s \mathbf{F} = \mathbf{0}, \quad (5.6)$$

$$M_s + N = 0, \quad (5.7)$$

where $\mathbf{f}_{vis}(s, t)$ is the viscous force density exerted by the fluid on the filament. The moment balance reduces to a scalar equation for planar deformations, and $\partial_s \mathbf{F} \equiv \mathbf{f}_e(s, t)$ is the internal force density resulting from elastic and active stresses.

Slender-body hydrodynamics: Given the assumption of slenderness $\epsilon \ll 1$, we model viscous stresses using non-local slender-body theory (SBT) [81,198–200] as discussed

in Chapter 2. The configuration-dependent mobility operator where \mathcal{M} can be split into two parts: $\mathcal{M} = \boldsymbol{\Lambda} + \mathbf{K}$. The first term $\boldsymbol{\Lambda}$, known as the local operator, can be represented in a simplified form for planar deformations and is given by:

$$\boldsymbol{\Lambda}[\mathbf{f}_e](s) = [(2 - c)\hat{\mathbf{n}}(s)\hat{\mathbf{n}}(s) - 2c\hat{\mathbf{t}}(s)\hat{\mathbf{t}}(s)] \cdot \mathbf{f}_e(s), \quad (5.8)$$

where $c = \log(\epsilon^2 e) < 0$ with $\epsilon = a/L$. By analogy with resistive force theory [201, 202] and for later convenience, we also introduce local anisotropic friction coefficients

$$\xi_{\parallel} = -\frac{1}{2c}, \quad \xi_{\perp} = \frac{1}{2 - c}, \quad (5.9)$$

which satisfy the well-known property: $\xi_{\perp}/\xi_{\parallel} \rightarrow 2$ as $\epsilon \rightarrow 0$. The second term \mathbf{K} in the mobility relation captures hydrodynamic interactions between distant parts of the filament as discussed in Chapter 2.3. In 2D we can represent it as follows:

$$\mathbf{K}[\mathbf{f}_e](s) = \int_0^L \left[\frac{\mathbf{I} + \hat{\mathbf{R}}(s, s')\hat{\mathbf{R}}(s, s')}{|\mathbf{R}(s, s')|} \cdot \mathbf{f}_e(s') - \frac{\mathbf{I} + \hat{\mathbf{t}}(s)\hat{\mathbf{t}}(s)}{|s - s'|} \cdot \mathbf{f}_e(s) \right] ds', \quad (5.10)$$

where $\mathbf{R}(s, s') = \mathbf{x}(s) - \mathbf{x}(s')$ and $\hat{\mathbf{R}} = \mathbf{R}/|\mathbf{R}|$. For the sake of simplicity, we also introduce the notations

$$u_t^d(s) = \mathbf{K}[\mathbf{f}_e](s) \cdot \hat{\mathbf{t}}(s), \quad u_n^d(s) = \mathbf{K}[\mathbf{f}_e](s) \cdot \hat{\mathbf{n}}(s). \quad (5.11)$$

Using these definitions along with relations (5.4)–(5.5), we can rewrite the equations of motion along the tangent and normal directions. After algebraic manipulations and using the fact that $\partial_s \hat{\mathbf{n}} = -\partial_s \phi \hat{\mathbf{t}}$, we arrive at:

$$\sigma_{ss} - \left(1 + \frac{\xi_{\parallel}}{\xi_{\perp}}\right) N_s \phi_s - N \phi_{ss} - \frac{\xi_{\parallel}}{\xi_{\perp}} \sigma \phi_s^2 = \xi_{\parallel} (\phi_s u_n^d - \partial_s u_t^d), \quad (5.12)$$

$$N_{ss} - \frac{\xi_{\perp}}{\xi_{\parallel}} N \phi_s^2 + \sigma \phi_{ss} + \left(1 + \frac{\xi_{\perp}}{\xi_{\parallel}}\right) \sigma_s \phi_s = \xi_{\perp} (8\pi\nu \phi_t - u_t^d \phi_s - \partial_s u_n^d), \quad (5.13)$$

$$M_s + N = 0, \quad (5.14)$$

which are statements of the tangential force, normal force and moment balances, respectively.

Boundary conditions: We assume the filaments have one fixed end at $s = 0$, and thus $v_t(0, t) = v_n(0, t) = 0$. On using the force balance in the tangential and normal directions at $s = 0$, this condition results in

$$(\sigma_s - N\phi_s) \Big|_{s=0} = 0, \quad (N_s + \sigma\phi_s) \Big|_{s=0} = 0. \quad (5.15)$$

The other end of the filament at $s = L$ is force- and torque-free, which translates to

$$\sigma(L, t) = N(L, t) = M(L, t) = 0. \quad (5.16)$$

For a clamped filament that cannot rotate about the fixed point we prescribe a fixed orientation of the tangent vector. Without loss of generality, we will assume that $\hat{\mathbf{t}}(0, t) = \hat{\mathbf{e}}_x$, and therefore

$$\phi(0, t) = 0. \quad (5.17)$$

We have yet to specify the nature of the active internal forces and induced moments that drive the filament dynamics. Next, we present the model for internal axoneme mechanics and for the kinematics of molecular motors that are responsible for spontaneous oscillations.

5.3.2 Forces, moment densities and motor kinetics

As a simplified model for the cross-linked flagellar bundle that composes the axoneme, we resort to a two-dimensional projection of the three-dimensional structure as illustrated in Figure 5.3. In the complete ‘9+2’ structure, the molecular motors connecting pairs of doublets lead to sliding forces that result in deformations. The structure of the axenomal cross-section, as depicted in Figure 5.1, involves a cyclic arrangement of the dyneins, and therefore motors on opposite sides of the axoneme operate antagonistically, as in a ‘tug-of-war’. To capture this process within a minimal framework, we follow previous

models [174, 175] and idealize the axoneme as a pair of two polar elastic filaments (+) and (−) separated by a constant distance a that are able to deform in tandem in the plane of motion. The centerline of this projected bundle is described by $\mathbf{x}(s, t)$ and the positions of the two filaments are given by $\mathbf{x}_\pm(s, t) = \mathbf{x}(s, t) \pm (a/2)\hat{\mathbf{n}}(s, t)$, where $\hat{\mathbf{n}}$ is the unit normal along the centerline.

Dynein motors extend from each filament, and bind with and walk along the opposite one, with the former acting as cargo. As the motors are activated, they push on both filaments and thereby exert tangential sliding forces $\pm f(s, t)$. These forces result in internal moments that can cause bending and induce an arc-length mismatch between the two filaments, known as the sliding displacement:

$$\Delta(s, t) = \int_0^s (|\partial_s \mathbf{x}_-| - |\partial_s \mathbf{x}_+|) ds' = a[\phi(s, t) - \phi_0], \quad (5.18)$$

where $\phi_0 = \phi(0, t) = 0$ for clamped boundary conditions. The relative sliding of the two filaments is not free, as it is resisted by nexin protein cross-linkers that act as linear springs and also contribute to the net internal shear force. Indeed, as mentioned previously, microtubules can actually slide apart in the absence of these linkers in demembraneted flagellar axonemes [176]. Following Oriola *et al.* [174], we model the sliding force density by coarse-graining the activity of the motors as

$$f(s, t) = \rho(n_+ F_+ + n_- F_-) - K\Delta. \quad (5.19)$$

Here, $\rho = \mathcal{N}/L$ is the mean density of motors along both filaments, and n_\pm are the fractions of motors on the (+) and (−) filaments that are in the bound state. F_\pm is the load exerted by individual (+) and (−) motors and K is the effective spring stiffness of the nexin cross-linkers.

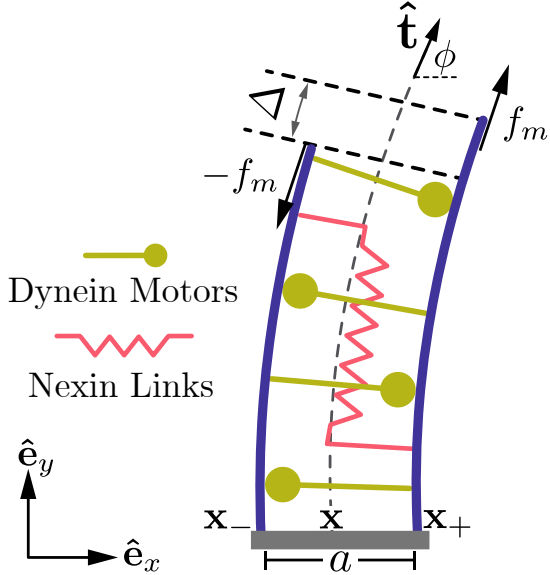


Figure 5.3: Schematic of the simplified two-dimensional projection of the axoneme. In this model, the axoneme is composed of two polar filaments x_+ and x_- and has centerline \mathbf{x} . Nexin links are shown as elastic springs that resist sliding Δ . Mechanical loads exerted by bound dynein motors result in an internal shear force density $\pm f(s, t)$ that acts in the opposite direction on the two filaments, generating an active internal moment.

By the law of action and reaction, the sliding forces $\pm f(s, t)$ are equal and opposite on both filaments, and thus the net active force on an axonemal cross-section is zero. However, an active internal moment is generated and competes against bending elasticity, yielding

$$M(s, t) = B\phi_s - aF, \quad (5.20)$$

where B is the net bending rigidity of the filament bundle and $F(s, t) = \int_s^L f(s', t)ds'$. The first term is the passive response from Euler-Bernoulli beam theory, while the second term captures the action of molecular motors. On inserting this expression in the moment balance Eq. (5.14), we obtain:

$$B\phi_{ss} + af(s, t) + N = 0, \quad (5.21)$$

where N is the contact force in the normal direction. This relation highlights the mechanism by which the internal force density generated from bound dynein motors induces internal moments that can cause bending and deformations of the bundle.

To complete the description of internal active forces, we must model motor binding kinetics as well as motor loads. The dynein kinetics is described by a two-state mechanochemical model consisting of bound and unbound dyneins, with a constant total number \mathcal{N} of dyneins (bound or unbound) on both filaments. A single motor can bind with the opposite filament with rate π and unbind with rate ϵ . The evolution of the bound motor populations is described as

$$\partial_t n_{\pm} = \pi_{\pm} - \epsilon_{\pm}. \quad (5.22)$$

The binding rate is proportional to the local fraction of unbound motors and given by $\pi_{\pm} = \pi_0(1 - n_{\pm})$, where π_0 is the characteristic rate constant. The unbinding rate of molecular motors is known to depend on the carried load [203]. In particular, experiments with kinesin motors have shown that the dissociation rate increases exponentially with F , and this functional dependence has previously been used in models of bidirectional cargo transport by molecular motors [204] and of dynein kinetics inside the axoneme [175]. Consistent with previous studies [174, 175], we thus express the detachment rate as $\epsilon_{\pm} = \epsilon_0 n_{\pm} \exp(\pm F_{\pm}/f_c)$, where f_c is a critical load beyond which rapid detachment takes place. We would like to emphasize, however, that the emergent filament dynamics explored in the following sections is insensitive to this functional choice, provided that the detachment rate increases sufficiently fast with the carried load. Following previous models [174, 204] and experiments [203], we also assume a linear force–velocity relationship for the molecular motors. At stall force f_0 , the motors are at complete rest, and the zero load velocity is v_0 . Intermediate loads can then be estimated by linear interpolation as $F_{\pm} = \pm f_0(1 \mp \Delta_t/v_0)$, where $\Delta_t = a\phi_t$ is the sliding velocity. With these assumptions, the

internal sliding force density of Eq. (5.19) becomes

$$f(s, t) = f_0 \rho \left(\bar{n} - \frac{\Delta_t}{v_0} \tilde{n} \right) - K \Delta, \quad (5.23)$$

where $\bar{n} = n_+ + n_-$ and $\tilde{n} = n_+ - n_-$. It is well known that the binding and unbinding of motors is a stochastic process due to the presence of intrinsic biochemical noise. In order to model this effect, we also incorporate a multiplicative noise term in Eq. (5.22) of the form $n^{\text{Br}}(s, t) = T_{\text{eff}} \delta(t - t') \delta(s - s')$, where T_{eff} is an effective temperature and where the noise is delta-correlated in both space and time. Including fluctuations and the expressions for the binding and unbinding rates, we rewrite the evolution equation for the fractions of bound motors as

$$\partial_t n_{\pm} = \pi_0 (1 - n_{\pm}) - \epsilon_0 n_{\pm} \exp \left[\frac{f_0}{f_c} (1 \mp \Delta_t/v_0) \right] + n^{\text{Br}}(s, t). \quad (5.24)$$

This completes the model for motor kinetics and internal forces. It is important to emphasize the two-way feedback that exists between filament geometry and dynamics and the kinetics of bound motors. Dynein activity causes internal shear and sliding of the filaments, which contributes to the active moment. In turn, the sliding displacement causes load-dependent binding and unbinding of motors and affects the magnitude of the internal shear force, possibly giving rise to filament oscillations.

5.3.3 Non-dimensionalization

We non-dimensionalize arc-length by L and time by the characteristic correlation time $\tau_0 = 1/(\epsilon_0 + \pi_0)$ of the dynein motors. The scale for internal elastic forces is given by the characteristic bending force B/L^2 , which implies $\mathcal{M}[\mathbf{f}_e] \sim B/L^3$, and finally the internal motor force density is scaled by ρf_0 . It is also evident from the expression of the sliding displacement that its appropriate scale is the axoneme diameter a . Non-dimensionalization of the governing equations results in four dimensionless parameters:

(a) $\text{Sp} = L(8\pi\nu/B\tau_0)^{1/4}$ is the sperm number that compares the characteristic time scale of relaxation of a bending mode to the motor correlation time. Smaller values of Sp describe short and rigid filaments. (b) $\mu = Ka^2L^2/B$ compares the elastic forces generated by the nexin links due to sliding to the characteristic magnitude of bending forces. (c) $\mu_a = a\rho f_0 L^2/B$ is the measure of motor activity (that is proportional to the active force) compared to bending forces. (d) $\zeta = a/(v_0\tau_0)$ compares the diameter of the filament bundle to the characteristic displacement due to motor activity.

With these scales, the dimensionless force density reads $f(s, t) = \bar{n} - \zeta \tilde{n}\Delta_t - (\mu/\mu_a)\Delta$, and the non-dimensionalized equations of motions are then given by

$$\sigma_{ss} - \left(1 + \frac{\xi_{\parallel}}{\xi_{\perp}}\right) N_s \phi_s - N \phi_{ss} - \frac{\xi_{\parallel}}{\xi_{\perp}} \sigma \phi_s^2 = \xi_{\parallel} (\phi_s u_n^d - \partial_s u_t^d), \quad (5.25)$$

$$N_{ss} - \frac{\xi_{\perp}}{\xi_{\parallel}} N \phi_s^2 + \sigma \phi_{ss} + \left(1 + \frac{\xi_{\perp}}{\xi_{\parallel}}\right) \sigma_s \phi_s = \xi_{\perp} (\text{Sp}^4 \phi_t - u_t^d \phi_s - \partial_s u_n^d), \quad (5.26)$$

$$\phi_{ss} + \mu_a f + N = 0. \quad (5.27)$$

The dimensionless stochastic equations for bound motor populations read:

$$\partial_t n_{\pm} = \eta(1 - n_{\pm}) - (1 - \eta)n_{\pm} \exp[f^*(1 \mp \zeta\Delta_t)] + \Lambda w_{\pm}, \quad (5.28)$$

where $\eta = \pi_0/(\epsilon_0 + \pi_0)$ is the duty ratio, $f^* = f_0/f_c$ is the ratio of the stall force to the characteristic unbinding force, w_{\pm} is a random vector drawn from a Gaussian distribution with zero mean and unit variance, and Λ is a numerical parameter characterizing the strength of biochemical noise. In order to solve the above equations numerically we use the expression for ϕ_t from Eq. (5.26) and insert it in the expression for the sliding velocity involved in the internal force density $f(s, t)$, which then enters the moment balance Eq. (5.27). On doing so, we obtain

$$\begin{aligned} \mu_a \zeta \tilde{n} & \left[N_{ss} - \frac{\xi_{\perp}}{\xi_{\parallel}} N \phi_s^2 + \sigma \phi_{ss} + \left(1 + \frac{\xi_{\perp}}{\xi_{\parallel}}\right) \sigma_s \phi_s \right] - \xi_{\perp} \text{Sp}^4 N \\ &= \xi_{\perp} \text{Sp}^4 (\phi_{ss} + \mu_a \bar{n} - \mu \phi) - \xi_{\perp} \mu_a \zeta \tilde{n} (u_t^d \phi_s + \partial_s u_n^d). \end{aligned} \quad (5.29)$$

The above system of equations is subject to boundary conditions (5.15), (5.16) and (5.17).

5.3.4 Numerical methods and parameter selection

We solve the system of governing equations numerically by discretizing the filament arc-length into $M - 1$ equal segments of size $\Delta s = L/(M - 1)$. Spatial derivatives are handled using a second order accurate finite difference scheme. Non-local terms arising from hydrodynamic interactions result in a dense linear system for the unknown tension σ and normal force N . To avoid this costly system inversion, we instead employ an iterative method. For a given filament conformation, we first solve for σ and N using Eqs. (5.25) and (5.29) with the non-local terms evaluated at the previous time step. This problem results in a band-diagonal linear system of size $2M \times 2M$ that can be solved at a cost of $\mathcal{O}(2M)$. While doing so we use zero velocity at the base and zero force at the end of the filament as boundary conditions. We then evaluate the non-local terms and re-compute the tension and normal forces. This process is repeated until convergence, and typically 3 to 4 iterations are required. Once σ and N are known, we use Eq. (5.26) to march forward in time. This is done by a second order accurate backward-difference scheme along with the clamped boundary condition at $s = 0$ and the moment free condition at $s = L$. The evolution equation for the bound dynein motors given by Eq. (5.28) is marched forward independently using an implicit Euler–Maruyama scheme, which is adequate given the stochastic term. The numerical parameter Λ characterizing the strength of noise in Eq. (5.28) is related to the effective temperature T_{eff} as $\Lambda = (T_{\text{eff}}/\Delta s \Delta t)^{1/2}$, where Δt is the simulation time step. Our numerical method scales linearly with the number of discretization points. In most results presented here, we use $M = 64\text{--}128$ and $\Delta t = 5 \times 10^{-4}\text{--}1 \times 10^{-5}$.

Table 5.1: Table listing the numerical values of the dimensional parameters as reported in various experiments.

Parameter	Numerical Value	Description
a	200 nm	Effective diameter of the axoneme [175]
L	50 μm	Length of human sperm flagellum [205]
B	$0.9\text{--}1.7 \times 10^{-21} \text{ N m}^2$	Bending rigidity of sea-urchin and bull sperm [175]
K	$2 \times 10^3 \text{ N m}^{-2}$	Nexin link stiffness for <i>Chlamydomonas</i> [174]
ξ_\perp	$10^{-3}\text{--}1 \text{ Pas}$	Normal drag coefficient in viscous media [174, 189]
f_0	1–5 pN	Stall force for motor dynamics [174]
f_c	0.5–2.5 pN	Characteristic unbinding force of the motors [206]
v_0	5–7 $\mu\text{m/s}$	Motor walking speed at zero load [206]
τ_0	50 ms	Correlation time of motor activity [174]
ρ	$10^3 \mu\text{m}^{-1}$	Mean number density of motors [174]

The model involves a fairly large number of parameters, many of which can be estimated from direct experimental measurements based on sperm flagella and the green alga *Chlamydomonas reinhardtii*. In most calculations and unless otherwise noted, we use the parameter values provided by Bayly and Wilson [189] and Oriola *et al.* [174], which are summarized in Table 5.1. Note that the motor correlation time, τ_0 , which sets the time scale in our model, is not known from measurements and must be guessed. Its chosen value results in a beating frequency of 10 Hz similar to a human spermatozoa [174]. Based on these values, we estimate the relevant dimensionless groups in Table 5.2. The sperm number Sp and activity number μ_a are found to have the widest ranges, allowing for various dynamical transitions and beating patterns as we explore next.

Table 5.2: Range of the dimensionless groups of the problem estimated using the parameter values of Table 5.1 .

Dimensionless number	Numerical value
$\text{Sp} \equiv L (\xi_{\perp}/B\tau_0)^{1/4}$	5–20
$\mu_a \equiv af_0\rho L^2/B$	$2 - 10 \times 10^3$
$\mu \equiv Ka^2L^2/B$	50–100
$f^* \equiv f_0/f_c$	2
$\zeta \equiv a/v_0\tau_0$	$\mathcal{O}(1)$

5.4 Spontaneous filament oscillations

In this section, we systematically explore the parameter space through numerical simulations of the non-linear equations and characterize transitions to spontaneous oscillations and beating patterns. A summary of the various dynamical regimes and beating patterns in the (Sp, μ_a) parameter space is presented as a phase chart in Figure 5.4.

5.4.1 Linear stability and geometrically linear regime

Before analyzing dynamics far from equilibrium, we briefly review results of the linear stability analysis of Oriola *et al.* [174] and discuss the geometrically linear regime of small curvature. The stability analysis reveals that for a given sperm number Sp there exists a critical activity level μ_a^{crit} above which the filament undergoes a Hopf bifurcation. Above the bifurcation, a linear mode becomes unstable and grows exponentially while oscillating with a characteristic frequency ω . The critical activity was reported to increase

almost linearly with sperm number [174] as also observed in our simulations in Figure 5.4. Note that Oriola *et al.* [174] used local resistive force theory instead of non-local slender body hydrodynamics, and thus the instability threshold they predict differs quantitatively from the one we observe. Nonetheless, our method was found to reproduce their results if we neglect the non-local operator \mathbf{K} and choose $\xi_{\perp}/\xi_{\parallel} = 2$ in the local mobility tensor. An increase in sperm number can be interpreted as an increase in viscosity resulting in larger viscous drag forces. As a result, a higher motor activity is required to induce an instability [207]. One can also appreciate this result based on reduced-order models of molecular-motor-induced oscillations [194, 208]. In these minimal models, the filament backbone is represented by a single lumped coordinate X and elasticity by a spring constant k with a viscous damping of strength ζ . Larger sperm number can then be interpreted as increased damping, resulting in an increased activity threshold for the onset of spontaneous oscillations.

Close to the bifurcation, the instability induces a traveling wave that propagates along the filament from tip to base (retrograde propagation). This direction of propagation is a common feature of linearized sliding control models with clamped boundary conditions [183, 190, 192, 193], but is inconsistent with the well-known beating patterns of swimming spermatozoa, which exhibit anterograde wave propagation from base to tip. It is important to point out that, unlike curvature control models, the present formulation has no inherently preferred direction of wave propagation, which instead is selected spontaneously by linear and nonlinear feedback mechanisms [175, 177]. Our results are consistent with linear predictions [174], which also show tip-to-base propagation near the Hopf bifurcation. Interestingly, most previous studies have focused on the geometrically linear or weak activity regimes and have overlooked nonlinear couplings. It is unclear *a priori* whether linear results adequately describe far-from-equilibrium dynamics, where

the effects of nonzero tension and geometric nonlinearities become significant.

5.4.2 Large deformations in the nonlinear regime

Further away from the bifurcation, our numerical simulations of the fully nonlinear sliding-control model reveal a second transition to base-to-tip (anterograde) wave propagation. This transition occurs at approximately twice the critical level of activity required to trigger the first onset of oscillations: it is a truly nonlinear phenomenon that involves saturation of motor kinetics in the presence of large deformations and internal tension forces, and is beyond the scope of previously studied linearized [174] or weakly nonlinear [192] models. It is worth noting that Bayly and Wilson [190] did study nonlinear dynamics using a variant of the sliding-control model presented here. They were unable to observe anterograde propagation even at finite amplitudes, and we attribute this discrepancy to their model for the sliding force density, which did not involve feedback from nexin links, and to their specific choice of dynein kinetics, which did not allow for self-sustained saturation. The transition from retrograde to anterograde wave propagation with increasing motor activity occurs through a narrow transitional band of intermediate states (gray region in the phase chart of Figure 5.4), whose width varies slightly with sperm number. The dynamics in this regime appears chaotic and combines standing waves with waves that switch quasi-periodically between the two directions of propagation. We also note that the emergence of anterograde wave propagation is primarily due to the geometric nonlinearities and happens even in the absence of non-local hydrodynamic interactions.

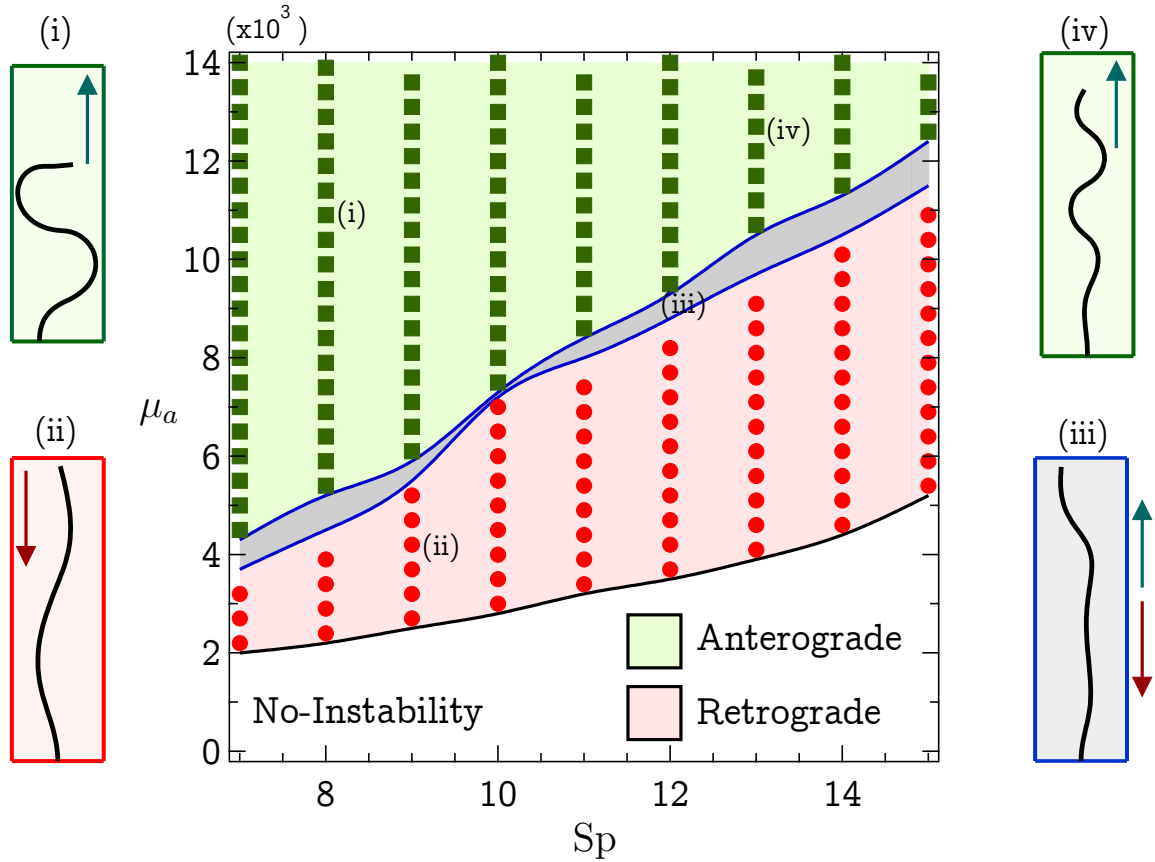


Figure 5.4: Phase chart highlighting the various dynamical transitions and beating patterns in the (Sp, μ_a) parameter space. Waveforms on both sides show characteristic filament conformations, where the arrows indicate the direction of wave propagation. Simulations for $\mu = 100$, $\zeta = 0.3$ and $\eta = 0.14$.

In addition to changes in the direction of wave propagation, it is apparent from the characteristic waveforms shown in Figure 5.4 that both sperm number and motor activity affect the qualitative features of the beating patterns. We explore these variations in Figure 5.5, showing the dependence of amplitude, wavelength and frequency of the waveforms as a function of μ_a for two different values of Sp . To measure wavelength, we determine the zero crossings of a given waveform, measure the distance between them as shown in the inset of Figure 5.5(b), and average it over one period of motion to obtain λ . In the retrograde regime, the amplitude and wavelength both increase monotonically with activity,

while the beating frequency decreases. The second transition to anterograde propagation causes all quantities to change abruptly as seen in Figure 5.5. After a significant reduction across the transition, the amplitude starts to grow again with activity. Since the filament is inextensible, this increase in amplitude is accompanied by a slight decrease in wavelength. The frequency of oscillations increases with the transition to anterograde waves and then decreases monotonically with μ_a . Recall that all times in the model are scaled by the characteristic motor correlation time τ_0 . We find that setting its value to $\tau_0 = 50$ ms produces dimensional beating frequencies in the range of $f \sim 6 - 14$ Hz.

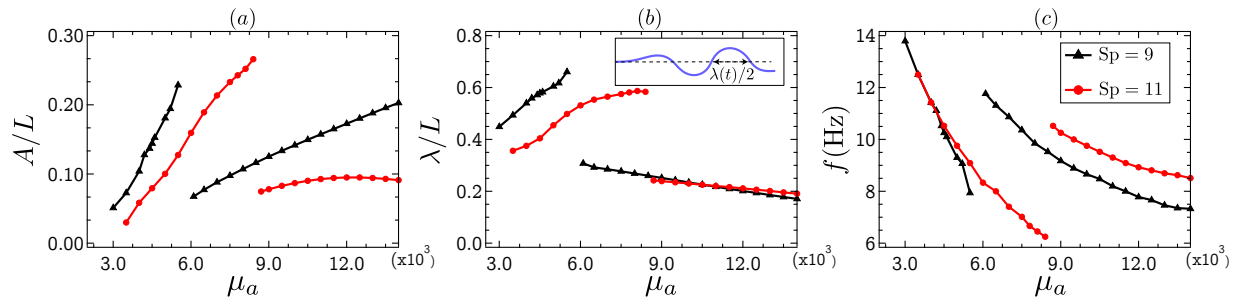


Figure 5.5: Dependence of (a) dimensionless amplitude, (b) dimensionless wavelength and (c) frequency of the beating patterns on motor activity μ_a for two values of the sperm number Sp . The dimensional frequency assumes the choice of $\tau_0 = 50$ ms for the motor correlation time. Jumps in the data are associated with the transition from retrograde to anterograde wave propagation. Simulations were performed with $\mu = 100$, $\zeta = 0.3$ and $\eta = 0.14$.

At a fixed μ_a , increasing Sp tends to reduce the amplitude as viscous resistance becomes more important. It may seem counter-intuitive that the wavelength of oscillations varies very little with Sp in the anterograde regime while the amplitudes differ significantly. This stems from the fact that, at low sperm numbers and high activity levels, the oscillations result in strong swaying motions as shown in Figure 5.4(i). These large angular oscillations contribute to the large amplitudes observed in Figure 5.5(a) for $Sp = 9$. A typical waveform resembling that of sperm cells is shown in Figure 5.6(a) and was obtained for $Sp = 12$. In the simulation shown, waves propagate from base to tip with a frequency

of $f \approx 8.8$ Hz, which is consistent with that of spermatozoa.

5.4.3 Asymmetric beating patterns

The same ‘9+2’ microtubule doublet structure that is found in sperm flagella also appears in pair in the bi-flagellate alga *Chlamydomonas reinhardtii*, which swims in a breaststroke fashion. It is also present in the ciliary structures that cover epithelial cells as well as unicellular organisms such *Paramecium* where they beat in asymmetric whipping patterns. The asymmetric beating of cilia is key to metachronal co-ordination in ciliary carpets that are useful for micro-organism motility as well as pumping and transport of fluid in the body. We now discuss modifications of the sliding control model that allow it to produce asymmetric beating patterns qualitatively similar to those of cilia and *Chlamydomonas*.

Ciliary beating: biased kinetics

The generation of asymmetric beat patterns in models for cilia has previously been approached in several ways. A geometric switch mechanism was proposed in [184, 209] with a detailed model of internal nexin links exerting forces on the microtubules that produced spontaneous oscillations of the filament. Dynein activation was initiated based on local microtubule curvature, allowing for asymmetric beats with a typical frequency of $f \sim 50 - 100$ Hz. A two-state model of molecular motors [194] was used in [195] to generate spontaneous oscillations close to the bifurcation limit, where an external flow was used to break the symmetry of beating. Another set of models with an internal ‘engine’ that coarse-grains dynein activity into a geometric-conformation-driven shear force was proposed in [208, 210] to generate cilia-like beating. Most recently, it was shown [211] that geometric constraints with a dynamical law for tension can also generate asymmetric

ciliary beating patterns. Most of these approaches, however, have not included detailed motor kinetics. Here, we show that asymmetric beating patterns that resemble those of cilia can be obtained within our sliding-control model through a biased dynein kinetics. This is inspired by the recent continuum formulation of Bayly and Wilson [189] of the geometric-clutch model [188], where a biased attachment-detachment probability was used to generate *Chlamydomonas*-like breaststrokes.

Biased kinetics is simply achieved by specifying distinct values for the characteristic binding and unbinding rate constants π_0^\pm and ϵ_0^\pm on both filaments. The actual binding and unbinding rates are thus written as

$$\pi_\pm = \pi_0^\pm(1 - n_\pm), \quad \epsilon_\pm = \epsilon_0^\pm n_\pm \exp(F_\pm/f_c). \quad (5.30)$$

This bias in rates causes motors on one side of the model axoneme to detach faster than on the other side, resulting in asymmetric bending. The new characteristic motor correlation timescale is now defined as $\tau_0 = 1 / [\langle \pi_0 \rangle + \langle \epsilon_0 \rangle]$, which involves the mean binding and unbinding rates:

$$\langle \pi_0 \rangle = \frac{\pi_0^+ + \pi_0^-}{2}, \quad \langle \epsilon_0 \rangle = \frac{\epsilon_0^+ + \epsilon_0^-}{2}. \quad (5.31)$$

Simulating cilia-like beating patterns requires adjusting parameter values. Cilia come in a variety of lengths in the range of $L \sim 4\text{--}20 \mu\text{m}$ [184], but are typically shorter than human sperm flagella. We choose a bending rigidity of $B \sim 5 \times 10^{-23} \text{ N m}^2$, which is slightly larger than that reported in [210]. The characteristic time scale $\tau_0 \approx 40 \text{ ms}$ is chosen to produce a dimensional beating frequency of $f \sim 10\text{--}20 \text{ Hz}$, which is typical of muco-ciliary transport [212]. With a choice of $L \approx 8 \mu\text{m}$, we estimate the typical sperm number to be $\text{Sp} \sim 2\text{--}3$. A typical waveform produced with these parameter is shown in Figure 5.6(b), and is characterized by distinct power and recovery strokes with curvature variations that propagate from base to tip. The waveform shown , which captures the salient features of ciliary beats, oscillates at a frequency of $f \approx 13 \text{ Hz}$.

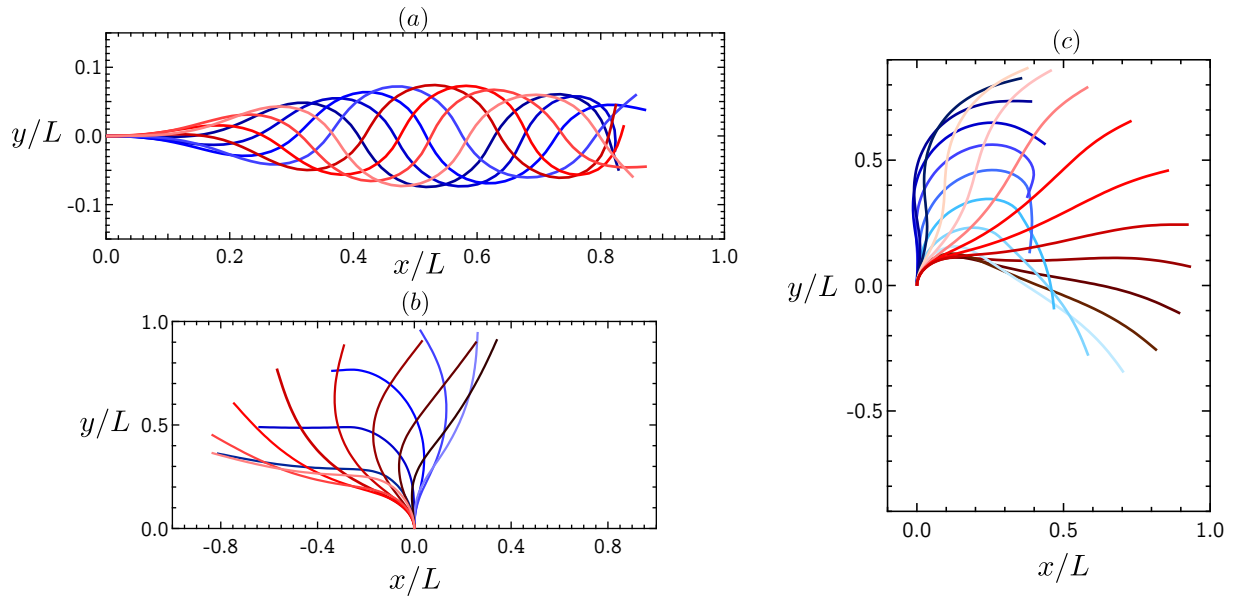


Figure 5.6: Overlaid characteristic waveforms at different time instants over the course of one beating period: (a) Symmetric sperm-like beat. Parameters: $Sp = 12$, $\mu_a = 12 \times 10^3$ and $\mu = 100$. (b) Asymmetric cilia-like beat obtained with biased dynein kinetics. Parameters: $Sp = 2.5$, $\mu_a = 2 \times 10^3$, $\mu = 90$, $(\pi_0^+, \epsilon_0^+) = (0.17, 0.73)$ and $(\pi_0^-, \epsilon_0^-) = (0.25, 0.75)$. (c) Asymmetric beating pattern resembling *Chlamydomonas*, obtained with biased kinetics in presence of both sliding and curvature control. Parameters: $Sp = 2.2$, $\mu_a = 1.5 \times 10^3$, $\mu = 80$, $f^* = 1.9$, $(\pi_0^+, \epsilon_0^+) = (0.24, 0.76)$, $(\pi_0^-, \epsilon_0^-) = (0.39, 0.61)$, $\kappa^0 = -2.0$ and $\kappa_c = 12$.

Breaststroke patterns: curvature control

As they perform their breaststroke, the two flagella of *Chlamydomonas* also undergo asymmetric patterns, with distinctly different waveforms from those of cilia. There have been fewer attempts in simulating these patterns. A modified version of the geometric-clutch mechanism was used in [213] that involved force-velocity relationships allowing for asymmetric flagellar beats similar to *Chlamydomonas*. Further developments of the geometric-clutch model [189] with excitable dynein kinetics were able to reproduce breaststroke-like beating patterns. Recently, Sartori *et al.* [187] analyzed the axonemes of both *wild-type* and *mbo2* strains of *Chlamydomonas*. Through Fourier decomposition of waveforms and a numerical fitting procedure, they found that sliding control provides a poor fit for the

waveform. Instead, curvature-control mechanisms provide the best fit to experimental data. Quite surprisingly, they noted that it is the rate of change of curvature that most likely controls the dynein activity. They also reported that the flagella have a non-zero static mode, suggesting an intrinsic curvature. However, their model neglected spatial variations of the motor control mechanism by non-uniform dynein distributions.

Our approach to capturing the beating patterns of *Chlamydomonas* is qualitative and extends the model discussed above for cilia. In addition to biased kinetics, we now also incorporate spontaneous filament curvature as well as a direct feedback from curvature on the dynein kinetics, whose detachment rate we model as

$$\epsilon_{\pm} = \epsilon_0^{\pm} n_{\pm} \exp(F_{\pm}/f_c \pm \kappa/\kappa_c), \quad (5.32)$$

where $\kappa(s, t)$ is the local curvature and κ_c is the critical value beyond which motors start to unbind. We set a constant non-zero intrinsic curvature $\kappa_0 = \phi_s^0$ that allows the flagella to spontaneously bend in absence of dynamic forces from the motors. With these modifications, the sliding displacement is now calculated from this reference configuration as $\Delta(s, t) = \phi(s, t) - \phi^0(s) = \phi(s, t) - \kappa_0 s$.

A typical waveform obtained with this model is shown in Figure 5.6(c) and resembles that of a wild-type *Chlamydomonas* flagellum. Parameters for this case were estimated as follows. *Chlamydomonas reinhardtii* has a typical body size of $7 - 10 \mu\text{m}$ with two flagella of length $10 - 12 \mu\text{m}$ [214]. The bending rigidity of the axoneme is estimated to be $B \sim 5.8 \times 10^{-22} \text{ N m}^2$. With these values, our numerical experiments indicate that waveforms of the type shown in Figure 5.6(c) are possible for $\text{Sp} \sim 2 - 3$. Using a characteristic time scale of $\tau_0 \approx 40 \text{ ms}$, we observe a beating frequency $f \sim 12 - 15 \text{ Hz}$, which is lower than the typical frequency of $50 - 60 \text{ Hz}$ observed in experiments.

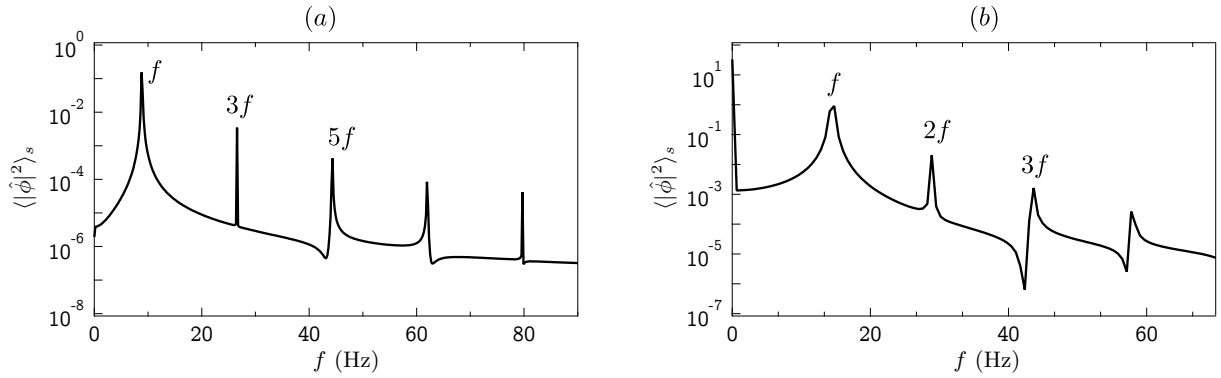


Figure 5.7: Power spectral density $\langle |\hat{\phi}|^2 \rangle_s$ of the averaged tangent angle for: (a) a sperm-like symmetric waveform and (b) *Chlamydomonas*-like breaststroke. Parameters are the same as in Figure 5.6(a, c).

5.5 Waveform analysis

5.5.1 Tangent angle dynamics and motor populations

We provide more quantitative details on the various waveforms of Figure 5.6 by analyzing tangent angle and motor population dynamics. Following Sartori *et al.* [173], we first present results on the power spectrum of the mean tangent angle, which is defined as $\langle \phi(t) \rangle_s = \int_0^L \phi(s, t) ds$. We show its power spectral density $\langle |\hat{\phi}|^2 \rangle_s$ for sperm-like and *Chlamydomonas*-like beats in Figure 5.7, where we observe distinct peaks at the various harmonics of the fundamental frequency f . In the case of symmetric sperm-like beats, only odd harmonics appear in the spectrum, which is a direct consequence of the symmetry property $\phi(s, t + T/2) = -\phi(s, t)$ where $T = 1/f$ is the period of oscillation. The *Chlamydomonas* waveform exhibits both odd and even harmonics, including a peak at zero frequency that points to the static mode of deformation $\phi^0(s)$ induced by the imposed spontaneous curvature. The spectrum produced by our model is qualitatively very similar to that measured in wild-type *Chlamydomonas reinhardtii* [187].

More details on the tangent angle and motor population dynamics are provided in

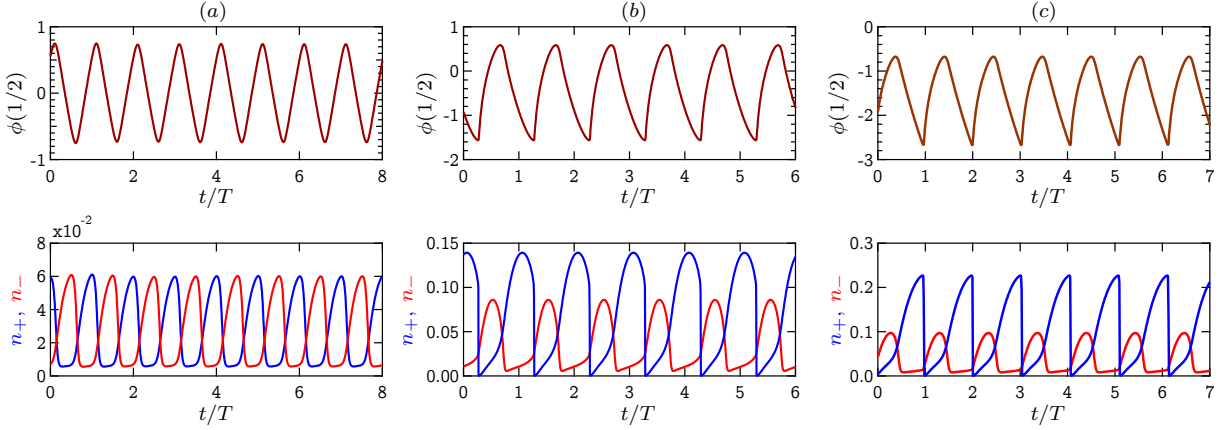


Figure 5.8: Tangent angle and motor population dynamics in the case of (a) sperm-like, (b) cilia-like and (c) *Chlamydomonas*-like beating patterns. The top panel shows the evolution of the tangent angle $\phi(s, t)$ measured at the midpoint of the filament ($s = 1/2$). The bottom panel shows the evolution of corresponding bound motor populations $n_+(s, t)$ and $n_-(s, t)$, also evaluated at the midpoint. Parameters are the same as in Figure 5.6.

Figure 5.8, where we plot ϕ and n_{\pm} at the filament midpoint ($s = 1/2$) as functions of time for the three beating patterns of Figure 5.6. These quantities were previously reported by Oriola *et al.* [174] close to the initial Hopf bifurcation, where the tangent angle and bound motor distributions were found to have similar waveforms with a constant phase difference. In the nonlinear regime, these waveforms start to differ as highlighted in Figure 5.8. The case of sperm-like beats in Figure 5.8(a) is characterized by a symmetric waveform for ϕ , which shares striking similarities with the experimental measurements of Riedel-Kruse *et al.* [175]. The two antagonistic motor populations have identical phase-shifted evolutions, which is expected for symmetric beats. They also show cusp-shaped oscillations that are characteristic of far-from-equilibrium dynamics [194, 208]. Remarkably, we find that only a fairly small fraction of bound dyneins is required to produce oscillations [174]. Figures 5.8(b,c) show the dynamics for ciliary and breaststroke patterns, respectively, and look qualitatively different from the case of sperm. In particular, the tangent angle evolution shows sharp cusps, with distinct rates of growth and decay that are indicative of the asym-

metric power and recovery strokes. The cusps in the dynamics of ϕ are accompanied by abrupt changes in the bound dynein populations, with n_+ and n_- now showing distinct waveforms as a result of biased kinetics. It is useful to recall that the kinetics of dynein motors in our model does not account for any form of motor transport along the arc-length, and as a result sharp changes in bound motor fractions are permissible when the local rate of attachment changes sign. It is likely that some amount of diffusion is present in biological systems and would somewhat smoothen motor population dynamics [215].

5.5.2 Reduced-order dynamics and limit cycles

The set of partial differential equations governing the evolution of the tangent angle $\phi(s, t)$ can be interpreted as an infinite dimensional dynamical system. As previously discussed, this dynamical system undergoes a Hopf bifurcation with increasing activity, leading to limit-cycle oscillations. In the standard analysis of Hopf bifurcations [216], limit cycles are typically described in terms of a characteristic radius r and a phase χ that grows linearly with time. This suggests seeking a lower-dimensional approximation of the full dynamical system that coarse-grains the dynamics into a simpler oscillator while retaining its essential features. Several studies of hydrodynamic synchronization have proposed similar approaches [4, 217, 218]. Here, we apply tools from Principal Component Analysis (PCA) to describe the waveforms, as was previously done in the past to analyze flagellar beats [174, 196, 219]. We restrict our analysis to sperm and ciliary beating patterns, as the breaststroke waveforms reveal very similar results as cilia.

A spatiotemporal representation of the beating patterns is first obtained in Figure 5.9(*a, d*) where we plot the tangent angle $\phi(s, t)$ as a function of both s and t . These so-called ‘kymographs’ are qualitatively similar to those obtained experimentally for both sperm and cilia, and clearly highlight the periodic nature of the dynamics, with bending

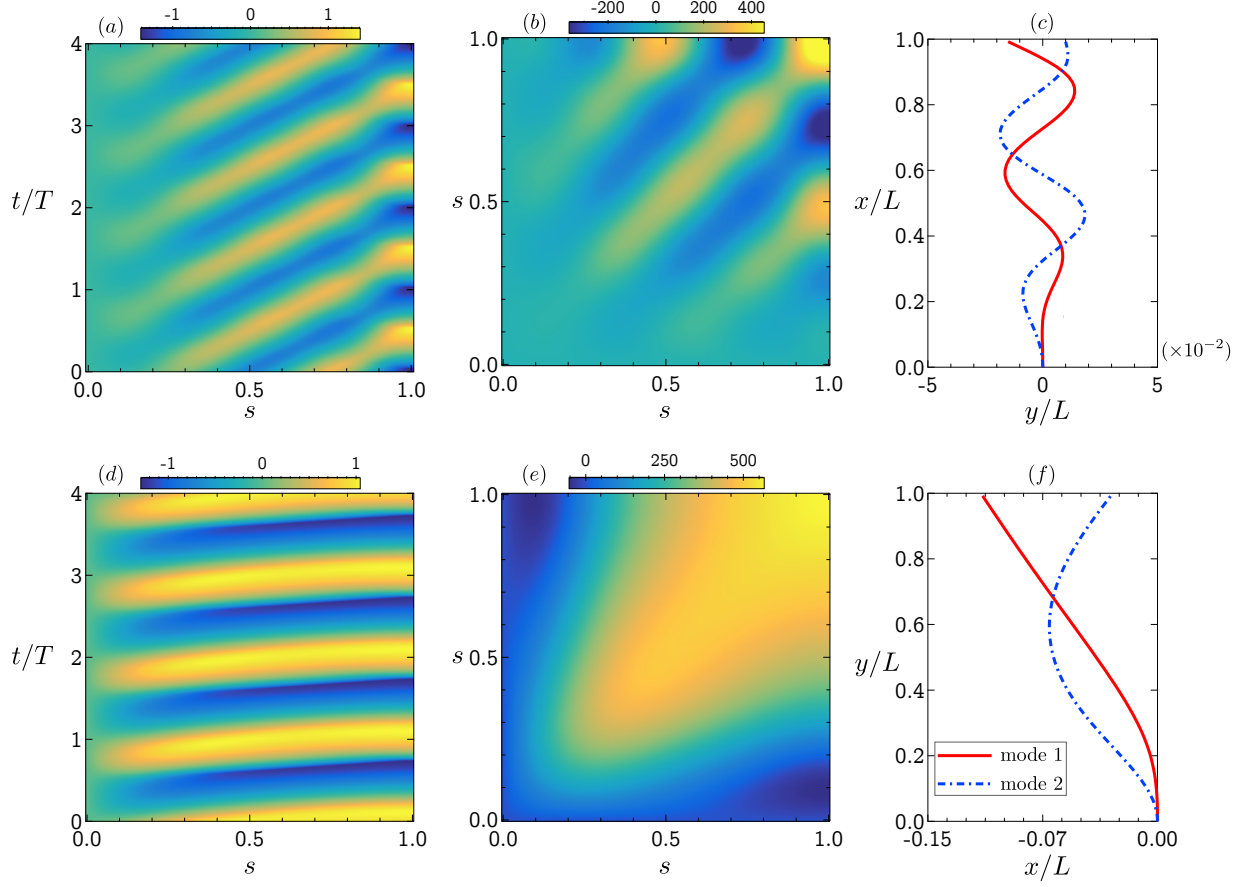


Figure 5.9: The first row shows: (a) the kymograph, (b) the covariance function C , and (c) the two dominant mode shapes from PCA in the case of a symmetric sperm-like beat. The bottom row (d, e, f) shows the same for the ciliary beating pattern. Parameters are identical to Figure 5.6(a, b).

waves that propagate from base ($s = 0$) to tip ($s = 1$). To further characterize deformations, we first define the covariance function $C(s, s')$ as

$$C(s, s') = \int_0^T \int_0^T [\phi(s, t) - \langle \phi(s, t) \rangle_t] [\phi(s', t') - \langle \phi(s', t') \rangle_{t'}] dt dt', \quad (5.33)$$

where $\langle \phi(s, t) \rangle_t = \frac{1}{T} \int_0^T \phi(s, t) dt$ is the time average of the tangent angle over one period and $C(s, s')$ is symmetric with respect to s and s' by construction. It is depicted in Figure 5.9(b, e) for both sperm and cilia waveform. In both cases, strong correlations are observed near the main diagonal, which are indicative of the finite bending stiffness [174,

196]. In the case of sperm-like beats in Figure 5.9(b), negatively correlated regions appear at a distance of $s = \lambda/2$ away from the diagonal, which is characteristic of propagating bending waves and provides another estimate of the wavelength. The number of local maxima in Figure 5.9(b) is accounted by the wavenumber of the traveling waves [174]. Close to the Hopf bifurcation, the number of local maxima decreases with increasing activity; however, as discussed previously in Figure 5.5, this behavior is not necessarily true in the nonlinear regime where abrupt transitions in wavenumbers can occur. Interestingly, we do not observe any negative correlations in the case of ciliary waveforms Figure 5.9(e), where the covariance instead systematically decays away from the diagonal.

To obtain a reduced-order representation of the dynamics, we apply PCA, which relies on the spectral decomposition of the covariance in terms of orthogonal deformation eigenmodes $\psi_n(s)$ with corresponding eigenvalues σ_n :

$$C(s, s') = \sum_{n=1}^{\infty} \sigma_n \psi_n(s) \psi_n(s'). \quad (5.34)$$

These modes are determined numerically by discretizing arclength into $M - 1$ segments and evaluating the covariance by quadrature. This produces an $M \times M$ symmetric positive matrix $C(s_i, s_j)$, which has real positive eigenvalues $\sigma_1 \geq \sigma_2 \geq \dots \geq \sigma_M > 0$ and real orthogonal eigenvectors describing fundamental modes of deformation. The first few eigenmodes are expected to capture the dominant spatial features of the waveforms, and in all the beat patterns considered here we find that truncating Eq. (5.34) after two terms provides a good approximation with less than 4% error [196]. Waveforms at any instant can now be approximated as a linear combination of eigenmodes. In the spirit of dimensional reduction [220], we propose an approximate representation in terms of the two dominant modes:

$$\phi(s, t) \approx \phi^0(s) + \beta_1(t)\psi_1(s) + \beta_2(t)\psi_2(s), \quad (5.35)$$

where $\phi^0(s)$ is the mean filament shape. The two coefficients $\{\beta_1, \beta_2\}$, known as ‘shape

scores' [196], capture the temporal evolution of the fundamental modes and can be calculated numerically by least-squares minimization. The two dominant PCA modes $\psi_1(s)$ and $\psi_2(s)$ are depicted in Figure 5.9(c) and (f) for sperm and ciliary beats.

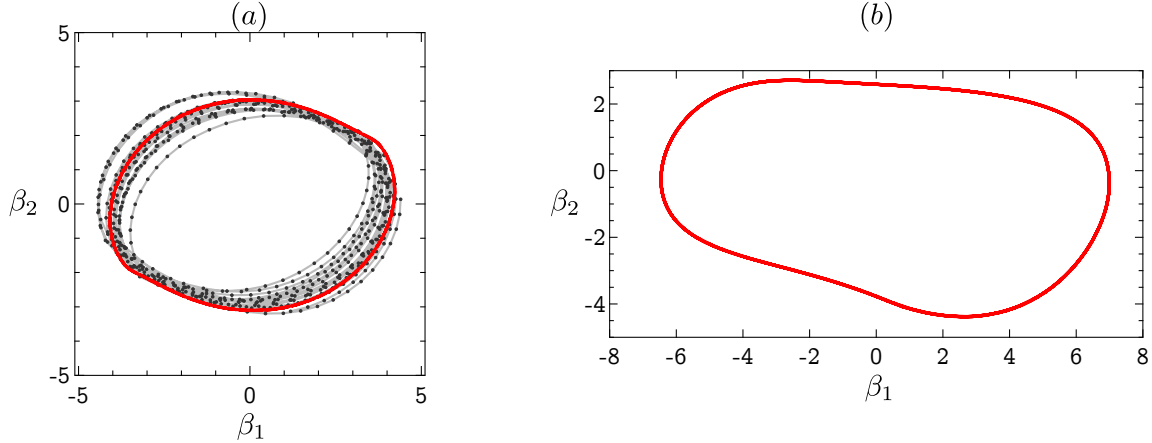


Figure 5.10: Limit cycle representation for (a) sperm-like and (b) ciliary beating patterns. The red curves show the deterministic limit cycles. In panel (a), the gray points show deviations from the deterministic cycle due to biochemical noise.

Within the approximation of Eq. (5.35), the temporal dynamics of a beating filament is represented as a trajectory in the two-dimensional phase space of $\{\beta_1, \beta_2\}$, where periodic waveforms are described by limit cycles. Figure 5.10(a) shows the reconstructed limit cycle for the symmetric sperm-like beat, both in the absence and presence of biochemical noise. In the absence of noise, the limit cycle has a characteristic shape with axial symmetry, which is more regular than that previously obtained close to the bifurcation limit [174]. As expected, biochemical noise leads to deviations from this periodic trajectory, with the system randomly exploring a band of possible states surrounding the deterministic cycle, as also seen in experimental waveforms [196, 219]. The deviations from the deterministic cycle are found to be non-uniform along the cycle, suggesting that certain filament conformations are more susceptible to noise than others. This curious feature is also observed experimentally [219]. The limit cycle for the cilia-like waveform is shown in

Figure 5.10(b) and is strikingly different, with an elongated asymmetric shape resulting from the asymmetry of the beating pattern.

5.6 Flow fields and fundamental singularities

5.6.1 Instantaneous and time-averaged flow fields

We now proceed to analyze the flow fields generated by the beating filaments and their descriptions in terms of fundamental singularities of Stokes flow. In the Stokes regime, the velocity at any point \mathbf{x} in the fluid is simply obtained in terms of the force distribution along the filament. In dimensionless form, it reads

$$\mathbf{u}(\mathbf{x}, t) = \frac{1}{\text{Sp}^4} \int_0^1 \mathbf{G}(\mathbf{x}, \mathbf{x}_0) \cdot \mathbf{f}_e(s_0, t) ds_0, \quad (5.36)$$

where $\mathbf{x}_0 = \mathbf{x}(s_0, t)$ is the Lagrangian point parametrized by arclength s_0 along the filament, $\mathbf{f}_e(s_0, t)$ is the local force per unit length exerted by the filament on the fluid, and $\mathbf{G}(\mathbf{x}, \mathbf{x}_0)$ is the appropriate Green's function scaled by $1/(8\pi\nu L)$. In free space, \mathbf{G} is simply given by the Oseen tensor. We also consider the case of a filament clamped against a flat wall, for which we use Blake's solution [221] for a point force next to a no-slip boundary. Note that the description of the disturbance flow field in terms of point forces in Eq. (5.36) becomes inaccurate very close to the filaments, where it can be improved using a distribution of source doublets [81] that scale as ϵ^2/r^3 , where r is distance from the filament and ϵ is the aspect ratio. This correction, however, only modifies the flow in the close vicinity of the filaments and does not alter the large-scale features of the disturbance fields.

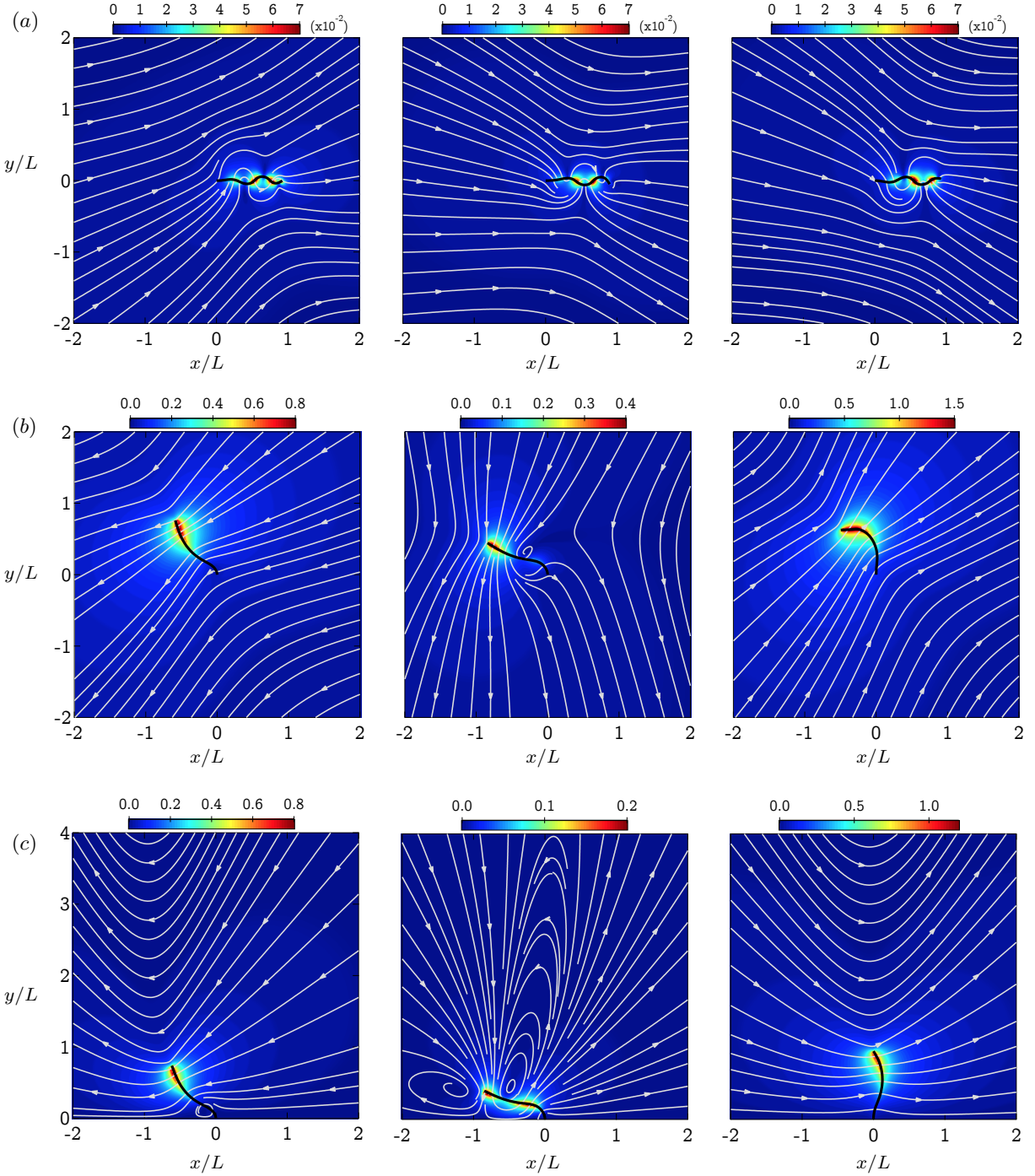


Figure 5.11: Magnitude and streamlines of the instantaneous velocity field obtained using Eq. (5.36) for three representative cases: (a) sperm-like beating pattern in free space, (b) ciliary beat in free space, and (c) ciliary beat against a no-slip wall at $y = 0$. The three columns correspond to three time instants during one period of oscillation.

Snapshots of instantaneous flows fields at three instants over the course of one beating period are shown in Figure 5.11, where we consider both sperm and ciliary beats in free space, as well as a cilium next to a no-slip wall. As expected, velocities are largest close to the filament, with maximum values attained near the inflection points of the waveform in the case of sperm, and near the tip of the filament in the case of cilia. In free space, the flow field away from the filament resembles the well-known Stokeslet flow field, which decays as $1/r$ in three dimensions. This does not come as a surprise as the filaments are not force-free in our model: in an experiment on spermatozoa, the net force imparted by the flagellum would instead balance the drag on the sperm head, resulting a net dipolar flow decaying as $1/r^2$. The case of a cilium next to a no-slip wall is shown in Figure 5.11(c) and exhibits a qualitatively different flow field, with the appearance of recirculation regions for certain conformations [222]. In this case, the Stokeslet contribution induced by the filament is canceled by the presence of the wall, resulting in a net flow that is either dipolar or quadrupolar, depending on the orientation of the applied force [221]: for a point force oriented parallel to the wall, the flow field is dipolar with a characteristic $1/r^2$ decay, while it is quadrupolar for a point force oriented perpendicular to the wall with a far-field decay of $1/r^3$.

These observations are reported in Figure 5.12, showing the time-averaged velocity fields for the same beating patterns, as well as the spatial decay of the velocity magnitude. Both cases in free space resemble Stokeslet flows and indeed exhibit a far-field decay of $1/r$. In the case of the ciliary beat above a no-slip boundary, the flow has a more complex structure with a recirculation bubble next to the wall, and also shows a much slower decay of $1/r^3$, which suggests that on average the net force exerted by the filament is normal to the wall [4].

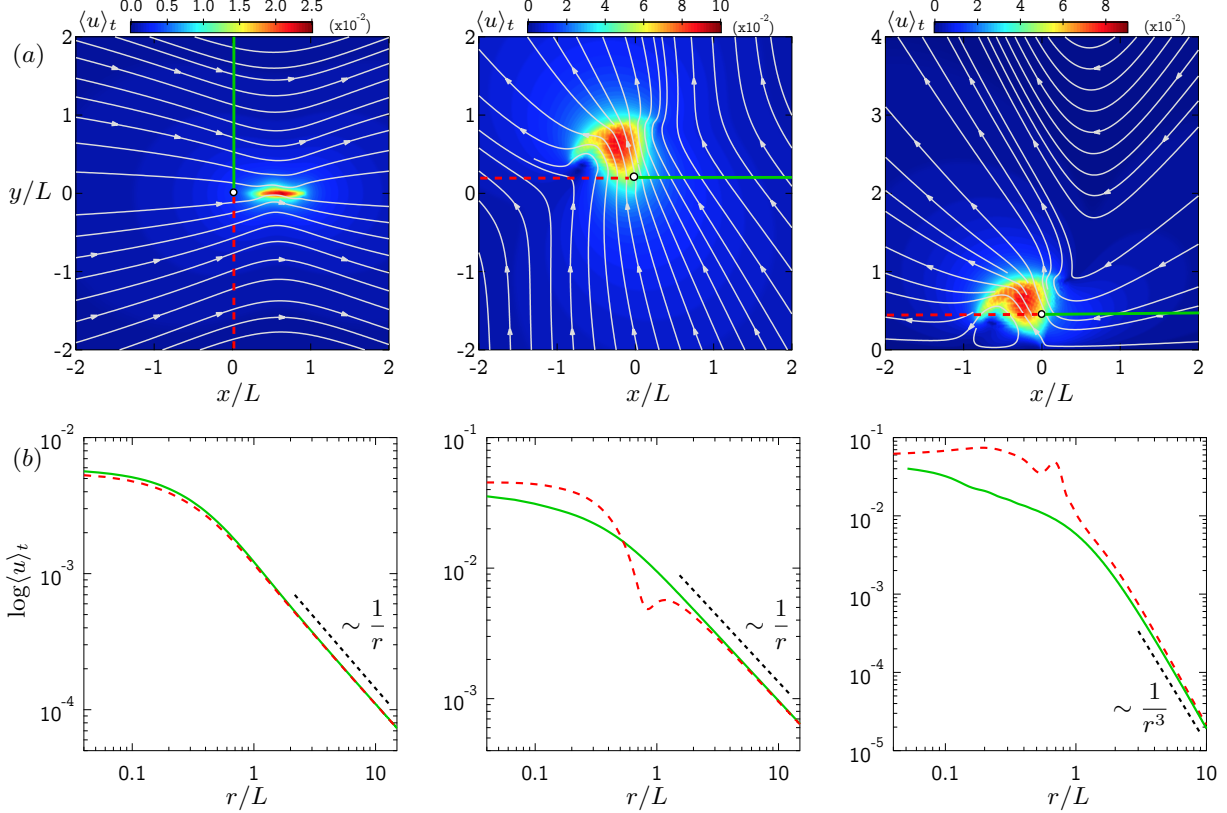


Figure 5.12: (a) Streamlines and magnitude of the time-averaged velocity field $\langle u \rangle_t$ for the three cases shown in Figure 5.11. From left to right: sperm in free space, cilium in free space, and cilium against a no-slip wall. (b) Log-log plot of the time-averaged velocity magnitude vs distance. The colors are associated with the lines along which the velocity are evaluated as shown in panel (a). In free space, the velocity fields show a decay of $1/r$ characteristic of a net Stokeslet. In the case of a cilium next to a wall, a faster decay of $1/r^3$ is found, which corresponds to a net force perpendicular to the no-slip wall.

Another interesting aspect revealed by the average flow fields is the net direction of pumping. In the case of a clamped sperm with anterograde wave propagation as shown in Figure 5.12(a), flagellar oscillations drive a net flow from tip to tail, which, in the case of a force-free cell, would enable propulsion in the forward direction. However, simulations at lower activity levels (not shown) reveal that the direction of propulsion is reversed when waves propagate in the retrograde direction. This hints at the importance of dynein level regulation for efficient sperm motility, and also has consequences for the hydrodynamic

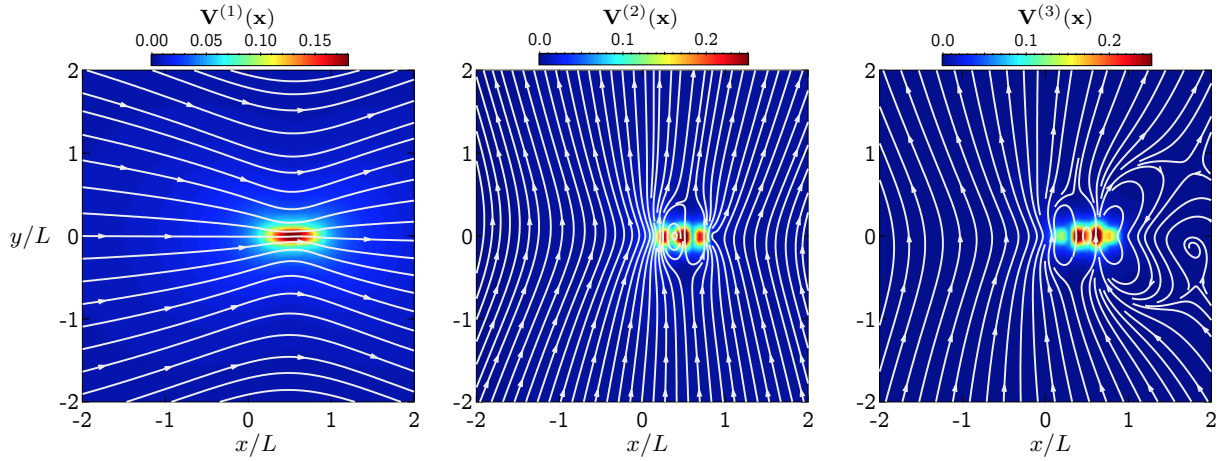


Figure 5.13: First three PCA velocity modes $\mathbf{V}^{(i)}(\mathbf{x})$ ($i = 1, 2, 3$) for a clamped beating sperm. The first mode is dominated by a Stokeslet flow, whereas the next two modes have a more complex spatial structure with multiple velocity peaks that echo the structure of the deformation eigenmodes found in Figure 5.9(c). All three velocity fields can be approximated in terms of regularized Stokeslets.

synchronization of nearby interacting flagella [223].

5.6.2 Singularity representation

The linearity of the Stokes equations allows us to represent the flow fields in terms of fundamental singular solutions. Several methods have been proposed for seeking such representations. In a simple model, Brumley *et al.* [218] used a single time-dependent Stokeslet to approximate the flow field of a *Volvox carteri* colony held in place by a micropipette. A more general method consists of seeking an unsteady multipole expansion [224], which was applied to describe the flow field generated by swimming *Chlamydomonas* [225]. More recently, PCA was also used to identify dominant contributions to the velocity fields. These modes were then approximated by a set of regularized Stokeslets [222] for quantitative representations of the flow fields [226, 227]. Here, we adopt this approach and apply it to analyze the flow field generated by a clamped sperm.

The numerical determination of the PCA modes involves similar steps as discussed in Sec. 5.5.2 for the analysis of waveforms and proceeds as follows. We focus on two-dimensional flow fields in the plane of motion, and first compute q snapshots of the velocity field on a $N \times N$ Cartesian grid over the course of one period of oscillation. In contrast to past studies [226], we do not subtract the time-averaged velocity field as usually done in PCA; this does not affect the representation of the flow field due to the linearity of Stokes flow. Each such snapshot contains $2N^2$ values for the two velocity components (u_x, u_y), which are used to populate the rows of a matrix $M \in \mathbb{R}^{q \times 2N^2}$:

$$\mathbf{v}_\alpha = \text{row}_\alpha M = [u_x^1, u_x^2, \dots, u_x^{N^2}, u_y^1, u_y^2, \dots, u_y^{N^2}]_\alpha, \quad \text{for } \alpha = 1, 2, \dots, q. \quad (5.37)$$

We then define the $2N^2 \times 2N^2$ covariance matrix $C = M^T M$, which encapsulates spatial features of the velocity field irrespective of time. The matrix C is real symmetric positive definite and thus has an eigendecomposition in terms of real orthogonal basis vectors $\mathbf{V}^{(i)}(\mathbf{x}) \in \mathbb{R}^{2N^2}$, where, $i = 1, \dots, 2N^2$. For all the beating patterns presented here, we find that the first 3 to 5 eigenmodes are sufficient to capture 95 % of the cumulative variations in the data. In the case of sperm, an excellent representation of the velocity field can be achieved as a linear combination of the three dominant modes:

$$\mathbf{u}^d(\mathbf{x}, t) = \alpha_1(t)\mathbf{V}^{(1)}(\mathbf{x}) + \alpha_2(t)\mathbf{V}^{(2)}(\mathbf{x}) + \alpha_3(t)\mathbf{V}^{(3)}(\mathbf{x}), \quad (5.38)$$

where the time-dependent coefficients are determined by least-squares minimization. The first three PCA modes $\mathbf{V}^{(i)}(\mathbf{x})$ are illustrated in Figure 5.13, and the corresponding amplitudes $\alpha_i(t)$ are show in Figure 5.14(a). The dominant mode ($i = 1$), which is almost steady, resembles the flow due to a Stokeslet and captures the net streaming motion induced by the filament. The next two modes ($i = 2, 3$) have a more complex spatial structure with multiple velocity peaks that echo the structure of the deformation eigenmodes found in Figure 5.9(c). These two modes are oscillatory with a constant phase difference and account for unsteady flow dynamics resulting from filament deformations.

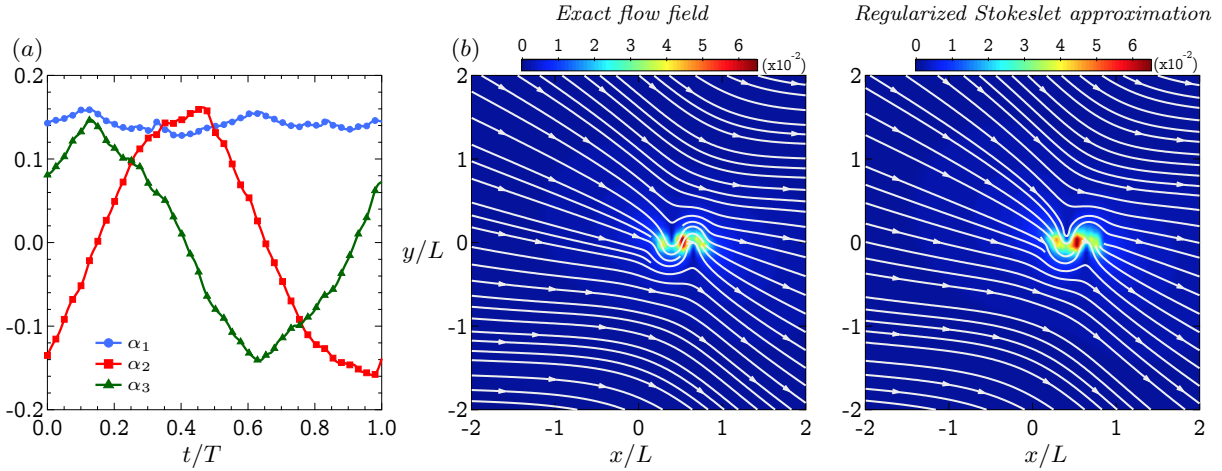


Figure 5.14: (a) Variation of the weighting coefficients $\alpha_i(t)$ of the three PCA velocity modes shown in Figure 5.13 over one period of oscillation. (b) Comparison of the approximated instantaneous flow-field (right) to the exact numerical one (left) at $t/T = 0.9$.

These various PCA modes can be further approximated in terms of collections of regularized Stokeslets [71, 222]. The flow field generated by a single regularized Stokeslet with regularization parameter ε and strength \mathbf{f} is given by

$$\mathbf{u}^S(\mathbf{x}; \varepsilon) = \left[\frac{(r^2 + 2\varepsilon^2) \mathbf{I} + \mathbf{r}\mathbf{r}}{(r^2 + \varepsilon^2)^{3/2}} \right] \cdot \mathbf{f}, \quad (5.39)$$

where $\mathbf{r} = \mathbf{x} - \mathbf{x}_0$ and \mathbf{x}_0 is the location of the singularity. Following Ishimoto *et al.* [226], we represent each mode in terms of p Stokeslets, where the parameters $(\varepsilon^p, x_0^p, y_0^p, f_x^p, f_y^p)$ are calculated through a least-squares solution that implements a Levenberg-Marquardt algorithm. The number p is chosen such that we obtain a satisfactory approximation to the basis vectors, and in the present case we use $p = 2, 5$ and 6 for each for the first three modes. A typical flow field obtained by this reconstruction method is compared to the full numerical flow field in Figure 5.14(b, c), where excellent agreement is found.

5.7 Conclusion

In this chapter, we have used numerical simulations of a sliding control model of the axoneme to highlight how spontaneous oscillations can emerge from the collective action of molecular motors. Our model for coupled elastohydrodynamics and motor kinetics follows that previously proposed by Oriola *et al.* [174] and allows for saturation of unstable modes following a Hopf bifurcation that leads to the propagation of bending waves resembling the beating patterns of spermatozoa. While the study of Oriola *et al.* [174] as well as other related numerical models [175, 192, 208] were restricted to the small curvature limit where retrograde wave propagation takes place, our fully nonlinear simulations demonstrated the existence of a second transition at higher activity levels giving rise to anterograde wave propagation consistent with observations of sperm [205]. We also demonstrated the ability of our model to capture asymmetric beating patterns resembling those of cilia and of *Chlamydomonas* flagella, which were obtained using a combination of biased motor kinetics and curvature control. Our model also allowed us to analyze disturbance flows induced by beating filaments, which are known in biological systems to play a crucial role in development, motility and sensing. We build on the hydrodynamics and will consider the problem related to hydrodynamic interaction and possible synchronization in pairs of filaments in the next chapter.

This chapter is primarily based on the material published in *Physical Review Fluids* (2019) authored by Brato Chakrabarti and David Saintillan [9]. The dissertation author was the primary researcher and author of this paper.

Chapter 6

Elastohydrodynamic synchronization in pair filaments

6.1 Fundamentals of sync

In the most classical sense synchronization (from the Greek $\sigma\bar{\nu}\nu$: *syn* = the same, and $\chi\rho\delta\nu\rho\zeta$: *chronos* = time) means adjustment of rhythms or periods of self-sustained periodic oscillators due to their (weak) interaction. The history of synchronization goes back to the 17th century when the famous Dutch scientist Christiaan Huygens reported on his observation of synchronization of two pendulum clocks which he had invented shortly before [228]. Another important observation of synchrony of organ pipes was described by Lord Rayleigh in his ‘Theory of Sound’. There are many more examples of synchrony in man-made devices ranging from lasers, and electric power systems to electronic generators. Over the last few decades the emphasis of research has shifted towards synchronization in biological systems. Examples include synchronous division of cells [229], synchronous firing of neurons [230], co-operative behavior among fireflies [231], animals and even humans [232].

The fundamental idea of phase synchronization, which will be the main focus of this chapter, hinges on interpreting self-sustained oscillators as stable limit cycles. Associated with a limit cycle one can define a unique phase $\psi(t)$ that grows linearly with time and remains neutrally stable. Due to the neutral stability of the phase, a small perturbation (e.g. external periodic forcing or coupling to another system) can cause relatively large deviations of the phase - contrary to the amplitude, which is only slightly perturbed due to the transversal stability of the limit cycle. Thus, with a weak coupling one can adjust the phase and the frequency of oscillations without significantly influencing the amplitude. This adjustment is the key to synchronization phenomenon [228]. Typically adjustments of oscillators to synchronize can be described in terms of phase locking, frequency entrainment and have also been generalized to chaotic systems [233]. Synchronization phenomena in large collection of oscillators often manifest themselves as collective coherent regimes appearing via non-equilibrium phase transitions [234], and can sometimes be responsible for catastrophic scenarios like the lateral swaying of the Millennium Bridge in London [235]. In this chapter we probe one of the long-standing and well studied problem of biological oscillators: the role of hydrodynamics in synchronization.

6.2 Synchronization in cilia and flagella

Studies on synchronization of cilia and flagella date back to observations by Rothschild [236] on nearby swimming sperm and subsequent theoretical work by Taylor [237], who proved that dissipation for two swimming sheets is minimized for an in-phase configuration. While biology is often not driven by dissipation principles, it has long been hypothesized that fluid-mediated hydrodynamic interactions play a central role in synchronization and in collective behaviors such as metachronal waves in large ciliary arrays [238]. Over the last two decades, experiments [218, 239–243] using micropipette-held

Chlamydomonas have revealed that elastohydrodynamic interactions may indeed be at play in causing its two flagella to synchronize their breaststrokes. Periods of asynchrony are thought to arise due to biochemical noise and are well described by a stochastic Adler equation [218, 233]. Understanding collective behaviors and synchronization holds the key to important biological questions such as evolution and origin of multi-cellularity.

Theoretical progress in understanding synchronization is complicated by the intricate internal structure and actuation of the flagellum core: the axoneme, whose structure was discussed in detail in the previous chapter. Much work has gone into developing minimal models that neglect this biological complexity and coarse-grain flagella as microspheres driven on compliant or tilted orbits [4, 217, 244, 245]. Introduction of elasticity in the classical Taylor swimming sheet model also suggests that how flexibility can spontaneously induce phase locked conformation [246]. More detailed numerical models have relied on pre-imposed internal or external actuators to analyze metachronal waves [209, 210] or the bistability of elastic filaments [247], yet these descriptions capture experimental waveforms poorly. Only recently have there been attempts to study the role of hydrodynamics in simplified models of active elastic filaments [183, 248].

The detailed process leading to spontaneous flagellar oscillations still remains unclear. However our microscopic model outlined in the previous chapter provides a good starting point since we have incorporated a basic structure of the planar axoneme and accounted for stochastic dynamics of molecular motors. Since all the oscillations described in the previous chapter emerges spontaneously it becomes a natural choice to study hydrodynamic synchronization. In this chapter, we analyze the temporal dynamics and synchronization of a pair of such spontaneously beating filaments. Our results are consistent with recent experiments [218], and we will elucidate the crucial roles of hydrodynamic interactions, mechanochemical feedback, and biochemical noise in the process of synchro-

nization.

6.3 Comments on waveforms

In the previous chapter we have provided the detailed characterization of various waveforms that are possible from our model. The major results were summarized in the phase chart provided in Figure 5.4. Before proceeding to study interaction between filaments we want to highlight a few more quantitative and qualitative features of the waveforms that make our model most suitable to tackle this problem.

6.3.1 Symmetric sperm like beating

In order to compare the anterograde regime of nonlinear, finite amplitude wave-propagation to experimental waveforms as shown previously in Figure 5.4, we report tangent angle dynamics and simulated snapshots of traveling waves in Figure. 6.1. We find that by tuning the two primary control parameters namely the Sperm number Sp and the activity number μ_a we find a variety of anterograde waveforms with different wavenumber, amplitude and frequency.

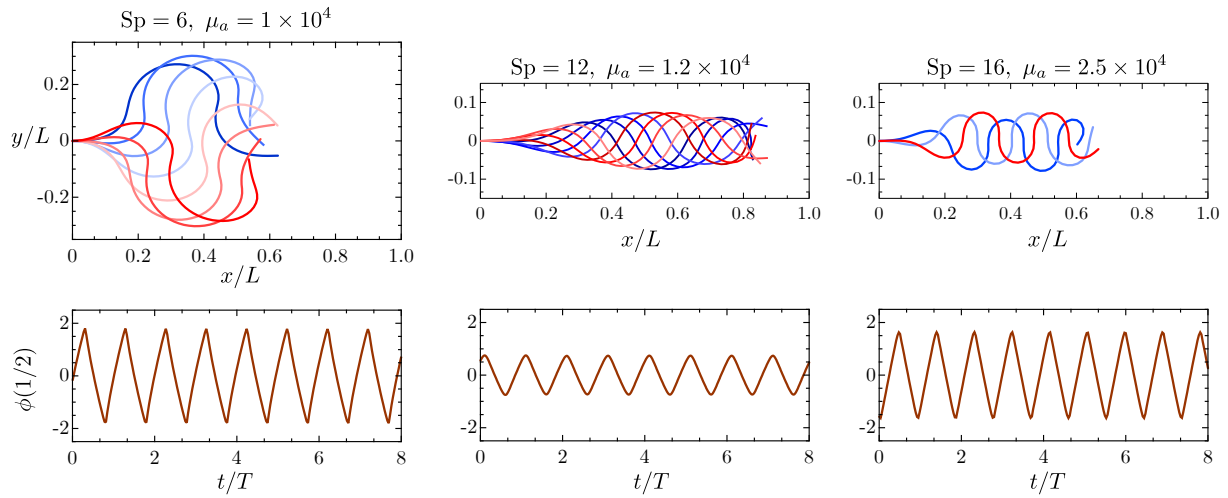


Figure 6.1: Sperm like waveforms for various combinations of (Sp, μ_a) and the corresponding evolution of the tangent angle at the mid point. Simulations are for $\mu = 100$, $\zeta = 0.3$ and $\eta = 0.14$.

The above waveforms compare extremely well with the experimental snapshots of various marine spermatozoa reported in [249] in different viscous media. In particular we are able to capture a range of wavenumber along the filament, consistent with experimental observations. Amplitude, frequency and the wavelengths depend non-trivially on the control parameters and have been explored in detail in [250]. The evolution of the tangent angle dynamics also compares quantitatively with the measurements in [175] for bull sperm.

6.3.2 Waveforms of *Chlamydomonas*

We have previously pointed out that the frequency of beating predicted by our model in the case of *Chlamydomonas*-like beats is off compared to experimental values. Nonetheless, the qualitative features of the beats are consistent with observations. In the previous chapter we discussed the main properties of the power spectrum of the mean angle. Here we characterize the waveform using a Fourier decomposition. Following [187, 251] we

seek a representation of the tangent angle as follows:

$$\phi(s, t) = \sum_{n=-\infty}^{\infty} \psi_n(s) \exp(in\omega t), \quad (6.1)$$

where ω is the angular frequency. In fig. 6.2, we show the static mode $\psi_0(s)$ and the first dynamic mode $\psi_1(s)$ and associated phase. In [187], this analysis was performed on a free axoneme, which is different from the clamped flagellum considered in our simulation. Our results, however, compare favorably with the images analyzed in [251] (for example, figure 4.12 of the thesis) for a flagellum attached to the cell body of *Chlamydomonas*. While there exist quantitative differences, our model is found to capture all the essential features of the beating pattern.

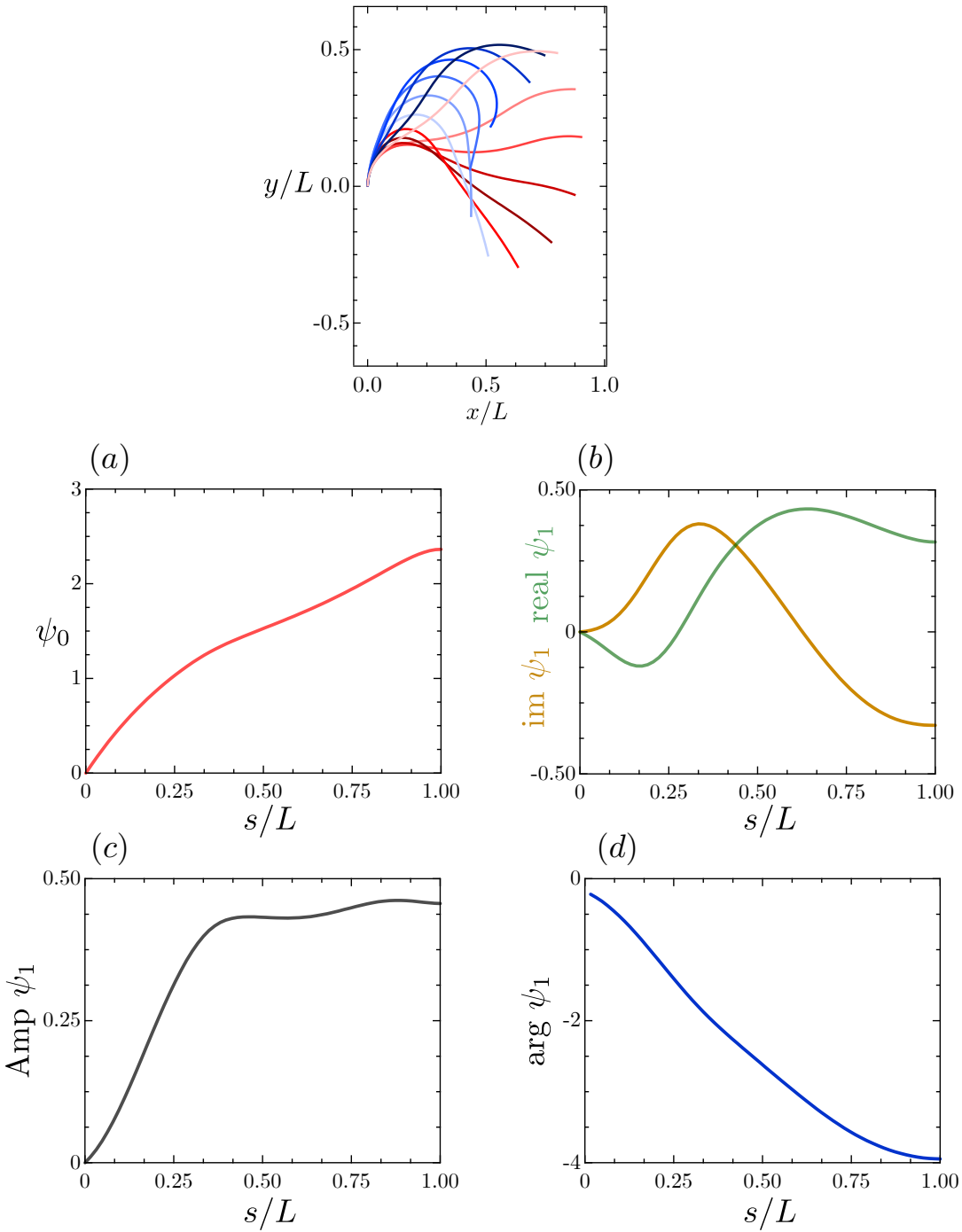


Figure 6.2: (a): Zeroth mode ψ_0 of the beating pattern showing the static curvature. (b) Real and imaginary parts of the first dynamic mode ψ_1 . Since the flagellum is clamped, we have $\psi_1(0) = 0$ which is different from the free axoneme considered in Ref. [187]. (c) Amplitude of the first dynamic mode. (d) Argument of ψ_1 , indicating the phase of the mode.

6.3.3 Ciliary beating patterns

In biology a wide variety of ciliary beating patterns are possible. Most of the waveforms are fully three dimensional [252]. Our present model and the associated formulation is restricted to planar beating patterns. However cilia in a few biological organisms like *Opalina* [253], *Ctenophore* [254], and mollusc [254] are known to have almost planar beating pattern for which our model can be relevant. Interestingly defective respiratory cilia beats entirely in a plane [255] with a waveform similar to that shown in the main text. Figure 6.3 show a couple of waveforms that can be obtained with our model using various geometric feedback mechanisms.

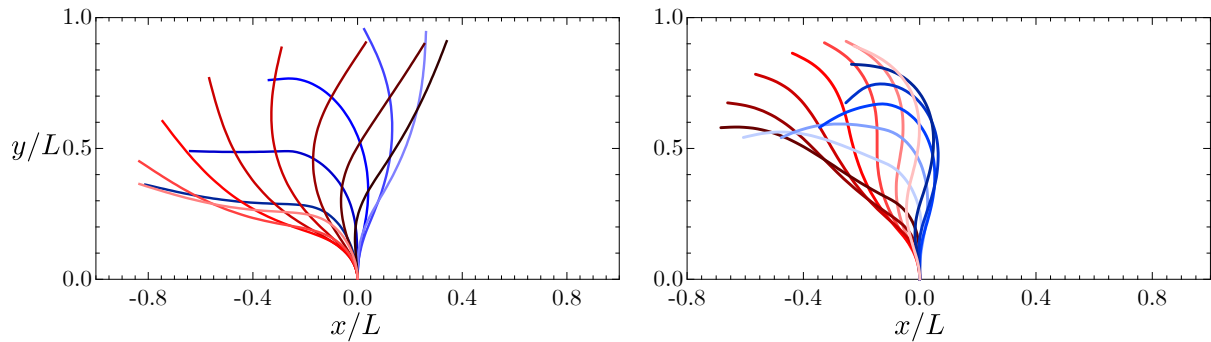


Figure 6.3: Possible ciliary beating patterns under pure sliding (left) and a combination of sliding and curvature (right) control.

In the following sections we will attempt to qualitatively capture the synchronization behavior observed in experiments with micropipette-held somatic cells *Volvox carteri* [218]. The flagella in these cells beat almost entirely in a plane [256]. We will find a *posteriori* that in order to reproduce the synchronization behavior, it is the asymmetry of the beating pattern that becomes crucial and not the non-planarity.

6.4 Review of the governing equations

We have outlined the governing equations for single filament oscillations in the previous chapter. The equations of motion for pair filaments are identical to equations (5.25)-(5.27). However the expression for the disturbance flow field is now altered in the presence of another filament. Given two filaments indexed by $\{\alpha, \beta\}$, the flow is obtained as

$$\mathbf{u}^d(s_\alpha) = \mathbf{K}[\mathbf{f}_e^\alpha](s_\alpha) + \int_0^1 \mathbf{G}(s_\alpha; s_\beta) \cdot \mathbf{f}_e^\beta(s_\beta) ds_\beta, \quad (6.2)$$

where \mathbf{f}_e is the elastic force density. The first term in Eq. (6.2) is the finite-part integral of slender body theory [81, 250] and captures hydrodynamic interactions within a filament. The second term accounts for the flow induced by the other filament, where the Green's function $\mathbf{G}(s_\alpha; s_\beta)$ is taken to be either the Oseen tensor in free space or Blake's tensor [221] in presence of a no-slip wall. The kinetics of the molecular motors obey (5.28) and the parameter Λ characterizes the strength of the biochemical noise.

6.5 Synchronization in sperm waveforms

We first focus on the synchronization of pairs of sperm placed side by side as shown in Figure 6.4. We initialize the simulation in the absence of inter-filament hydrodynamic interactions (HI) by letting spontaneous oscillations reach steady state after saturation of dynein kinetics. The initial configuration is chosen such that the filaments are almost in antiphase (AP). We then switch on HI and, after several periods, the sperms go in-phase (IP) and remain phase-locked thereafter.

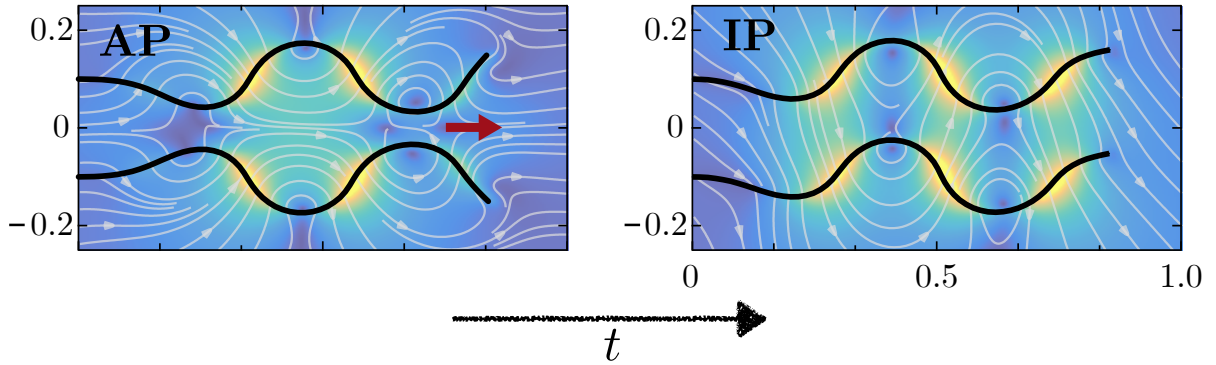


Figure 6.4: In-phase synchronization of anterograde sperm waveforms. The red arrow indicates the direction of wave propagation. On left we show the initial anti-phase conformation and on right we highlight the emerging in-phase waveform.

The key role of hydrodynamics in this process is best illustrated by Figure 6.5, showing the evolution of the bound motor populations n_+ at $s = 1/4$ on both filaments (the behavior is identical for n_- and at other locations). Before HI are switched on, motor populations are uncoupled and undergo periodic oscillations in antiphase with cusp-shaped waveforms typical of motors far from equilibrium [257] and only a small fraction of bound motors at any given time. Once HI start acting, both the phase and amplitude of the motor populations change. This is attributed to elastic deformations of the filaments in their induced flow fields, which feed back to the kinetics through the change in sliding displacement and velocity. As seen in Figure 6.5, the two motor populations rapidly go in phase with a marginally increased amplitude, resulting in spontaneous IP synchronization of the beating patterns. The cartoon in Figure 6.5 highlights this cyclic process fundamental to elastohydrodynamic synchronization, by which HI affect beating patterns via geometry dependent motor kinetics. This feedback is most dramatic when the filaments are closeby and sufficiently flexible.

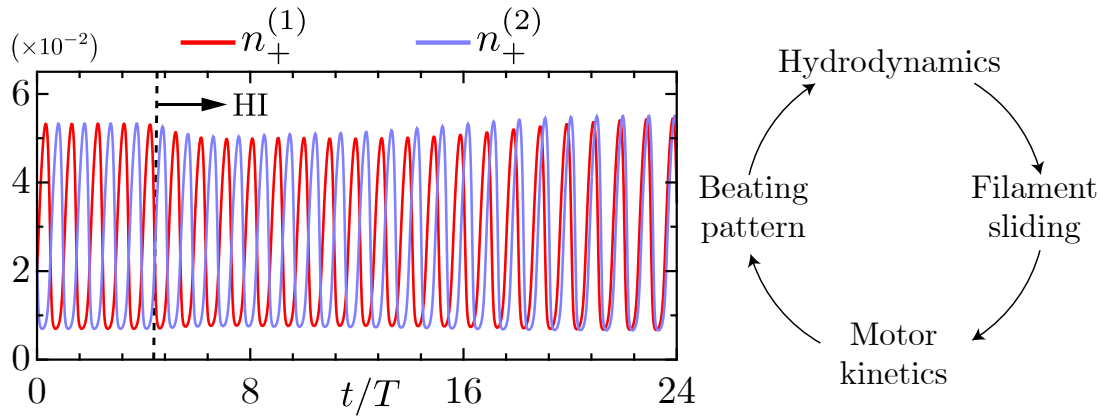


Figure 6.5: Evolution of dynein motor populations at $s = 1/4$ on two nearby sperms as a result of HI. The dashed line indicates the instant when interactions are turned on. Time is scaled by the oscillation period T of an isolated filament. Cartoon on the right illustrates the feedback loop leading to synchronization.

6.6 Synchronization in ciliary beating

A similar mechanism is at play for asymmetric ciliary beats in Figure 6.6(a, b). When the power strokes of the two cilia indicated by red arrows point in the same direction, an IP beat emerges with net unidirectional pumping of the fluid. When the power strokes are in opposite directions, our model leads to AP synchronization with beating patterns resembling a ‘freestyle’ swimming gait as shown in Figure 6.6(b).

Similar AP patterns are obtained for *Chlamydomonas* beats, supporting the hypothesis [258] that the IP breaststrokes seen in wildtype cells result from elastic basal couplings between the two flagellar axonemes rather than from HI alone. Indeed, experiments with *vfl* mutants that are deficient in these filamentary connections [258] or with *Volvox* cells held in separate micropipettes [218] have shown AP synchronization for power strokes with opposite orientations, consistent with our model findings.

Note that in the case of swimming or even weakly clamped cells flagellar synchro-

nization can also happen through a rocking motion of the cell body independent of HI or in absence of basal coupling [259–263]. The relative importance of these mechanisms remains to be explored for the various asymmetric waveforms [263] arising in our model.

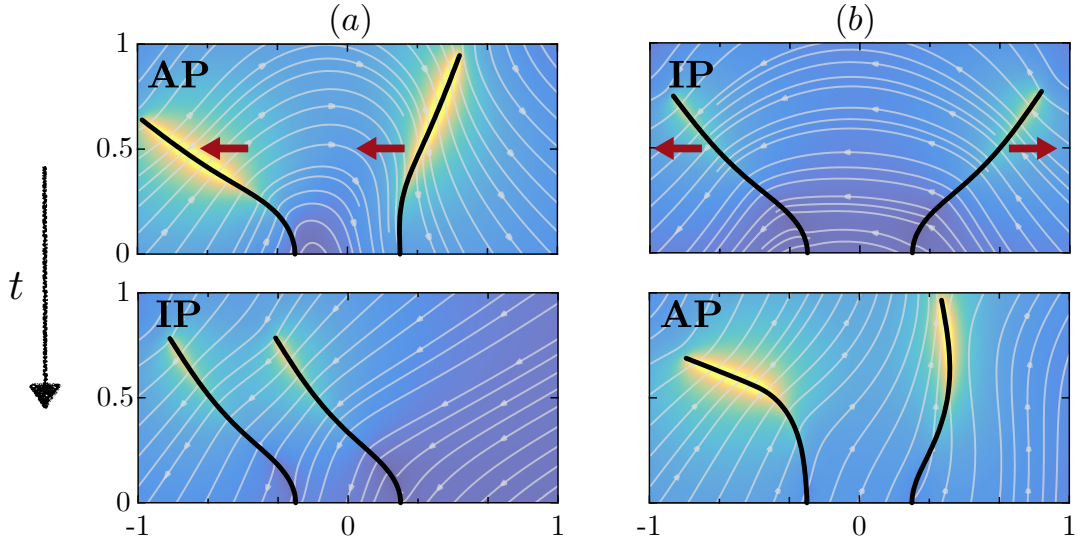


Figure 6.6: cilia can achieve both IP (a) or AP (b) synchronization depending on the orientation of the power stroke indicated by red arrows. Synchronization for *Chlamydomonas* (not shown) is identical to that of cilia.

6.7 Adler equation and minimal models

For a more quantitative analysis of synchronization, we introduce a definition of the phase ψ of a waveform. To this end, we perform the Hilbert transform of the continuous periodic time series $\beta(t) = \phi(1/2, t)$, providing the analytic continuation $\zeta(t) = \beta(t) + i\hat{\beta}(t)$ where

$$\hat{\beta}(t) := \frac{1}{\pi} \int_{-\infty}^{\infty} \frac{\beta(\tau)}{t - \tau} d\tau. \quad (6.3)$$

The phase of the waveform is then calculated as $\psi(t) = \arctan[\hat{\beta}(t)/\beta(t)]$, and we use an appropriate geometric gauge to define a true phase that grows linearly with time [264]. The phase difference $\delta(t) = \psi_1 - \psi_2$ for two nearby sperms going from AP to IP is shown

in Figure 6.7(a) and decays to zero over the course of several periods.

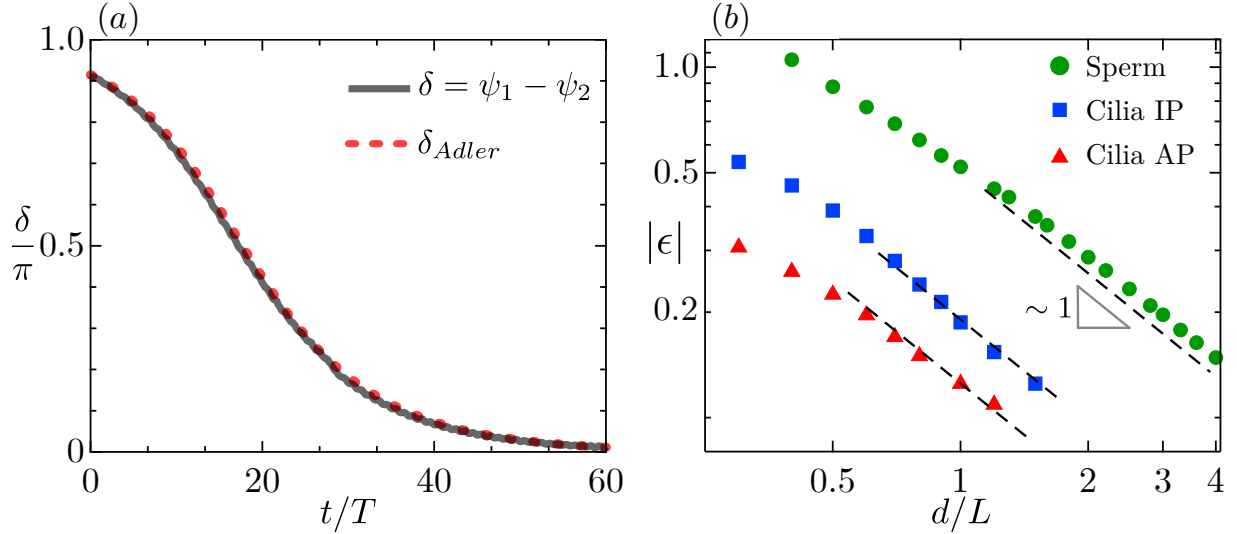


Figure 6.7: (a) Evolution of the phase difference $\delta(t)$ during synchronization of two nearby sperms and comparison to the Adler equation (6.4). (b) Coupling strength $|\epsilon|$ as a function of interflagellar distance d for various beating patterns.

In spite of the complexity of the governing equations in presence of HI, the phase difference is well described by a simple low-dimensional Adler equation as in past experiments with *Chlamydomonas* [241]. Here, we seek a two-parameter equation of the form

$$\dot{\delta} = \epsilon \sin \delta + \alpha \sin 2\delta, \quad (6.4)$$

where constants ϵ, α are estimated numerically. A solution to this equation follows the numerical data very well in Figure 6.7(a). In all our computations, we find that $|\epsilon| \gg |\alpha|$ and thus define $|\epsilon|$ as the effective coupling strength. When plotted as a function of interflagellar distance d in Figure 6.7(b), $|\epsilon|$ decays algebraically as $1/d$ in the far field due to dominant Stokeslet HI, with a slower decay at short separations where complex near-field interactions take place. Stronger coupling arises for symmetric spermlike beats than for ciliary beats, primarily due to the longer lengths of sperm flagella. For cilia, we also find that $|\epsilon|_{IP} > |\epsilon|_{AP}$ in agreement with experiments [218], which can be attributed

to the fact that filaments spend more time close to one another during IP beats and thus interact more strongly.

It is important to point out that we have not systematically reduced the infinite dimensional PDE's to a one dimensional dynamical system. This is a problem in its own right and has only been partially resolved recently in a simpler model of spontaneous oscillations [265]. However it is still instructive to consider how one may coarse-grain such a system to an Adler model. To this end we start with the classical rotor model [4] where we represent the flagellar oscillator as a micro-sphere driven on a compliant circular orbit as shown in Figure 6.8.

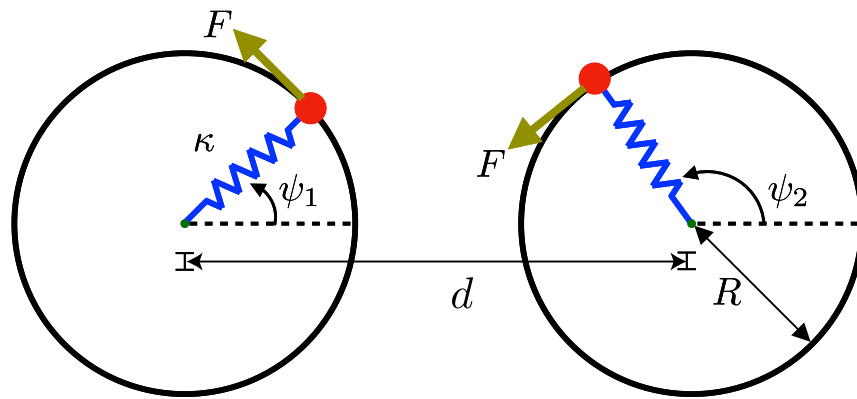


Figure 6.8: Schematic of coarse-grained minimal model where the beating filaments are represented as rotors on circular orbits [4].

The radius of this orbit $R \sim L$ is comparable to the length of flagella or cilia. The radial stiffness of the orbit is given by $\kappa \sim B/L^3$ and serves as a measure of elasticity. The bead is driven on the orbit by a force that is tangent to the circular path. In the classical [4] model the force is constant. However in a flagella or cilia the flow-field is time dependent and it is more appropriate to use a phase dependent force profile. One such approximation is given by:

$$F(\psi) = \int_0^L |\mathbf{f}_{vis}(s, \psi)| \, ds. \quad (6.5)$$

This effective force that scales as B/L^2 and can be interpreted as the leading order Stokeslet approximation to the instantaneous flow-field. It has also been measured in experiments [218]. We can chose the radius a of the micro-spheres to obtain the right frequency or average angular velocity of rotation that match our simulations. The phase dependent force profile for sperm-like and ciliary beating is shown in Figure 6.9. The two distinctive peaks in the ciliary beating pattern is indicative of the power and recovery strokes.

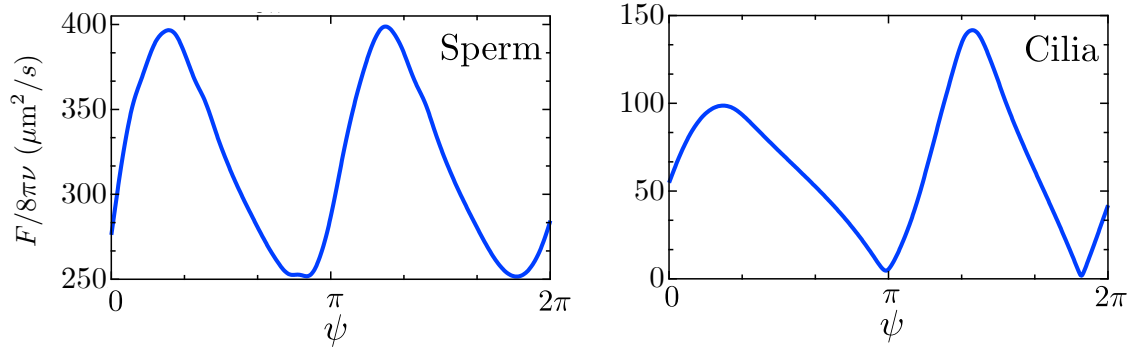


Figure 6.9: Phase dependent force profile used to drive the micro-spheres.

In order to find the evolution of the micro-sphere we balance forces in both the tangential and radial direction and account for the disturbance velocity fields due to hydrodynamic interactions. For one sphere we have:

$$\dot{\psi}_1 = \frac{F(\psi)}{6\pi\nu a} + \frac{1}{R_1} \hat{\mathbf{e}}_{\psi_1} \cdot [\mathbf{G}_{12}(\mathbf{x}_1, \mathbf{x}_2) \cdot F(\psi_2) \hat{\mathbf{e}}_{\psi_2}], \quad (6.6)$$

$$\dot{R}_1 = -\frac{\kappa}{6\pi\nu a} (R_1 - R) + \hat{\mathbf{e}}_{R_1} \cdot [\mathbf{G}_{12}(\mathbf{x}_1, \mathbf{x}_2) \cdot F(\psi_2) \hat{\mathbf{e}}_{\psi_2}], \quad (6.7)$$

where $\hat{\mathbf{e}}_R$ and $\hat{\mathbf{e}}_\psi$ are unit vectors in the radial and tangential direction respectively and ν is simply the viscosity of the fluid. The equation of motion for the other sphere is simply obtained by changing the indices: $1 \rightarrow 2$. It is straight forward to integrate the system of ODEs numerically. We summarize the observed results below.

- When the beads are rotating in the same direction we observe in-phase synchrony

for both sperm and ciliary beating pattern. This corresponds to the case when the power strokes of the filaments are in the same direction and is consistent with our full nonlinear simulations.

- For counter rotating beads with $F_1 = -F_2$ we do not observe either in-phase or anti-phase synchronization for ciliary beating pattern. Instead the system is phase locked into a constant phase-difference mode. This corresponds to filaments with opposite power strokes and is in disagreement with our nonlinear simulations that predict an anti-phase behavior.

The above observations point to the limitation of such coarse-grained descriptions. Indeed as pointed in [244,245] one can possibly observe both IP and AP configurations depending on the exact force-profiles and the stiffness of the orbit. While the minimal description is attractive due to its simplicity, the conclusion for an actual system can often be misleading and is probably more appropriate for describing synthetic systems [245]. However if we drive the beads by a constant force instead of a phase dependent one, we do recover the right behavior. In this simple case it can be shown that the evolution of the phase difference between the oscillators obey an Adler equation given by:

$$\frac{d}{dt}(\psi_1 - \psi_2) = \dot{\delta} = -\epsilon \sin \delta, \quad (6.8)$$

where $\epsilon \sim a\omega^2\nu L^3/Bd$, where ω is the angular frequency of rotation. We can relate the rotation rate ω to the driving force simply as $\omega = F/R\zeta$. This allows us to determine the scaling of the coupling constant in terms of the physical parameters of the problem:

$$\epsilon \sim \frac{a\rho^2 f_0^2 L}{\nu Bd}. \quad (6.9)$$

Indeed the above relation makes the $1/d$ scaling recovered in Figure 6.7 apparent. The above expression was used in several experiments [240,241] to calculate the coupling be-

tween *Chlamydomonas* flagella that also obeyed the Adler equation for phase synchronization.

6.8 Biochemical noise: phase slips

Intrinsic to the kinetics of molecular motors is biochemical noise, which alters the precise notion of synchronization. To probe its effects, we study the long-time statistics of the phase difference in presence of noise for spermlike waveforms in Figure 6.10(a). Fluctuations follow a Gaussian distribution centered around the mean IP configuration of $\delta = 0$, with a variance scaling linearly with separation distance d . This is a consequence of the $1/d$ decay of the coupling strength $|\epsilon|$ and is further corroborated by the collapse of the distributions under the rescaling $\delta \rightarrow \delta/\sqrt{d}$ in Figure 6.10(b) [218]. We model the noisy phase dynamics by a stochastic Adler equation:

$$\dot{\delta} = \epsilon \sin \delta + \chi(t), \quad (6.10)$$

with $\langle \chi(t) \rangle = 0$ and $\langle \chi(t)\chi(t') \rangle = 2D\delta(t-t')$, where D is the phase diffusivity with units of s^{-1} . Associated with the Adler equation is a Fokker-Planck description for the probability distribution $P(\delta)$ of the phase difference that is given by:

$$\frac{\partial P}{\partial t} + \frac{\partial}{\partial \delta} (\epsilon \sin \delta P) = D \frac{\partial^2 P}{\partial \delta^2}. \quad (6.11)$$

The steady-state solution when the advective and diffusive flux balance each other is given by:

$$P(\delta) = \frac{1}{2\pi I_0(|\epsilon|/D)} \exp\left(-\frac{\epsilon}{D} \cos \delta\right), \quad (6.12)$$

where I_0 is the modified Bessel function of order zero and we estimate D numerically [250, 266]. The interaction potential $U(\delta) = -\ln P(\delta)$, which is 2π -periodic, is shown in Figure 6.10(d) for increasing noise levels.

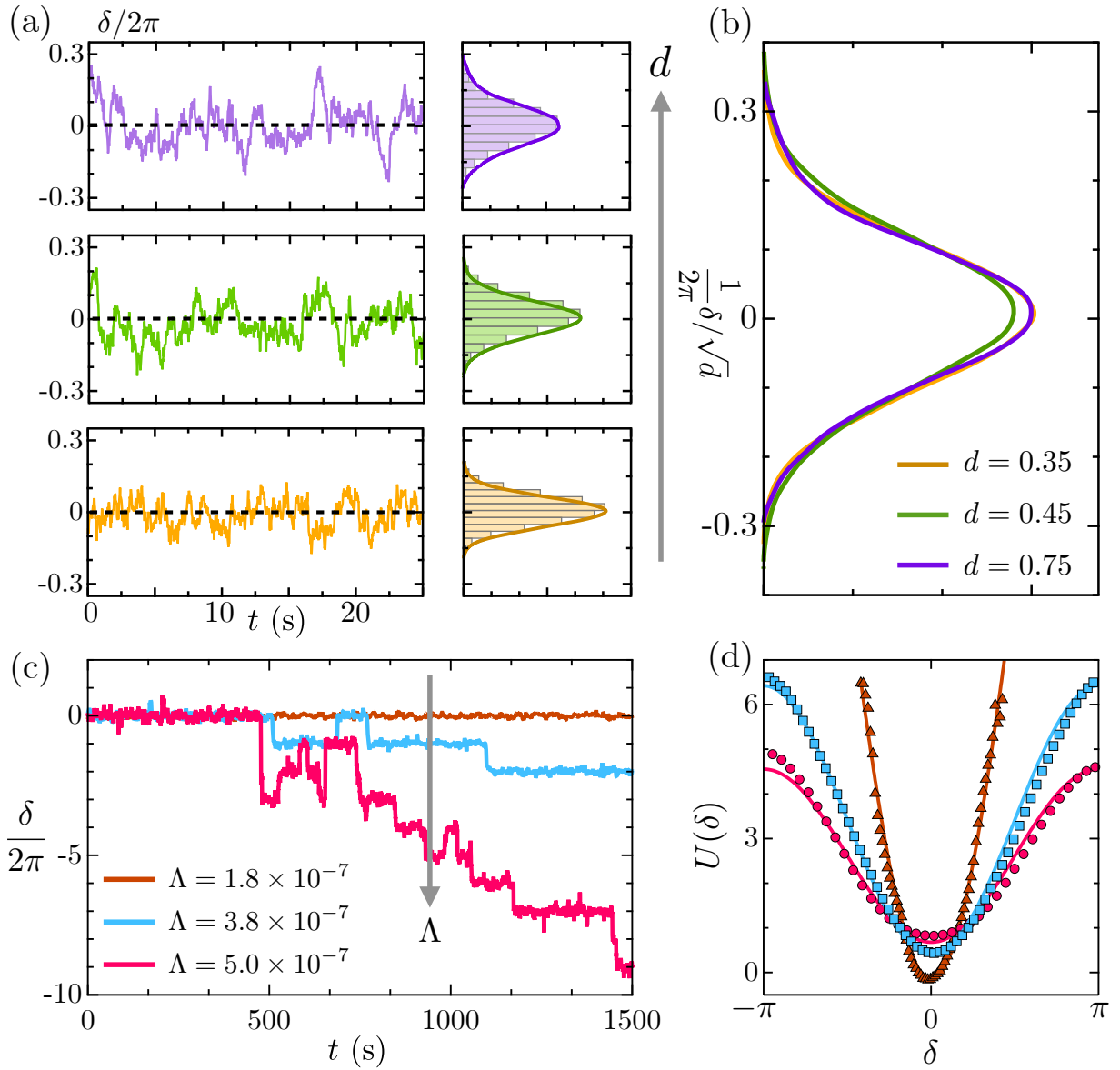


Figure 6.10: (a) Gaussian distributions of the fluctuations of the phase difference for varying separation distance d . (b) Collapse of the distributions in the rescaled variable δ/\sqrt{d} . (c) Long-time evolution of $\delta(t)$ for increasing biochemical noise Λ at a fixed separation distance d , showing the emergence of slips. (d) Effective interaction potential $U(\delta)$ estimated from the statistics (symbols) and compared to the Fokker-Planck prediction (lines).

When noise is weak, the filaments remain phase-locked and fluctuate around the IP configuration, which translates into a deep potential well at $\delta = 0$. With increasing noise,

the potential well flattens as deviations from perfect AP synchrony become more frequent and intense. Occasionally, accumulated noise allows the filaments to gather a complete phase of 2π , causing them to ‘slip’ towards $\delta \pm 2\pi$. These slips are visible in the phase trajectories of Figure 6.10(c) and can be interpreted as thermally assisted hops between neighboring wells in the flattened periodic potential.

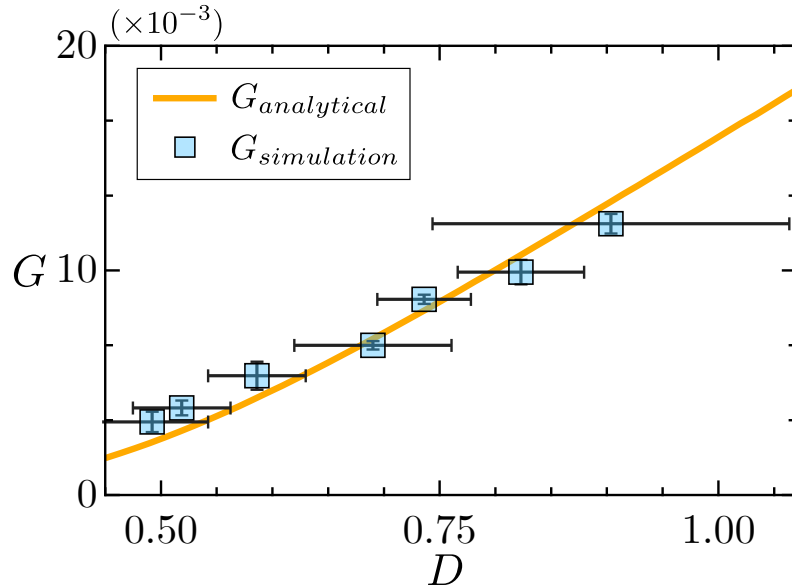


Figure 6.11: Comparison of the measured frequency of phase slips G in s^{-1} to the analytical prediction.

In the absence of frequency mismatch, slips are equally probable in $\pm 2\pi$, and the stochastic Adler model predicts a hopping frequency [266]:

$$G = \frac{D}{4\pi^2} |I_0(|\epsilon|/D)|^{-2}. \quad (6.13)$$

We can now compare the frequency of slips computed from the numerical estimate D of diffusivity and the above expression. Figure 6.10 highlight this comparison. For stronger noise-floor the error in predicting the diffusivity increases as frequent events of slip. However it is evident from Figure 6.11 that the our simulations capture the right behavior.

6.9 Conclusions

Using a detailed microscopic model of the flagellar axoneme that produces spontaneous oscillations similar to those seen in nature, we have illuminated the role of hydrodynamic interactions and associated mechanochemical feedback in enabling synchronization of nearby flagella and cilia. Our model predictions for various beating patterns and orientations all agree with experiments and give credence to the sliding control mechanism responsible for the spontaneous beats. While we have focused on interactions in free space, our simulations suggest that the qualitative behavior is unaltered in presence of no-slip walls albeit with weaker coupling strengths due to the additional viscous damping. We were also able to reproduce experimentally observed phase slips induced by biochemical noise. Future studies with our model will probe the role of elastic basal couplings [258], swimming sperms that are free to adjust phase by sliding past one another [267], and emergent dynamics in large-scale ciliary arrays [209].

This chapter 6 is primarily based on the material accepted for publication in *Physical Review Letters* (2019) authored by Brato Chakrabarti and David Saintillan [10]. The dissertation author was the primary researcher and author of this paper.

Chapter 7

Transport of semiflexible filaments in porous media

In Chapter 3 and 4 we have focused on the dynamics of passive actin filaments in viscous flow and how buckling instabilities can make way for non-trivial filament morphologies. In the spirit of understanding the coupling between morphologies of soft-matter and mechanics we take up another problem in this chapter concerned with transport of semiflexible polymers in porous media.

7.1 Introduction

Transport of a dilute cloud of non-interacting particles in structured complex media underlie a variety of important physical processes in nature. Examples range from spreading of water and contaminants in porous media [268] to solute transport in biofilms [269] and motion of engineered drugs inside tumors [270]. In these problems, typically a concentrated particle distribution spreads as it is transported in the tortuous geometry due to the action of external flow, forces and molecular diffusion. For a large number of such problems

the long-time transport process can be described by an effective hydrodynamic dispersion tensor \mathbf{D} that depends on the *microtransport* dictated by flow topologies, physio-chemical processes and the micro-structure geometry. Theoretical description of asymptotic transport coefficients forms the basis of *macrotransport* theory [271] that serves as the backbone of many industrial applications ranging from filtration to the design of chromatographic device.

Even though the macrotransport theory of point-like passive [272] and active [273] Brownian particles in porous media is well developed, modeling transport of elongated or deformable finite-size particles remains a challenging task due to non-trivial particle-obstacle interactions and excluded volume effects. Probably one of the earliest examples of this problem is in the celebrated reptation theory of de Gennes [274]. In reptation one is concerned with the thermal motion of a long linear polymer chain past fixed obstacles that serves as a model of entangled macromolecules in polymer melts [95]. Diffusion of stiffer semiflexible filaments in porous media have also been shown to follow the reptation picture, albeit with different kinetic exponents [275]. Understanding the transport of flexible polymers in porous media under the application of external forces also has extensive applications in chromatographic device designs for long chain DNA molecules. Fast and efficient size dependent separation of DNA molecules play an important role in their mapping and sequencing, crucial for genomic analysis [276]. Compared to classical gel based electrophoretic separation, modern microfluidic chromatographic devices have proven to be much more efficient for these problems [277]. In these devices DNA molecules are transported in a 2D lattice of structured microposts under the application of an external electric field. The DNA repetitively collides with the posts of the array, with a size-dependent collision time leading to rapid separation [278]. DNA molecules' their persistence length ℓ_p is much smaller than their contour length L , and the dynamics is governed by a competition

between stretching and entropic preference of a coiled state. As a result, during transport, the molecules hook and unhook from the micro-posts with a dynamics similar to a rope over pulley and conformations resembling various English alphabets which have been studied extensively in experiments, simulations and through continuous time random walk (CTRW) models [278–285].

Contrary to long chain polymer molecules, dynamics of semiflexible polymers with $L \sim \ell_p$ is dominated by a competition between local bending forces, line tension that enforces inextensibility and thermal fluctuations. These lead to a number of dynamic buckling instabilities and lead to non-trivial filament conformations that have been well characterized in unbounded flows [7,8]. Filament transport has also been studied in cellular flows where buckling instability driven stretch-coil transition can lead to diffusive or sub-diffusive transport of the center-of-mass [111,113,115]. However stiff polymer dynamics in structured porous media has largely been overlooked and most of the studies are restricted to the limit of reptation [275,286]. Understanding their dynamics in crowded environment is relevant for transport of stiff biopolymers like actin and microtubules [287], movements of micro-organisms in porous media [288] and for biological agents, with the potential to maximize their transport through interactions with the environment [289].

In this chapter, we use direct numerical simulations to study transport of semiflexible polymers modeled as fluctuating inextensible Euler elastica, past a 2D periodic lattice of circular obstacles in presence of a streaming flow. We aim to characterize essential features of the transport that results from coupling between deformations due to dynamic buckling and polymer-obstacle scattering, finally leading to a long-time diffusive behavior. This is in contrast with active filaments that have a sub-diffusive transport in disordered media as shown recently in numerical simulations [287]. In Section 7.2 we discuss the theoretical model for the fluctuating polymer and the scattering dynamics. In Section 7.3

we describe three main modes of polymer transport and how they can be used to explain asymptotic hydrodynamic dispersion. In Section 7.4 we build on our understanding of polymer-obstacle interactions to propose a simple design of a chromatographic device that is able to sort polymers based on their lengths. We conclude in Section 7.5.

7.2 Problem setup and methods

We study the dynamics, morphologies and long-time asymptotic transport of a dilute suspension of semi-flexible polymers with $L \sim \ell_p$ in a doubly periodic two-dimensional porous media under the influence of a streaming flow. The porous medium as shown in Figure 7.2 is idealized as an infinite lattice comprised of rigid circular obstacles of diameter a . The distance between successive pillars λ is identical in the (x, y) direction resulting in a representative square unit cell. The ordered array is characterized by the porosity $\epsilon = S_f/S_t$, or ratio of the fluid area S_f of an unit cell over its net area S_t . Under the application of a macroscopic pressure gradient, a flow develops in the porous media with far-stream velocity u_∞ . The velocity field $\mathbf{u}(\mathbf{x})$ in the unit cell is the solution of Stokes equation obtained numerically using the boundary integral method with an appropriate choice of Green's function [40, 273]. Computed streamlines for two representative cases are shown in Figure 7.1. The flow topologies are governed by the distance between obstacles λ and the incidence angle Θ made by the streaming flow with the x -axis.

We model the polymers as fluctuating Euler-elastic with the hydrodynamics given by the local slender body theory as described in Chapter 2. The filament length is given by L and ℓ_p denotes the persistence length like before. In order to non-dimensionalize the governing equation we use the diameter of the pillars a as the length scale, u_∞ as the velocity scale for the external flow, B/L^2 as the scale for elastic forces, $\sqrt{L/\ell_p}B/L^2$ as the scale for Brownian forces [115] and the relaxation time of the polymer $\tau = 8\pi\mu L_f^4/Bc$ as

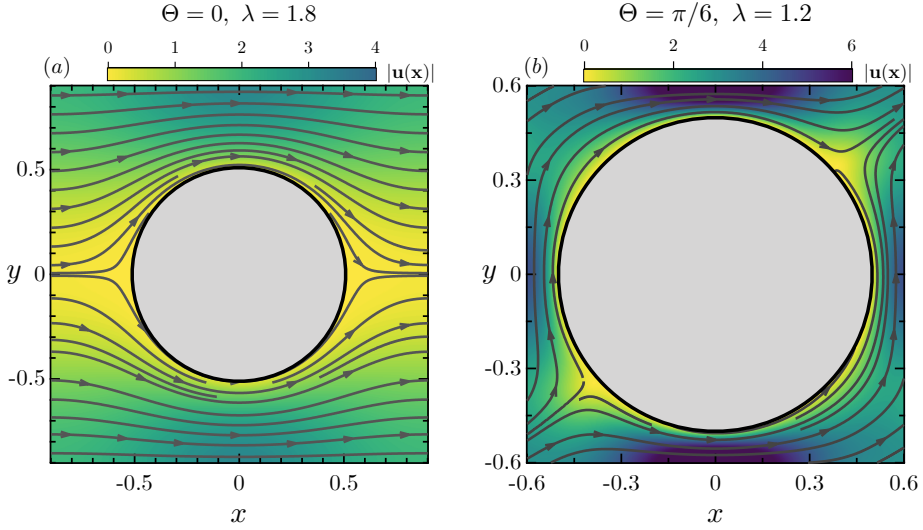


Figure 7.1: Streamlines inside an unit cell for two different lattice porosity and incidence angle of the flow.

the time scale. With these choices the dimensionless governing equation is given by:

$$\frac{\partial \mathbf{x}(s, t)}{\partial t} = \bar{\mu} \mathbf{u}(\mathbf{x}(s, t)) - \boldsymbol{\Lambda} \cdot \left(\mathbf{x}_{ssss} - (\sigma \mathbf{x}_s)_s + \sqrt{L/\ell_p} \boldsymbol{\xi} \right), \quad (7.1)$$

where $\bar{\mu} = 8\pi\mu L^4 u_\infty / Bac$ is the familiar elastoviscous number comparing the time scale of bending relaxation to the time scale of the characteristic shear u_∞/a by the imposed flow and serves as an effective measure of mean hydrodynamic forcing. $\boldsymbol{\xi}$ is a Gaussian random vector with zero-mean and unit variance and $\boldsymbol{\Lambda}$ is the local operator of SBT (see Chapter 2). As outlined previously, the resulting dynamics depend strongly on the flow-topology and the micro-structure geometry. This is characterized by three additional dimensionless parameters:

$$\frac{L}{a}, \quad \epsilon = 1 - \frac{\pi a^2}{\lambda^2} \quad \text{and} \quad \Theta, \quad (7.2)$$

where L/a compares the filament length to the obstacle diameter, ϵ is the porosity and Θ as defined before is the direction of the streaming flow u_∞ with respect to the x axis. In order to perform a systematic study in this high dimensional parameter space we focus at a fixed $\ell_p/L = 20$ that characterizes the typical thermal fluctuations in the problem and

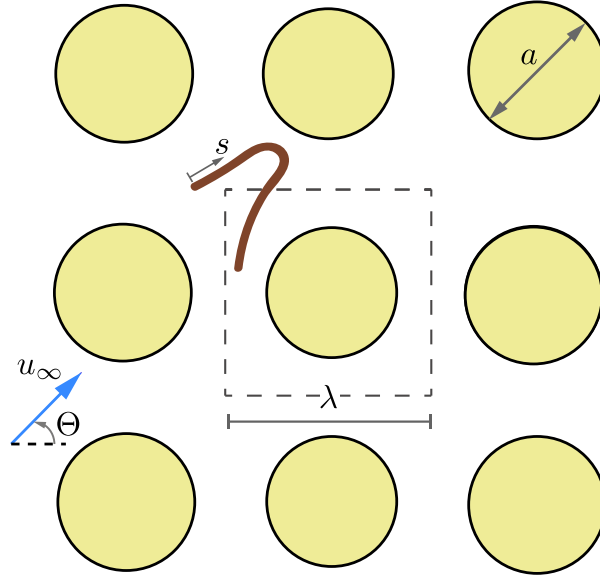


Figure 7.2: Schematic of the 2D lattice and a representative unit cell.

also limit ourselves on $L/a = 0.7$ until our discussion on sorting of polymers in Section 7.4. Central to the present study is the prescribed mechanism of polymer-pillar scattering. For this, we allow the filaments to have tangential motion past the obstacles that result in a *gliding* behavior. Any motions normal to the pillars are avoided by a smooth hydrodynamic repulsion as outlined in [290] that prevents filament penetration. Details of the contact mechanism is described in Appendix D.

7.3 Results and discussion

7.3.1 Modes of transport

With the aim of understanding long-time transport properties we first focus on characterizing the key features of individual filament dynamics at the pore scale that dictate the emerging behavior.

The interstitial velocity field can be approximated as a linear flow at the scale

of the filament. This allows us to understand a few aspects of the dynamics from the known results in unbounded shear flows [7]. Typically, in weak flows the fibers tumble quasi-periodically with small shape fluctuations reminiscent of classical Jeffery orbits [97]. Increasing the elastoviscous number $\bar{\mu}$ results in *C* and *U* shaped conformation due to buckling instabilities. However, the scattering dynamics introduce additional subtleties in this description where now a filament can strongly deform or buckle while interacting with an obstacle even in relatively weak flows. In the explored parameter space this results in primarily three modes of transport as discussed below.

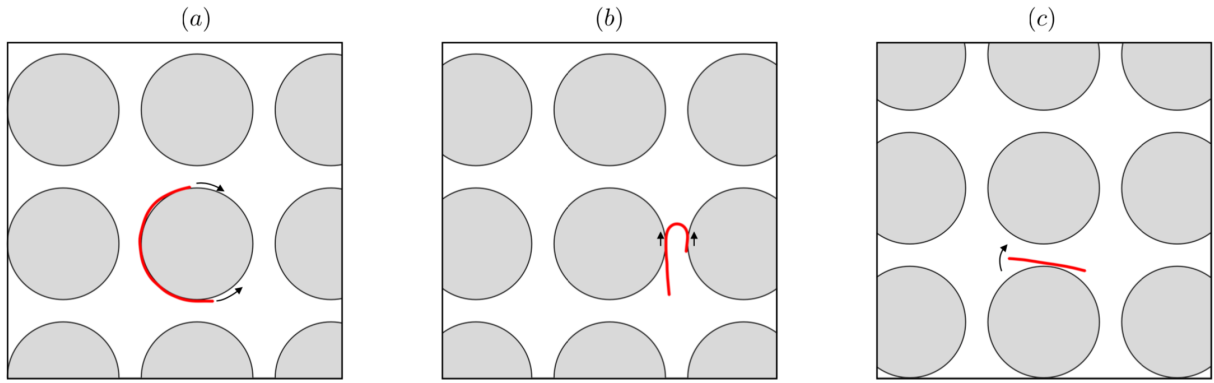


Figure 7.3: Typical conformations of the filaments and resulting dynamics: (a) trapping, (b) Gliding and (c) vaulting from scattering with micro-pillars. The arrows indicate possible direction of motion.

- *Trapping:* During the transport process polymers can wrap around the circular obstacles as shown in Figure 7.3(a) resulting in periods of prolonged trapping. As expected, trapping events are frequent for long polymers or with strong flows in densely packed lattices. The filament relies fundamentally on Brownian motion for shape fluctuations that allow it to escape a trapped mode by sliding along the obstacles.
- *Gliding:* Irrespective of the filament length and porosity of the lattice, a polymer can glance or slide past obstacles which is a direct consequence of the intrinsic scattering

mechanism. In dense beds this results in a *squeezing* mode of transport as illustrated in Figure 7.3(b) with the black arrows indicating allowable directions of motion. The incidence angle Θ of the incoming flow plays an important role in the selection between trapping and gliding. For $\Theta = 0$ or $\pi/2$ the filaments almost always avoid being trapped and can get locked in the *squeezing* mode of transport which we reveal in the subsequent discussions.

- *Vaulting:* Finally below the threshold of buckling we observe Brownian vaulting of fibers. These vaults as shown in Figure 7.3(c) are distinct from Jefferey orbits in unbounded flows. In this mode, a filament uses its contact point with a pillar as a hinge to slide, rotate and move forward in a fashion similar to what has been observed during oscillations of fibers in confined micro-channels [291].

7.3.2 Probability distributions and filament trajectories

With our understanding of the three distinctive modes of transport we now proceed to explain main features of the filament trajectories as a function of various dimensionless numbers.

We first consider the probability distribution function of the entire polymer chain inside a representative unit cell. The distribution is computed by averaging over all the unit cells visited by the polymer and is subsequently normalized to unity. Figure 7.4(a)-(c) exhibit this distribution in a dense lattice for different incidence angle Θ of the streaming flow. We notice that for $\Theta = 0$ and $\pi/4$ this distribution has a mirror symmetry with respect to the flow direction. As discussed previously and also evident from Figure 7.4(a), for $\Theta = 0$ the filament is locked in a *squeezing* mode between two successive pillars of the dense bed where it relies on gliding between the obstacles to move forward. This is further highlighted in the Figure 7.4(d) where we plot the associated center-of-mass

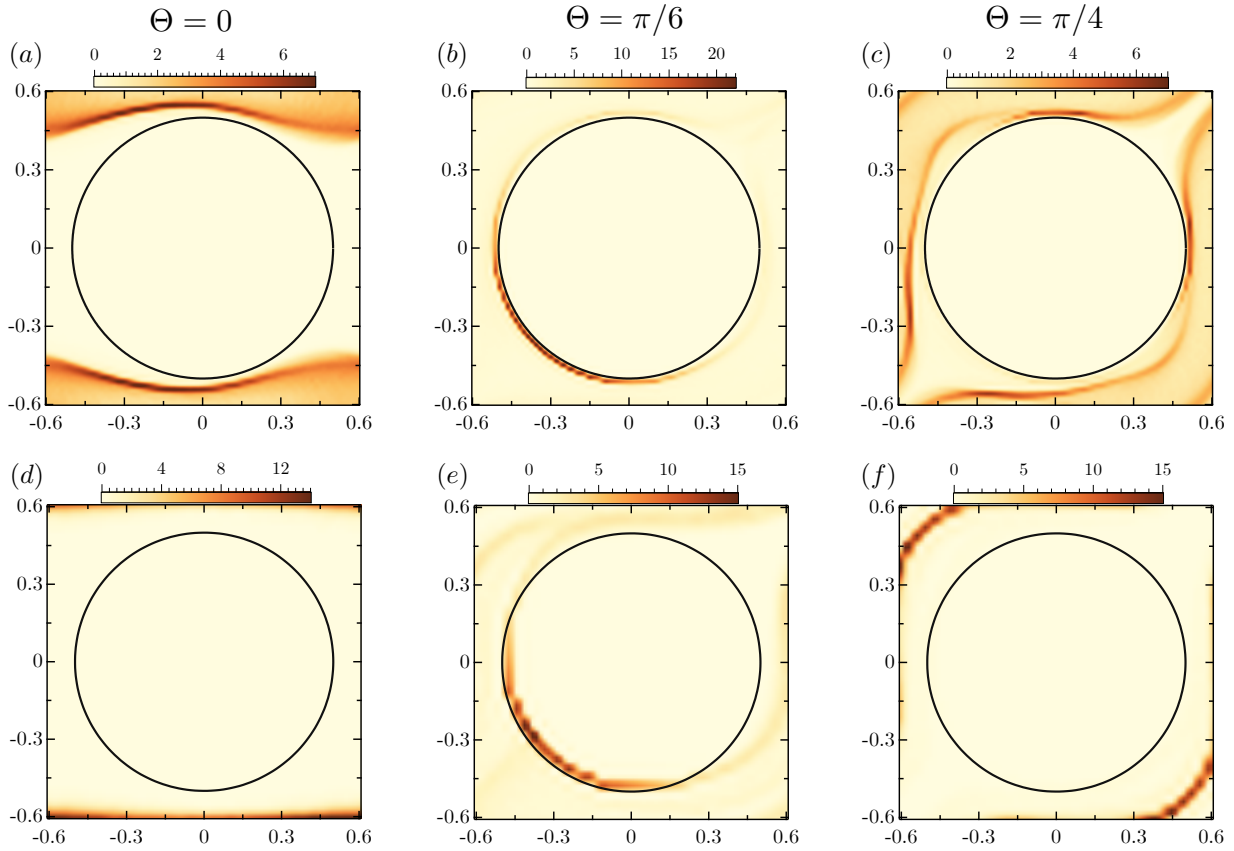


Figure 7.4: Top: (a)-(c) The panel shows the probability distribution of full polymer conformation for different incidence angle of the streaming flow. Bottom: (d)-(e) Probability distribution of the center-of-mass. The black circle represents the circular pillar. Parameter values: $L_f/a = 0.7$, $\epsilon = 0.4546$ and $\bar{\mu} = 8 \times 10^3$.

(COM) distribution of the polymer. The COM distribution function peaks at the symmetry plane of the lattice and is vanishingly small elsewhere inside the unit cell. This further corroborates the caged dynamics of the polymer and its inability to diffuse in the vertical direction with the spaces between pillars acting as entropic traps [292]. *Gliding* still remains the primary mode of transport for $\Theta = \pi/4$, but the dynamics is not caged in this case. Due to symmetry the filament can glide in both x -and y -directions with equal probability resulting in a distribution shown in Figure 7.4(c) that bears resemblance to the streamlines of the flow. Finally, we observe a transition to the *trapping* mode when

the flow is at $\Theta = \pi/6$. In absence of symmetry the transport results in chaotic scattering dynamics with frequent events of trapping of polymers around the obstacles. This is evident in Figure 7.4(b) where the distribution peaks only in the vicinity of the obstacle. The accompanying COM distribution in Figure 7.4(c) shows a peak inside the obstacle which must correspond to frequent wrapping of polymers around pillars, a typical characteristic of the trapping mode as shown in Figure 7.3(a). A similar alteration between *gliding* and *trapping* can take place as a function of the flow strength $\bar{\mu}$. This is illustrated in Figure 7.5 where we show COM probability distribution for two different flows with $\Theta = \pi/6$. As evident from the distribution in Figure 7.5(a), in weak flow both trapping and gliding contribute to the transport while the polymer remains predominantly trapped in strong flows. The dominant mode of transport in this case is selected from a competition between flow induced buckling instabilities preferring deformed conformations and sliding resulting from filament-obstacle interactions.

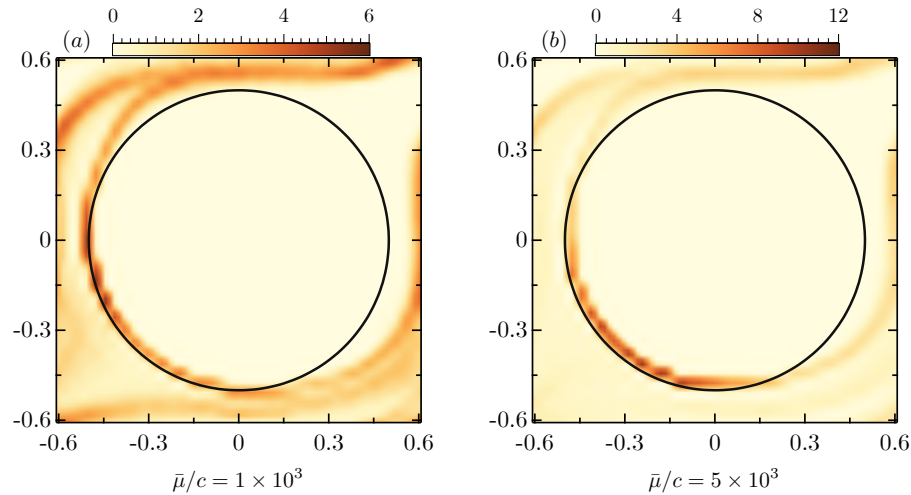


Figure 7.5: Probability distribution of polymer center-of-mass for different flow strengths. Parameter values identical to that in Figure 7.4 with $\Theta = \pi/6$.

Features of the scattering process are further revealed in Figure 7.6 where we display distributions of successive filament conformations overlaid by subtracting the instant-

taneous COM. Figure 7.6(a) now clearly captures the caged behavior of the filament where one can observe two dominant conformations, both resembling the rotated letter U , one being more concave than the other. As the filament squeezes through two pillars, it oscillates between these two dominant shapes in a breathing pattern. Conformations for angle $\Theta = \pi/4$ exhibit a sweeping pattern spanning an angle of $\pi/2$ that results from symmetric gliding in the horizontal and vertical direction. The chaotic scattering process for $\Theta = \pi/6$ is captured in Figure 7.6(b) where we observe a zoo of conformations without any distinct peaks, hinting at the randomness of the process.

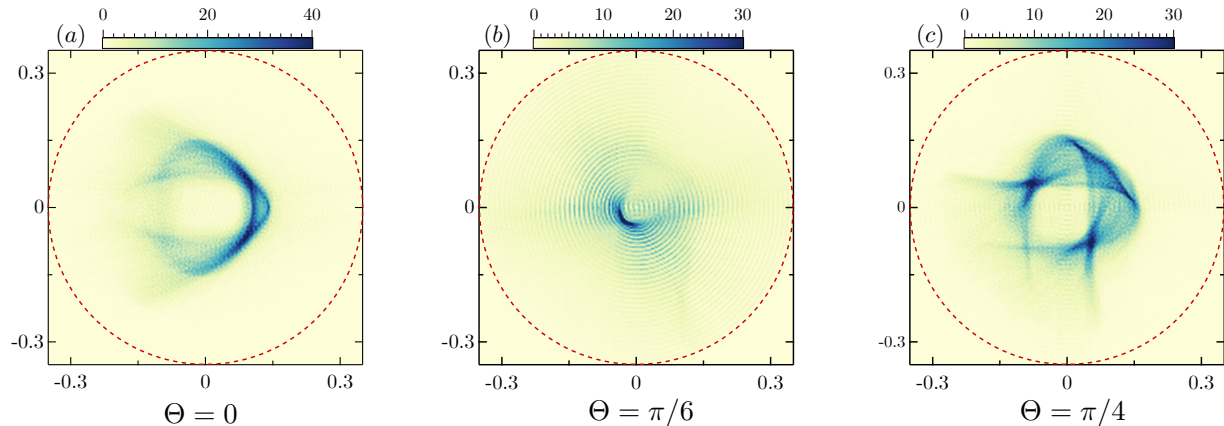


Figure 7.6: (a)-(c) Probability distribution of overlayed filament conformation inside a unit cell for different incidence angle of the streaming flow. The red circle with diameter $L_f/a = 0.7$, represents the allowable spread of the filament.

In order to quantitatively characterize these three distinctive dynamics we use the Gyration tensor introduced in Chapter 3 which is defined as:

$$G_{ij}(t) = \frac{1}{L} \int_0^L [x_i(s, t) - \bar{x}_i(t)] [x_j(s, t) - \bar{x}_j(t)] ds, \quad (7.3)$$

where $\bar{\mathbf{x}}(t)$ is the COM of the filament. The angle ϕ between the mean filament orientation and the flow direction is provided by the eigenvector of G_{ij} associated with the dominant eigenvalue [7]. Figure 7.7 shows the power-spectral density of the filament mean orientation as a function of dimensionless frequency. We notice that for $\Theta = 0$ there are two

sharp peaks that can be mapped back to the filament breathing between two dominant conformations in an almost time-periodic trajectory. For $\Theta = \pi/4$ we observe multiple peaks in the spectrum indicative of quasi-periodicity [216] that results from gliding of several repeating conformations in the lattice. Finally the chaotic trajectory for $\Theta = \pi/6$ is well characterized by the absence of any peaks in the power spectrum of mean orientation. As discussed the filament remains mostly trapped around the obstacles in this case. However, the distribution of stopping times between successive trapping events is well spread, resulting in chaotic trajectories.

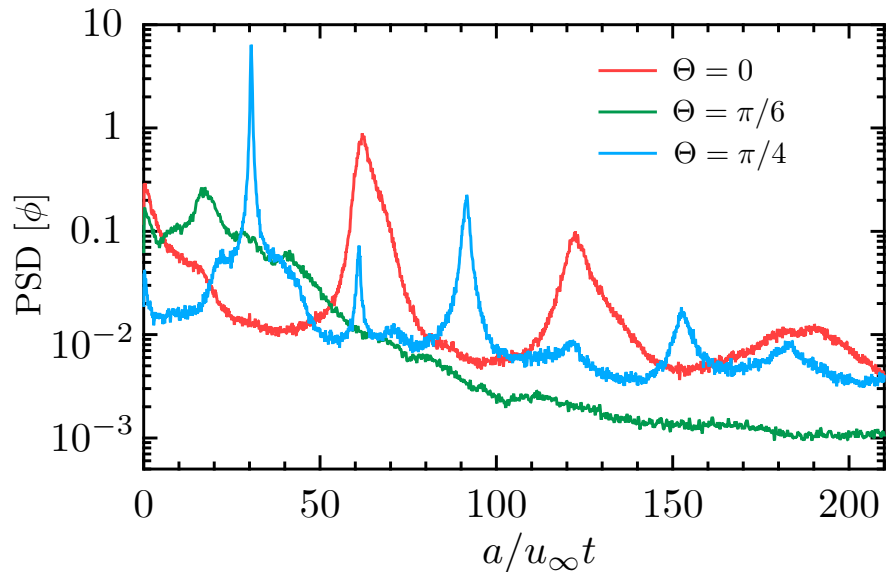


Figure 7.7: Power spectral density of the mean orientation angle ϕ of the filament with the flow as a function of dimensionless frequency. Parameter values identical to that in Figure 7.4.

7.3.3 Asymptotic transport and hydrodynamic dispersion

With the understanding of individual filament dynamics at the pore-scale we now proceed to quantify asymptotic transport properties of the problem.

The asymptotic dispersivity is a symmetric tensor given by:

$$\mathbf{D} = \frac{1}{2} \lim_{t \rightarrow \infty} \frac{d}{dt} \boldsymbol{\Sigma}(t). \quad (7.4)$$

In the above expression $\boldsymbol{\Sigma}(t)$ is the mean-square displacement dyadic defined as:

$$\boldsymbol{\Sigma}(t) = \langle [\bar{\mathbf{x}}(t) - \langle \bar{\mathbf{x}}(t) \rangle] [\bar{\mathbf{x}}(t) - \langle \bar{\mathbf{x}}(t) \rangle]^T \rangle, \quad (7.5)$$

where $\bar{\mathbf{x}}(t)$ is the instantaneous COM as defined previously and $\langle \cdot \rangle$ denotes ensemble average. We have computed $\boldsymbol{\Sigma}(t)$ for different setups of the present problem by averaging over more than hundred long-time filament trajectories over thousand unit cells. We first show the result for two representative cases in Figure 7.8 with $\Theta = 0$ and $\Theta = \pi/6$ that allows us to relate the *microtransport* described in previous section to the *macrotransport*.

Figure 7.8(a) shows the two relevant components of the mean-squared-displacement (MSD) as a function of time for the previously discussed case of a flow at $\Theta = 0$. Two interesting features stand out. First, we notice that the MSD in the y direction completely saturates. While we also observe saturation in Σ_{xx} as indicated by the shaded regime, it eventually grows linearly with time. The pre-asymptotic saturation in Σ_{xx} is a direct consequence of periodic trajectories of filament discussed in previous section that results in ballistic transport with the finite value of Σ_{xx} in the saturation regime resulting from averaging over different initial conditions. We attribute the linear growth in MSD at asymptotic times to shear induced dispersion that follows the classical mechanism first proposed by Taylor [293]. The resulting diffusivity depends on the flow strength $\bar{\mu}$. The complete saturation of Σ_{yy} results from the caged dynamics that restricts the filament between two pillars preventing any transverse motion apart from molecular diffusion as seen in Figure 7.4(d). We believe for very long times the molecular diffusion in the transverse direction will result in a diffusive transport which is difficult to capture in our simulations. Figure 7.8(b) shows time evolution of all the components of $\Sigma(t)$ for the flow at $\Theta = \pi/6$.

In this case all the three components that specify the tensor grows linearly with t in the asymptotic limit. The pre-asymptotic time is also shorter in this case since the filament is able to sample the unit cell efficiently through its chaotic dynamics.

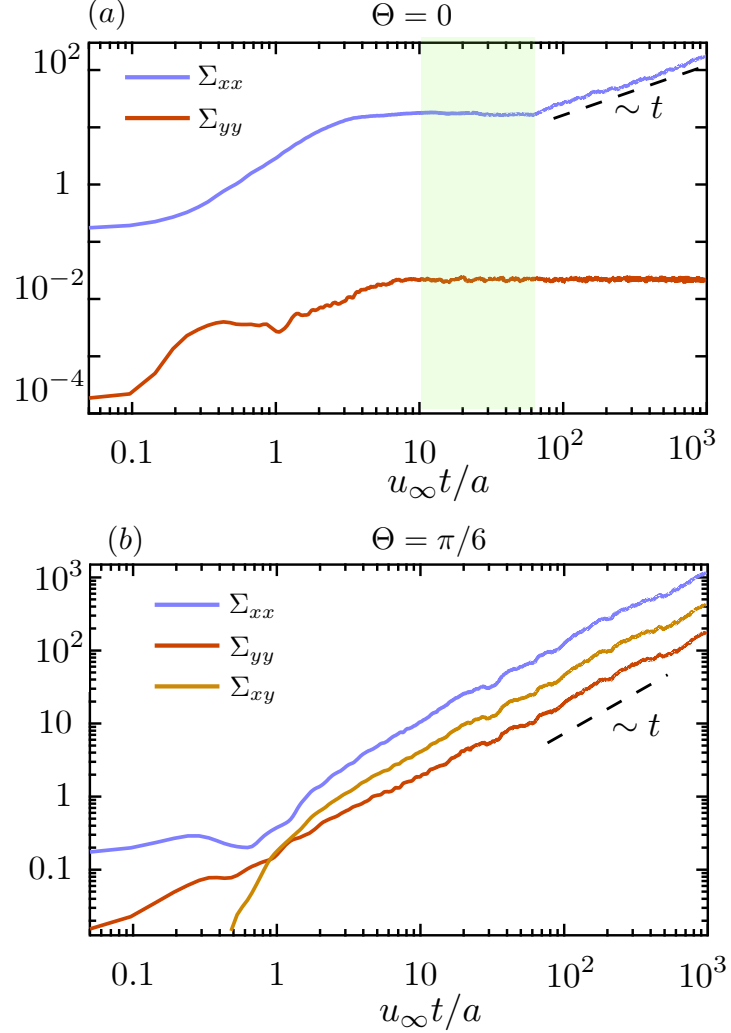


Figure 7.8: Components of the mean squared displacement as a function of time for two different incidence angles of the streaming flow. Parameter values identical to that in Figure 7.4.

As seen in this example, for an arbitrary incoming flow, the dispersion tensor is non-diagonal and can be expressed as $\mathbf{D} = D_1 \mathbf{e}_1 \mathbf{e}_1 + D_2 \mathbf{e}_2 \mathbf{e}_2$ where (D_1, D_2) are its eigenvalues with corresponding eigenvectors $(\mathbf{e}_1, \mathbf{e}_2)$. In this case we quantify dispersion by the

maximum eigenvalue $D^{\max} = \max(D_1, D_2)$ that dictates the rate of spreading of a dilute suspension of filaments.

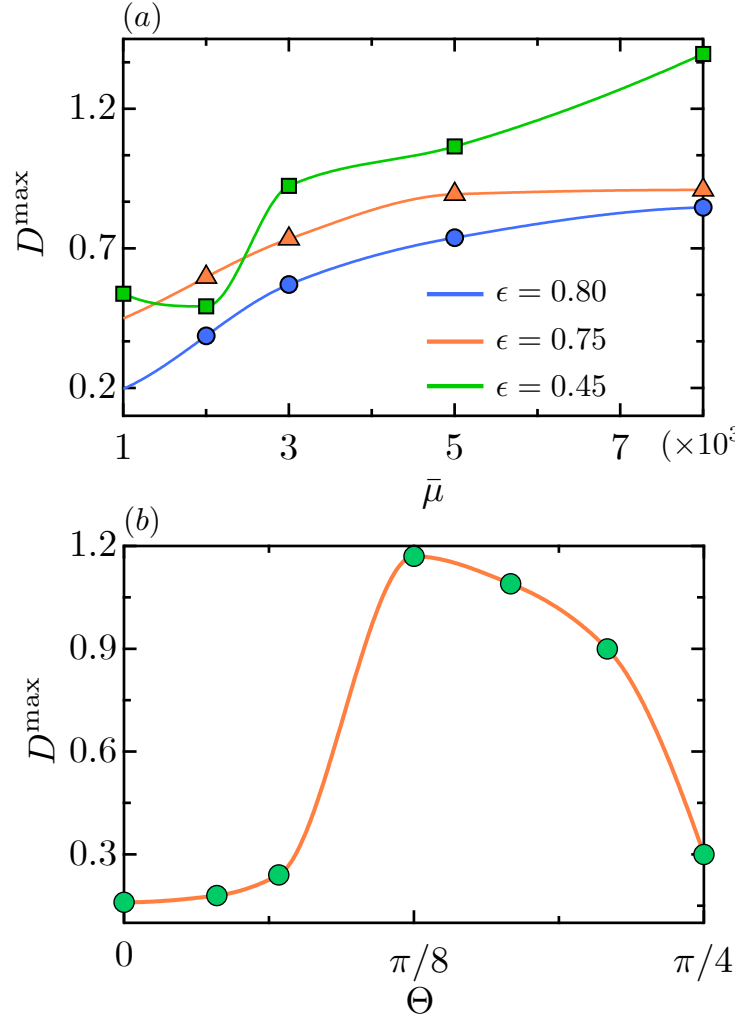


Figure 7.9: (a) Variation of D^{\max} with Θ , with other parameters being same as as Figure 7.4. (b) Variation of D^{\max} with $\bar{\mu}$ at a fixed value of $\Theta = \pi/6$ for different porosity of the lattice.

We now discuss the variation of this dominant eigenvalue D^{\max} as a function of the incidence angle and the flow-strength. Figure 7.9(a) shows the dependence of dispersivity with flow strength in lattices with varying porosity for a fixed incidence angle of $\Theta = \pi/6$. For large porosity (small volume fraction) the filament is transported with-

out much hindrance and the dispersion increases monotonically with flow strength due to shear-enhanced dispersion [271]. However, in dense lattices D^{\max} can be non-monotonic with $\bar{\mu}$ as seen from the green curve of 7.9(a). This illustrates an additional subtlety in the transport process: the competition between trapping and shear. Shear enhances dispersion but in a dense lattice it also increases the probability of trapping around obstacles. These frequent trapping events act as entropic barriers and have the potential to hinder asymptotic transport as seen in 7.9(a) for $\epsilon = 0.45$. On the other hand for a weaker flow, the filament alternates between the trapping, gliding and the squeezing mode to spread more efficiently. Finally for large $\bar{\mu}$ the transport is dictated by shear which subsequently leads to a monotonic growth in dispersivity.

In Figure 7.9(b) we kept $\bar{\mu}$ or the shear in the unit cell fixed and varied the incidence angle Θ to understand its role in dispersion. The results suggest that dispersion is maximum for $\Theta \approx \pi/8$ and is minimum for $\Theta = 0$. This can be appreciated by the micro-transport outlined in the previous sections. For a fixed shear, a dilute cloud is spread in the lattice most efficiently when there are chaotic trajectories allowing fast separation of nearby polymers. Any symmetric flow-patterns hinder dispersion due to quasi-periodic or periodic trajectories of the filaments [294].

7.4 Chromatographic separation

We have so far analyzed different modes of polymer transport and how their dynamics dictate asymptotic dispersivity. We now discuss how the scattering dynamics can be leveraged to use a 2D micro-patterned porous media as a chromatographic device that sort filaments based on their lengths.

For an illustrative example of the main features we have considered two filaments with $L/a = 0.7$ and $L/a = 1.7$. Assuming the two polymers have the same persistence

length ℓ_p , the shorter filament is subjected to smaller thermal fluctuations. In a typical microfluidic experiment the macroscopic pressure gradient sets up the flow in the porous media which fixes the characteristic shear rate u_∞/a of the problem. As a result, the longer polymer has a larger elasto-viscous number that scales as $\sim L^4$.

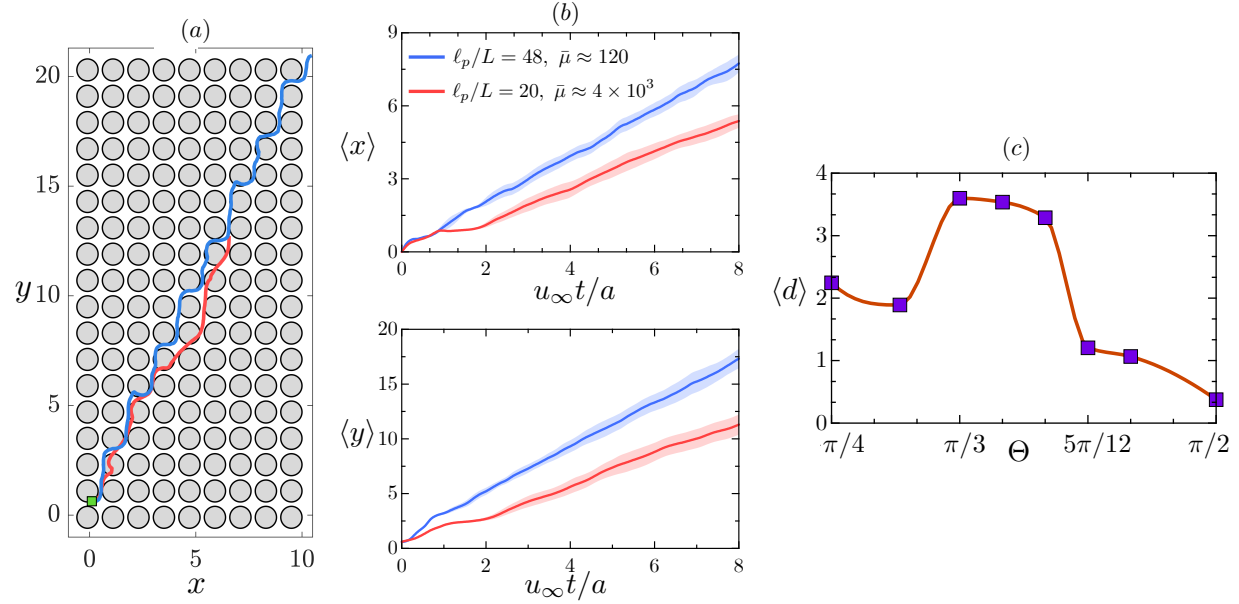


Figure 7.10: (a) A typical center-of-mass trajectory of two polymers of length $L/a = 0.7$ (blue) and $L/a = 1.7$ (red) over a given period of time with flow at $\Theta = \pi/3$. Both the polymers started from the marked point at $t = 0$. (b) Ensemble averaged x and y co-ordinates of the COM for the two polymers for the same case. (c) Time averaged separation of the two polymers as a function of the incidence angle. For all the simulations we had $\lambda = 1.2$.

Figure 7.10(a) shows typical COM trajectories of the two polymers over a given period of time, starting from the same position highlighted on the figure at $t = 0$. It is evident from the Lagrangian trajectories that over the course of time the filaments separate out quite efficiently after interacting only over 6-7 pillars. The shorter polymer (indicated in blue) experiences a $\bar{\mu}$ that is below the buckling threshold [7]. As a result it slides past the obstacles and relies on the *vaulting* mode discussed in Section 7.2 to get transported without much effective hindrance. On the other hand the longer polymer is trapped around

the obstacles and remains in a folded conformations due to buckling instabilities. Events of wrapping around the obstacles are further corroborated by the COM trajectory passing through the obstacles as shown in red on Figure 7.10(a). Ensemble averaged trajectories of the COM as a function of time is shown in Figure 7.10(b) that highlights the increasing separation of the polymers through interaction with pillars.

In order to characterize the efficiency of the separation process we define mean separation distance as

$$\langle d \rangle(T) = \frac{1}{T} \int_0^T |\bar{\mathbf{x}}_1(t) - \bar{\mathbf{x}}_2(t)| dt, \quad (7.6)$$

where $\bar{\mathbf{x}}_i(t)$ denotes the COM co-ordinate of the i^{th} polymer. Fiugre 7.10(c) shows the variation of the mean separation distance as a function of the incidence angle Θ , averaged over a dimensionless time of $T = 8$. Similar to the result on dispersivity shown in Figure 7.9(b), the separation $\langle d \rangle(T)$ is maximized for an incidence angle close to $\Theta = \pi/3$. We attribute this to chaotic scattering dynamics of the Lagrangian trajectories discussed previously. Consistent with our earlier discussions, symmetric flow patterns at $\Theta = \pi/2$ or $\Theta = \pi/4$ also result in poor separation.

7.5 Concluding remarks

We have analyzed long time transport properties of semiflexible polymers with $L \sim \ell_p$ in structured porous media under the action of an imposed flow. In contrast to entropic polymer molecules, dynamics in this case is dictated by trapping, sliding and vaulting of filaments. The dominant mode of transport results from a competition between dynamic buckling instabilities and interactions with obstacles that depend on several geometric factors like the incidence angle of the streaming flow, lattice porosity and polymer length. In the spirit of recently studied bacterial scattering in microfluidic crystals [295], we revealed that polymer-filament interactions lead to shear induced dispersion. The clas-

sical mechanism of Taylor dispersion [293] shear enhances diffusion. However, shear can also lead to trapping of polymers, hindering dispersivity in some cases: a phenomenon unique to deformable particles that bears similarities with entropic trapping.

Understanding the scattering dynamics helped us to suggest how an array of micro-post can be used to sort polymers according to their length which has potential applications in suspension rheology. The chromatographic design borrows similarities from deterministic lateral displacement devices (DLD) that are classically used to sort biological cells based on their size and deformability [296, 297]. The explored parameter space reveals how the angle of the flow can be optimized for efficient sorting of filaments. However it remains to be explored that how geometric shape optimization of pillars can enhance Lagrangian separation of polymers [298]. Future work will also address non-trivial role of hydrodynamic interactions [81] that is important in semi-dilute suspension and can potentially alter the scattering dyanmics.

This Chapter is largely based on a manuscript under preparation authored by Brato Chakrabarti, Charles Gaillard and David Saintillan. The dissertation author was the primary contributer for this work.

Chapter 8

Shear dispersion in peristaltic pumping

8.1 Introduction

In all the previous chapters we have focused on the dynamics of semiflexible polymers in flows, their morphology and transport. In Chapter 7 we have outlined a problem on polymer transport in 2D structured porous media that we idealized as an arrangement of circular pillars. In this chapter we study another relatively simple but overlooked transport problem of passive Brownian tracers in 1D periodic lattices.

Brownian tracers or solutes in a quiescent fluid disperse as a result of molecular diffusion only. Unidirectional flows such as pipe flows, however, stretch and enhance tracer concentration gradients, leading to an increased effective diffusivity at long times. In a landmark paper, Taylor [293] built upon this basic picture to analyze dispersion of a solute in a tube. He arrived at a cross-sectionally averaged advection-diffusion equation for the tracer concentration with a shear-dependent diffusivity known as the dispersivity. This effective dispersion coefficient was found to scale as Pe^2 , where $\text{Pe} = Ua/D$ is the

Péclet number of the flow expressed in terms of the mean velocity U , channel radius a and molecular diffusivity D . Taylor's calculations were based on strong intuition that was later made rigorous by [299] in the so-called method of moments. In the context of transport in a tube, Taylor's results are applicable only once the tracers have had sufficient time to sample all the transverse positions in the cross-section. The effective dispersivity is thus an asymptotic result. Since the seminal models of Taylor and Aris, many other methods have been proposed to calculate the effective dispersivity that involve: asymptotic expansions [300], Frankel and Brenner's generalized Taylor dispersion theory [301], center-manifold reduction [302, 303] and, more recently, a formulation based on Dirac's bra-ket notation [304]. All of these methods rely on a well-known asymptotic technique consisting of eliminating fast modes in a problem [303] to arrive at a simpler equation for the long-time behavior of a slow mode. The concept of a simplified cross-sectionally averaged transport equation is appealing, since in many applications one is primarily interested in determining asymptotic transport properties such as the mean velocity or mean square displacement. For this reason, the theory of shear-induced dispersion has been extensively applied to industrial problems, as well as porous media flows [305], hydrology, geophysical flows [306] and microfluidics [307]. The transport of solutes in porous media flows was formalized by Brenner [272], who proposed a general theory for dispersion in a spatially periodic matrix based on the method of moments. Brenner introduced so-called 'local' and 'global' coordinates and derived consistency conditions on statistical moments to calculate the effective dispersivity by solution of a conservation equation and quadratures over a unit cell of the periodic lattice. This technique has since been used extensively to study shear dispersion in porous materials [268, 308], electrophoretic [309] and pressure-driven flows [310] in periodic and serpentine channels [311] and in periodic networks [312] in the context of microfluidic applications. Details of many other applications and the theoret-

ical developments have been documented in [271]. These various models come under the purview of ‘macrotransport theory,’ which aims to derive asymptotic equations for measurable long-term quantities from the governing equations of microscopic field variables.

In this chapter we make use of Brenner’s generalized Taylor dispersion theory for porous media to study shear dispersion in peristaltic flow in a wavy channel. The flow is driven by a periodic wave train on the walls of the channel that produces unidirectional pumping. Peristaltic pumping is common in biological processes such as transport through the ureter and stomach by waves of cross-sectional contractions along a flexible tube; it has also been implemented in microfluidic settings [313]. The concept of shear dispersion has been used to study transport in a variety of flows with biological applications, including: dispersion in pulsatile flows [299], flows in flexible tubes with connections to respiration [314] and dispersion inside blood vessels with non-Newtonian fluids [315]. Particle transport in peristaltic pumping is a relevant biofluids problem with potential applications in micro-pumps [316, 317]. There has been a number of numerical investigation of transport in peristaltic flows involving particle simulations and Poincaré maps [317, 318] and a recent theoretical study by [304]. However, to our best knowledge the problem has not been studied theoretically in the spirit of macrotransport theory in periodic geometries.

In the absence of flow, the transport of Brownian tracers in periodic geometries has been analyzed in the context of Fick-Jacobs (FJ) theory [319]. This approach models effective diffusive dynamics of particle positions in entropic potentials [320]. Macrotransport theory has been proposed as an alternative to FJ theory to understand force-driven transport through entropic barriers [321]. Recently, [322] developed asymptotic results for the effective dispersivity using Padé approximations in the limit of pure diffusion. The theory and numerics developed in the present chapter capture this classical limit of pure diffusion as a special case but also extend it to account for peristaltic pumping.

8.2 Problem definition

8.2.1 Review of peristaltic flow

We are interested in studying dispersion using macro-transport theory in the context of peristaltic flow. In these flows, the flexible walls of a channel deform in a prescribed manner which in turn creates motion in the confined fluid. It has been found that depending on the geometry and wave speed it is possible to achieve unidirectional pumping which is also known as *peristaltic pumping* [323]. These flows are quite efficient for sanitary fluid transport and has been utilized in industries. As mentioned in the introduction, peristaltic pumping occurs in physiological processes like transport in ureter, small blood vessels and in intestine. Taylor [237], in the process of studying swimming micro-organisms, solved a problem of peristalsis. Most of the early experimental and asymptotic developments in peristalsis have been reported in [324]. Using finite difference and Lagrangian simulations, [325] studied peristalsis in a tube for finite wavelength and finite Reynolds number. There has been a number of other numerical studies involving finite elements [326], curvilinear finite differences [327] and the boundary integral method [328]. While all the above mentioned studies focus on Newtonian fluids, [329] have studied the effect of fluid rheology for a second-order fluid in axisymmetric peristaltic flow.

We have looked at the flow problem under a long wavelength approximation using lubrication theory and also for finite aspect ratio channels using a boundary integral method in the limit of Stokes flow. In this section we discuss various geometric aspects and reference frames for the problem that are relevant for both the flow and dispersion problem.

Geometry and reference frames

The geometry of unbounded peristaltic flow is that of an infinitely long channel with traveling waves on the wall. In an unbounded domain the traveling waves do not reflect back. The half-width of such a channel from centerline is then given by:

$$\tilde{w}(x, t) = h \left[1 + \gamma \sin \frac{2\pi}{\lambda} (x - ct) \right], \quad (8.1)$$

where, h is the mean height of the channel, c is the wave-speed, λ is the wavelength of the channel and γ is a geometric parameter that controls the geometry of opening of the channel. The above equation is for the upper wall and the lower wall is located at, $-\tilde{w}(x, t)$.

The problem can be looked at from a fixed reference frame (known as the laboratory frame) and denoted by (x, y) . In this reference frame every point on the wall has a transverse velocity given by $\partial_t \tilde{w}(x, t)$. However in order to solve for the hydrodynamics it is more convenient to use a translating frame of reference (ζ, η) that moves with the wave speed c in the ζ direction [323]. The fixed and translating reference frames are related as follows:

$$\zeta = x - ct, \quad (8.2)$$

$$\eta = y, \quad (8.3)$$

$$\tau = t. \quad (8.4)$$

In this moving reference frame the width of the channel walls do not vary with time. However for the chosen form of wave-form, the walls move with a velocity $-c$ in the ζ direction. Let us denote the fluid velocity by (\tilde{u}, \tilde{v}) in the fixed reference frame. The transformed variables in the translating frames are related to their counterparts as follows:

$$u(\zeta, \eta) \rightarrow \tilde{u}(x, y, t) - c, \quad (8.5)$$

$$v(\zeta, \eta) \rightarrow \tilde{v}(x, y, t). \quad (8.6)$$

We also note that the partial derivative with respect to time is transformed according to:

$$\frac{\partial}{\partial t} \Big|_{\mathbf{x}} = \frac{\partial}{\partial \tau} \Big|_{\zeta} \frac{\partial \tau}{\partial t} + \frac{\partial}{\partial \zeta} \Big|_{\tau} \frac{\partial \zeta}{\partial t} = \frac{\partial}{\partial \tau} - c \frac{\partial}{\partial \zeta}. \quad (8.7)$$

We will later see that in order to solve the dispersion problem we need to find the area of the channel enclosed by one wavelength (or an unit cell). This is readily obtained as:

$$A = \int_0^\lambda \int_{-w(\zeta)}^{w(\zeta)} d\eta d\zeta = 2h\lambda. \quad (8.8)$$

After this discussion on geometric aspects of peristaltic flow we briefly review the macrotransport theory that forms the basis of our analysis for the dispersion problem.

8.2.2 Brief review of Brenner's theory

The most general formulation for calculating dispersivity in structured, spatially periodic porous media is provided in [272] and [271]. The Taylor-Aris dispersion theory is restricted to unidirectional fluid motions, that is for flows where the mean velocity is aligned with the local flow direction. However, Brenner's formulation is not limited to such assumptions. In this section we briefly highlight the key aspects of the formulation and possible simplifications in the context of periodic geometry under consideration.

Consider a 2D geometry that is periodic and unbounded in the x direction (with unit vector $\hat{\mathbf{i}}$) and period λ . Each period of the domain consists of what we call an *unit cell*.

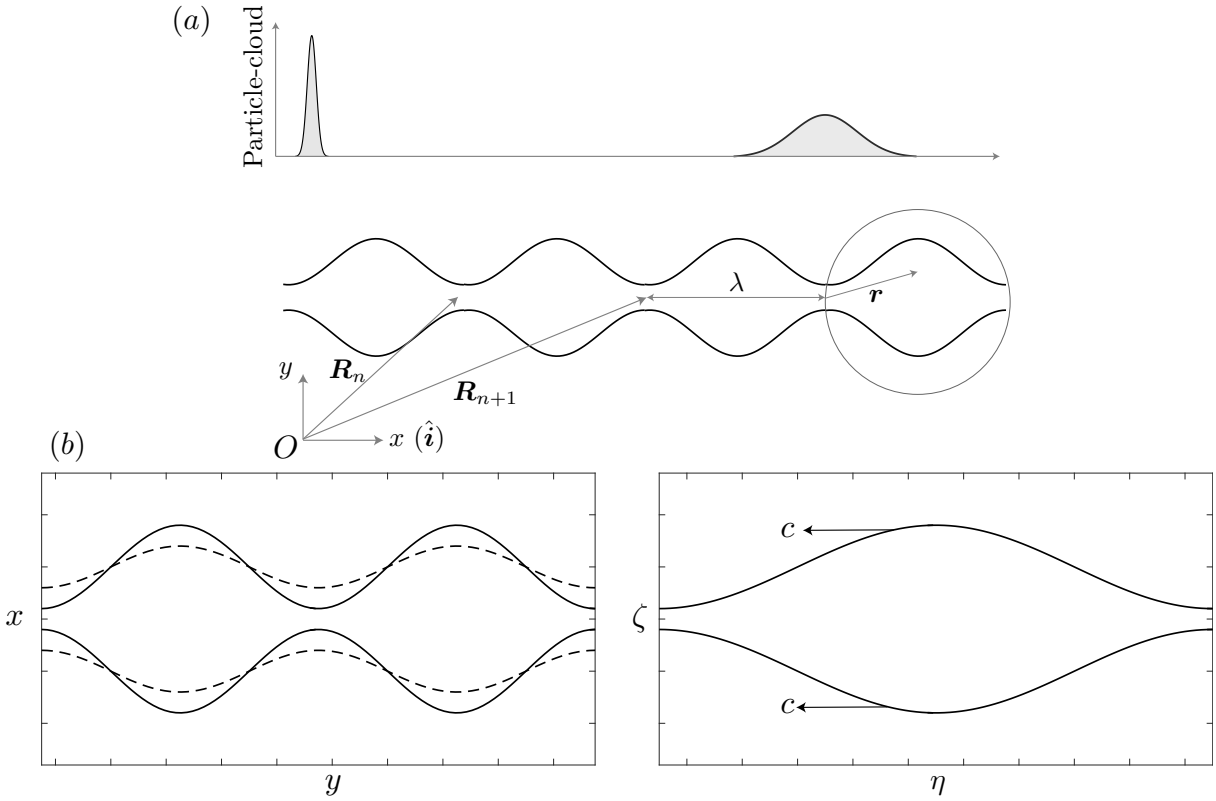


Figure 8.1: (a) A cartoon of the periodic geometry and unit cell (circled) with periodicity λ . Two consecutive cell centers w.r.t a global origin O are pointed out in the figure and inside the cell we have a local coordinate \mathbf{r} . We have also shown qualitatively the Lagrangian description of dispersion where a particle cloud gets smeared out as it moves down axially. The width or spread of the particle cloud depends on the effective dispersivity. (b) This shows the traveling waves of peristaltic flow on channel walls. The figure on the left shows the wavy wall in the fixed reference frame. For the dashed curve, $\gamma = 0.4$ and for the solid curve has $\gamma = 0.8$. The figure on the right shows a representative *unit cell* in the translating frame.

Fluid flow in this domain can happen because of pressure gradients, wall motions or through any other electro-kinetic phenomenon. In the context of the peristaltic flow there is a slip velocity on the walls. However the discussion that follows is not restricted to peristalsis. Any position in this geometry can now be described by a global position vector, \mathbf{R} , with respect to some fixed origin, O . An alternative description uses the fact

that the cell center of an unit cell, $\{n\}$ can be located by a global position vector, \mathbf{R}_n and points inside the cells are described through a cell-centered, local co-ordinate system, \mathbf{r} . Since periodicity requires, $\mathbf{u}(\mathbf{R}) = \mathbf{u}(\mathbf{R} + \mathbf{R}_n)$ where \mathbf{u} is the velocity field, it follows from this that the velocity is field is purely a function of the cell-centered local co-ordinate, $\mathbf{u} = \mathbf{u}(\mathbf{r})$.

The transport of tracer is described through a Fokker-Planck equation of the following form:

$$\frac{\partial \psi(\mathbf{R}, t | \mathbf{R}')}{\partial t} + \nabla \cdot \mathbf{J} = \delta(\mathbf{R} - \mathbf{R}')\delta(t), \quad (8.9)$$

where $\psi(\mathbf{R}, t | \mathbf{R}')$ is the probability density of finding a particle at a location, \mathbf{R} at time, t given that it was located at \mathbf{R}' at $t = 0$. \mathbf{J} is the flux associated with the pdf in a fixed reference frame and is given by

$$\mathbf{J} = \mathbf{u}\psi - D\nabla\psi, \quad (8.10)$$

where the second term is due to molecular diffusion and the first term. as Brenner mentioned is due to convection by flow arising from ‘piggy-back transport’. Since at any instant the tracer is located at some point in the domain, the normalization condition requires:

$$\int_{\Omega_\infty} \psi d^2\mathbf{R} = 1, \quad (8.11)$$

where, Ω_∞ is th entire domain. As mentioned in [271] the convergence of this integral requires sufficient fast decay of the probability density as $|\mathbf{R} - \mathbf{R}'| \rightarrow \infty$. In fact one can show that the decay of the pdf is exponential. Through the above mentioned description of cell counters and local coordinates it follows that, $\psi = \psi(\mathbf{R}_n, \mathbf{r}, t | \mathbf{R}'_n, \mathbf{r}')$. The translational symmetry in the x direction of the problem allows us to write $\psi = \psi(\mathbf{R}_n - \mathbf{R}'_n, \mathbf{r}', t | \mathbf{r}')$. This leads us to write the normalization condition as:

$$\sum_{n=-\infty}^{\infty} \int_{\Omega_c} \psi d^2\mathbf{r} = 1, \quad (8.12)$$

where Ω_c is the domain of an unit cell. Brenner's use of discrete summation over all cells and quadratures over unit cells simplifies the calculations. Due to periodicity, the consistency condition requires,

$$\psi(\mathbf{R}_n^*, \mathbf{r} + \lambda \hat{\mathbf{i}}) = \psi(\mathbf{R}_n, \mathbf{r}), \quad (8.13)$$

where \mathbf{R}_n^* and \mathbf{R}_n are global coordinates of two adjacent cell centers as indicated in figure. One can also write similar consistency condition for the gradient of the pdf. Brenner's solution then adopts the method of moments as proposed by [299]. The details of the derivation of the moment equations and consistency conditions are involved and interested readers are referred to [272] and [271]. Here we briefly outline the steps to calculate moments, their physical intepretations and introduce the so called \mathbf{B} -field equation that provides us the effective dispersivity.

- The local moment of order m is defined as follows:

$$\boldsymbol{\mu}_m(\mathbf{r}, t | \mathbf{r}') = \sum_{n=-\infty}^{n=\infty} (\mathbf{R}_n - \mathbf{R}'_n)^m \psi(\mathbf{R}_n - \mathbf{R}'_n, \mathbf{r}, t | \mathbf{r}'), \quad m \in \mathbb{Z}_0^+, \quad (8.14)$$

where, \mathbb{Z}_0^+ is the set of positive integer including zero. For our present problem with periodicity only along $\hat{\mathbf{i}}$ direction a moment of order m is a m -adic with one representative scalar. That means:

$$\boldsymbol{\mu}_m = \mu_m \underbrace{\hat{\mathbf{i}} \otimes \hat{\mathbf{i}} \cdots \otimes \hat{\mathbf{i}}}_{m-times}, \quad (8.15)$$

where, \otimes indicates direct vector product. The moments satisfy certain jump conditions across the cell-faces that can be derived by demanding consistency conditions from translational symmetry. It is also important to realize that the local moments satisfy their own FP equation that is identical to (8.9).

- Global moments of order m are now defined by quadratures over unit cells:

$$\mathbf{M}_m(t | \mathbf{r}') = \int_{\Omega_c} \boldsymbol{\mu}_m d^2 \mathbf{r}. \quad (8.16)$$

Due to the inclusion of the Dirac delta function in (8.9) as a source term it follows that $M_0 = 1$. Asumptotic solutions to moment equations (upto order 2) lead to the calculation of dispersivity. It is worth pointing out that when one takes moments of any PDE it generally leads to a hierarchy that has to be solved in steps. Consistency conditions (or jump conditions) on local moments allow one to calculate M_m through the knowledge of lower order local moments. A pictorial representation of this can be found in [271].

- The first step involves finding an asymptotic solution to μ_0 . When $t \gg \lambda^2/D$ (the residence time) the Brownian tracer has sampled many cells. At this limit the probability of finding the tracer at any local coordinate r (irrespective of the cell number) is given by:

$$\mu_0^\infty(\mathbf{r}) = \lim_{t \rightarrow \infty} \mu_0(t, \mathbf{r}). \quad (8.17)$$

Even though the tracer is performing intracellular sampling, periodicity makes it irrelevant which cell it is in. In general $\mu_0(t, \mathbf{r})$ involves this constant asymptotic value and other terms that decay exponentially fast in time. Aris's [299] analysis of dispersion also indicated exponential decay of moments over time.

- The normalization condition on the pdf, ψ requires

$$\int_{\Omega_c} \mu_0^\infty d^2\mathbf{r} = 1. \quad (8.18)$$

Associated with the asymptotic moment, μ_0^∞ there is an asymptotic flux, $\mathbf{J}_0^\infty = \mathbf{u}(\mathbf{r})\mu_0^\infty - D\nabla\mu_0^\infty(\mathbf{r})$. This flux yields the first quantity of interest namely the mean velocity of transport. It is given by:

$$\mathbf{U}^* = \int_{\Omega_c} \mathbf{J}_0^\infty d^2\mathbf{r}. \quad (8.19)$$

The asymptotic solution, $\mu_0^\infty(\mathbf{r})$ and its gradients are periodic in the x -direction and satisfy no-flux boundary condition.

- The final step involves determining the so-called $\mathbf{B}(\mathbf{r})$ -field defined in the interior of a cell that satisfies the following advection-diffusion equation:

$$D\nabla \cdot (\mu_0^\infty \nabla \mathbf{B}) - \mathbf{J}_0^\infty \cdot \nabla \mathbf{B} = \mu_0^\infty \mathbf{U}^*. \quad (8.20)$$

All the Brownian tracers are not located at the mean position \mathbf{U}^*t , and this deviation gives rise to this \mathbf{B} field that has dimensions of length. The B -field satisfies the no flux boundary condition at the walls given by $\hat{\mathbf{n}} \cdot \nabla \mathbf{B} = 0$. The consistency condition demands, $\mathbf{B} + \lambda \hat{\mathbf{i}}$ to be a periodic vector field. This can also be formulated as a jump condition on the field, \mathbf{B} :

$$\mathbf{B}(x = -\lambda) - \mathbf{B}(x = \lambda) = [\![\mathbf{B}]\!] = -\lambda \hat{\mathbf{i}}. \quad (8.21)$$

The solution of \mathbf{B} field is only determined up to a constant. The calculation of the dispersion tensor involves only gradients of \mathbf{B} , and as a result the undetermined constant does not affect the solution. In this paper we are only interested in longitudinal dispersion, parallel to the direction of mean transport. For the problem under consideration the mean transport is in the x direction. For this case we can define the longitudinal dispersivity as, $d^* = \hat{\mathbf{i}} \cdot \mathcal{D} \cdot \hat{\mathbf{i}}$, where \mathcal{D} is the dispersion tensor. This longitudinal dispersivity is given by:

$$d^* = D \int_{\Omega_c} \mu_0^\infty \nabla B \cdot \nabla B d^2 r, \quad (8.22)$$

where $B(\mathbf{r}) = \hat{\mathbf{i}} \cdot \mathbf{B}$ and D is defined earlier as the molecular diffusivity of the Brownian tracer. This completes the discussion on the calculation of effective longitudinal dispersivity.

8.3 Hydrodynamics: long wavelength approximation

We have already discussed the geometry of traveling waves and the choice of a translating reference frame with wave velocity, c , in the previous section. In this section we use the classical lubrication approximation for small aspect ratio channels to obtain the flow fields. In what follows, we have the aspect ratio of the channel $h/\lambda = \epsilon \ll 1$. Our calculation closely follows [323].

Governing equations and boundary conditions

Since time does not show up explicitly in the translating frame the governing equations for the hydrodynamics are the steady state Navier-Stokes equation along with the continuity equation for an incompressible fluid. The boundary condition is no penetration and no-slip. The no-slip condition requires, $u(\zeta, \eta)$ to have a slip velocity of $-c$ at the wall. So we have:

$$\nabla \cdot \mathbf{u} = 0, \quad (8.23a)$$

$$\rho \left[u \frac{\partial u}{\partial \zeta} + v \frac{\partial u}{\partial \eta} \right] = - \frac{\partial p}{\partial \zeta} + \mu \left(\frac{\partial^2 u}{\partial \zeta^2} + \frac{\partial^2 u}{\partial \eta^2} \right), \quad (8.23b)$$

$$\rho \left[u \frac{\partial v}{\partial \zeta} + v \frac{\partial v}{\partial \eta} \right] = - \frac{\partial p}{\partial \eta} + \mu \left(\frac{\partial^2 v}{\partial \zeta^2} + \frac{\partial^2 v}{\partial \eta^2} \right), \quad (8.23c)$$

$$u(\eta = \pm w) = -c; \hat{\mathbf{n}} \cdot \mathbf{u}(\eta = \pm w) = 0, \quad (8.23d)$$

where the symbols have their usual meaning. The symmetry of the unit cells about the centerline suggests that the axial velocity, u will be an even function of the transverse coordinate, η while the transverse velocity, v will be an odd function. These conditions result in:

$$\partial_\eta u|_{\eta=0} = 0 \text{ and } v|_{\eta=0} = 0. \quad (8.24)$$

The use of symmetry conditions allows us to solve the problem only in half of the

domain. The unit normal at the top wall is given by:

$$\hat{\mathbf{n}} = \frac{1}{\sqrt{1 + w'(\zeta)^2}} \left(-w'(\zeta) \hat{\boldsymbol{\zeta}} + \hat{\boldsymbol{\eta}} \right). \quad (8.25)$$

The no penetration condition on the top wall then provides the transverse velocity as, $v(\eta = w) = -cw'(\zeta)$. We shall later use this condition to solve for the hydrodynamics above the centerline. Often the quantity of interest in peristaltic pumping is the flow rate or pumping rate. The flow rate in the fixed reference frame at any given location is given by:

$$Q(x, t) = 2 \int_0^{\tilde{w}} \tilde{u}(x, y) dy. \quad (8.26)$$

On moving to the translating frame of reference with the use of transformed variables we have:

$$Q(x, t) = 2 \int_0^w [u(\zeta, \eta) + c] d\eta = q + 2c\tilde{w}, \quad (8.27)$$

where, q is the flow rate in the translating reference frame and is independent of time [330].

Non-dimensionalization

The non-dimensionalization is identical to the classical lubrication scalings. There are two dimensionless parameter in the problem, the aspect ratio (ϵ) and the Reynolds number. The following scales were chosen for scaling the dimensional variables:

$$\zeta \sim \lambda \quad \eta \sim \epsilon\lambda, \quad (8.28a)$$

$$\tilde{u} \sim c, \quad \tilde{v} \sim \epsilon c, \quad (8.28b)$$

$$p \sim \frac{\mu c}{\epsilon^2 \lambda}. \quad (8.28c)$$

These yields the following dimensionless equations and boundary conditions.

$$\nabla \cdot \mathbf{u} = 0, \quad (8.29a)$$

$$\epsilon Re \left[u \frac{\partial u}{\partial \zeta} + v \frac{\partial u}{\partial \eta} \right] = - \frac{\partial p}{\partial \zeta} + \left(\epsilon^2 \frac{\partial^2 u}{\partial \zeta^2} + \frac{\partial^2 u}{\partial \eta^2} \right), \quad (8.29b)$$

$$\epsilon^3 Re \left[u \frac{\partial v}{\partial \zeta} + v \frac{\partial v}{\partial \eta} \right] = - \frac{\partial p}{\partial \eta} + \left(\epsilon^2 \frac{\partial^2 v}{\partial \zeta^2} + \epsilon^4 \frac{\partial^2 v}{\partial \eta^2} \right), \quad (8.29c)$$

$$u(\eta = w) = -1, u_\eta(\eta = 0) = 0; v(\eta = w) = -w', v(\eta = 0) = 0. \quad (8.29d)$$

where the Reynolds number is given by, $Re = \rho c \epsilon \lambda / \mu$. The dimensionless width of the channel reads as, $w(\zeta) = 1 + \gamma \sin(2\pi\zeta)$. The boundary conditions of the problem were written keeping in mind that we want to solve for the velocity field in the upper half of the channel. We also note that with the given choices of the scales the flow rate is now given by:

$$q = 2\epsilon c \lambda \int_0^w u d\eta. \quad (8.30)$$

This provides us a scale for the flow rate as, $\epsilon c \lambda$. The non-dimensional flow rate is then simply given by:

$$q = 2 \int_0^w u d\eta. \quad (8.31)$$

We have intentionally not introduced separate symbols for dimensionless variables in order to keep our formulation concise. However from here on all the variables are dimensionless unless specified otherwise.

Leading order solution

In order to solve the dimensionless NS equations we seek a regular perturbation expansion in small aspect ratio (ϵ):

$$\mathbf{u} \sim \mathbf{u}_0 + \epsilon \mathbf{u}_1 + \epsilon^2 \mathbf{u}_2 \dots \quad (8.32)$$

$$p \sim p_0 + \epsilon p_1 + \epsilon^2 p_2 \dots \quad (8.33)$$

We shall later see that in order to consider the problem of dispersion we only need the leading order axial velocity field. Here we provide the leading order axial and the transverse velocity ($\mathcal{O}(\epsilon)$) field. We plug our expansions in (8.29) and from the η momentum equation we obtain:

$$\frac{\partial p_0}{\partial \eta} = 0 \implies p_0 = p_0(\zeta). \quad (8.34)$$

Since the leading order transverse velocity field is $\mathcal{O}(\epsilon)$, from the ζ momentum equation we obtain:

$$\frac{\partial^2 u_0}{\partial \eta^2} = \frac{dp_0}{d\zeta}. \quad (8.35)$$

Using the no-slip and symmetry boundary conditions we obtain the well-known parabolic profile of a lubrication problem [331]:

$$u_0 = -1 - \frac{1}{2} \frac{dp_0}{d\zeta} (w^2 - \eta^2). \quad (8.36)$$

The above solution must yield the flow rate, q . On substituting the velocity profile in (8.31) we can obtain an expression for the pressure gradient as follows:

$$\frac{dp_0}{d\zeta} = -\frac{3}{2w^3} (q + 2w). \quad (8.37)$$

In peristaltic flow one can define the mean pressure gradient that acts over one period of unit cell. This quantity is known as pressure rise (PR) [323] and is given by:

$$PR = \int_0^1 \frac{dp_0}{d\zeta} d\zeta. \quad (8.38)$$

If there is no imposed pressure gradient then the pressure rise is identically zero due to periodicity. This is a case of *pure peristalsis* where the flow takes place only due to the imposed motion of the walls. In this present paper we are only going to consider pure peristaltic flow in absence of pressure gradients. Under this condition the flow rate, q is completely determined from the geometry of the walls. Setting, PR to zero we obtain:

$$q = -2 \frac{\int_0^1 1/w^2 d\zeta}{\int_0^1 1/w^3 d\zeta} = -4 \frac{1 - \gamma^2}{2 + \gamma^2}, \quad (8.39)$$

where the integrals can be carried out using standard techniques of contour integration. Substituting the expression for pressure gradient provides us the velocity profile in terms of the flow rate and the width of the wall as:

$$u_0 = \frac{3}{4w^3} (q + 2w) (w^2 - \eta^2) - 1. \quad (8.40)$$

In order to obtain the leading order transverse velocity, $\mathcal{O}(\epsilon)$ we make use of the continuity equation. Using the above solution for the axial velocity and appropriate boundary conditions from (8.29) we obtain

$$v_0 = \frac{w'(\zeta)\eta}{4w^4} [3q(w^2 - \eta^2) - 4\eta^2 w]. \quad (8.41)$$

This completes the solution to the leading-order hydrodynamic problem.

8.4 Dispersion in the long wavelength approximation

8.4.1 Fokker-Planck in the translating frame

We have previously discussed how macrotransport theory describes the transport of Brownian tracers in terms of a Fokker-Planck (FP) equation. The FP equation of interest here is an advection-diffusion equation for the probability density of finding a Brownian tracer inside an unit cell. For a tracer located at $\mathbf{r} = \mathbf{r}'$ at $t = 0$, we have:

$$\frac{\partial \tilde{\psi}}{\partial t} + \nabla_{\tilde{\mathbf{r}}} \cdot \tilde{\mathbf{J}} = \delta(\tilde{\mathbf{r}} - \tilde{\mathbf{r}'})\delta(t), \quad (8.42)$$

where, $\tilde{\psi}(n, x, y, t)$ denotes the probability density and $\tilde{\mathbf{J}}$ is the flux given by:

$$\tilde{\mathbf{J}} = \tilde{\mathbf{u}}\tilde{\psi} - D\nabla_{\tilde{\mathbf{r}}}\tilde{\psi}. \quad (8.43)$$

In the above equations, $\tilde{\mathbf{r}}$ simply the local co-ordinate specific to an unit cell with respect to the laboratory frame. We rewrite the above equation in the translating frame of reference

and recall the definition of (8.7) to obtain:

$$\frac{\partial \psi}{\partial \tau} - c \frac{\partial \psi}{\partial \zeta} + \nabla_{\mathbf{r}} \cdot \mathbf{J} = \delta(\mathbf{r} - \mathbf{r}') \delta(t), \quad (8.44)$$

where $\psi(n, \zeta, \eta, \tau)$ denotes the probability density in the translating frame of reference.

Simplifying the divergence of the flux and recalling (8.5) we obtain:

$$\frac{\partial \psi}{\partial \tau} + u \frac{\partial \psi}{\partial \zeta} + v \frac{\partial \psi}{\partial \eta} - D \left(\frac{\partial^2 \psi}{\partial \zeta^2} + \frac{\partial^2 \psi}{\partial \eta^2} \right) = \delta(\mathbf{r} - \mathbf{r}') \delta(t). \quad (8.45)$$

We note that there is an interesting cancellation of terms that leaves us with the familiar form of the FP equation in the translating frame of reference. This form is amenable to the treatment of macrotransport theory for calculating effective dispersivity [271].

8.4.2 Asymptotic moments and mean velocity of transport

In order to find asymptotic solutions (long time) to the problem, the method of moment is used. Then the first step of macrotransport theory requires us to calculate the intracellular field, $\mu_0^\infty(\mathbf{r})$, that describes the long term probability of finding a tracer at a position \mathbf{r} irrespective of the cell counter, n . This is the asymptotic solution for the first local moment. For an incompressible fluid it can be shown that μ_0^∞ is always a constant [309]. Then the normalization condition readily yields:

$$\mu_0^\infty = \frac{1}{A}, \quad (8.46)$$

where A is the area of the unit cell as obtained in (8.8). The asymptotic flux associated with this moment is then given by:

$$\mathbf{J}_0^\infty = \mathbf{u} \mu_0^\infty - D \nabla \mu_0^\infty. \quad (8.47)$$

The no-flux boundary condition at the top walls are identically satisfied due to the boundary conditions on the velocity field. The mean velocity with which the tracer moves

at long time is now given by:

$$\mathbf{u}^* = \int_{\Omega_c} \mathbf{J}_0^\infty d\zeta d\eta, \quad (8.48)$$

where, Ω_c is the domain of an unit cell. Since the mean transport is in the $-\hat{\zeta}$ direction the mean solute velocity will also be in the same direction. So we seek a solution of the form, $\mathbf{u}^* = U^* \hat{\zeta}$. An appropriate scale for this mean transport velocity will be, λ/D . Using this we obtain:

$$\frac{D}{\lambda} U^* = \frac{2\epsilon\lambda^2 c}{A} \int_0^1 \int_0^w u_0 d\eta d\zeta, \quad (8.49)$$

where u_0 is the leading order solution for the axial velocity. Recalling the definition of flowrate (8.31) and the unit cell area (8.8) we obtain

$$U^* = \frac{qPe}{2}, \quad (8.50)$$

where, $Pe = c\lambda/D$ is the Péclet number that measures the relative strength of advection over diffusion.

8.4.3 Dimensionless B -field equation and boundary conditions

In order to calculate the effective dispersivity one needs to solve for the so called \mathbf{B} -field equation. As mentioned previously, the \mathbf{B} field can be interpreted as the dispersion potential. Using the previously obtained asymptotic solution for the zeroth moment we can write:

$$\frac{D}{A} \nabla^2 \mathbf{B} - \mathbf{J}_0^\infty \cdot \nabla \mathbf{B} = \frac{\mathbf{u}^*}{A}. \quad (8.51)$$

The \mathbf{B} -field as mentioned in section 8.2.2 satisfies the no-flux boundary condition, $\hat{\mathbf{n}} \cdot \nabla \mathbf{B} = 0$ at $\eta = \pm w$. We also know that the field, $\mathbf{B} + \zeta$ is periodic. This provides a jump condition:

$$\mathbf{B}(\zeta = 0, \eta) - \mathbf{B}(\zeta = \lambda, \eta) = -\lambda \hat{\zeta}. \quad (8.52)$$

We are only interested in the axial dispersion of tracers. Since the mean transport is in the axial direction, we define the following scalar field of interest, $b = \mathbf{B} \cdot \hat{\zeta}$. We

scale the variable, b with the length scale, λ . Using the expression for the asymptotic flux, dimensional scales from (8.28) and the dimensionless mean transport velocity from (8.50) we obtain

$$\frac{\partial^2 b}{\partial \eta^2} = \epsilon^2 \left[U^* + Pe \left(u \frac{\partial b}{\partial \zeta} + v \frac{\partial b}{\partial \eta} \right) - \frac{\partial^2 b}{\partial \zeta^2} \right]. \quad (8.53)$$

The boundary conditions once non-dimensionalized become:

$$\frac{\partial b}{\partial \eta} = \epsilon^2 w'(\zeta) \frac{\partial b}{\partial \zeta}; \quad \eta = w(\zeta), \quad (8.54a)$$

$$\frac{\partial b}{\partial \eta} = -\epsilon^2 w'(\zeta) \frac{\partial b}{\partial \zeta}; \quad \eta = -w(\zeta), \quad (8.54b)$$

$$[b] = -1. \quad (8.54c)$$

For the most general \mathbf{B} field, the effective dispersivity can be obtained by performing the following quadrature over a unit cell:

$$\mathcal{D} = \int_{\Omega_c} \mu_0^\infty (\nabla \mathbf{B})^\dagger \cdot (\nabla \mathbf{B}) d\zeta d\eta. \quad (8.55)$$

In the context of axial dispersion and under the long wavelength approximation, with the use of symmetry the above expression for dispersivity can be simplified to

$$d^* = \int_0^1 \int_0^w \left[\frac{1}{\epsilon^2} \frac{\partial^2 b}{\partial \eta^2} + \frac{\partial^2 b}{\partial \zeta^2} \right] d\zeta d\eta, \quad (8.56)$$

where d^* is the dimensionless axial dispersivity defined as, $d^* = \hat{\zeta} \cdot \mathcal{D} \cdot \hat{\zeta}$. A value of $d^* = 1$ implies that the effective dispersivity is same as the molecular diffusivity of the Brownian tracers.

Leading-order dispersivity

In order to find the dispersivity we need to solve the dimensionless \mathbf{B} field equation (8.53). We notice that the small parameter arising in the differential equation is ϵ^2 . We seek a regular perturbation expansion of b :

$$b \sim b_0 + \epsilon^2 b_1 + \dots \quad (8.57)$$

We note that the validity of this expansion is more subtle than the hydrodynamics. In (8.53) due to non-dimensionalization all the terms are of $\mathcal{O}(1)$. However for large Péclet number the advective terms will no longer be $\mathcal{O}(1)$ and the appropriate condition for the validity of the perturbation expansion becomes, $\epsilon^2 Pe \ll 1$ [309, 321]. Plugging in the expansion in (8.53), we proceed to the solution of b for the first two orders.

Solution at $\mathcal{O}(0)$: At zeroth order we simply have

$$\frac{\partial^2 b_0}{\partial \eta^2} = 0, \quad \text{and} \quad \frac{\partial b_0}{\partial \eta} = 0; \quad \text{at } \eta = \pm w(\zeta). \quad (8.58)$$

The above set of equations imply, $b_0 = b_0(\zeta)$. To leading order, the b -field is independent of the transverse direction. In order to solve for this leading order field, we move on to the next order solution.

Solution at $\mathcal{O}(\epsilon^2)$: Upon collecting terms of $\mathcal{O}(\epsilon^2)$ from (8.53) the governing equation for b_1 is obtained as

$$\frac{\partial^2 b_1}{\partial \eta^2} = U^* + Pe u_0 b'_0(\zeta) - b''_0(\zeta), \quad (8.59)$$

where, u_0 is the zeroth order solution of the hydrodynamic problem. The boundary condition at this order is given by:

$$\begin{aligned} \frac{\partial b_1}{\partial \eta} &= w'(\zeta) \frac{\partial b_0}{\partial \zeta}; & \eta &= w(\zeta), \\ \frac{\partial b_1}{\partial \eta} &= -w'(\zeta) \frac{\partial b_0}{\partial \zeta}; & \eta &= -w(\zeta). \end{aligned}$$

We now integrate (8.59) with respect to η over the width of the channel. Using the above mentioned boundary conditions, the definition of the flow rate, q from (8.31) and recalling the expression for mean transport velocity, U^* from (8.50) we obtain:

$$b''_0 + \left(\frac{w'}{w} - \frac{Pe q}{2w} \right) b'_0 = \frac{q Pe}{2}. \quad (8.60)$$

The leading order field must also satisfy the jump condition, $\llbracket b_0 \rrbracket = -1$. This can be re-casted in the following form [309]:

$$\llbracket b_0 \rrbracket = \int_0^1 \frac{db_0}{d\zeta} d\zeta = \langle b_0 \rangle = -1, \quad (8.61)$$

where the angled brackets indicate axial average over an unit cell as before. We now note that (8.60) is a linear differential equation that can be easily solved using integrating factors (IF). For the present problem, the IF is given by:

$$\alpha(\zeta) = \exp \left[\int \left(\frac{w'}{w} - \frac{\text{Pe}}{2w} \right) d\zeta \right]. \quad (8.62)$$

With the use of the above integrating factor, (8.60) can be integrated once to obtain:

$$b'_0(\zeta) = \frac{q\text{Pe}}{2\alpha(\zeta)} \int_0^\zeta \alpha(\zeta') d\zeta' + \frac{K}{\alpha(\zeta)}, \quad (8.63)$$

where K is an integration constant that needs to be determined. We use the modified jump condition on b_0 to determine the integration constant. Solving for K we obtain:

$$b'_0(\zeta) = \frac{q\text{Pe}}{2\alpha(\zeta)} \int_0^\zeta \alpha(\zeta') d\zeta' - \frac{1 + \frac{q\text{Pe}}{2} \int_0^1 \frac{d\zeta}{\alpha(\zeta)} \int_0^\zeta \alpha(\zeta') d\zeta'}{\alpha(\zeta) \int_0^1 \frac{1}{\alpha(\zeta)} d\zeta}. \quad (8.64)$$

One can go ahead and integrate the above expression one more time to obtain the b field. However the solution is only determined up to an constant and in order to calculate the effective dispersivity from (8.56), we are interested in the first derivative only. Once the above quadratures are carried out, we use the relation in (8.56) to obtain:

$$d_0^* = \int_0^1 w(\zeta) b_0'^2(\zeta) d\zeta, \quad (8.65)$$

where d_0^* denotes the leading order effective dispersivity obtained using the zeroth order solution of the b field. As noted in [309] the numerical quadratures become difficult for large values of the Pe number. However one can get around this difficulty by solving (8.60) numerically using the Matlab tool `chebfun` [332].

8.4.4 Asymptotics for large and small Péclet

We have provided analytical expressions for the b -field that can be used to compute the dispersivity. As mentioned the numerical quadratures are difficult at high Pe number. In order to have a better understanding of the physics we now provide asymptotic results for the two limits of large and small Pe.

Small Péclet

In the limit of small Pe the solution to b_0 is a regular perturbation problem. We may formally seek an expansion of the form:

$$b_0 = \beta^{(0)} + \text{Pe}\beta^{(1)} + \dots \quad (8.66)$$

The leading order differential equation then simply becomes

$$\beta''^{(0)} + \frac{w'}{w} \beta'^{(0)} = 0. \quad (8.67)$$

This is an exact differential and can be integrated to obtain:

$$\beta'^{(0)} = \frac{K}{w}. \quad (8.68)$$

The boundary condition, $\langle \beta'^{(0)} \rangle = -1$ on the above quantity yields: $K = -\langle 1/w \rangle^{-1}$.

If we now substitute this in the expression for effective dispersivity we obtain

$$d_0^* = \langle 1/w \rangle^{-1} \int_0^1 \frac{w}{w^2} dx = 1. \quad (8.69)$$

So to the leading order the effective dispersivity is simply due to molecular diffusion. This should not come as a surprise since in the limit of very weak flow shear does not play much role in dispersion. In order to find the effect of flow on this we need to go to the $\mathcal{O}(\text{Pe})$ correction. After some simplifications this leads to the following differential equation:

$$\left(w\beta'^{(1)} \right)' = \frac{q}{2} \left(w - \langle 1/w \rangle^{-1} \right). \quad (8.70)$$

As the above equation being an exact derivative, it is straightforward to integrate it and obtain

$$\beta'^{(1)} = \frac{q}{2w} \left(\int_0^\zeta w d\zeta' - \zeta \langle 1/w \rangle^{-1} \right) + K'/w. \quad (8.71)$$

The jump condition on $\mathcal{O}(\text{Pe})$ correction is simply, $\langle \beta'^{(1)} \rangle = 0$. Using this condition one can solve for the integration constant, K' , as:

$$K' = -\langle 1/w \rangle^{-1} \frac{q}{2} \left[\int_0^1 \frac{1}{w} \int_0^\zeta w d\zeta' d\zeta - \langle 1/w \rangle^{-1} \int_0^1 \frac{\zeta}{w} d\zeta \right]. \quad (8.72)$$

One can carry out the above integrals numerically to obtain the solution. The dispersivity can then be calculated and is given by:

$$d_0^* = 1 + \text{Pe}^2 \left\langle w \left(\beta'^{(1)} \right)^2 \right\rangle + \mathcal{O}(\text{Pe}^4) \quad (8.73)$$

The above expression is a reminiscent of well-known Taylor dispersion, showing the Pe^2 scaling in dispersivity.

Large Péclét

In this limit we first divide (8.60) to obtain a small parameter, $\delta = 1/\text{Pe}$ for our problem. We obtain:

$$\delta b_0'' + \left(\delta \frac{w'}{w} - \frac{q}{2w} \right) b_0' = \frac{q}{2}, \quad \text{where } \delta = 1/\text{Pe}. \quad (8.74)$$

This at first look appears to be a boundary layer problem with a boundary layer of thickness δ [333]. However the asymptotics are simplified by a regular perturbation expansion in the small parameter, δ and the leading order solutions do satisfy all the boundary conditions. So we seek an expansion of the form:

$$b_0 \sim \beta^{(0)} + \delta \beta^{(1)} + \delta^2 \beta^{(2)} + \dots \quad (8.75)$$

At order zero the solution simply becomes:

$$\beta'^{(0)} = -w. \quad (8.76)$$

Since w is a periodic function of the form, $w = 1 + f(\zeta)$ where, $f(\zeta)$ is a periodic function, it already satisfies the jump condition, $\langle \beta'^{(0)} \rangle = -1$.

$$\beta'^{(0)} + \frac{w'}{w} \beta'^{(0)} - \frac{q}{2w} \beta'^{(1)} = 0. \quad (8.77)$$

On using the zeroth order solution we find:

$$\beta'^{(1)} = -\frac{4}{q} w w'. \quad (8.78)$$

Finally using the first order solution we can obtain:

$$\beta'^{(2)} = \frac{8}{q^2} (-2w w'^2 - w^2 w''). \quad (8.79)$$

It is easy to verify that by virtue of the periodic form of the width both the first and second-order solution naturally satisfy the boundary conditions. The dispersivity is now given by

$$d_0^* = \langle w^3 \rangle + \mathcal{O}(\delta^2) + \dots \quad (8.80)$$

At the next order we need to evaluate the following integral:

$$\mathcal{O}(\delta^2) : \int_0^1 \left[\left(\beta'^{(1)} \right)^2 + 2\beta'^{(2)} \beta'^{(0)} \right] d\zeta = \frac{4}{q^2} \langle w^4 w'' \rangle \quad (8.81)$$

In the above calculation we have used the expressions for first and second order solution and also used integration by parts. The final expression for dispersivity is then given by

$$d_0^* = \langle w^3 \rangle + \frac{4}{q^2 \text{Pe}^2} \langle w^4 w'' \rangle + \mathcal{O}(\text{Pe}^{-4}). \quad (8.82)$$

We should point out that the large Pe asymptotics are valid when, $1 \ll \text{Pe} \ll \epsilon^{-2}$.

8.4.5 Brownian simulations

In order to validate the theory we have carried out Brownian dynamics simulations with large number of particles. The Langevin equations for the present problem in

dimensionless form are given by:

$$\frac{d\mathbf{r}}{dt} = \mathbf{u}(\mathbf{r}) + \mathbf{f}^{Br}(t). \quad (8.83)$$

where, \mathbf{f}^{Br} is the Brownian fluctuations that satisfy the fluctuation-dissipation theorem:

$$\langle f_i \rangle = 0 \quad (8.84)$$

$$\langle f_i(t) f_j(t') \rangle = 2D\delta_{ij}\delta(t - t'), \quad (8.85)$$

where D is the molecular diffusivity and $\delta(t - t')$ is the Dirac's delta function. In order to numerically march forward in time we used an explicit Euler scheme of the form

$$\mathbf{r}^{(n+1)} = \mathbf{r}^{(n)} + \text{Pe}\mathbf{u}(\mathbf{r})\Delta t + \sqrt{2\Delta t}\mathbf{w}(t), \quad (8.86)$$

where $\mathbf{w}(t)$ is a Gaussian random vector with zero mean and unit variance. The no flux condition on the walls were imposed through the method of specular reflection [334]. We have carried out the simulations with, $N = 10^5$ particles and statistics at long time were collected. All the particles started from an initial position of $\mathbf{r} = 0$. The typical time step for most of the simulations were, $\Delta t = 10^{-6}$. The first two moments of the particle position are then given by:

$$m_1(t) = \frac{1}{N} \sum_{i=1}^N \zeta_i \quad (8.87)$$

$$m_2(t) = \frac{1}{N} \sum_{i=1}^N \zeta_i^2. \quad (8.88)$$

Using these two moments the effective dispersivity can be calculated as follows:

$$d^* = \frac{1}{2} \lim_{t \rightarrow \infty} \frac{d}{dt} [m_2(t) - m_1^2(t)]. \quad (8.89)$$

A representative snapshot from Brownian simulation is shown below. We also show the plot of mean square displacement with time and the linear fit through which effective dispersivity was calculated.

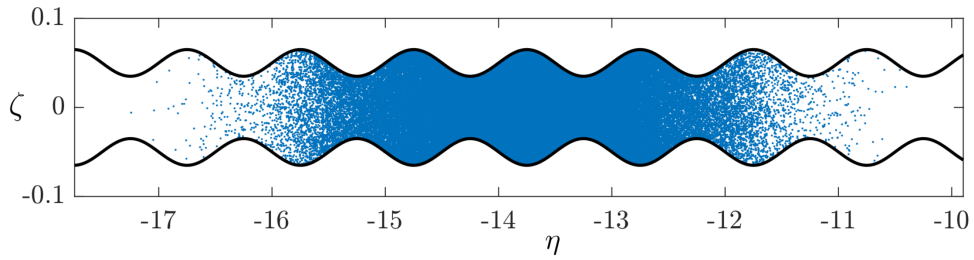


Figure 8.2: Snapshot of Brownian simulations for $\epsilon = 0.05$, $\gamma = 0.3$ and $\text{Pe} = 50$.

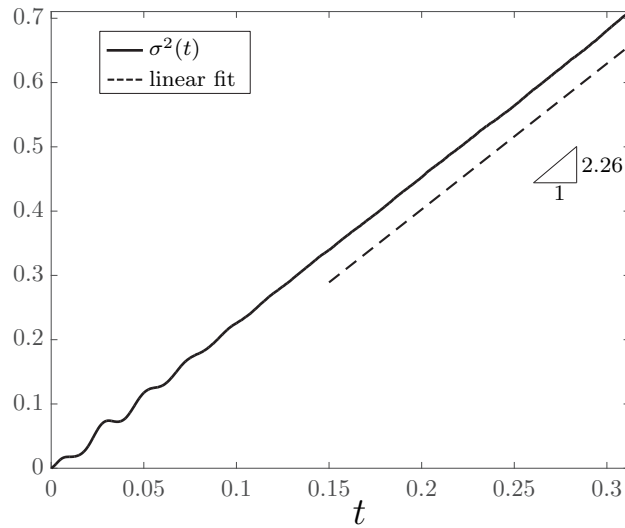


Figure 8.3: Mean squared displacement, $\sigma^2(t)$ as function of time and the linear fit from which dispersivity. The parameters are identical to that of figure 8.2.

8.4.6 Results

We use (8.64) in conjunction with (8.65) to calculate effective dispersivity for a range of Pe numbers and for several values of the geometric parameter, γ . For large Pe number the numerical quadratures in (8.64) becomes challenging and we resorted to using `chebfun` and solved (8.60) instead. The numerical solutions also validate the large Pe asymptotics. The Brownian simulations show excellent agreement with the theory and are shown on the figure for a few representative cases.

In order to understand the results, let us first consider the case, $\gamma = 0$, representing a straight channel. We note that $d^* = 1$ for all Pe in this case. This should not come as a surprise since the motion of walls create only a plug flow in this limit that has no variation in the transverse direction. A simple change of reference frame suggests this is the case of a quiescent fluid and the diffusion is purely molecular. As γ is increased the dispersivity at low Pe falls below unity. In the limit, $\text{Pe} \rightarrow 0$ the process is purely molecular and the decrease in effective diffusivity can be understood using Ficks-Jacobs theory [319]. At a given axial position, ζ , let $S(\zeta)$ represent the entropy that measures the number of available transverse configurations for a Brownian tracer. When $\gamma > 0$ the narrow pores act as ‘entropic barriers’ since the number of available configurations are reduced. The wide regions of the channel then act as ‘entropic traps’ where the Brownian motion on average is ‘slower’ compared to a straight channel. As a combined effect, the effective diffusivity is hindered for constricted wavy channels in this diffusive limit. With decreasing pore opening (indicating increasing γ) the dispersivity decreases [322].

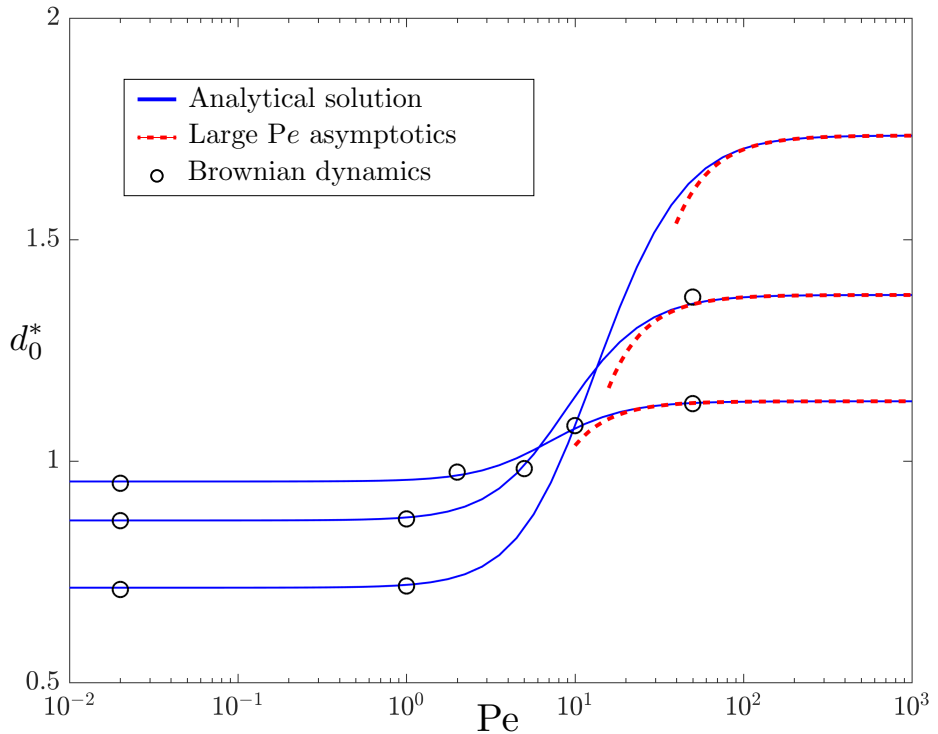


Figure 8.4: Variation of effective dispersivity with Pe calculated quadratures and its comparisons with Brownian simulations and large Pe asymptotics.

The scenario starts becoming different as Pe becomes greater than $\mathcal{O}(1)$. The advection process starts to dominate and higher constriction results in larger dispersivity. The velocity at the pore openings is significantly higher due to continuity, and particles are advected rapidly to the next cell after crossing this entropic barrier. Similarly, once the particles escape the entropic traps due to diffusion they are pushed towards the barrier and subsequently convected due to an increasing velocity field. The gradients in the velocity field increase as the pore opening is reduced resulting in enhanced dispersivity at high Pe . In this context we point out, $\gamma = 1$ is a singular limit that indicates completely closed pores and trapped Brownian particles in an unit cell.

8.5 Beyond small aspect ratio

8.5.1 Boundary integral for hydrodynamics

So far we have only considered the problem of dispersion using long wavelength asymptotics. The applicability of these asymptotic results are only confined to geometries having small aspect ratio. However many biological peristaltic pumping happen at channels with finite aspect ratio where one will need to go beyond the lubrication approximation to solve for the fluid velocity. For different physiological flows inertia is negligible [324]. [335] has estimated the Reynolds number in the ureter to be order unity suggesting that the flow is completely dominated by viscous forces. With these applications in mind we generalize the hydrodynamics in the Stokes regime using a boundary integral formulation as developed in [328]. We have discussed the boundary integral formulation and fundamental solutions to the Stokes equation in Chapter 1. For consistency we briefly review the key aspects here. The velocity of a point on the boundary of the channel can be represented as follows: [40]:

$$u_j(\mathbf{x}) = \frac{1}{2\pi\mu} \int [G_{ij}(\mathbf{x}, \mathbf{x}') f_i(\mathbf{x}') - T_{ijk}(\mathbf{x}, \mathbf{x}') u_i(\mathbf{x}') n_k] ds(\mathbf{x}'), \quad (8.90)$$

where, n_k is the unit normal of the boundaries and $f_j = n_k \sigma_{kj}$ is the traction on the boundaries. The tensor G_{ij} is the appropriate Green's function for the problem and T_{ijk} is the stresslet associated with the Green's functions. In the context of the present problem of pure peristalsis, we first account for the periodicity in the ζ direction by using a periodic form of two dimensional Stokeslet. We also note that the flow is symmetric about the centerline and is bounded by another wall. Following [328, 336] the Green's function appropriate for this problem is \mathbf{G}^{WP} that satisfies all the above mentioned characteristics. The above notation has been used to be consistent with [328]. The choice of an appropriate Green's function reduces the computation and allows us to perform the integrals over only

one of the walls.

Through the no-slip and no-penetration boundary conditions we already know the fluid velocities at the boundary. As shown in the (cartoon) we use $N + 1$ collocation points and N linear elements to approximate the top wall. In the absence of mean pressure gradient there is no contribution from the vertical sides of the unit cell.

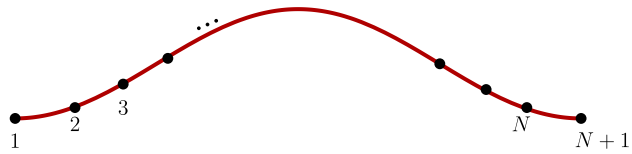


Figure 8.5: Collocation points for approximating the boundary.

The unknown tractions are constant along a linear element and the velocities are assumed to vary linearly. Applying a discrete form of the boundary integral equations (8.90) we obtain a linear system for the unknown tractions:

$$u_j(\mathbf{x}_m) + \sum_{n=1}^N B_j^n(\mathbf{x}_m) = \sum_{n=1}^N A_{ij}^n(\mathbf{x}_m) f_i^n, \quad (8.91)$$

where we have:

$$A_{ij}^n = \frac{1}{2\pi\mu} \int_{l_n} G_{ij}^{WP}(\mathbf{x}_m, \mathbf{x}') ds(\mathbf{x}'), \quad (8.92a)$$

$$B_j^n = \frac{1}{2\pi\mu} \int_{l_n} T_{ijk}^{WP}(\mathbf{x}_m, \mathbf{x}') u_i(\mathbf{x}') n_k ds(\mathbf{x}'), \quad (8.92b)$$

where l_n are the linear elements used to approximate the boundary. The integrations over each of the elements were performed using a Gauss-Legendre quadrature rule with 16 weighing points. The linear system resulting from the use of a discrete boundary integral formulation results in a dense matrix that is solved using *LU* decomposition. For all the results shown here we have used $N = 256$ collocation points on the boundary. Once the tractions are calculated we can use the boundary integral equations to calculate velocity

at any interior point in the domain. The boundary integral implementation was validated against [328] and our asymptotic calculations for small aspect ratio. The streamlines for studied geometries are shown later.

8.5.2 Finite volume method for dispersivity

We have discussed that how the boundary integral formulation can be used to calculate flow fields in Stokes regime for arbitrary aspect ratio channels. In order to solve for the effective dispersivity we need to find a solution to the \mathbf{B} -field. For large aspect ratio we cannot use asymptotics and we need to resort to numerical techniques for solving equation (8.53). The so called b equation has been previously solved [268] using finite-element techniques in the context of transport in spatially periodic porous media. In this paper we solve the hyperbolic conservation law using finite volume method (FVM).

We can use symmetry and solve the \mathbf{B} field only in half of the domain. Apart from the no flux condition at the walls, symmetry requires $b_\eta(\eta = 0) = 0$. Numerically it is more convenient to make use of the transformation $b^* = b + \zeta$ where b^* is now periodic in the ζ direction. With the use of the transformation we can now rewrite (8.53) as:

$$-\text{Pe} \left(\frac{\partial(ub^*)}{\partial\zeta} + \frac{\partial(vb^*)}{\partial\eta} \right) + \left(\frac{\partial^2 b^*}{\partial\zeta^2} + \frac{\partial^2 b^*}{\partial\eta^2} \right) + \left(\frac{1}{\epsilon^2} - 1 \right) \frac{\partial^2 b^*}{\partial\eta^2} = U^* - \text{Pe}u. \quad (8.93)$$

An additional source term $-\text{Pe}u$ arises in the problem due to the transformation of variables. The diffusion term was split to facilitate the formulation. Here, ϵ is the aspect ratio and can take any values in principle. In order to solve the above equation we use a coordinate transformation that maps the physical domain to a square where computations are carried out. The computational co-ordinates are obtained as:

$$\bar{x} = \zeta, \quad (8.94a)$$

$$\bar{y} = \frac{1}{w(\zeta)}\eta, \quad (8.94b)$$

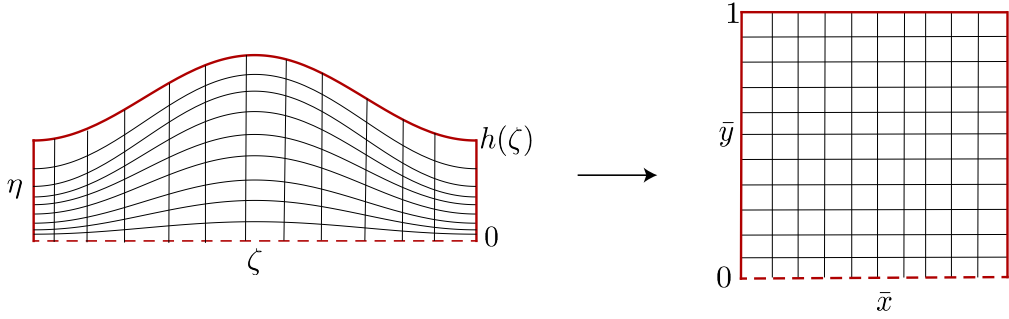


Figure 8.6: Mapping between physical and computational domain.

where, $w(\zeta)$ is the width of the channel at a given location. The partial derivatives are related through the Jacobian matrix and are given by:

$$\begin{pmatrix} \frac{\partial}{\partial \zeta} \\ \frac{\partial}{\partial \eta} \end{pmatrix} = \frac{1}{w} \underbrace{\begin{bmatrix} w & -w' \bar{y} \\ 0 & 1 \end{bmatrix}}_{\equiv \Gamma} \begin{pmatrix} \frac{\partial}{\partial \bar{x}} \\ \frac{\partial}{\partial \bar{y}} \end{pmatrix}, \quad (8.95)$$

where the Jacobian of the transformation is $J = w(\zeta)$ and the 2×2 matrix is denoted by Γ . In order to proceed with FVM we integrate (8.93) over the square cells with sides Δ . The coordinate transformation results in additional non-orthogonal terms that were dealt using an implicit formulation [337].

The no-flux boundary condition on the top wall reads $\hat{\mathbf{n}} \cdot \nabla b = 0$. Making use of the transformed derivatives from (8.95) we obtain:

$$\frac{\partial b^*}{\partial \bar{y}} = \underbrace{\epsilon^2 \left(\frac{w(\bar{x})w'(\bar{x})}{\epsilon^2 w'(\bar{x})^2 + 1} \right)}_{\Phi(\bar{x})} \left(\frac{\partial b^*}{\partial \bar{x}} - 1 \right) \quad \text{at } \bar{y} = 1. \quad (8.96)$$

This boundary condition is treated using an iterative method which is discussed in the subsequent section. The discretized form of equation results in a sparse linear system

which needs to be solved with the following boundary conditions:

$$\frac{\partial b^*}{\partial \bar{y}} = \Phi(\bar{x}), \quad \text{at, } \bar{y} = 1, \quad (8.97a)$$

$$\frac{\partial b^*}{\partial \bar{y}} = 0, \quad \text{at, } \bar{y} = 0, \quad (8.97b)$$

$$b^*(\bar{x} = 0, \bar{y}) = b^*(\bar{x} = 1, \bar{y}), \quad (8.97c)$$

where the last two conditions are attributed to symmetry and periodicity respectively. We now point out that the quadrature for effective dispersivity is modified in the transformed coordinates and also due to the use of b^* . We now have:

$$d^* = \frac{1}{A} \int_0^1 \int_0^1 \left[\frac{1}{\epsilon^2 w^2} \left(\frac{\partial b^*}{\partial \bar{y}} \right)^2 + \left(\frac{\partial b^*}{\partial \bar{x}} - \bar{y} \frac{w'}{w} \frac{\partial b^*}{\partial \bar{y}} - 1 \right)^2 \right] w \, d\bar{x} d\bar{y}, \quad (8.98)$$

where A is the area of the unit cell and from periodicity it is simply given by, ϵ .

8.5.3 Numerical method and validation

The discretized equations from the FVM formulation results in a linear system of the form, $A\mathbf{b}^* = \mathbf{f}$, where A is a sparse matrix with 9 nonzero diagonals. In order to evaluate the advection terms the boundary integral equations were solved and pre-tabulated on a grid. For points outside the tabulated grid a linear interpolation was carried out. This saves computational cost in constructing the matrix A .

The boundary conditions of the problem results in a singular matrix. This should not come as a surprise since we are only interested in the gradient of \mathbf{b}^* . Solvability criterion for these set of problems demand the so called Dirichlet compatibility of zero mean of \mathbf{f} . It is important to obtain regularized solution of the problem, since we are interested in the gradient of the b^* field. Heuristic pinning of the unknown at any point in the domain often results in non-smooth solutions [338]. In this problem, following [310], we impose the constraint of zero mean for b^* through a Lagrange multiplier. This constraint

does not affect the dispersion problem. The modified linear system reads as:

$$\begin{bmatrix} A & \mathbf{e} \\ \mathbf{e}^T & 0 \end{bmatrix} \begin{bmatrix} \mathbf{b}^* \\ \omega \end{bmatrix} = \begin{bmatrix} \mathbf{f}^* \\ 0 \end{bmatrix}, \quad (8.99)$$

where, $\mathbf{e} = [1; 1 \cdots ; 1]$ and ω is the Lagrange multiplier enforcing zero mean.

The no-flux boundary condition on the top wall is satisfied iteratively using the method of ‘deferred correction’ introduced in [339]. This uses solutions from previous iterations to calculate $\Phi(\bar{x})$ and update the source terms resulting from boundary conditions. The steps involved in the solution are outlined below:

- Make an initial guess for $\Phi(\bar{x})$. This is chosen to be zero at the start of the problem.
- Construct the linear system and solve for $\mathbf{x}^{(n)}$, where n is the iteration counter.
- Update $\Phi(\bar{x})$ and also the right hand side of the linear system that depends on boundary terms.
- Obtain a new solution, $\mathbf{x}^{(n+1)}$.
- Check to see whether tolerance is reached: $|\mathbf{x}^{(n+1)} - \mathbf{x}^{(n)}| < tol$. The tolerance for the presented simulations was set to 10^{-9} .

Typically the solutions took between 5 to 40 iterations to converge for a typical cell number of, $M = 200$. In the diffusion dominated regime for channels with large aspect ratio, the convergence is challenging. In order to facilitate it we employed the method of under-relaxation where the relaxation parameter was chosen to be around 0.5.

The asymptotics on dispersivity is valid in the limit, $\epsilon^2 Pe \ll 1$. As a result, in order to validate our FVM method for finite or high Pe numbers we need channels with decreasing aspect ratios. The co-ordinate transformation in the FVM method makes the computation

challenging particularly for small aspect ratio channels and small pore opening. On the other hand, as the aspect ratio is decreased, the boundary integral method also needs a high number of quadrature points and that proves to be time consuming. We have thus compared our FVM to the asymptotics in the diffusive limit in absence of any flow. In this limit both the results match almost exactly (see table 8.1). We have also made a comparison up to $\text{Pe} \sim \mathcal{O}(5)$ (not presented) and the results were within 5% of each other. For the latter we used the lubrication solution for the velocity fields in order to calculate the advection terms in our FVM.

Table 8.1: Comparison between effective diffusivity between FVM and asymptotics in absence of flow ($\text{Pe} = 0$). The aspect ratio for the FVM simulation was chosen to be, $\epsilon = 0.05$.

Pore opening (γ)	FVM	Asymptotics
0.1	0.9950	0.9950
0.3	0.9539	0.9539
0.5	0.8661	0.8660
0.7	0.7140	0.7141

We have used Brownian dynamics simulations as outlined in section 8.4.5 to test our FVM for finite aspect ratio channels. The velocity field computed using boundary integrals was pre-tabulated. Linear interpolation was then used to carry out Brownian dynamics simulations. The performed simulations show excellent agreement with FVM (see table 8.2) over the tested regime.

Table 8.2: Comparison of effective dispersivity, d^* , between Brenner's theory and Brownian dynamics for a channel with $\epsilon = 0.7$ and $\gamma = 0.2$.

Péclet number (Pe)	FVM	Brownian dynamics
0	0.9431	0.9214
10	0.9803	0.9844
20	1.0119	1.0199
50	1.0970	1.1690

8.6 Results and Discussion

In this section we discuss some aspects of dispersion in finite aspect ratio channel with the help on numerical techniques outlined in previous section. It is important to point out that the streamlines presented in this sections are all in the moving reference frame.

8.6.1 Pure diffusion

First we consider the diffusive limit in absence of any flow ($\text{Pe} = 0$). In this limit our previous discussions in terms of entropic barriers and ideas from Ficks-Jacobs theory hold. For a given pore opening controlled by the geometric parameter γ wider channels have smaller diffusivity. For wide channels the entropic barrier is reduced for given width modulation. However our results suggest that the slowing down of Brownian tracers in an entropic trap of a wide channel dominates the effect of entropic barrier.

Table 8.3: Effect of varying geometric parameters in the pure diffusive limit.

Pore opening (γ)	Aspect ratio (ϵ)	Effective diffusivity (d^*)
0.4	0.5	0.8720
	0.7	0.8090
	1	0.7329
0.2		0.9431
	0.7	0.6400
		0.4426

On the other hand, for a given aspect ratio, ϵ , decreasing pore opening by increasing γ results in lower effective dispersivity. In this case both the effect of entropic trap and barrier are amplified. This is consistent with our previous asymptotic results.

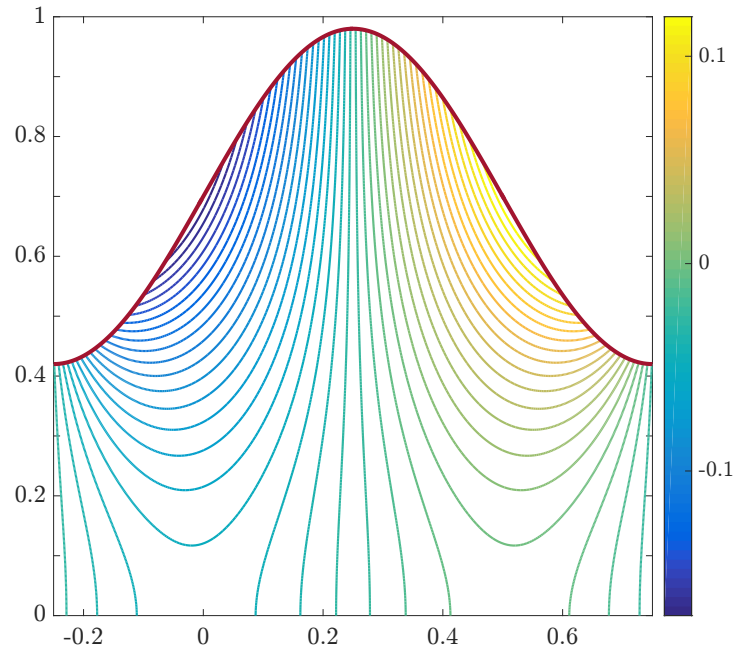


Figure 8.7: Representative contour plot of b^* field for $\epsilon = 0.7$ and $\gamma = 0.4$ in the diffusive limit. Only upper half of the channel is shown.

8.6.2 Effect of re-circulation

As the aspect ratio ϵ is increased re-circulation bubbles starts to appear. Existence of these bubbles is well known in shear flow over cavities [340]. These recirculation zones make a significant contribution in the context of dispersion. [341] studied pressure driven Stokes flow in slowly varying periodic pores using stream-functions. On retaining higher order terms in the asymptotics it was possible to see immobile regions in flow due to recirculations. [310] used their solution to study the associated problem on dispersion. Even though it is possible to observe re-circulation bubbles with asymptotic approximations the solutions are still limited to long-wavelength approximation. The boundary integral method allows us to get around this problem.

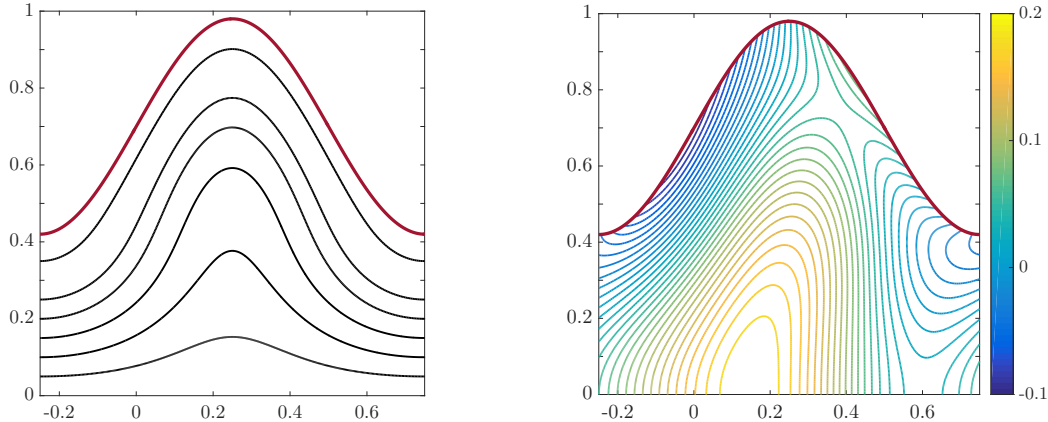


Figure 8.8: Streamlines (on left) and contour lines of b^* field for $Pe = 20$. The aspect ratio of the channel, $\epsilon = 0.7$ and width modulation parameter, $\gamma = 0.4$.

Recirculation bubbles can appear in two ways: increasing aspect ratio, ϵ at a given pore opening, γ , or by decreasing pore opening at a given aspect ratio. Figure 8.10 shows the variation of effective dispersivity for different values of pore opening. Representative streamlines for this case is shown in figure 8.9. A similar behavior in dispersivity is observed in figure 8.12 where the aspect ratio is increased at a given pore opening.

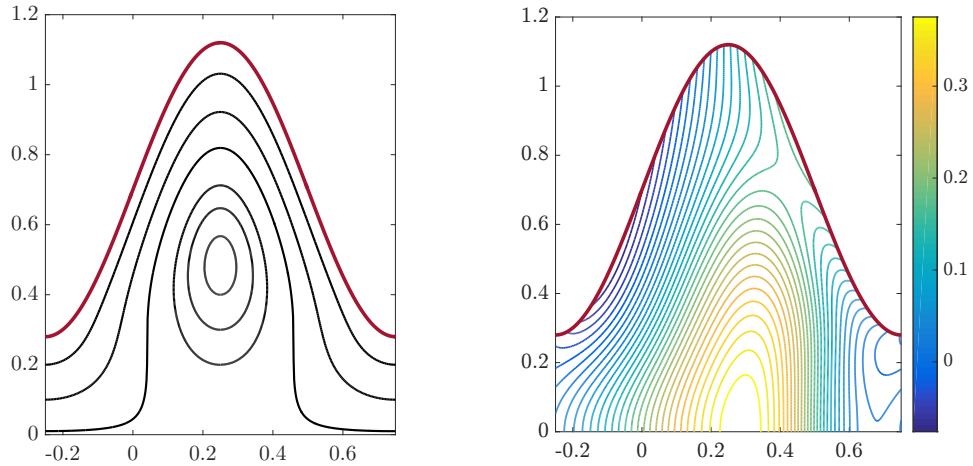


Figure 8.9: Same conditions as in figure 8.8 except now the width modulation parameter, $\gamma = 0.6$. This leads to recirculation bubbles in the flow.

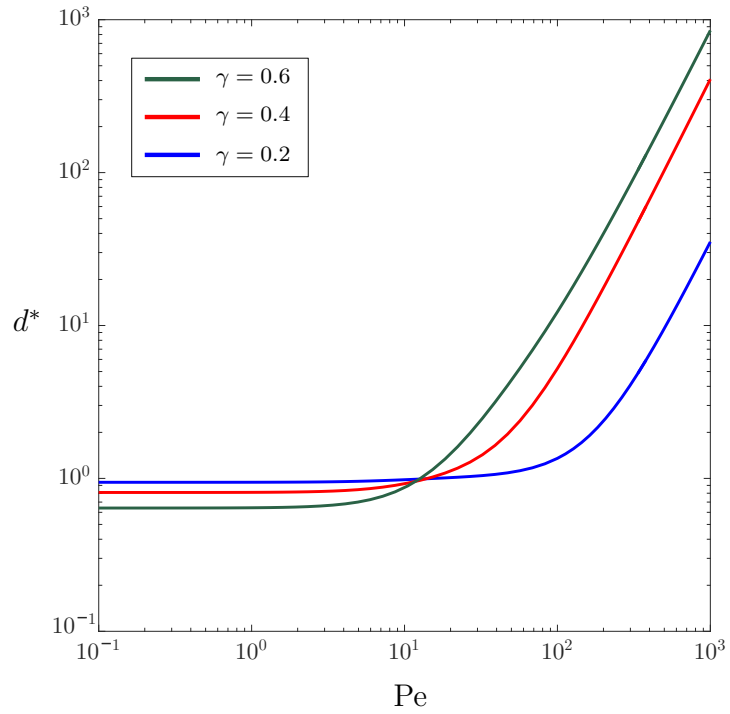


Figure 8.10: Variation of the effective dispersivity, d^* with Pe number for $\epsilon = 0.7$ with different pore openings. Recirculation bubbles exist only for $\gamma = 0.6$.

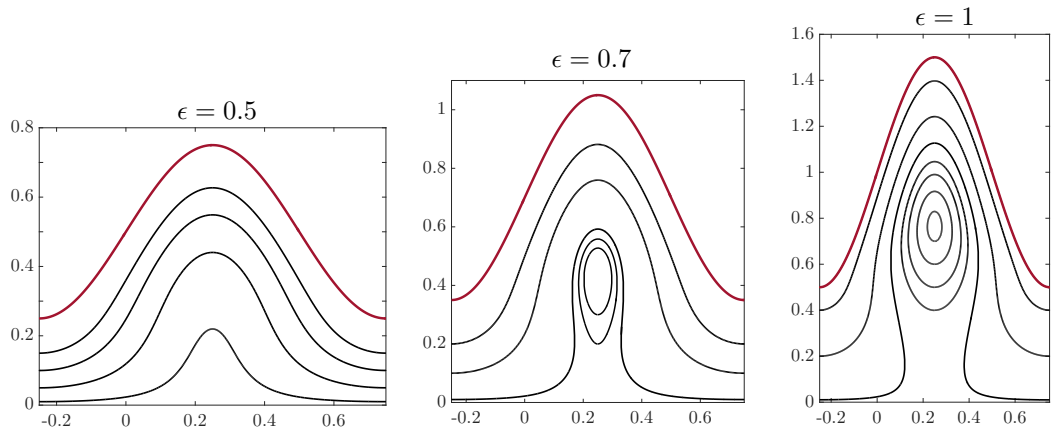


Figure 8.11: Appearance of re-circulation bubbles for different aspect ratio at a fixed pore opening of, $\gamma = 0.5$.

We have previously discussed the diffusion dominated low Pe behavior. The dispersivity curves changes its slope between $Pe = 1$ to $Pe = 10$. This change is an indication of shear dominated effects over molecular diffusivity. It is also noticeable from figure 8.11 that the appearance of recirculation regions lead to increase in dispersivity. This may come as a surprise initially because recirculation is like a ‘hydrodynamic trap’. However one can appreciate the increase in dispersivity from a Lagrangian point of view. The effect of dispersion as shown in figure 8.1 is to smear out the distribution of particle clouds. Recirculation increases the residence time of particles in an unit cell through trapping. However, as a result of this trapping the Lagrangian particle cloud is significantly widened within a cell and cross-streamline migration due to diffusion becomes easily accessible.

Hence the asymptotic dispersivity is increased even though it takes more time to reach the limit due to longer residence time [310]. The behavior of effective dispersivity with Pe are similar to that observed by [269] where they studied dispersion problem related to reactive solute in porous media. Similar trends in dispersivity have also been observed by [268, 342] and [343] in the context of dispersion in porous media. For very high Pe numbers the asymptote of dispersivity tends towards the classical Taylor dispersion limit

of Pe^2 .

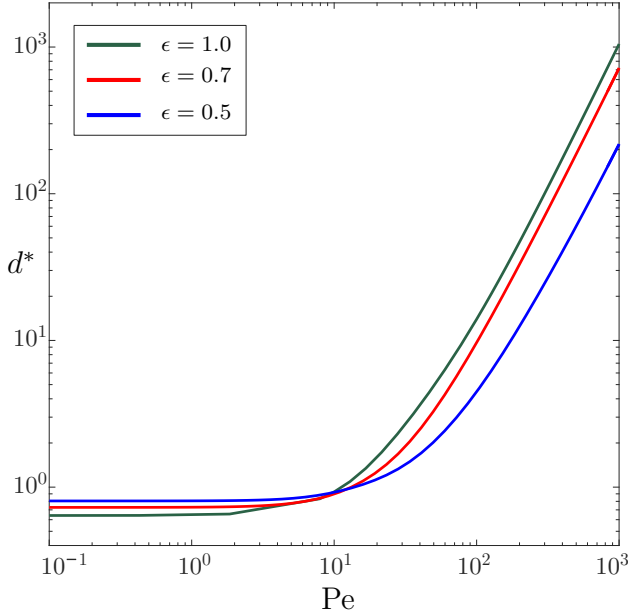


Figure 8.12: Variation of the effective dispersivity, d^* with Pe number for $\gamma = 0.5$ with different aspect ratios. Streamlines for each of the cases are shown in figure 8.11.

8.7 Concluding remarks

In this chapter we have presented an analytical calculation of effective dispersivity for long wavelength peristaltic pumping using Brenner's [272] theory. We have further extended the asymptotics for finite aspect ratio channels in the limit of Stokes flow using the boundary integral method and finite volume techniques. Our results were also validated against Brownian dynamics simulations. [299] theory of dispersion using moments is only applicable for unidirectional flows. The variation of channel width causes the flow field to lose uni-directionality the effect of which can only be captured through generalized dispersion theory. In particular we have seen that in the diffusion dominated regime (low Pe), the small pores act like entropy barrier and the expanding region of the channel acts as entropic trap that reduces the effective diffusivity. However at large Pe this

effect is reversed. Channels with finite aspect ratio also create recirculation bubbles that are not captured by lubrication approximations in long wavelength channels. We have seen that these eddies significantly impact the effective dispersivity. In particular these ‘hydrodynamic traps’ enhance the effective dispersivity.

It is interesting to note that there is a simple connection between peristaltic flow and ‘Taylor’s swimming sheet’ [237]. Taylor’s swimming sheet attains a non-zero swimming speed using traveling waves on its surface in contrast to peristalsis where the walls are not allowed to drift. This similarity is well known in the literature [344, 345]. Recently there has been a considerable interest in the study of effective diffusivity, drift and related ideas in bacterial suspensions [346, 347]. In a similar spirit it may be interesting to look at dispersion by ciliated organisms near a wall. The present analysis can be modified slightly to study dispersion by a swimming sheet in vicinity of a wall for which the hydrodynamics is solved by [348]. We have carried out the leading-order asymptotics for this problem and the results are very similar to those presented in this paper. The problem can be entitled in good humor as ‘*Taylor dispersion by Taylor’s swimming sheet*’!

This Chapter is largely based on a manuscript under preparation authored by Brato Chakrabarti, and David Saintillan. The dissertation author was the primary contributer for this work.

Chapter 9

Concluding remarks and future direction

9.1 Conclusion

In the body of work presented in this thesis we have considered a variety of problems related to the dynamics of passive and active filaments or polymers in viscous flow. The key theme of most of the problems has been performing detailed numerical simulations and comparing them quantitatively with available experiments performed in collaboration. Our simulations have been complemented with analytical solutions, asymptotic calculations, scaling theories and simplified dynamical models that underline the physical underpinnings of most of the observations.

In Chapter 2, we discussed various aspects of elasticity and hydrodynamics of slender structures. Our discussions also provide a number of useful results on appropriate boundary conditions that are often interpreted incorrectly [84] in the literature. We also discuss a few unresolved issues related to dynamics of fluctuations and mechanical properties of semiflexible polymers in flows that constitute part of a ongoing work.

Building on the tools and physics discussed in Chapter 2 we studied morphologies of actin filaments in simple shear flow in Chapter 3. The recurring theme of this study was to point out how competition between viscous loading, bending forces and line tension leads to various buckling instabilities that lead to non-trivial filament morphologies. While Brownian fluctuations induce shape perturbations that are essential for all the instabilities, we found that the threshold and mechanism of morphological transitions are unaltered by the presence of thermal fluctuations which only acts to smooth out sharp bifurcations. Our discussion on rheology in the dilute limit is an ongoing work where we have highlighted that contrary to the intuition for 2D non-Brownian filaments where buckling instabilities lead to a clear signature in rheology, semiflexible polymers do not alter the stress significantly due to its rotation in 3D and due to the presence of thermal fluctuations.

In Chapter 4 we highlighted another morphological transition of actin filaments in a canonical compressional flow. We discussed how interaction and coupling of unstable modes lead to a spontaneous symmetry breaking that makes way for 3D chiral structures. Our simulations, backed with experiments, theory and scaling arguments, suffice to explain a number of observations reported previously in the literature.

Chapter 5 and 6 focus on dynamics of active filaments that are driven by internal moments generated by molecular motors. These filaments serve as a model of spontaneous oscillations observed in eucaryotic cilia and flagella that are hairlike cellular appendages. Using a bottom-up modeling approach that accounts for all the necessary structural details and stochastic kinetics of molecular motors, we were able to observe a variety of beating patterns that mimic the waveforms of cilia, *Chlamydomonas* and sperm flagella. In Chapter 6 we discussed how our model can be used to study the role of hydrodynamics in flagellar synchronization, a long-standing problem that holds the key to fundamental questions related to multicellularity. Our computations revealed that both in-phase and anti-phase

synchrony can emerge for asymmetric beats while symmetric wave-forms go in-phase, and elucidate the mechanism for phase slips due to biochemical noise. Model predictions agreed with recent experiments and illuminated the crucial roles of hydrodynamics and mechano-chemical feedback in synchronization.

Chapter 7 and 8 focused on two problems in the spirit of so called macrotransport theory [271]. Chapter 7 discusses transport of a semiflexible filament in a 2D structured, periodic lattice that serves as an idealization of a porous media. We highlighted how the finite size of the polymer and its interaction with the pillars lead to non-trivial dynamics and transport properties. We further illustrated how an understanding of such behavior can be leveraged to design chromatographic separation device for different sizes of polymers. Chapter 8 discusses transport of Brownian tracers in a 1D lattice with application to peristaltic pumping. Our results show how channel-width modulation can create entropic barriers and trapping that lead to interesting dispersion relations.

9.2 Ongoing work and future directions

A number of avenues and problems have opened up that can be approached based on our work so far. We discuss a few major directions along with a few comments related to ongoing work.

- *Rheology of suspension:* In Chapter 3 we discussed how morphologies of actin filaments affect the rheological properties of dilute suspensions. Simulations in the dilute limit are easy to perform and the deformations can be mapped back to stress signatures. However it remains a challenge in experiments to observe any interesting rheological properties for a dilute suspension [3], and one only observes signatures like shear-thinning or normal stress differences in semi-dilute suspensions [128]. The

rheology of semi-dilute suspension of semiflexible polymers has been largely overlooked and remains an open problem both in terms of theory and simulations [129]. Efficient computation of long-range hydrodynamic interactions in the overlap regime remain a challenge that needs to be tackled in any such modeling problems. While semi-dilute suspensions exhibit shear thinning, dense suspension of flexible filaments in shear flow can form knots and entanglements that lead to shear thickening or gelation [349]. In such dense suspensions hydrodynamic interactions are screened and non-local frictional contact becomes relevant. Modeling of such problems is an exciting avenue and is relevant to understand viscoelastic properties of the cytoskeleton [350].

- *Problems on hydrodynamic synchronization:* In Chapter 6 we considered the simplest elasto-hydrodynamic problem: the pair interaction. There are a number of problems related to hydrodynamics and synchronization that are yet to be answered. Perhaps the most obvious extension is to study dynamics of swimming organisms. Instead of a clamped filament, if we have an actual sperm-head or *Chlamydomonas* cell body attached to the beating filament the organism will swim. In this case the system will be force-free and that dominant hydrodynamics is given by a dipolar field that decays as $1/r^2$. The mechanism of phase synchronization in swimming organisms can be very different from that illustrated in Chapter 6. For example, swimming sperm cells can adjust flagellar phase by moving past each other [267, 351], and *Chlamydomonas* flagella can be phase locked due to the rocking motion of cell body independent of pair interactions [261, 263].

Another important problem that remains to be investigated is the interaction of spontaneously beating filaments in large-scale ciliary arrays. Preliminary numerical investigations suggest that one may expect to observe spontaneous symmetry break-

ing and emergence of metachronal waves [210,252], unidirectional pumping [195,209] and related collective behavior. The fundamental challenge is to compute efficiently large scale hydrodynamic interactions that typically scale as $\mathcal{O}(N^2)$ [93]. An alternative but attractive approach is to incorporate models of spontaneous oscillations in continuum frameworks such as in [352] that allows one to probe oscillations in dense bed of fibers appropriate to biology efficiently.

- *Filaments in complex fluids:* In all the problems considered here the filaments or polymers are suspended in a Newtonian fluid that allows us to exploit tools such as SBT. However much of biological fluid-structure-interaction problems hinge upon dynamics of flexible objects in complex fluids that exhibit non-Newtonian behaviors such as viscoelasticity. Only recently there have been theoretical attempts to study the transport of fibers in complex cellular flows [353] or understand undulatory swimming in viscoelastic fluids [354]. The fundamental theoretical difficulty in all such problems is the necessity of evolving bulk elastic stresses via transport nonlinearities. It remains to be probed how active filament models developed in this thesis behave in complex fluids, a problem relevant for various swimming micro-organisms [205].

Appendix A

Measurement of bend radius

The theoretical model discussed in 3.3.2 approximates the *J* shape by a straight segment and a semi-circular arc. In this idealized configuration, the curvature is zero along the straight segment and then constant at $1/R$ over a length of $\delta_s = \pi R$. In experiments and simulations, however, the curvature varies smoothly and must reach zero at $s = L$ due to the boundary conditions. A typical curvature profile from a simulation is shown in Figure A.1. An alternative measure of the radius can also be obtained from the plateau of the bending energy during a snaking turn as seen in Figure 3.2(*c*) of Chapter 3. Since the majority of the energetic contribution comes from the sharp fold, we can get an estimate of the radius as

$$R = \frac{\delta_s}{\pi} \approx \frac{B\pi}{2\langle E \rangle}, \quad (\text{A.1})$$

where $\langle E \rangle$ is the average bending energy over the plateau. This measure is also plotted against the theoretical predictions in Figure 3.9(*b*) and follows similar trends.

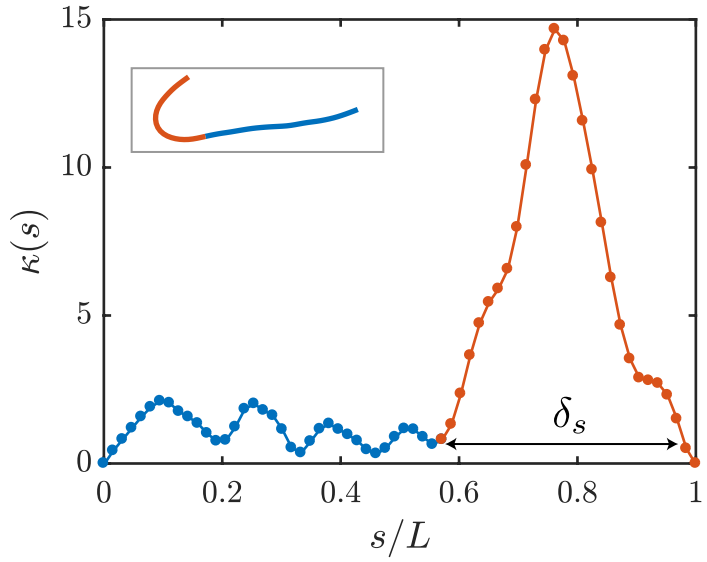


Figure A.1: Variation of curvature κ along the filament centerline for a typical J shape chosen from a simulation. The length marked as δ_s provides an estimate for the arclength of the bent portion.

In previous work, Harasim *et al.* [30] provided an expression for the bend radius that was independent of the length of the filament. For the parameter space explored in their study, they estimated $R \approx 1 \mu\text{m}$. Our results partially agree with their finding in the limit of long filaments and strong shear.

Appendix B

Diatom chains and regularized Stokeslets

In this appendix we provide the details of the non-Brownian simulations performed at University of Tulane for helical buckling problem discussed in Chapter 4. We first discuss the structure of the so called ‘diatom chains’ that were used to model the non-Brownian filaments and then we outline the method of regularized Stokeslet used for the hydrodynamics.

B.1 Fiber model as a network of springs

In the non-Brownian simulations the filaments are represented as networks of Hookean springs of stiffness k that provide structural rigidity and bending resistance. The springs connect all possible pairs of vertices of a hexagonal cross section and additionally link neighboring cross-sections as shown in Figure B.1. For an initially straight fiber, the rest length of the spring connecting nodes i and j is set to Δ_{ij} .

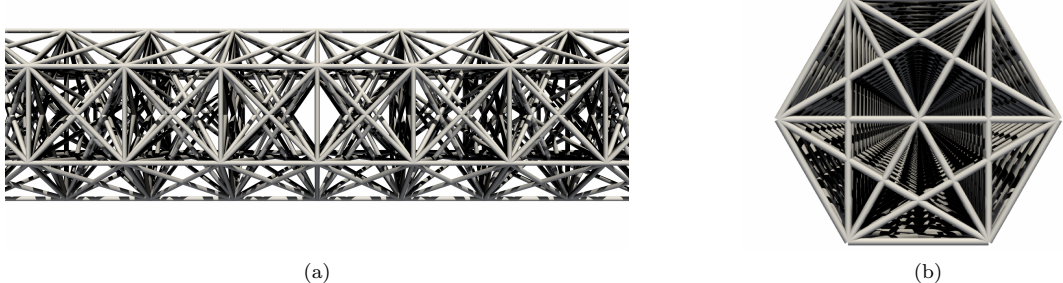


Figure B.1: Schematic of a non-Brownian filament comprised of network of Hookean springs as viewed from the side (a) and from the end (b).

The elastic energy resulting from the network of springs is given by:

$$E = \frac{1}{2} \sum_{i,j \in \text{springs}} k \left(\frac{\ell_{ij}}{\Delta_{ij}} - 1 \right)^2 \Delta_{ij}, \quad (\text{B.1})$$

where ℓ_{ij} is the instantaneous length of the spring. We can estimate the bending rigidity B , of a filament by bending it to a known curvature κ and equating this elastic energy to the bending energy $E_B = B\kappa^2 L/2$, thus providing

$$B = \frac{2E}{\kappa^2 L}. \quad (\text{B.2})$$

We have repeated the above procedure for a number of curvature values to estimate the bending rigidity [117, 355] and use this computed value of B to estimate the elastoviscous number $\bar{\mu}$ in the non-Brownian simulations.

B.2 Method of regularized Stokeslets

As discussed in Chapter 4, the experiments were performed in rectangular hyperbolic channels, while Brownian simulations were carried out in a two-dimensional flow field in absence of any walls. In an attempt to highlight the robustness of helical buckling, we perform non-Brownian simulations in an axisymmetric channel with a circular cross-section. In order to mimic the extensional and compressional flow of the experiment, the

dimensionless radius $\rho(z)$ of the channel varies along the axis as follows:

$$\rho(z) = \begin{cases} 0.5 & \text{for } |z| \geq 2.5, \\ 0.286z^3 + 1.63z^2 + 2.78z + 1.74 & \text{for } -2.5 < z \leq -1.5, \\ 0.2375(z+2.27)^{-1/2} & \text{for } -1.5 < z \leq 0, \\ 0.2375(2.27-z)^{-1/2} & \text{for } 0 < z \leq 1.5, \\ -0.286z^3 + 1.63z^2 - 2.78z + 1.74 & \text{for } 1.5 < z \leq 2.5. \end{cases} \quad (\text{B.3})$$

As we demonstrate below, this shape yields a nearly constant extensional rate along the centerline in the central part of the channel.

We represent the fluid velocity induced by the spring forces on the fiber using the method of regularized Stokeslets as discussed in detail in [356, 357]. By exploiting the linearity of the Stokes equations, we solve for the tractions on the boundary and compute the background flow inside the channel using the same method. For an axisymmetric channel, the fluid velocity is expressed linearly in terms of the tractions on the channel wall:

$$\mathbf{u}(\mathbf{x}) = \int_0^L \int_0^{2\pi} S_\delta \mathbf{F}(\rho(z) \cos(\theta), \rho(z) \sin(\theta), z) \rho(z) d\theta dz, \quad (\text{B.4})$$

where S_δ is the regularized Stokeslet kernel with regularization parameter δ . $\mathbf{F} = f^r \mathbf{n}_k + f^z \mathbf{e}_3$ are the wall tractions, where $\mathbf{n}_k = (\cos(\theta), \sin(\theta), 0)$. The integral in the azimuthal direction can be evaluated exactly to obtain a formula for the radial and axial velocities:

$$\mathbf{u}(\mathbf{x}) = \begin{bmatrix} U^r(\mathbf{x}) \\ U^z(\mathbf{x}) \end{bmatrix} = \int_0^L \begin{bmatrix} f^r A_r(z) + f^z A_z(z) \\ f^r B_r(z) + f^z B_z(z) \end{bmatrix} dz = \int_0^L \mathcal{R}_\delta \mathbf{F} dz, \quad (\text{B.5})$$

where A_r , A_z , B_r , and B_z are comprised of complete elliptic integrals, and we approximate Eq. (B.5) using quadrature (see [358] for more details). By using this methodology, we are able to discretize the boundary of the tube as a curve of N_T points from $z = 0$ to

$z = L$ and N_{in} points discretizing the inlet of the tube from $r = 0$ to $\rho(0)$, which yields a significantly reduced total system size of $2(N_T + N_{in}) \times 2(N_T + N_{in})$.

We then follow the update procedure in [359], and compute the flow induced from the no-slip boundary conditions on the tube and the elastic dynamics of the fiber by the following procedure:

1. Compute the forces required for the background flow induced by the shape of the tube by solving the linear system

$$\mathbf{u}_{target}(\mathbf{x}_i) = \sum_{j=1}^{N_T+N_{in}} \mathcal{R} \mathbf{f}_j h_{tube},$$

where $\mathbf{u}_{target} = \mathbf{0}$ on the tube surface and matches the parabolic flow $\mathbf{u}_{inflow}(r) = U_{max} \left(1 - \frac{r^2}{\rho(0)^2}\right) \mathbf{e}_3$ at the inlet, where r is the radial coordinate with respect to the tube axis and U_{max} is the speed at the center of the tube. We note that this is a dense linear system of size $2(N_T + N_{in}) \times 2(N_T + N_{in})$ that need only be solved a single time. Once we have solved for the forces, Eq. (B.5) is used evaluate the background flow at any required point.

2. Compute the velocity on all of the fiber nodes resulting from the spring forces using the method of regularized Stokeslets and add the background velocity generated by the boundary forces.
3. Update the position of the fiber by taking a forward Euler time step.

The described method produces a dimensionless strain rate of $|\dot{\epsilon}| = 4.6$ and the velocity and strain rate profiles along the centerline are shown in Fig. B.2.

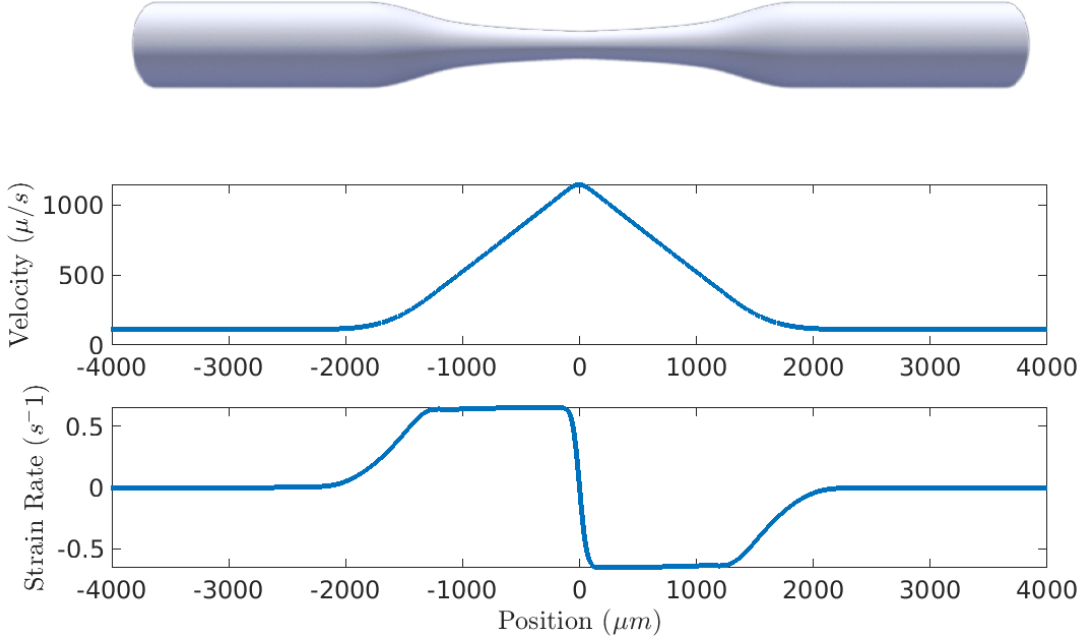


Figure B.2: Top: the axisymmetric tube profile. Middle: the simulated axial velocity along the centerline of the tube using the shape defined in Eq. (B.3). Bottom: strain rate $\dot{\epsilon}$ along the centerline, which is the z derivative of the velocity and is approximately constant as desired.

B.3 Simulation parameters and computed values

We use non-dimensional parameters in the simulations and convert to physical units using the following characteristic scales for length, time, and force: $L_{scale} = 800 \mu\text{m}$, $T_{scale} = 7.149 \text{ s}$, and $F_{scale} = 3.482 \times 10^{-10} \text{ N}$. These scales were chosen to match experimental values approximately. In particular, we normalize the diameter of the experimental channel inlet ($800 \mu\text{m}$) to 1, normalize the experimental inlet velocity ($111.9 \mu\text{m/s}$) to be 1, and normalize the experimental viscosity ($3.89 \times 10^{-3} \text{ N s/m}^2$) to 1.

Parameter values used in these non-Brownian simulations are summarized in Table B.1.

Table B.1: Simulation parameters and computed values from non-Brownian simulations.

Parameter	Simulation Values	Dimensional Values
Number of points on tube profile, N_T	2000	2000
Number of points on tube inlet, N_{in}	400	400
Tube grid spacing, h_{tube}	0.005	4 μm
Tube regularization parameter, δ_{tube}	0.013	10.4 μm
Inlet speed, U_{max}	1	111.9 $\mu\text{m}/\text{s}$
Shear rate, $\dot{\epsilon}$	4.64	0.65 s^{-1}
Viscosity, μ	1	$3.89 \times 10^{-3} \text{ N s/m}^2$
Filament radius, r	1.25×10^{-4}	0.1 μm
Filament length, L	0.0134 – 0.143	10.7 – 114 μm
Filament discretization size, h	1.25×10^{-4}	0.1 μm
Filament regularization parameter, δ	2.88×10^{-4}	0.23 μm
Number of filament nodes, N	738 – 5550	738 – 5550
Spring constant, k	0.004	$1.40 \times 10^{-12} \text{ N}$
Elastoviscous number, $\bar{\mu}$	$10^3 - 10^7$	$10^3 - 10^7$
Bending rigidity, B	2.96×10^{-10}	$6.60 \times 10^{-26} \text{ N m}^2$
Time step, Δt	1×10^{-5}	$7.15 \times 10^{-5} \text{ s}$

Appendix C

Adjoint operator of the linearized SBT

The linear operator associated with the linear stability problem defined by local slender body theory (SBT) is given by:

$$\mathcal{L} = f(s)\partial_{ss} + \bar{\mu}s\partial_s - \partial_{ssss}, \quad s \in [-1/2, 1/2], \quad (\text{C.1})$$

where $f(s) = \bar{\mu}(s^2 - 1/4)/4$, is the line tension associated with the base state of the filament. For force-free boundary conditions the line tension $f(s)$ vanishes at $s = \pm 1/2$. Eigenfunctions for this operator will satisfy the boundary condition $v_{ss} = v_{sss}$ at $s = \pm 1/2$. This linear operator is non-adjoint and as a result the eigenfunctions are not orthogonal to each other. Let us denote the adjoint operator as L^\dagger and the associated eigenfunctions as u^\dagger for which we do not know the appropriate boundary conditions. From the definition of an adjoint operator with unit weighing function we have:

$$\langle u^\dagger, \mathcal{L}v \rangle = \langle L^\dagger u^\dagger, v \rangle. \quad (\text{C.2})$$

We now attempt to derive the functional form of the adjoint operator and the boundary conditions on u^\dagger . To this end we start from the left-hand side of the above equation that

given by

$$\langle u^\dagger, \mathcal{L}v \rangle = \int_{-1/2}^{1/2} [u^\dagger f(s) \partial_{ss} v + u^\dagger \bar{\mu} s \partial_s v - u^\dagger \partial_{ssss} v] ds. \quad (\text{C.3})$$

We now apply successive integration by parts to the above expression and have:

$$\begin{aligned} \langle u^\dagger, \mathcal{L}v \rangle &= - \int \frac{d}{ds} (u^\dagger f) \partial_s v ds + \bar{\mu} u^\dagger s v \Big|_{-1/2}^{1/2} + \int u_s^\dagger v_{sss} ds, \\ &= - \frac{d}{ds} (u^\dagger f) v \Big|_{-1/2}^{1/2} + \bar{\mu} u^\dagger s v \Big|_{-1/2}^{1/2} + \int \frac{d^2}{ds^2} (u^\dagger f) v ds - \int u_{ss}^\dagger v_{ss} ds, \\ &= - \frac{d}{ds} (u^\dagger f) v \Big|_{-1/2}^{1/2} + \bar{\mu} u^\dagger s v \Big|_{-1/2}^{1/2} - u_{ss}^\dagger v_s \Big|_{-1/2}^{1/2} + \int \frac{d^2}{ds^2} (u^\dagger f) v ds + \int u_{sss}^\dagger v_s ds. \\ \langle u^\dagger, \mathcal{L}v \rangle &= - \frac{d}{ds} (u^\dagger f) v \Big|_{-1/2}^{1/2} + \bar{\mu} u^\dagger s v \Big|_{-1/2}^{1/2} - u_{ss}^\dagger v_s \Big|_{-1/2}^{1/2} + u_{sss}^\dagger v \Big|_{-1/2}^{1/2} + \int \frac{d^2}{ds^2} (u^\dagger f) v ds \\ &\quad - \int u_{ssss}^\dagger v ds. \end{aligned} \quad (\text{C.4})$$

While leading to the above equations we have used the boundary conditions on f and v . The boundary terms in the above expression will help us determine the boundary conditions on u^\dagger . Demanding that the boundary terms vanish, we find

$$u_{ss}^\dagger = 0, \quad \text{at } s = \pm 1/2, \quad (\text{C.5})$$

$$u_{sss}^\dagger - \bar{\mu} \frac{u^\dagger}{4} = 0, \quad \text{at } s = -1/2, \quad (\text{C.6})$$

$$u_{sss}^\dagger + \bar{\mu} \frac{u^\dagger}{4} = 0, \quad \text{at } s = 1/2. \quad (\text{C.7})$$

$$(C.8)$$

Finally from equation C.4 we can read off the adjoint operator as:

$$L^\dagger = \frac{\bar{\mu}}{4} \left(s^2 - \frac{1}{4} \right) \frac{\partial^2}{\partial s^2} + \bar{\mu} s \frac{\partial}{\partial s} + \frac{\bar{\mu}}{2} - \frac{\partial^4}{\partial s^4}. \quad (\text{C.9})$$

Appendix D

Algorithm for filament contact

In Chapter 7 we studied the transport of polymers in structured porous media. Central to the problem was the interaction or contact of the filament with the pillar. Here we outline the algorithm that allows for tangential motion past the obstacles and prevents penetration. The local SBT equation can be re-arranged as follows:

$$\frac{\partial \mathbf{x}}{\partial t} + \boldsymbol{\Lambda} \cdot \mathbf{x}_{ssss} = \bar{\mu} \mathbf{u}_\infty - \boldsymbol{\Lambda} \cdot \left(-(\sigma \mathbf{x}_s)_s + \sqrt{L_f/\ell_p} \boldsymbol{\xi} \right) = \mathbf{F}. \quad (\text{D.1})$$

After the above re-arrangement \mathbf{F} now contains all the terms due to the background flow and non-linear terms from elastic forces. For any given point on the filament $\mathbf{x}(s)$ we first identify the cell center $\mathbf{x}_c = (x_c, y_c)$, in which it is located. Let d denote the Euclidean distance between $\mathbf{x}(s)$ and the cell center. Following [290] we define a unit vector $\hat{\mathbf{p}}$ as:

$$\hat{\mathbf{p}} = \frac{\mathbf{x}(s) - \mathbf{x}_c}{d}. \quad (\text{D.2})$$

For a pillar of diameter a , if $d - a < \varepsilon$, where ε is a cut-off distance we project the force \mathbf{F} parallel and perpendicular to $\hat{\mathbf{p}}$ to define:

$$F_n = \hat{\mathbf{p}} \cdot \mathbf{F}, \quad (\text{D.3})$$

$$F_t = (\mathbf{I} - \hat{\mathbf{p}}\hat{\mathbf{p}}) \cdot \mathbf{F}. \quad (\text{D.4})$$

The subscript n and t in the above expression stands for normal and tangential. After the projection we keep F_t the same and alter the component F_n as follows [290]:

$$F_n = \min \left[F_n, \left(1 - \left(\frac{\varepsilon}{d-a} \right)^m \right) F_n \right], \quad (\text{D.5})$$

where $m = 4$. The above definition is such that if the fluid and tension forces try to separate the filament from each other the force component is unaltered. However if the fluid and tension forces are pushing the filament to an overlapped or penetrating state the sign of this force is reversed. Since the tangential component is unchanged, this treatment allows the filament to glide or wrap around the obstacles without significant numerical difficulties. In the event of contacts we have adaptively reduced the time-step to ensure numerical stability. For all the simulations we had $\varepsilon = 5L_f \times 10^{-3}$.

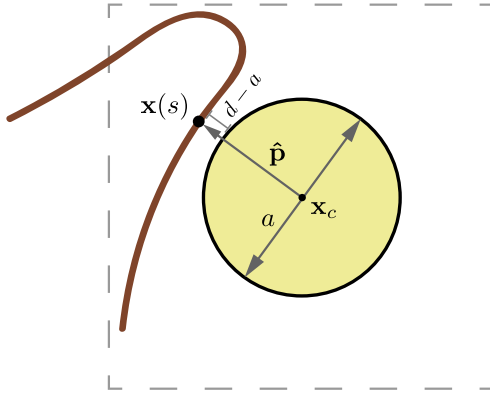


Figure D.1: Schematic of a polymer close to contact with a pillar and the relevant quantities.

Bibliography

- [1] A. J. Spakowitz, *Semiflexible polymers: fundamental theory and applications in DNA packaging*. PhD thesis, California Institute of Technology, 2005.
- [2] V. Kantsler and R. E. Goldstein, “Fluctuations, dynamics, and the stretch-coil transition of single actin filaments in extensional flows,” *Phys. Rev. Lett.*, vol. 108, p. 038103, 2012.
- [3] Y. Liu, *Dynamics of flexible and Brownian filaments in viscous flows*. PhD thesis, ESPCI, 2018.
- [4] T. Niedermayer, B. Eckhardt, and P. Lenz, “Synchronization, phase locking, and metachronal wave formation in ciliary chains,” *Chaos*, vol. 18, no. 3, p. 037128, 2008.
- [5] E. Hinch and L. Leal, “The effect of brownian motion on the rheological properties of a suspension of non-spherical particles,” *Journal of Fluid Mechanics*, vol. 52, no. 4, pp. 683–712, 1972.
- [6] H. Brenner, “Rheology of a dilute suspension of axisymmetric brownian particles,” *International journal of multiphase flow*, vol. 1, no. 2, pp. 195–341, 1974.
- [7] Y. Liu, B. Chakrabarti, D. Saintillan, A. Lindner, and O. du Roure, “Morphological transitions of elastic filaments in shear flow,” *Proceedings of the National Academy of Sciences*, vol. 115, no. 38, pp. 9438–9443, 2018.
- [8] B. Chakrabarti, Y. Liu, J. LaGrone, R. Cortez, L. Fauci, O. d. Roure, D. Saintillan, and A. Lindner, “Flexible filaments buckle into helicoidal shapes in strong compressional flows,” *arXiv preprint arXiv:1910.04558*, 2019.
- [9] B. Chakrabarti and D. Saintillan, “Spontaneous oscillations, beating patterns, and hydrodynamics of active microfilaments,” *Physical Review Fluids*, vol. 4, no. 4, p. 043102, 2019.
- [10] B. Chakrabarti and D. Saintillan, “Hydrodynamic synchronization of spontaneously beating filaments,” *arXiv preprint arXiv:1904.10088*, 2019.

- [11] P.-G. De Gennes, “Soft matter,” *Reviews of modern physics*, vol. 64, no. 3, p. 645, 1992.
- [12] M. Kleman and O. D. Laverntovich, *Soft matter physics: an introduction*. Springer Science & Business Media, 2007.
- [13] P.-G. De Gennes and J. Prost, *The physics of liquid crystals*, vol. 83. Oxford university press, 1993.
- [14] M. Doi, “Molecular dynamics and rheological properties of concentrated solutions of rodlike polymers in isotropic and liquid crystalline phases,” *Journal of Polymer Science: Polymer Physics Edition*, vol. 19, no. 2, pp. 229–243, 1981.
- [15] A. Keller and J. Odell, “The extensibility of macromolecules in solution; a new focus for macromolecular science,” *Colloid and Polymer Science*, vol. 263, no. 3, pp. 181–201, 1985.
- [16] P. De Gennes, “Coil-stretch transition of dilute flexible polymers under ultrahigh velocity gradients,” *J. Chem. Phys.*, vol. 60, pp. 5030–5042, 1974.
- [17] B. Alberts, D. Bray, K. Hopkin, A. Johnson, J. Lewis, M. Raff, K. Roberts, and P. Walter, *Essential Cell Biology*. Garland Science, New York, 2013.
- [18] S. Ganguly, L. S. Williams, I. M. Palacios, and R. E. Goldstein, “Cytoplasmic streaming in drosophila oocytes varies with kinesin activity and correlates with the microtubule cytoskeleton architecture,” *Proc. Natl. Acad. Sci. USA*, vol. 109, pp. 15109–15114, 2012.
- [19] K. Suzuki, M. Miyazaki, J. Takagi, T. Itabashi, and S. Ishiwata, “Spatial confinement of active microtubule networks induces large-scale rotational cytoplasmic flow,” *Proc. Natl. Acad. Sci. USA*, vol. 114, pp. 2922–2927, 2017.
- [20] C. Brennen and H. Winet, “Fluid mechanics of propulsion by cilia and flagella,” *Annual Review of Fluid Mechanics*, vol. 9, no. 1, pp. 339–398, 1977.
- [21] J. R. Blake, “Fluid mechanics of ciliary propulsion,” in *Computational Modeling in Biological Fluid Dynamics*, pp. 1–51, Springer, 2001.
- [22] C. M. Schroeder, H. P. Babcock, E. S. Shaqfeh, and S. Chu, “Observation of polymer conformation hysteresis in extensional flow,” *Science*, vol. 301, pp. 1515–1519, 2003.
- [23] C. M. Schroeder, “Single polymer dynamics for molecular rheology,” *Journal of Rheology*, vol. 62, no. 1, pp. 371–403, 2018.
- [24] T. T. Perkins, D. E. Smith, and S. Chu, “Single polymer dynamics in an elongational flow,” *Science*, vol. 276, no. 5321, pp. 2016–2021, 1997.

- [25] J. S. Hur, E. S. Shaqfeh, and R. G. Larson, “Brownian dynamics simulations of single DNA molecules in shear flow,” *J. Rheol.*, vol. 44, no. 4, pp. 713–742, 2000.
- [26] S. Gerashchenko and V. Steinberg, “Statistics of tumbling of a single polymer molecule in shear flow,” *Phys. Rev. Lett.*, vol. 96, no. 3, p. 038304, 2006.
- [27] C. M. Schroeder, E. S. G. Shaqfeh, and S. Chu, “Effect of hydrodynamic interactions on DNA dynamics in extensional flow: Simulation and single molecule experiment,” *Macromolecules*, vol. 37, pp. 9242–9256, 2004.
- [28] C. M. Schroeder, R. E. Texeira, E. S. G. Shaqfeh, and S. Chu, “Characteristic periodic motion of polymers in shear flow,” *Phys. Rev. Lett.*, vol. 95, p. 018301, 2005.
- [29] C. C. Hsieh and R. G. Larson, “Prediction of coil-stretch hysteresis for dilute polystyrene molecules in extensional flow,” *J. Rheol.*, vol. 49, pp. 1081–1089, 2005.
- [30] M. Harasim, B. Wunderlich, O. Peleg, M. Kröger, and A. R. Bausch, “Direct observation of the dynamics of semiflexible polymers in shear flow,” *Physical review letters*, vol. 110, no. 10, p. 108302, 2013.
- [31] A. Lindner and M. Shelley, “Elastic fibers in flows,” in *Fluid-Structure Interactions in Low-Reynolds-Number Flows*, pp. 168–192, The Royal Society of Chemistry, 2016.
- [32] R. B. Bird, R. C. Armstrong, O. Hassager, and C. F. Curtiss, *Dynamics of polymeric liquids*, vol. 1. Wiley New York, 1977.
- [33] L. E. Becker and M. J. Shelley, “Instability of elastic filaments in shear flow yields first-normal-stress differences,” *Phys. Rev. Lett.*, vol. 87, p. 198301, 2001.
- [34] E. S. G. Shaqfeh, “Purely elastic instabilities in viscometric flows,” *Annu. Rev. Fluid Mech.*, vol. 28, pp. 129–185, 1996.
- [35] A. N. Morozov and W. van Saarloos, “An introductory essay on subcritical instabilities and the transition to turbulence in visco-elastic parallel shear flows,” *Phys. Rep.*, vol. 447, pp. 112–143, 2007.
- [36] E. M. Purcell, “Life at low reynolds number,” *American journal of physics*, vol. 45, no. 1, pp. 3–11, 1977.
- [37] T. M. Squires and S. R. Quake, “Microfluidics: Fluid physics at the nanoliter scale,” *Reviews of modern physics*, vol. 77, no. 3, p. 977, 2005.
- [38] NCFMF, “Fluid films,” 2007. <http://web.mit.edu/hml/ncfmf.html>, Last accessed on 2017-11-30.
- [39] E. Guazzelli and J. F. Morris, *A physical introduction to suspension dynamics*, vol. 45. Cambridge University Press, 2011.

- [40] C. Pozrikidis, *Boundary integral and singularity methods for linearized viscous flow*. Cambridge University Press, 1992.
- [41] J. Happel and H. Brenner, *Low Reynolds number hydrodynamics: with special applications to particulate media*, vol. 1. Springer Science & Business Media, 2012.
- [42] O. A. Ladyzhenskaya, *The mathematical theory of viscous incompressible flow*, vol. 2. Gordon and Breach New York, 1969.
- [43] R. P. Feynman, R. B. Leighton, and M. Sands, *The Feynman lectures on physics, Vol. I: The new millennium edition: mainly mechanics, radiation, and heat*, vol. 1. Basic books, 2011.
- [44] E. Hinch, “Application of the langevin equation to fluid suspensions,” *Journal of Fluid Mechanics*, vol. 72, no. 3, pp. 499–511, 1975.
- [45] E. Frey, K. Kroy, J. Wilhelm, and E. Sackmann, “Statistical mechanics of semiflexible polymers: theory and experiment,” in *Dynamical Networks in Physics and Biology*, pp. 103–119, Springer, 1998.
- [46] O. Kratky and G. Porod, “Röntgenuntersuchung gelöster fadenmoleküle,” *Recueil des Travaux Chimiques des Pays-Bas*, vol. 68, no. 12, pp. 1106–1122, 1949.
- [47] T. R. Powers, “Dynamics of filaments and membranes in a viscous fluid,” *Reviews of Modern Physics*, vol. 82, no. 2, p. 1607, 2010.
- [48] F. Gittes, B. Mickey, J. Nettleton, and J. Howard, “Flexural rigidity of microtubules and actin filaments measured from thermal fluctuations in shape,” *J. Cell. Biol.*, vol. 120, pp. 923–923, 1993.
- [49] P.-G. De Gennes and P.-G. Gennes, *Scaling concepts in polymer physics*. Cornell university press, 1979.
- [50] B. Audoly and Y. Pomeau, “Elasticity and geometry,” in *Peyresq Lectures On Non-linear Phenomena*, pp. 1–35, World Scientific, 2000.
- [51] H. Singh and J. Hanna, “On the planar elastica, stress, and material stress,” *Journal of Elasticity*, vol. 136, no. 1, pp. 87–101, 2019.
- [52] L. D. Landau and E. M. Lifshitz, *Course of Theoretical Physics Vol 7: Theory and Elasticity*. Pergamon press, 1959.
- [53] M. P. Do Carmo, *Differential Geometry of Curves and Surfaces: Revised and Updated Second Edition*. Courier Dover Publications, 2016.
- [54] C. Duprat and H. A. Shore, *Fluid-Structure Interactions in Low-Reynolds-Number Flows*. Royal Society of Chemistry, 2015.

- [55] F. Bertails, B. Audoly, M.-P. Cani, B. Querleux, F. Leroy, and J.-L. Lévéque, “Super-helices for predicting the dynamics of natural hair,” in *ACM Transactions on Graphics (TOG)*, vol. 25, pp. 1180–1187, ACM, 2006.
- [56] M. Bergou, M. Wardetzky, S. Robinson, B. Audoly, and E. Grinspun, “Discrete elastic rods,” in *ACM transactions on graphics (TOG)*, vol. 27, p. 63, ACM, 2008.
- [57] “Leaves and flower of paphiopedilum orchid.” <https://www.orchidya.com/team/paphiopedilum-slipper-orchid/>. Accessed: 2019-10-01.
- [58] R. Levien, “The elastica: a mathematical history,” *University of California, Berkeley, Technical Report No. UCB/EECS-2008-103*, 2008.
- [59] I. M. Mladenov and M. Hadzhilazova, *The many faces of elastica*. Springer, 2017.
- [60] S. S. Antman, “Nonlinear plasticity,” in *Nonlinear Problems of Elasticity*, pp. 603–628, Springer, 1995.
- [61] S. Lim, A. Ferent, X. S. Wang, and C. S. Peskin, “Dynamics of a closed rod with twist and bend in fluid,” *SIAM Journal on Scientific Computing*, vol. 31, no. 1, pp. 273–302, 2008.
- [62] J. L. Silverberg, R. D. Noar, M. S. Packer, M. J. Harrison, C. L. Henley, I. Cohen, and S. J. Gerbode, “3d imaging and mechanical modeling of helical buckling in medicago truncatula plant roots,” *Proceedings of the National Academy of Sciences*, vol. 109, no. 42, pp. 16794–16799, 2012.
- [63] J. Coyne, “Analysis of the formation and elimination of loops in twisted cable,” *IEEE Journal of Oceanic Engineering*, vol. 15, no. 2, pp. 72–83, 1990.
- [64] G. Van der Heijden and J. Thompson, “Helical and localised buckling in twisted rods: a unified analysis of the symmetric case,” *Nonlinear dynamics*, vol. 21, no. 1, pp. 71–99, 2000.
- [65] J. Thompson, M. Silveira, G. Van der Heijden, and M. Wiercigroch, “Helical post-buckling of a rod in a cylinder: with applications to drill-strings,” *Proceedings of the Royal Society A: Mathematical, Physical and Engineering Sciences*, vol. 468, no. 2142, pp. 1591–1614, 2012.
- [66] J. Miller, T. Su, J. Pabon, N. Wicks, K. Bertoldi, and P. M. Reis, “Buckling of a thin elastic rod inside a horizontal cylindrical constraint,” *Extreme Mechanics Letters*, vol. 3, pp. 36–44, 2015.
- [67] A. Goriely and M. Tabor, “Nonlinear dynamics of filaments. iii. instabilities of helical rods,” *Proceedings of the Royal Society of London. Series A: Mathematical, Physical and Engineering Sciences*, vol. 453, no. 1967, pp. 2583–2601, 1997.

- [68] C. S. Peskin, “The immersed boundary method,” *Acta numerica*, vol. 11, pp. 479–517, 2002.
- [69] M. Somasi, B. Khomami, N. J. Woo, J. S. Hur, and E. S. Shaqfeh, “Brownian dynamics simulations of bead-rod and bead-spring chains: numerical algorithms and coarse-graining issues,” *Journal of non-newtonian fluid mechanics*, vol. 108, no. 1-3, pp. 227–255, 2002.
- [70] B. Delmotte, E. Climent, and F. Plouraboué, “A general formulation of bead models applied to flexible fibers and active filaments at low reynolds number,” *Journal of Computational Physics*, vol. 286, pp. 14–37, 2015.
- [71] R. Cortez, “The method of regularized stokeslets,” *SIAM Journal on Scientific Computing*, vol. 23, no. 4, pp. 1204–1225, 2001.
- [72] D. J. Smith, “A boundary element regularized stokeslet method applied to cilia-and flagella-driven flow,” *Proceedings of the Royal Society A: Mathematical, Physical and Engineering Sciences*, vol. 465, no. 2112, pp. 3605–3626, 2009.
- [73] E. L. Bouzarth and M. L. Minion, “Modeling slender bodies with the method of regularized stokeslets,” *Journal of Computational Physics*, vol. 230, no. 10, pp. 3929–3947, 2011.
- [74] G. Gompper, T. Ihle, D. Kroll, and R. Winkler, “Multi-particle collision dynamics: A particle-based mesoscale simulation approach to the hydrodynamics of complex fluids,” in *Advanced computer simulation approaches for soft matter sciences III*, pp. 1–87, Springer, 2009.
- [75] G. Batchelor, “Slender-body theory for particles of arbitrary cross-section in stokes flow,” *Journal of Fluid Mechanics*, vol. 44, no. 3, pp. 419–440, 1970.
- [76] J. B. Keller and S. I. Rubinow, “Slender-body theory for slow viscous flow,” *Journal of Fluid Mechanics*, vol. 75, no. 4, pp. 705–714, 1976.
- [77] R. E. Johnson, “An improved slender-body theory for stokes flow,” *Journal of Fluid Mechanics*, vol. 99, no. 2, pp. 411–431, 1980.
- [78] T. Götz, *Interactions of fibers and flow: asymptotics, theory and numerics*. dissertation. de, 2001.
- [79] L. Koens and E. Lauga, “The boundary integral formulation of stokes flows includes slender-body theory,” *Journal of Fluid Mechanics*, vol. 850, 2018.
- [80] M. J. Shelley and T. Ueda, “The stokesian hydrodynamics of flexing, stretching filaments,” *Physica D: Nonlinear Phenomena*, vol. 146, no. 1-4, pp. 221–245, 2000.

- [81] A.-K. Tornberg and M. J. Shelley, “Simulating the dynamics and interactions of flexible fibers in stokes flows,” *Journal of Computational Physics*, vol. 196, no. 1, pp. 8–40, 2004.
- [82] S. G. Prasath, J. Marthelot, R. Govindarajan, and N. Menon, “Relaxation of a highly deformed elastic filament at a fluid interface,” *arXiv preprint arXiv:1601.07278*, 2016.
- [83] T. Munk, O. Hallatschek, C. H. Wiggins, and E. Frey, “Dynamics of semiflexible polymers in a flow field,” *Physical Review E*, vol. 74, no. 4, p. 041911, 2006.
- [84] N. Autrusson, L. Guglielmini, S. Lecuyer, R. Rusconi, and H. A. Stone, “The shape of an elastic filament in a two-dimensional corner flow,” *Physics of Fluids*, vol. 23, no. 6, p. 063602, 2011.
- [85] H. Manikantan, *Bending, Buckling, Tumbling, Trapping: Viscous Dynamics of Elastic Filaments*. PhD thesis, UC San Diego, 2015.
- [86] W. H. Press, S. A. Teukolsky, W. T. Vetterling, and B. P. Flannery, “Numerical recipes in c++,” *The art of scientific computing*, vol. 2, p. 1002, 1992.
- [87] B. N. Parlett and D. S. Scott, “The lanczos algorithm with selective orthogonalization,” *Mathematics of computation*, vol. 33, no. 145, pp. 217–238, 1979.
- [88] H. Manikantan and D. Saintillan, “Effect of flexibility on the growth of concentration fluctuations in a suspension of sedimenting fibers: Particle simulations,” *Physics of Fluids*, vol. 28, no. 1, p. 013303, 2016.
- [89] E. Nazockdast, A. Rahimian, D. Zorin, and M. Shelley, “A fast platform for simulating semi-flexible fiber suspensions applied to cell mechanics,” *Journal of Computational Physics*, vol. 329, pp. 173–209, 2017.
- [90] J. F. Brady and G. Bossis, “Stokesian dynamics,” *Annual review of fluid mechanics*, vol. 20, no. 1, pp. 111–157, 1988.
- [91] D. Saintillan, E. Darve, and E. S. Shaqfeh, “A smooth particle-mesh ewald algorithm for stokes suspension simulations: The sedimentation of fibers,” *Physics of Fluids*, vol. 17, no. 3, p. 033301, 2005.
- [92] L. Greengard and V. Rokhlin, “A fast algorithm for particle simulations,” *Journal of computational physics*, vol. 73, no. 2, pp. 325–348, 1987.
- [93] W. Yan and M. Shelley, “Flexibly imposing periodicity in kernel independent fmm: A multipole-to-local operator approach,” *Journal of Computational Physics*, vol. 355, pp. 214–232, 2018.

- [94] M. Doi and S. Edwards, “Dynamics of rod-like macromolecules in concentrated solution. part 1,” *Journal of the Chemical Society, Faraday Transactions 2: Molecular and Chemical Physics*, vol. 74, pp. 560–570, 1978.
- [95] M. Doi and S. F. Edwards, *The theory of polymer dynamics*, vol. 73. oxford university press, 1988.
- [96] R. G. Larson, *The structure and rheology of complex fluids*, vol. 150. Oxford university press New York, 1999.
- [97] G. B. Jeffery, “The motion of ellipsoidal particles immersed in a viscous fluid,” *Proceedings of the Royal Society of London. Series A, Containing papers of a mathematical and physical character*, vol. 102, no. 715, pp. 161–179, 1922.
- [98] H. Kobayashi and R. Yamamoto, “Tumbling motion of a single chain in shear flow: A crossover from brownian to non-brownian behavior,” *Physical Review E*, vol. 81, no. 4, p. 041807, 2010.
- [99] C. P. Broedersz and F. C. MacKintosh, “Modeling semiflexible polymer networks,” *Reviews of Modern Physics*, vol. 86, no. 3, p. 995, 2014.
- [100] E. Farge and A. C. Maggs, “Dynamic scattering from semiflexible polymers,” *Macromolecules*, vol. 26, no. 19, pp. 5041–5044, 1993.
- [101] R. Everaers, F. Jülicher, A. Ajdari, and A. Maggs, “Dynamic fluctuations of semiflexible filaments,” *Physical review letters*, vol. 82, no. 18, p. 3717, 1999.
- [102] R. Granek, “From semi-flexible polymers to membranes: anomalous diffusion and reptation,” *Journal de Physique II*, vol. 7, no. 12, pp. 1761–1788, 1997.
- [103] A. Ashkin, “Acceleration and trapping of particles by radiation pressure,” *Physical review letters*, vol. 24, no. 4, p. 156, 1970.
- [104] G. Binnig, C. F. Quate, and C. Gerber, “Atomic force microscope,” *Physical review letters*, vol. 56, no. 9, p. 930, 1986.
- [105] S. B. Smith, L. Finzi, and C. Bustamante, “Direct mechanical measurements of the elasticity of single dna molecules by using magnetic beads,” *Science*, vol. 258, no. 5085, pp. 1122–1126, 1992.
- [106] J. M. Schurr and S. B. Smith, “Theory for the extension of a linear polyelectrolyte attached at one end in an electric field,” *Biopolymers: Original Research on Biomolecules*, vol. 29, no. 8-9, pp. 1161–1165, 1990.
- [107] T. T. Perkins, D. E. Smith, R. G. Larson, and S. Chu, “Stretching of a single tethered polymer in a uniform flow,” *Science*, vol. 268, no. 5207, pp. 83–87, 1995.

- [108] T. Odijk, “Stiff chains and filaments under tension,” *Macromolecules*, vol. 28, no. 20, pp. 7016–7018, 1995.
- [109] J. F. Marko and E. D. Siggia, “Stretching dna,” *Macromolecules*, vol. 28, no. 26, pp. 8759–8770, 1995.
- [110] A. Marantan and L. Mahadevan, “Mechanics and statistics of the worm-like chain,” *American Journal of Physics*, vol. 86, no. 2, pp. 86–94, 2018.
- [111] Y.-N. Young and M. J. Shelley, “Stretch-coil transition and transport of fibers in cellular flows,” *Phys. Rev. Lett.*, vol. 99, p. 058303, 2007.
- [112] H. Manikantan and D. Saintillan, “Buckling transition of a semiflexible filament in extensional flow,” *Phys. Rev. E*, vol. 92, no. 4, p. 041002, 2015.
- [113] N. Quennouz, M. Shelley, O. du Roure, and A. Lindner, “Transport and buckling dynamics of an elastic fibre in a viscous cellular flow,” *J. Fluid Mech.*, vol. 769, pp. 387–402, 2015.
- [114] L. Guglielmini, A. Kushwaha, E. Shaqfeh, and H. Stone, “Buckling transitions of an elastic filament in a viscous stagnation point flow,” *Phys. Fluids*, vol. 24, p. 123601, 2012.
- [115] H. Manikantan and D. Saintillan, “Subdiffusive transport of fluctuating elastic filaments in cellular flows,” *Phys. Fluids*, vol. 25, no. 7, p. 073603, 2013.
- [116] P. S. Lang, B. Obermayer, and E. Frey, “Dynamics of a semiflexible polymer or polymer ring in shear flow,” *Phys. Rev. E*, vol. 89, no. 2, p. 022606, 2014.
- [117] H. Nguyen and L. Fauci, “Hydrodynamics of diatom chains and semiflexible fibres,” *J. R. Soc. Interface*, vol. 11, no. 96, p. 20140314, 2014.
- [118] O. Forgacs and S. Mason, “Particle motions in sheared suspensions: X. Orbits of flexible threadlike particles,” *J. Colloid Sci.*, vol. 14, no. 5, pp. 473–491, 1959.
- [119] S. Pawowska, P. Nakielski, F. Pierini, I. K. Piechocka, K. Zembrzycki, and T. A. Kowalewski, “Lateral migration of electrospun hydrogel nanofilaments in an oscillatory flow,” *PLOS ONE*, vol. 12, pp. 1–21, 11 2017.
- [120] B. Delmotte, E. Climent, and F. Plouraboué, “A general formulation of Bead Models applied to flexible fibers and active filaments at low Reynolds number,” *Journal of Computational Physics*, vol. 286, pp. 14–37, 2015.
- [121] R. Chelakkot, R. G. Winkler, and G. Gompper, “Migration of semiflexible polymers in microcapillary flow,” vol. 14001, 2010.

- [122] K. Baczynski, R. Lipowsky, and J. Kierfeld, “Stretching of buckled filaments by thermal fluctuations,” *Phys. Rev. E*, vol. 76, no. 6, p. 061914, 2007.
- [123] F. Rioual, T. Biben, and C. Misbah, “Analytical analysis of a vesicle tumbling under a shear flow,” *Phys. Rev. E*, vol. 69, no. 6, p. 061914, 2004.
- [124] T. W. Liu, “Flexible polymer chain dynamics and rheological properties in steady flows,” *The Journal of Chemical Physics*, vol. 90, no. 10, pp. 5826–5842, 1989.
- [125] P. Grassia and E. Hinch, “Computer simulations of polymer chain relaxation via brownian motion,” *Journal of Fluid Mechanics*, vol. 308, pp. 255–288, 1996.
- [126] P. S. Doyle, E. S. Shaqfeh, and A. P. Gast, “Dynamic simulation of freely draining flexible polymers in steady linear flows,” *Journal of Fluid Mechanics*, vol. 334, pp. 251–291, 1997.
- [127] R. G. Winkler, “Semiflexible polymers in shear flow,” *Physical review letters*, vol. 97, no. 12, p. 128301, 2006.
- [128] B. Huber, M. Harasim, B. Wunderlich, M. Kroger, and A. R. Bausch, “Microscopic origin of the non-newtonian viscosity of semiflexible polymer solutions in the semidilute regime,” *ACS Macro Letters*, vol. 3, no. 2, pp. 136–140, 2014.
- [129] A. Nikoubashman and M. P. Howard, “Equilibrium dynamics and shear rheology of semiflexible polymers in solution,” *Macromolecules*, vol. 50, no. 20, pp. 8279–8289, 2017.
- [130] S. Goto, H. Nagazono, and H. Kato, “The flow behavior of fiber suspensions in newtonian fluids and polymer solutions.,” *Rheologica acta*, vol. 25, no. 2, pp. 119–129, 1986.
- [131] M. Zirnsak, D. Hur, and D. Boger, “Normal stresses in fibre suspensions,” *Journal of non-newtonian fluid mechanics*, vol. 54, pp. 153–193, 1994.
- [132] L. Leal and E. Hinch, “The effect of weak brownian rotations on particles in shear flow,” *Journal of Fluid Mechanics*, vol. 46, no. 4, pp. 685–703, 1971.
- [133] W. E. Stewart and J. P. Sorensen, “Hydrodynamic interaction effects in rigid dumbbell suspensions. ii. computations for steady shear flow,” *Transactions of the Society of Rheology*, vol. 16, no. 1, pp. 1–13, 1972.
- [134] G. Batchelor, “The stress system in a suspension of force-free particles,” *Journal of fluid mechanics*, vol. 41, no. 3, pp. 545–570, 1970.
- [135] G. Batchelor, “The effect of brownian motion on the bulk stress in a suspension of spherical particles,” *Journal of fluid mechanics*, vol. 83, no. 1, pp. 97–117, 1977.

- [136] S. B. Chen and L. Jiang, “Orientation distribution in a dilute suspension of fibers subject to simple shear flow,” *Physics of Fluids*, vol. 11, no. 10, pp. 2878–2890, 1999.
- [137] D. Saintillan, “The dilute rheology of swimming suspensions: A simple kinetic model,” *Experimental Mechanics*, vol. 50, no. 9, pp. 1275–1281, 2010.
- [138] D. Saintillan, “Extensional rheology of active suspensions,” *Physical Review E*, vol. 81, no. 5, p. 056307, 2010.
- [139] D. Saintillan and M. J. Shelley, “Active suspensions and their nonlinear models,” *Comptes Rendus Physique*, vol. 14, no. 6, pp. 497–517, 2013.
- [140] J. Irving and J. G. Kirkwood, “The statistical mechanical theory of transport processes. iv. the equations of hydrodynamics,” *The Journal of chemical physics*, vol. 18, no. 6, pp. 817–829, 1950.
- [141] H. C. Öttinger, “Stochastic processes, polymer dynamics, and fluid mechanics,” in *Stochastic Processes in Polymeric Fluids*, pp. 1–15, Springer, 1996.
- [142] L. Guglielmini, A. Kushwaha, E. S. G. Shaqfeh, and H. A. Stone, “Buckling transitions of an elastic filament in a viscous stagnation point flow,” *Phys. Fluids*, vol. 24, p. 123601, 2012.
- [143] A. Lindner and M. Shelley, “Elastic fibers in flows,” in *Fluid-Structure Interactions in Low-Reynolds-Number Flows*, pp. 168–192, Royal Society of Chemistry, 2015.
- [144] O. du Roure, A. Lindner, E. N. Nazockdast, and M. J. Shelley, “Dynamics of flexible fibers in viscous flows and fluids,” *Annu. Rev. Fluid Mech.*, vol. 51, pp. 539–572, 2019.
- [145] J. LaGrone, R. Cortez, W. Yan, and L. Fauci, “Complex dynamics of long, flexible fibers in shear,” *Journal of Non-Newtonian Fluid Mechanics*, 2019.
- [146] C. Mercader, A. Lucas, A. Derré, C. Zakri, S. Moisan, M. Maugey, and P. Poulin, “Kinetics of fiber solidification,” *Proc. Natl. Acad. Sci. USA*, vol. 107, pp. 18331–18335, 2010.
- [147] S. Ryu, R. E. Pepper, M. Nagai, and D. C. France, “*Vorticella*: a protozoan for bio-inspired engineering,” *Micromachines*, vol. 8, no. 1, p. 4, 2016.
- [148] S. Allende, C. Henry, and J. Bec, “Stretching and buckling of small elastic fibers in turbulence,” *Phys. Rev. Lett.*, vol. 121, p. 154001, 2018.
- [149] S. Kuei, A. M. Słowicka, M. L. Ekiel-Jeżewska, E. Wajnryb, and H. A. Stone, “Dynamics and topology of a flexible chain: knots in steady shear flow,” *New J. Phys.*, vol. 17, p. 053009, may 2015.

- [150] A. Goriely and M. Tabor, “The nonlinear dynamics of filaments,” *Nonlinear Dyn.*, vol. 21, no. 1, pp. 101–133, 2000.
- [151] S. S. Antman, *Nonlinear Problems of Elasticity*. Springer, 2005.
- [152] D. Svenšek and R. Podgornik, “Confined nanorods: Jamming due to helical buckling,” *Phys. Rev. E*, vol. 77, no. 3, p. 031808, 2008.
- [153] W. S. Klug, M. T. Feldmann, and M. Ortiz, “Three-dimensional director-field predictions of viral DNA packing arrangements,” *Comput. Mech.*, vol. 35, no. 2, pp. 146–152, 2005.
- [154] K. Zografas, F. Pimenta, M. A. Alves, and M. S. N. Oliveira, “Microfluidic converging/diverging channels optimised for homogeneous extensional deformation,” *Biomicrofluidics*, vol. 10, no. 4, p. 043508, 2016.
- [155] Y. Liu, J. Fidalgo, K. Zografas, C. Duchene, M. S. N. Oliveira, O. Du Roure, and A. Lindner, “Optimized hyperbolic microchannels for the mechanical characterization of bio-particles,” *submitted*, 2019.
- [156] J. LaGrone, R. Cortez, and L. Fauci, “Elastohydrodynamics of swimming helices: Effects of flexibility and confinement,” *Phys. Rev. Fluids*, vol. 4, p. 033102, 2019.
- [157] R. Chelakkot, R. G. Winkler, and G. Gompper, “Flow-induced helical coiling of semi-flexible polymers in structured microchannels,” *Phys. Rev. Lett.*, vol. 109, no. 17, p. 178101, 2012.
- [158] A. Goriely and M. Tabor, “Spontaneous helix hand reversal and tendril perversion in climbing plants,” *Phys. Rev. Lett.*, vol. 80, pp. 1564–1567, 1998.
- [159] G. K. Batchelor, “Slender-body theory for particles of arbitrary cross-section in Stokes flow,” *J. Fluid Mech.*, vol. 44, pp. 419–440, 1970.
- [160] T. Su, J. Liu, D. Terwagne, P. M. Reis, and K. Bertoldi, “Buckling of an elastic rod embedded on an elastomeric matrix: planar vs. non-planar configurations,” *Soft Matter*, vol. 10, no. 33, pp. 6294–6302, 2014.
- [161] P. G. Drazin and W. H. Reid, *Hydrodynamic Stability*. Cambridge University Press, 2004.
- [162] E. Byskov and W. Hutchinson, “Mode interaction in axially stiffened cylindrical shells,” *AIAA Journal*, vol. 15, no. 7, pp. 941–948, 1977.
- [163] M. C. Marchetti, J.-F. Joanny, S. Ramaswamy, T. B. Liverpool, J. Prost, M. Rao, and R. A. Simha, “Hydrodynamics of soft active matter,” *Reviews of Modern Physics*, vol. 85, no. 3, p. 1143, 2013.

- [164] L. Bourdieu, T. Duke, M. Elowitz, D. Winkelmann, S. Leibler, and A. Libchaber, “Spiral defects in motility assays: a measure of motor protein force,” *Physical review letters*, vol. 75, no. 1, p. 176, 1995.
- [165] T. Duke, T. E. Holy, and S. Leibler, ““ gliding assays” for motor proteins: A theoretical analysis,” *Physical review letters*, vol. 74, no. 2, p. 330, 1995.
- [166] F. Juelicher, K. Kruse, J. Prost, and J.-F. Joanny, “Active behavior of the cytoskeleton,” *Physics reports*, vol. 449, no. 1-3, pp. 3–28, 2007.
- [167] V. Schaller, C. Weber, C. Semmrich, E. Frey, and A. R. Bausch, “Polar patterns of driven filaments,” *Nature*, vol. 467, no. 7311, p. 73, 2010.
- [168] Y. Sumino, K. H. Nagai, Y. Shitaka, D. Tanaka, K. Yoshikawa, H. Chaté, and K. Oiwa, “Large-scale vortex lattice emerging from collectively moving microtubules,” *Nature*, vol. 483, no. 7390, p. 448, 2012.
- [169] R. G. Winkler, J. Elgeti, and G. Gompper, “Active polymers?emergent conformational and dynamical properties: A brief review,” *Journal of the Physical Society of Japan*, vol. 86, no. 10, p. 101014, 2017.
- [170] M. A. Sleigh, J. R. Blake, and N. Liron, “The propulsion of mucus by cilia,” *Am. Rev. Respir. Dis.*, vol. 137, no. 3, pp. 726–741, 1988.
- [171] C. D. Silflow and P. A. Lefebvre, “Assembly and motility of eukaryotic cilia and flagella. lessons from *Chlamydomonas reinhardtii*,” *Plant Physiol.*, vol. 127, pp. 1500–1507, 2001.
- [172] E. F. Smith and P. A. Lefebvre, “PF16 encodes a protein with armadillo repeats and localizes to a single microtubule of the central apparatus in *Chlamydomonas* flagella.,” *J. Cell Biol.*, vol. 132, no. 3, pp. 359–370, 1996.
- [173] P. Sartori, V. F. Geyer, J. Howard, and F. Jülicher, “Curvature regulation of the ciliary beat through axonemal twist,” *Phys. Rev. E*, vol. 94, no. 4, p. 042426, 2016.
- [174] D. Oriola, H. Gadélha, and J. Casademunt, “Nonlinear amplitude dynamics in flagellar beating,” *R. Soc. Open Science*, vol. 4, no. 3, p. 160698, 2017.
- [175] I. H. Riedel-Kruse, A. Hilfinger, J. Howard, and F. Jülicher, “How molecular motors shape the flagellar beat,” *HFSP J.*, vol. 1, no. 3, pp. 192–208, 2007.
- [176] K. E. Summers and I. R. Gibbons, “Adenosine triphosphate-induced sliding of tubules in trypsin-treated flagella of sea-urchin sperm,” *Proc. Natl. Acad. Sci. USA*, vol. 68, no. 12, pp. 3092–3096, 1971.

- [177] S. Camalet and F. Jülicher, “Generic aspects of axonemal beating,” *New J. Phys.*, vol. 2, no. 1, p. 24, 2000.
- [178] P. V. Bayly and S. K. Dutcher, “Steady dynein forces induce flutter instability and propagating waves in mathematical models of flagella,” *J. R. Soc. Interface*, vol. 13, no. 123, p. 20160523, 2016.
- [179] G. De Canio, E. Lauga, and R. E. Goldstein, “Spontaneous oscillations of elastic filaments induced by molecular motors,” *J. R. Soc. Interface*, vol. 14, no. 136, p. 20170491, 2017.
- [180] F. Ling, H. Guo, and E. Kanso, “Instability-driven oscillations of elastic microfilaments,” *Journal of the Royal Society Interface*, vol. 15, no. 149, p. 20180594, 2018.
- [181] V. V. Bolotin, *Nonconservative Problems of the Theory of Elastic Stability*. Macmillan, 1963.
- [182] R. Chelakkot, A. Gopinath, L. Mahadevan, and M. F. Hagan, “Flagellar dynamics of a connected chain of active, polar, Brownian particles,” *J. R. Soc. Interface*, vol. 11, no. 92, p. 20130884, 2014.
- [183] R. E. Goldstein, E. Lauga, A. I. Pesci, and M. R. E. Proctor, “Elastohydrodynamic synchronization of adjacent beating flagella,” *Phys. Rev. Fluids*, vol. 1, no. 7, p. 073201, 2016.
- [184] R. H. Dillon and L. J. Fauci, “An integrative model of internal axoneme mechanics and external fluid dynamics in ciliary beating,” *J. Theor. Biol.*, vol. 207, no. 3, pp. 415–430, 2000.
- [185] C. J. Brokaw, “Bend propagation by a sliding filament model for flagella,” *Journal of Experimental Biology*, vol. 55, no. 2, pp. 289–304, 1971.
- [186] M. Hines and J. J. Blum, “Bend propagation in flagella. I. Derivation of equations of motion and their simulation,” *Biophys. J.*, vol. 23, no. 1, pp. 41–57, 1978.
- [187] P. Sartori, V. F. Geyer, A. Scholich, F. Jülicher, and J. Howard, “Dynamic curvature regulation accounts for the symmetric and asymmetric beats of chlamydomonas flagella,” *Elife*, vol. 5, p. e13258, 2016.
- [188] C. B. Lindemann, “A ‘geometric clutch’ hypothesis to explain oscillations of the axoneme of cilia and flagella,” *J. Theor. Biol.*, vol. 168, no. 2, pp. 175–189, 1994.
- [189] P. V. Bayly and K. S. Wilson, “Equations of interdoublet separation during flagella motion reveal mechanisms of wave propagation and instability,” *Biophys. J.*, vol. 107, no. 7, pp. 1756–1772, 2014.

- [190] P. V. Bayly and K. S. Wilson, “Analysis of unstable modes distinguishes mathematical models of flagellar motion,” *J. R. Soc. Interface*, vol. 12, no. 106, p. 20150124, 2015.
- [191] H. Gadêlha, E. Gaffney, D. Smith, and J. Kirkman-Brown, “Nonlinear instability in flagellar dynamics: a novel modulation mechanism in sperm migration?,” *Journal of The Royal Society Interface*, vol. 7, no. 53, pp. 1689–1697, 2010.
- [192] A. Hilfinger, A. K. Chattopadhyay, and F. Jülicher, “Nonlinear dynamics of cilia and flagella,” *Phys. Rev. E*, vol. 79, no. 5, p. 051918, 2009.
- [193] S. Camalet, F. Jülicher, and J. Prost, “Self-organized beating and swimming of internally driven filaments,” *Phys. Rev. Lett.*, vol. 82, no. 7, p. 1590, 1999.
- [194] F. Jülicher and J. Prost, “Spontaneous oscillations of collective molecular motors,” *Phys. Rev. Lett.*, vol. 78, no. 23, p. 4510, 1997.
- [195] B. Guirao and J.-F. Joanny, “Spontaneous creation of macroscopic flow and metachronal waves in an array of cilia,” *Biophys. J.*, vol. 92, no. 6, pp. 1900–1917, 2007.
- [196] S. Werner, J. C. Rink, I. H. Riedel-Kruse, and B. M. Friedrich, “Shape mode analysis exposes movement patterns in biology: Flagella and flatworms as case studies,” *PLoS one*, vol. 9, no. 11, p. e113083, 2014.
- [197] S. S. Antman, *Nonlinear Problems of Elasticity*. Springer, New York, 1995.
- [198] J. Keller and S. Rubinow, “Slender-body theory for slow viscous flow,” *J. Fluid Mech.*, vol. 75, pp. 705–714, 1976.
- [199] R. E. Johnson, “An improved slender-body theory for Stokes flow,” *J. Fluid Mech.*, vol. 99, pp. 411–431, 1980.
- [200] L. Koens and E. Lauga, “The boundary integral formulation of Stokes flow includes slender-body theory,” *J. Fluid Mech.*, vol. 850, p. R1, 2018.
- [201] J. Gray and G. Hancock, “The propulsion of sea-urchin spermatozoa,” *Journal of Experimental Biology*, vol. 32, no. 4, pp. 802–814, 1955.
- [202] J. Lighthill, “Flagellar hydrodynamics,” *SIAM Rev.*, vol. 18, pp. 161–230, 1976.
- [203] K. Svoboda and S. M. Block, “Force and velocity measured for single kinesin molecules,” *Cell*, vol. 77, no. 5, pp. 773–784, 1994.
- [204] M. J. I. Müller, S. Klumpp, and R. Lipowsky, “Tug-of-war as a cooperative mechanism for bidirectional cargo transport by molecular motors,” *Proc. Natl. Acad. Sci. USA*, vol. 105, no. 12, pp. 4609–4614, 2008.

- [205] E. A. Gaffney, H. Gadêlha, D. J. Smith, J. R. Blake, and J. C. Kirkman-Brown, “Mammalian sperm motility: observation and theory,” *Annu. Rev. Fluid Mech.*, vol. 43, pp. 501–528, 2011.
- [206] J. Howard, *Mechanics of Motor Proteins and the Cytoskeleton*. Sinauer Associates, Sunderland, MA, 2001.
- [207] D. J. Smith, E. A. Gaffney, H. Gadêlha, N. Kapur, and J. C. Kirkman-Brown, “Bend propagation in the flagella of migrating human sperm, and its modulation by viscosity,” *Cytoskeleton*, vol. 66, no. 4, pp. 220–236, 2009.
- [208] T. Guérin, J. Prost, and J.-F. Joanny, “Dynamical behavior of molecular motor assemblies in the rigid and crossbridge models,” *Eur. Phys. J. E*, vol. 34, no. 6, p. 60, 2011.
- [209] J. Elgeti and G. Gompper, “Emergence of metachronal waves in cilia arrays,” *Proc. Natl. Acad. Sci. USA*, vol. 110, no. 12, pp. 4470–4475, 2013.
- [210] S. Gueron, K. Levit-Gurevich, N. Liron, and J. J. Blum, “Cilia internal mechanism and metachronal coordination as the result of hydrodynamical coupling,” *Proc. Natl. Acad. Sci. USA*, vol. 94, no. 12, pp. 6001–6006, 1997.
- [211] J. Han and C. S. Peskin, “Spontaneous oscillation and fluid–structure interaction of cilia,” *Proc. Natl. Acad. Sci. USA*, vol. 115, no. 17, pp. 4417–4422, 2018.
- [212] P. Delmotte and M. J. Sanderson, “Ciliary beat frequency is maintained at a maximal rate in the small airways of mouse lung slices,” *Am. J. Respir. Cell Mol. Biol.*, vol. 35, no. 1, pp. 110–117, 2006.
- [213] C. B. Lindemann, “Geometric clutch model version 3: The role of the inner and outer arm dyneins in the ciliary beat,” *Cytoskeleton*, vol. 52, no. 4, pp. 242–254, 2002.
- [214] J. S. Guasto, K. A. Johnson, and J. P. Gollub, “Oscillatory flows induced by microorganisms swimming in two dimensions,” *Phys. Rev. Lett.*, vol. 105, no. 16, p. 168102, 2010.
- [215] S. P. Pearce, M. Heil, O. E. Jensen, G. W. Jones, and A. Prokop, “Curvature-sensitive kinesin binding can explain microtubule ring formation and reveals chaotic dynamics in a mathematical model,” *arXiv preprint arXiv:1803.07312*, 2018.
- [216] S. H. Strogatz, *Nonlinear Dynamics and Chaos: with Applications to Physics, Biology, Chemistry, and Engineering*. CRC Press, Boca Raton, 2018.
- [217] A. Vilfan and F. Jülicher, “Hydrodynamic flow patterns and synchronization of beating cilia,” *Phys. Rev. Lett.*, vol. 96, no. 5, p. 058102, 2006.

- [218] D. R. Brumley, K. Y. Wan, M. Polin, and R. E. Goldstein, “Flagellar synchronization through direct hydrodynamic interactions,” *Elife*, vol. 3, p. e02750, 2014.
- [219] R. Ma, G. S. Klindt, I. H. Riedel-Kruse, F. Jülicher, and B. M. Friedrich, “Active phase and amplitude fluctuations of flagellar beating,” *Phys. Rev. Lett.*, vol. 113, no. 4, p. 048101, 2014.
- [220] J. N. Kutz, *Data-Driven Modeling and Scientific Computation: Methods for Complex Systems and Big Data*. Oxford University Press, 2013.
- [221] J. Blake, “A note on the image system for a Stokeslet in a no-slip boundary,” in *Mathematical Proceedings of the Cambridge Philosophical Society*, vol. 70, pp. 303–310, Cambridge University Press, 1971.
- [222] J. Ainley, S. Durkin, R. Embid, P. Boindala, and R. Cortez, “The method of images for regularized Stokeslets,” *J. Comp. Phys.*, vol. 227, no. 9, pp. 4600–4616, 2008.
- [223] B. Chakrabarti and D. Saintillan *in preparation*, 2018.
- [224] S. Ghose and R. Adhikari, “Irreducible representations of oscillatory and swirling flows in active soft matter,” *Phys. Rev. Lett.*, vol. 112, p. 118102, 2014.
- [225] G. S. Klindt and B. M. Friedrich, “Flagellar swimmers oscillate between pusher-and puller-type swimming,” *Phys. Rev. E*, vol. 92, no. 6, p. 063019, 2015.
- [226] K. Ishimoto, H. Gadêlha, E. A. Gaffney, D. J. Smith, and J. Kirkman-Brown, “Coarse-graining the fluid flow around a human sperm,” *Phys. Rev. Lett.*, vol. 118, no. 12, p. 124501, 2017.
- [227] K. Ishimoto, H. Gadêlha, E. A. Gaffney, D. J. Smith, and J. Kirkman-Brown, “Human sperm swimming in a high viscosity mucus analogue,” *J. Theor. Biol.*, vol. 446, pp. 1–10, 2018.
- [228] Scholarpedia, “Synchronization,” 2007. <http://www.scholarpedia.org/article/Synchronization>, Last accessed on 2017-11-30.
- [229] T. Terasima and L. Tolmach, “Growth and nucleic acid synthesis in synchronously dividing populations of hela cells,” *Experimental cell research*, vol. 30, no. 2, pp. 344–362, 1963.
- [230] P. N. Steinmetz, A. Roy, P. Fitzgerald, S. Hsiao, K. Johnson, and E. Niebur, “Attention modulates synchronized neuronal firing in primate somatosensory cortex,” *Nature*, vol. 404, no. 6774, p. 187, 2000.
- [231] J. Buck and E. Buck, “Synchronous fireflies,” *Scientific American*, vol. 234, no. 5, pp. 74–85, 1976.

- [232] A. Weller and L. Weller, “Menstrual synchrony in female couples,” *Psychoneuroendocrinology*, vol. 17, no. 2-3, pp. 171–177, 1992.
- [233] A. Pikovsky, M. Rosenblum, and J. Kurths, *Synchronization: A Universal Concept in Nonlinear Sciences*, vol. 12. Cambridge university press, 2003.
- [234] J. A. Acebrón, L. L. Bonilla, C. J. P. Vicente, F. Ritort, and R. Spigler, “The kuramoto model: A simple paradigm for synchronization phenomena,” *Reviews of modern physics*, vol. 77, no. 1, p. 137, 2005.
- [235] S. H. Strogatz, D. M. Abrams, A. McRobie, B. Eckhardt, and E. Ott, “Theoretical mechanics: Crowd synchrony on the millennium bridge,” *Nature*, vol. 438, no. 7064, p. 43, 2005.
- [236] V. Rothschild, “Measurement of sperm activity before artificial insemination,” *Nature*, vol. 163, no. 4140, pp. 358–359, 1949.
- [237] G. I. Taylor, “Analysis of the swimming of microscopic organisms,” *Proc. R. Soc. London A*, vol. 209, no. 1099, pp. 447–461, 1951.
- [238] R. Golestanian, J. M. Yeomans, and N. Uchida, “Hydrodynamic synchronization at low reynolds number,” *Soft Matter*, vol. 7, no. 7, pp. 3074–3082, 2011.
- [239] U. Rüffer and W. Nultsch, “High-speed cinematographic analysis of the movement of chlamydomonas,” *Cell Motility*, vol. 5, no. 3, pp. 251–263, 1985.
- [240] M. Polin, I. Tuval, K. Drescher, J. P. Gollub, and R. E. Goldstein, “Chlamydomonas swims with two gears in a eukaryotic version of run-and-tumble locomotion,” *Science*, vol. 325, no. 5939, pp. 487–490, 2009.
- [241] R. E. Goldstein, M. Polin, and I. Tuval, “Noise and synchronization in pairs of beating eukaryotic flagella,” *Phys. Rev. Lett.*, vol. 103, no. 16, p. 168103, 2009.
- [242] K. C. Leptos, K. Y. Wan, M. Polin, I. Tuval, A. I. Pesci, and R. E. Goldstein, “Antiphase synchronization in a flagellar-dominance mutant of chlamydomonas,” *Phys. Rev. Lett.*, vol. 111, no. 15, p. 158101, 2013.
- [243] K. Y. Wan, K. C. Leptos, and R. E. Goldstein, “Lag, lock, sync, slip: the many phases of coupled flagella,” *J. R. Soc. Interface*, vol. 11, no. 94, p. 20131160, 2014.
- [244] N. Uchida and R. Golestanian, “Generic conditions for hydrodynamic synchronization,” *Phys. Rev. Lett.*, vol. 106, no. 5, p. 058104, 2011.
- [245] A. Maestro, N. Bruot, J. Kotar, N. Uchida, R. Golestanian, and P. Cicuta, “Control of synchronization in models of hydrodynamically coupled motile cilia,” *Commun. Phys.*, vol. 1, no. 1, p. 28, 2018.

- [246] G. J. Elfring and E. Lauga, “Hydrodynamic phase locking of swimming microorganisms,” *Phys. Rev. Lett.*, vol. 103, no. 8, p. 088101, 2009.
- [247] H. Guo, L. Fauci, M. Shelley, and E. Kanso, “Bistability in the synchronization of actuated microfilaments,” *J. Fluid Mech.*, vol. 836, pp. 304–323, 2018.
- [248] A. Vilfan, S. Subramani, E. Bodenschatz, R. Golestanian, and I. Guido, “Flagella-like beating of a single microtubule,” *Nano Lett.*, vol. 19, no. 5, pp. 3359–3363, 2019.
- [249] C. Brokaw, “Non-sinusoidal bending waves of sperm flagella,” *J. Exp. Biol.*, vol. 43, no. 1, pp. 155–169, 1965.
- [250] B. Chakrabarti and D. Saintillan, “Spontaneous oscillations, beating patterns, and hydrodynamics of active microfilaments,” *Phys. Rev. Fluids*, vol. 4, p. 043102, Apr 2019.
- [251] V. Geyer, *Characterization of the Flagellar Beat of the Single Cell Green Alga Chlamydomonas Reinhardtii*. PhD thesis, Sächsische Landesbibliothek – Staats- und Universitätsbibliothek Dresden, 2013.
- [252] J. R. Blake, “A spherical envelope approach to ciliary propulsion,” *Journal of Fluid Mechanics*, vol. 46, no. 1, pp. 199–208, 1971.
- [253] M. Sleigh, “The form of beat in cilia of stentor and opalina,” *Journal of Experimental Biology*, vol. 37, no. 1, pp. 1–10, 1960.
- [254] I. Gibbons, “The relationship between the fine structure and direction of beat in gill cilia of a lamellibranch mollusc,” *The Journal of Cell Biology*, vol. 11, no. 1, pp. 179–205, 1961.
- [255] M. A. Chilvers, A. Rutman, and C. O’callaghan, “Ciliary beat pattern is associated with specific ultrastructural defects in primary ciliary dyskinesia,” *Journal of Allergy and Clinical Immunology*, vol. 112, no. 3, pp. 518–524, 2003.
- [256] H. J. Hoops, “Flagellar, cellular and organismal polarity in volvox carteri,” *Journal of Cell Science*, vol. 104, no. 1, pp. 105–117, 1993.
- [257] F. Jülicher and J. Prost, “Cooperative molecular motors,” *Phys. Rev. Lett.*, vol. 75, no. 13, p. 2618, 1995.
- [258] K. Y. Wan and R. E. Goldstein, “Coordinated beating of algal flagella is mediated by basal coupling,” *Proc. Natl. Acad. Sci. USA*, vol. 113, no. 20, pp. E2784–E2793, 2016.
- [259] B. M. Friedrich and F. Jülicher, “Flagellar synchronization independent of hydrodynamic interactions,” *Phys. Rev. Lett.*, vol. 109, no. 13, p. 138102, 2012.

- [260] K. Polotzek and B. M. Friedrich, “A three-sphere swimmer for flagellar synchronization,” *New J. Phys.*, vol. 15, no. 4, p. 045005, 2013.
- [261] V. F. Geyer, F. Jülicher, J. Howard, and B. M. Friedrich, “Cell-body rocking is a dominant mechanism for flagellar synchronization in a swimming alga,” *Proc. Natl. Acad. Sci. USA*, vol. 110, no. 45, pp. 18058–18063, 2013.
- [262] R. R. Bennett and R. Golestanian, “Emergent run-and-tumble behavior in a simple model of chlamydomonas with intrinsic noise,” *Phys. Rev. Lett.*, vol. 110, no. 14, p. 148102, 2013.
- [263] R. R. Bennett and R. Golestanian, “Phase-dependent forcing and synchronization in the three-sphere model of chlamydomonas,” *New J. Phys.*, vol. 15, no. 7, p. 075028, 2013.
- [264] B. Kralemann, L. Cimponeriu, M. Rosenblum, A. Pikovsky, and R. Mrowka, “Phase dynamics of coupled oscillators reconstructed from data,” *Phys. Rev. E*, vol. 77, no. 6, p. 066205, 2008.
- [265] Y. Kawamura and R. Tsubaki, “Phase reduction approach to elastohydrodynamic synchronization of beating flagella,” *Physical Review E*, vol. 97, no. 2, p. 022212, 2018.
- [266] R. L. Stratonovich, *Topics in the Theory of Random Noise*. CRC Press, 1967.
- [267] Y. Yang, J. Elgeti, and G. Gompper, “Cooperation of sperm in two dimensions: synchronization, attraction, and aggregation through hydrodynamic interactions,” *Phys. Rev. E*, vol. 78, no. 6, p. 061903, 2008.
- [268] D. Edwards, M. Shapiro, H. Brenner, and M. Shapira, “Dispersion of inert solutes in spatially periodic, two-dimensional model porous media,” *Transport in Porous Media*, vol. 6, no. 4, pp. 337–358, 1991.
- [269] B. B. Dykaar and P. K. Kitanidis, “Macrotransport of a biologically reacting solute through porous media,” *Water Resources Research*, vol. 32, no. 2, pp. 307–320, 1996.
- [270] O. Felfoul, M. Mohammadi, S. Taherkhani, D. De Lanauze, Y. Z. Xu, D. Loghin, S. Essa, S. Jancik, D. Houle, M. Lafleur, *et al.*, “Magneto-aerotactic bacteria deliver drug-containing nanoliposomes to tumour hypoxic regions,” *Nature nanotechnology*, vol. 11, no. 11, p. 941, 2016.
- [271] H. Brenner, *Macrotransport processes*. Elsevier, 2013.
- [272] H. Brenner, “Dispersion resulting from flow through spatially periodic porous media,” *Philosophical Transactions of the Royal Society of London. Series A, Mathematical and Physical Sciences*, vol. 297, no. 1430, pp. 81–133, 1980.

- [273] R. Alonso-Matilla, B. Chakrabarti, and D. Saintillan, “Transport and dispersion of active particles in periodic porous media,” *Physical Review Fluids*, vol. 4, no. 4, p. 043101, 2019.
- [274] P.-G. de Gennes, “Reptation of a polymer chain in the presence of fixed obstacles,” *The journal of chemical physics*, vol. 55, no. 2, pp. 572–579, 1971.
- [275] G. Nam, A. Johner, and N.-K. Lee, “Reptation of a semiflexible polymer through porous media,” *The Journal of chemical physics*, vol. 133, no. 4, p. 044908, 2010.
- [276] K. D. Dorfman, S. B. King, D. W. Olson, J. D. Thomas, and D. R. Tree, “Beyond gel electrophoresis: Microfluidic separations, fluorescence burst analysis, and dna stretching,” *Chemical reviews*, vol. 113, no. 4, pp. 2584–2667, 2012.
- [277] H. Sambrook, “Molecular cloning: a laboratory manual. cold spring harbor, ny,” 1989.
- [278] C.-F. Chou, O. Bakajin, S. W. Turner, T. A. Duke, S. S. Chan, E. C. Cox, H. G. Craighead, and R. H. Austin, “Sorting by diffusion: An asymmetric obstacle course for continuous molecular separation,” *Proceedings of the National Academy of Sciences*, vol. 96, no. 24, pp. 13762–13765, 1999.
- [279] E. M. Sevick and D. Williams, “Long-lived states in electrophoresis: Collision of a polymer chain with two or more obstacles,” *EPL (Europhysics Letters)*, vol. 56, no. 4, p. 529, 2001.
- [280] J. M. Kim and P. S. Doyle, “Brownian dynamics simulations of a dna molecule colliding with a small cylindrical post,” *Macromolecules*, vol. 40, no. 25, pp. 9151–9163, 2007.
- [281] N. P. Teclemariam, V. A. Beck, E. S. Shaqfeh, and S. J. Muller, “Dynamics of dna polymers in post arrays: Comparison of single molecule experiments and simulations,” *Macromolecules*, vol. 40, no. 10, pp. 3848–3859, 2007.
- [282] J. Cho and K. D. Dorfman, “Brownian dynamics simulations of electrophoretic dna separations in a sparse ordered post array,” *Journal of Chromatography A*, vol. 1217, no. 34, pp. 5522–5528, 2010.
- [283] K. D. Dorfman, “Dna electrophoresis in microfabricated devices,” *Reviews of Modern Physics*, vol. 82, no. 4, p. 2903, 2010.
- [284] D. W. Olson, J. Ou, M. Tian, and K. D. Dorfman, “Continuous-time random walk models of dna electrophoresis in a post array: Part i. evaluation of existing models,” *Electrophoresis*, vol. 32, no. 5, pp. 573–580, 2011.
- [285] D. Kawale, G. Bouwman, S. Sachdev, P. L. Zitha, M. T. Kreutzer, W. R. Rossen, and P. E. Boukany, “Polymer conformation during flow in porous media,” *Soft matter*, vol. 13, no. 46, pp. 8745–8755, 2017.

- [286] A. Milchev, “Single-polymer dynamics under constraints: scaling theory and computer experiment,” *Journal of Physics: Condensed Matter*, vol. 23, no. 10, p. 103101, 2011.
- [287] Z. Mokhtari and A. Zippelius, “Dynamics of active filaments in porous media,” *arXiv preprint arXiv:1903.03815*, 2019.
- [288] T. Majmudar, E. E. Keaveny, J. Zhang, and M. J. Shelley, “Experiments and theory of undulatory locomotion in a simple structured medium,” *Journal of The Royal Society Interface*, vol. 9, no. 73, pp. 1809–1823, 2012.
- [289] T. Ohta and T. Ohkuma, “Deformable self-propelled particles,” *Physical review letters*, vol. 102, no. 15, p. 154101, 2009.
- [290] A. A. Evans, S. E. Spagnolie, D. Bartolo, and E. Lauga, “Elastocapillary self-folding: buckling, wrinkling, and collapse of floating filaments,” *Soft Matter*, vol. 9, no. 5, pp. 1711–1720, 2013.
- [291] M. Nagel, P.-T. Brun, H. Berthet, A. Lindner, F. Gallaire, and C. Duprat, “Oscillations of confined fibres transported in microchannels,” *Journal of Fluid Mechanics*, vol. 835, pp. 444–470, 2018.
- [292] J. Han and H. G. Craighead, “Separation of long dna molecules in a microfabricated entropic trap array,” *Science*, vol. 288, no. 5468, pp. 1026–1029, 2000.
- [293] G. I. Taylor, “Dispersion of soluble matter in solvent flowing slowly through a tube,” *Proceedings of the Royal Society of London. Series A. Mathematical and Physical Sciences*, vol. 219, no. 1137, pp. 186–203, 1953.
- [294] P. Gaspard and F. Baras, “Chaotic scattering and diffusion in the lorentz gas,” *Physical Review E*, vol. 51, no. 6, p. 5332, 1995.
- [295] A. Dehkharghani, N. Waisbord, J. Dunkel, and J. S. Guasto, “Bacterial scattering in microfluidic crystal flows reveals giant active taylor–aris dispersion,” *Proceedings of the National Academy of Sciences*, vol. 116, no. 23, pp. 11119–11124, 2019.
- [296] N. M. Karabacak, P. S. Spuhler, F. Fachin, E. J. Lim, V. Pai, E. Ozkumur, J. M. Martel, N. Kojic, K. Smith, P.-i. Chen, *et al.*, “Microfluidic, marker-free isolation of circulating tumor cells from blood samples,” *Nature protocols*, vol. 9, no. 3, p. 694, 2014.
- [297] M. G. OConnell, N. B. Lu, C. A. Browne, and S. S. Datta, “Cooperative size sorting of deformable particles in porous media,” *Soft matter*, vol. 15, no. 17, pp. 3620–3626, 2019.

- [298] G. Kabacaoglu and G. Biros, “Optimal design of deterministic lateral displacement device for viscosity-contrast-based cell sorting,” *Physical Review Fluids*, vol. 3, no. 12, p. 124201, 2018.
- [299] R. Aris, “On the dispersion of a solute in a fluid flowing through a tube,” in *Proceedings of the Royal Society of London A: mathematical, physical and engineering sciences*, vol. 235, pp. 67–77, The Royal Society, 1956.
- [300] P. Chatwin, “The approach to normality of the concentration distribution of a solute in a solvent flowing along a straight pipe,” *Journal of Fluid Mechanics*, vol. 43, no. 2, pp. 321–352, 1970.
- [301] I. Frankel and H. Brenner, “On the foundations of generalized taylor dispersion theory,” *Journal of Fluid Mechanics*, vol. 204, pp. 97–119, 1989.
- [302] G. Mercer and A. Roberts, “A centre manifold description of contaminant dispersion in channels with varying flow properties,” *SIAM Journal on Applied Mathematics*, vol. 50, no. 6, pp. 1547–1565, 1990.
- [303] W. a. Young and S. Jones, “Shear dispersion,” *Physics of Fluids A: Fluid Dynamics*, vol. 3, no. 5, pp. 1087–1101, 1991.
- [304] S. Vedel and H. Bruus, “Transient taylor–aris dispersion for time-dependent flows in straight channels,” *Journal of Fluid Mechanics*, vol. 691, pp. 95–122, 2012.
- [305] T. Perkins, O. Johnston, *et al.*, “A review of diffusion and dispersion in porous media,” *Society of Petroleum Engineers Journal*, vol. 3, no. 01, pp. 70–84, 1963.
- [306] H. B. Fischer, J. E. List, C. R. Koh, J. Imberger, and N. H. Brooks, *Mixing in inland and coastal waters*. Elsevier, 2013.
- [307] S. Ghosal, “Electrokinetic flow and dispersion in capillary electrophoresis,” *Annu. Rev. Fluid Mech.*, vol. 38, pp. 309–338, 2006.
- [308] D. L. Koch, R. G. Cox, H. Brenner, and J. F. Brady, “The effect of order on dispersion in porous media,” *Journal of Fluid Mechanics*, vol. 200, pp. 173–188, 1989.
- [309] E. Yariv and K. D. Dorfman, “Electrophoretic transport through channels of periodically varying cross section,” *Physics of Fluids*, vol. 19, no. 3, p. 037101, 2007.
- [310] D. Bolster, M. Dentz, and T. Le Borgne, “Solute dispersion in channels with periodically varying apertures,” *Physics of Fluids*, vol. 21, no. 5, p. 056601, 2009.
- [311] B. M. Rush, K. D. Dorfman, H. Brenner, and S. Kim, “Dispersion by pressure-driven flow in serpentine microfluidic channels,” *Industrial & engineering chemistry research*, vol. 41, no. 18, pp. 4652–4662, 2002.

- [312] K. D. Dorfman and H. Brenner, “Generalized taylor-aris dispersion in discrete spatially periodic networks: Microfluidic applications,” *Physical Review E*, vol. 65, no. 2, p. 021103, 2002.
- [313] O. C. Jeong, S. W. Park, S. S. Yang, and J. J. Pak, “Fabrication of a peristaltic pdms micropump,” *Sensors and Actuators A: Physical*, vol. 123, pp. 453–458, 2005.
- [314] C. A. Dragon and J. B. Grotberg, “Oscillatory flow and mass transport in a flexible tube,” *Journal of Fluid Mechanics*, vol. 231, pp. 135–155, 1991.
- [315] S. Ghoshal, “Dispersion of solutes in non-newtonian flows through a circular tube,” *Chemical Engineering Science*, vol. 26, no. 2, pp. 185–188, 1971.
- [316] S. Chakraborty, “Augmentation of peristaltic microflows through electro-osmotic mechanisms,” *Journal of Physics D: Applied Physics*, vol. 39, no. 24, p. 5356, 2006.
- [317] J. Jiménez-Lozano and M. Sen, “Particle dispersion in two-dimensional peristaltic flow,” *Physics of Fluids*, vol. 22, no. 4, p. 043303, 2010.
- [318] J. Jiménez-Lozano, M. Sen, and P. F. Dunn, “Particle motion in unsteady two-dimensional peristaltic flow with application to the ureter,” *Physical Review E*, vol. 79, no. 4, p. 041901, 2009.
- [319] M. H. Jacobs, *Diffusion processes*. Springer Science & Business Media, 2012.
- [320] R. Zwanzig, “Diffusion past an entropy barrier,” *The Journal of Physical Chemistry*, vol. 96, no. 10, pp. 3926–3930, 1992.
- [321] N. Laachi, M. Kenward, E. Yariv, and K. D. Dorfman, “Force-driven transport through periodic entropy barriers,” *EPL (Europhysics Letters)*, vol. 80, no. 5, p. 50009, 2007.
- [322] M. Mangeat, T. Guérin, and D. Dean, “Geometry controlled dispersion in periodic corrugated channels,” *EPL*, vol. 118, no. 4, p. 40004, 2017.
- [323] T. W. Latham, *Fluid motions in a peristaltic pump*. PhD thesis, Massachusetts Institute of Technology, 1966.
- [324] M. Jaffrin and A. Shapiro, “Peristaltic pumping,” *Annual Review of Fluid Mechanics*, vol. 3, no. 1, pp. 13–37, 1971.
- [325] S. Takabatake, K. Ayukawa, and A. Mori, “Peristaltic pumping in circular cylindrical tubes: a numerical study of fluid transport and its efficiency,” *Journal of Fluid Mechanics*, vol. 193, pp. 267–283, 1988.
- [326] P. Tong and D. Vawter, “An analysis of peristaltic pumping,” *Journal of Applied Mechanics*, vol. 39, no. 4, pp. 857–862, 1972.

- [327] T. D. Brown and T.-K. Hung, “Computational and experimental investigations of two-dimensional nonlinear peristaltic flows,” *Journal of Fluid Mechanics*, vol. 83, no. 2, pp. 249–272, 1977.
- [328] C. Pozrikidis, “A study of peristaltic flow,” *Journal of Fluid Mechanics*, vol. 180, pp. 515–527, 1987.
- [329] A. Siddiqui and W. Schwarz, “Peristaltic flow of a second-order fluid in tubes,” *Journal of Non-Newtonian Fluid Mechanics*, vol. 53, pp. 257–284, 1994.
- [330] J. Jiménez-Lozano and M. Sen, “Streamline topologies of two-dimensional peristaltic flow and their bifurcations,” *Chemical Engineering and Processing: Process Intensification*, vol. 49, no. 7, pp. 704–715, 2010.
- [331] G. K. Batchelor, *An introduction to fluid dynamics*. Cambridge university press, 2000.
- [332] T. A. Driscoll, N. Hale, and L. N. Trefethen, “Chebfun guide,” 2014.
- [333] C. M. Bender and S. A. Orszag, *Advanced mathematical methods for scientists and engineers I: Asymptotic methods and perturbation theory*. Springer Science & Business Media, 2013.
- [334] P. Szymczak and A. Ladd, “Boundary conditions for stochastic solutions of the convection-diffusion equation,” *Physical review E*, vol. 68, no. 3, p. 036704, 2003.
- [335] A. H. Shapiro, M. Y. Jaffrin, and S. L. Weinberg, “Peristaltic pumping with long wavelengths at low reynolds number,” *Journal of Fluid Mechanics*, vol. 37, no. 4, pp. 799–825, 1969.
- [336] C. Pozrikidis, “Creeping flow in two-dimensional channels,” *Journal of Fluid Mechanics*, vol. 180, pp. 495–514, 1987.
- [337] S. Mazumder, *Numerical methods for partial differential equations: finite difference and finite volume methods*. Academic Press, 2015.
- [338] C. Pozrikidis, “A note on the regularization of the discrete poisson–neumann problem,” *Journal of Computational Physics*, vol. 172, no. 2, pp. 917–923, 2001.
- [339] J. H. Ferziger and M. Peric, *Computational methods for fluid dynamics*. Springer Science & Business Media, 2012.
- [340] J. J. Higdon, “Stokes flow in arbitrary two-dimensional domains: shear flow over ridges and cavities,” *Journal of Fluid Mechanics*, vol. 159, pp. 195–226, 1985.
- [341] P. K. Kitanidis and B. B. Dykaar, “Stokes flow in a slowly varying two-dimensional periodic pore,” *Transport in porous media*, vol. 26, no. 1, pp. 89–98, 1997.

- [342] A. Eidsath, R. Carbonell, S. Whitaker, and L. Herrmann, “Dispersion in pulsed systemsiii: comparison between theory and experiments for packed beds,” *Chemical Engineering Science*, vol. 38, no. 11, pp. 1803–1816, 1983.
- [343] J. Salles, J.-F. Thovert, R. Delannay, L. Prevors, J.-L. Auriault, and P. Adler, “Taylor dispersion in porous media. determination of the dispersion tensor,” *Physics of Fluids A: Fluid Dynamics*, vol. 5, no. 10, pp. 2348–2376, 1993.
- [344] B. Felderhof, “Swimming and peristaltic pumping between two plane parallel walls,” *Journal of Physics: Condensed Matter*, vol. 21, no. 20, p. 204106, 2009.
- [345] M. Sauzade, G. J. Elfring, and E. Lauga, “Taylors swimming sheet: Analysis and improvement of the perturbation series,” *Physica D: Nonlinear Phenomena*, vol. 240, no. 20, pp. 1567–1573, 2011.
- [346] Z. Lin, J.-L. Thiffeault, and S. Childress, “Stirring by squirmers,” *Journal of Fluid Mechanics*, vol. 669, pp. 167–177, 2011.
- [347] K. C. Leptos, J. S. Guasto, J. P. Gollub, A. I. Pesci, and R. E. Goldstein, “Dynamics of enhanced tracer diffusion in suspensions of swimming eukaryotic microorganisms,” *Physical Review Letters*, vol. 103, no. 19, p. 198103, 2009.
- [348] A. Reynolds, “The swimming of minute organisms,” *Journal of Fluid Mechanics*, vol. 23, no. 02, pp. 241–260, 1965.
- [349] A. Perazzo, J. K. Nunes, S. Guido, and H. A. Stone, “Flow-induced gelation of microfiber suspensions,” *Proceedings of the National Academy of Sciences*, vol. 114, no. 41, pp. E8557–E8564, 2017.
- [350] F. MacKintosh, J. Käs, and P. Janmey, “Elasticity of semiflexible biopolymer networks,” *Physical review letters*, vol. 75, no. 24, p. 4425, 1995.
- [351] B. J. Walker, K. Ishimoto, and E. A. Gaffney, “Pairwise hydrodynamic interactions of synchronized spermatozoa,” *Phys. Rev. Fluids*, vol. 4, p. 093101, Sep 2019.
- [352] D. B. Stein and M. J. Shelley, “Coarse graining the dynamics of immersed and driven fiber assemblies,” *Phys. Rev. Fluids*, vol. 4, p. 073302, Jul 2019.
- [353] Q. Yang and L. Fauci, “Dynamics of a macroscopic elastic fibre in a polymeric cellular flow,” *Journal of Fluid Mechanics*, vol. 817, pp. 388–405, 2017.
- [354] B. Thomases and R. D. Guy, “The role of body flexibility in stroke enhancements for finite-length undulatory swimmers in viscoelastic fluids,” *Journal of Fluid Mechanics*, vol. 825, pp. 109–132, 2017.

- [355] S. Lim and C. S. Peskin, “Simulations of the whirling instability by the immersed boundary method,” *SIAM J. Sci. Comp.*, vol. 25, no. 6, pp. 2066–2083, 2004.
- [356] R. Cortez, “The method of regularized Stokeslets,” *SIAM J. Sci. Comput.*, vol. 23, no. 4, pp. 1204–1225, 2001.
- [357] R. Cortez, L. Fauci, and A. Medovikov, “The method of regularized Stokeslets in three dimensions: Analysis, validation, and application to helical swimming,” *Phys. Fluids*, vol. 17, no. 3, p. 031504, 2005.
- [358] J. Tyrrell, D. J. Smith, and R. J. Dyson, “Regularized Stokeslet rings: An efficient method for axisymmetric Stokes flow with application to the growing pollen tube,” *Phys. Rev. Fluids*, vol. 4, p. 063102, Jun 2019.
- [359] J. LaGrone, R. Cortez, and L. Fauci, “Elastohydrodynamics of swimming helices: Effects of flexibility and confinement,” *Phys. Rev. Fluids*, vol. 4, p. 033102, Mar 2019.